FACULTY OF ENGINEERING AND ARCHITECTURE

Modeling and Characterization of Electrically Pumped InGaAs/GaAs Nano-Ridge Lasers Monolithically Grown on Silicon

Andualem Ali Yimam

Doctoral dissertation submitted to obtain the academic degree of
Doctor of Photonics Engineering

Supervisors

Prof. Dries Van Thourhout, PhD - Prof. Geert Morthier, PhD

Department of Information Technology
Faculty of Engineering and Architecture, Ghent University

GHENT UNIVERSITY

ISBN null
NUR 926, 959
Wettelijk depot: null

Members of the Examination Board

Chair

Prof. Filip De Turck, PhD, Ghent University

Other members entitled to vote

Charles Caer, PhD, Centre Suisse d'Electronique et de Microtechnique, Switzerland
Prof. Frédéric Grillot, PhD, Télécom Paris, France
Prof. Günther Roelkens, PhD, Ghent University
Prof. Kasper Van Gasse, PhD, Ghent University

Supervisors

Prof. Dries Van Thourhout, PhD, Ghent University
Prof. Geert Morthier, PhD, Ghent University

Acknowledgements

Ghent, November 2025
Andualem Ali Yimam

Contents

List of Acronyms

A

AI artificial intelligence

AOM acousto-optic modulator

APD anti-phase domain

AR aspect ratio

ART Aspect Ratio Trapping

AWG arrayed waveguide grating

C

CELOG Corrugated Epitaxial Lateral Overgrowth

CMOS Complementary Metal-Oxide-Semiconductor

CW continuous-wave

D

DC direct current

DFB distributed feedback

DH double-heterostructure

DIM dielectric-insulator-metal

DUT device under test

DUV deep-ultraviolet

F

FCA free-carrier absorption

FDE Finite Difference Eigenmode

FDTD finite-difference time-domain

FP Fabry–Perot

FPI Fabry–Perot Interferometric

FSR free spectral range

FWHM Full Width at Half Maximum

H

HAADF-STEM high-angle annular dark-field scanning transmission electron microscopy

HWHM half-width at half maximum

I

IV current–voltage

IVBA intervalence band absorption

L

LED light emitting diode

LiDAR light detection and ranging

LIV light–current–voltage

LSI large-scale integration

M

MC Metallic Cavity

MD misfit dislocation

MMI-MZI multi-mode interferometer-Mach-Zehnder interferometer

MOVPE vapour-phase epitaxy

MRR microring resonator

MSI medium-scale integration

MZI Mach–Zehnder interferometer

N

NRE Nano-ridge Engineering

NRW nano-ridge waveguide

O

OSA optical spectrum analyzer

P

PC polarization controller

PCC Photonic Crystal Cavity

PD planar defect

PhC photonic crystal

PIC photonic integrated circuit

Q

quasi-TE quasi-transverse electric

QW quantum well

R

RC resistive-capacitive

RF radio-frequency

RIN relative intensity noise

RMSE root-mean-square error

S

SAG selective area growth

SCH separate-confinement heterostructure

SEM scanning electron microscopy

SHB spectral hole burning

SMF single mode fiber

SMSR side mode suppression ratio

spaser surface plasmon amplification by stimulated emission of radiation

SPP surface plasmon polariton

SRS stimulated Raman scattering

SSI small-scale integration

SSRM Scanning Spreading Resistance Microscopy

STI shallow trench isolation

SWG subwavelength grating

T

TASE Template-Assisted Selective Epitaxy

TCAD Technology Computer-Aided Design

TD threading dislocation

TDD threading dislocation density

TEM transmission electron microscopy

TPA two-photon absorption

U

UV ultraviolet

V

VCSEL vertical-cavity surface-emitting laser

VLSI very-large-scale integration

VNA vector network analyzer

W

WGM Whispering Gallery Mode

Samenvatting

Introductie

Siliciumfotonica biedt een weg naar dichte, compacte optische verbindingen, die gefabriceerd kunnen worden met processen oorspronkelijk ontwikkeld binnen het Complementary Metal-Oxide-Semiconductor (CMOS)-ecosysteem. De voordelen zijn onder meer transparantie in het infrarood, sterke optische opsluiting door een hoog indexcontrast en een matuur fabricageproces. Ook naadloze co-integratie met elektronica is in principe mogelijk. Ondanks opmerkelijke vooruitgang op het gebied van passieve componenten, modulatoren en fotodetectoren, blijft het ontbreken van een efficiënte lichtbron op de chip – als gevolg van de indirecte bandkloof van silicium – echter het belangrijkste obstakel voor volledig geïntegreerde fotonische systemen.

Om deze beperking te overwinnen, zijn verschillende III–V-on-Si integratiestrategieën onderzocht. Flip-chip integratie biedt architecturale flexibiliteit, maar is duur en minder compatibel met productie in grote volumes, terwijl heterogene die-to-wafer-bonding de schaalbaarheid verbetert, maar uitdagend is op het gebied van thermische eigenschappen en materiaalgebruik. Transfer printing is een alternatief, maar vereist een hoge uitlijningsnauwkeurigheid. Monolithische integratie van III–V-materialen op silicium biedt de meest schaalbare en kosteneffectieve route, maar brengt aanzienlijke materiaaluitdagingen met zich mee vanwege rooster-, polariteits- en thermische mismatches tussen silicium en III–V halfgeleiders. Deze mismatches resulteren in roosterfouten zoals dislocaties, antifase-vlakken en door spanning veroorzaakte defecten die de prestaties van de laser verslechteren. Om deze uitdagingen aan te pakken, zijn verschillende benaderingen ontwikkeld die defecten kunnen beperken of stoppen voordat ze het actieve gebied bereiken, vaak door de toevoeging van bufferlagen of het gebruik van selectieve epitaxiale technieken. Met name selectieve groei binnen smalle openingen in een oxidemasker onderdrukt effectief de verspreiding van defecten, terwijl daaropvolgende nanoridge-engineering de groei van het III-V-materiaal mogelijk maakt en zo toelaat om een hoge modale versterking te bereiken. Met behulp van deze aanpak werden in het verleden reeds optisch gepompte $In_{0,2}Ga_{0,8}As$/GaAs multi-kwantumput nano-ridge lasers die in de buurt van 1020 nm emitteren, met succes gedemonstreerd.

Het bereiken van een efficiënte elektrische injectie in dergelijke monolithische nano-ridge lasers bleef echter moeilijk, omdat de geometrie ervan het contactoppervlak beperkt en de optische overlap met het metaal vergroot, wat leidt tot sterke absorptie. Aan het begin van dit doctoraat realiseerde imec een belangrijke doorbraak door continuous-wave (CW)-lasering bij kamertemperatuur te demonstreren in elektrisch gepompte $In_{0,2}Ga_{0,8}As$/GaAs-kwantumput-nano-ridge-lasers met periodieke p-type contacten. Dit was mogelijk door gebruik te maken van een mode-beating-mechanisme langs de caviteit, dat de optische veldintensiteit onder de contacten minimaliseert en laserwerking mogelijk maakt.

In dit proefschrift wordt voortgebouwd op die basis door (i) een fysisch model te ontwikkelen dat de werking beschrijft van elektrisch geïnjecteerde InGaAs/GaAs-nano-rigdelasers op Si, (ii) uitgebreide statische en dynamische karakterisering uit te voeren om intrinsieke laserparameters te extraheren en prestatiebeperkende factoren te identificeren, en (iii) nieuwe distributed feedback (DFB)-caviteitsarchitecturen voor te stellen en te evalueren die zijn ontworpen voor compacte, single-mode werking met verbeterde prestaties. Samen vormen deze inspanningen een coherent kader dat de realisatie van monolithische III–V nano-ridge lasers vooruithelpt in de richting van schaalbare, hoogwaardige silicium-fotonische integratie.

Resultaten

De eerste stap van dit werk was gericht op het ontwikkelen van een semi-analytisch model dat de werkingsprincipes van elektrisch geïnjecteerde nano-ridge-lasers met mode beating kan beschrijven en toelaat deze lasers verder te optimaliseren. Het model reproduceerde met succes de waargenomen laserdynamica en drempelstroom, door te beschrijven hoe de interactie (beating) tussen de fundamentele en hogere transversale modi de contactgeïnduceerde absorptie kunnen verminderen. De voorspellingen kwamen uitstekend overeen met zowel experimentele metingen als finite-difference time-domain (FDTD)-simulaties, wat de onderliggende fysische aannames valideerde en de effectiviteit ervan als voorspellend instrument voor het optimaliseren van monolithische nano-ridge lasers aantoonde.

Optische verliesmetingen uitgevoerd met behulp van de Fabry–Perot Interferometric (FPI)-techniek brachten verstrooiingsverliezen van ongeveer $8,5\ \mathrm{cm}^{-1}$ aan het licht in ongedoteerde nano-ridge-golfgeleiders met sleufbreedtes tussen 150 nm en 300 nm, wat neerkomt op ongeveer 30% van het totale interne verlies in de elektrisch gepompte lasers. De afhankelijkheid van het verstrooiingsverlies van de sleufbreedte werd systematisch geanalyseerd, waaruit bleek dat het verlies toenam bij bredere sleuven als gevolg van een verminderde defectbeperking. Daarnaast werd de vrije-dragerabsorptie in gedoteerde gebieden gekwantificeerd, waaruit een sterke afhankelijkheid van de dragerconcentratie en het type dotering bleek. Dit liet toe een uitgebreid inzicht te verkrijgen in de intrinsieke optische verliezen die bepalend zijn voor de efficiëntie van de apparaten.

Door middel van uitgebreide statische en dynamische karakterisatie werden de belangrijkste parameters van de vervaardigde lasers bepaald. De gemeten lijnbreedtes varieerden van 37 tot 216 MHz, terwijl analyses van het verre veld een uitgesproken emissie-anisotropie aan het licht brachten als gevolg van de asymmetrische golfgeleider. Uit kleinsignaalmodulatie en relative intensity noise (RIN)-analyses werd een levensduur van 100–125 ps, D-factoren van ongeveer 1 GHz/mA$^{1/2}$ en K-factoren van 0,5–0,8 ns bepaald. De geëxtraheerde carrier capture-tijden zijn aanzienlijk langer dan die van conventionele kwantumput-lasers, voornamelijk als gevolg van de contactconfiguratie met een beperkt aantal wolfraam plugs, die de carrier-transporttijd vóór capture verlengt en daarmee de modulatiesnelheid beperkt.

Recombinatieanalyse op basis van S_{11}-metingen toonde aan dat defectgerelateerde niet-stralingsprocessen minder dan 5% van de drempelstroom bijdragen in sleuven van 60 nm en 80 nm en minder dan 10% in lasers van 100 nm, wat de effectiviteit bevestigt van aspectratio-trapping en nano-ridge-engineering bij de groei van het III–V-materiaal. De afhankelijkheid van recombinatiecoëfficiënten van de sleufbreedte werd ook vastgesteld, wat trends aan het licht bracht die consistent zijn met dislocatiebeperking en variaties in passiveringskwaliteit tussen verschillende geometrieën.

Op basis van deze inzichten werden verschillende DFB-laserarchitecturen voorgesteld en geëvalueerd, waaronder DFBs met gedeeltelijk verliesgekoppelde, zijdelingse Si- en bovenste p-GaAs-roosters. Deze ontwerpen bereikten single-mode laser werking in aanzienlijk kortere caviteiten (300–800 µm) met behoud van een acceptabele optische efficiëntie en smalle lijnbreedtes. Daarvan boden de eerste-orde zij-Si- en bovenste p-GaAs-structuren de beste prestaties, terwijl het tweede-orde p-GaAs-ontwerp volledige compatibiliteit met 193 nm deep-ultraviolet (DUV) vertoont. Complementaire Technology Computer-Aided Design (TCAD)-simulaties bevestigden dat architecturen met continu contact waarin matig gedoteerde InGaP-lagen zijn opgenomen, de uniformiteit van de dragerinjectie verbeteren met minimale spanningsoverhead, wat een veelbelovende weg biedt naar efficiëntere en beter produceerbare monolithische nano-ridge lasersystemen.

Conclusie en Toekomstperspectief

Dit werk presenteerde een uitgebreid analytisch en experimenteel kader voor monolithische InGaAs/GaAs-nano-ridge-lasers op silicium. Hiermee wordt hun potentieel aangetoond als compacte, efficiënte en schaalbare lichtbronnen voor CMOS-compatibele siliciumfotonica. Door een combinatie van gedetailleerde karakterisering van optische verliezen, semi-analytische modellering en uitgebreide statische en dynamische metingen, biedt het onderzoek diepgaand inzicht in de mechanismen die optische verliezen, modulatiesnelheid en ladingsdragersdynamica in nano-ridge structuren bepalen. De voorgestelde DFB-laserarchitecturen pakken bovendien de beperkingen van mode-beating gebaseerde kasers aan en beloven

single-mode werking met concurrentiële efficiëntie, smalle lijnbreedte en goede reproduceerbaarheid.

Toekomstig onderzoek moet zich richten op het verminderen van verstrooiingsverliezen – gemeten op ongeveer $8,5\ \mathrm{cm}^{-1}$ in ongedoteerde nano-ridge golfgeleiders – door de uniformiteit van de fabricage te verfijnen en het structurele ontwerp te optimaliseren. De fabricage en het testen van de voorgestelde DFB-architecturen zullen cruciaal zijn voor het benchmarken van de prestaties, ondersteund door systematische statische en dynamische karakterisering om de meest efficiënte configuraties te identificeren en hun schaalbaarheid te beoordelen door middel van DUV-lithografie. Verdere verbetering kan ook komen van alternatieve geometrieën, zoals continu-contactschema's met een gefacetteerde, hoedvormige p-GaAs-laag die de optische absorptie minimaliseert en tegelijkertijd een efficiënte dragerinjectie toelaat. Voor de toekomst blijft het verschuiven van de emissiegolflengte van elektrisch geïnjecteerde nano-rdige-lasers naar de O- en C-banden een belangrijk onderzoeksgebied. Dit kan worden bekomen met behulp van $In_{0,45}Ga_{0,55}As$-kwantumputten op $In_{0,25}Ga_{0,75}As$ nano-ridge-basissen, GaInNAs/GaAs-materiaalsystemen of InAs-kwantumdots in combinatie met $In_xGa_{1-x}As$ metamorfe buffers om een emissie van 1,3–1,5 µm te bereiken. Tegelijkertijd zullen voortdurende verbeteringen op het gebied van thermisch beheer en efficiënte optische koppeling aan siliciumfotoniccircuits van cruciaal belang zijn voor de realisatie van volledig geïntegreerde, hoogwaardige III–V/Si-lasersystemen.

Summary

Introduction

Silicon photonics offers a pathway to dense, energy-efficient optical interconnects within the CMOS ecosystem. Its advantages include infrared transparency, strong optical confinement through high index contrast, and mature wafer-scale fabrication enabling seamless co-integration with electronics. Despite remarkable advances in passive components, modulators, and photodetectors, the lack of an efficient on-chip light source—stemming from silicon's indirect bandgap—remains the principal obstacle to fully integrated photonic systems.

To overcome this limitation, several III–V-on-Si integration strategies have been explored. Hybrid flip-chip bonding offers architectural flexibility but is costly and slow for high-volume manufacturing, while heterogeneous die-to-wafer bonding improves scalability yet faces thermal and material-utilization challenges. Transfer printing enhances throughput but requires high alignment precision. In contrast, monolithic integration of III–V materials on silicon provides the most scalable and cost-effective route but introduces significant materials challenges due to lattice, polarity, and thermal mismatches between silicon and III–V compounds. These mismatches generate threading dislocations, antiphase boundaries, and strain-induced defects that degrade device performance. To address these challenges, various approaches have been developed to confine and terminate defects before they reach the active region, often through the incorporation of buffer layers or selective epitaxial techniques. In particular, selective growth within narrow oxide trenches effectively suppresses defect propagation, while subsequent nano-ridge engineering enables the outgrowth of the III–V material to achieve high modal gain. Using this approach, optically pumped $In_{0.2}Ga_{0.8}As$/GaAs multi-quantum-well nano-ridge lasers emitting near 1020 nm have been successfully demonstrated.

Achieving efficient electrical injection in such monolithic nano-ridge lasers, however, remained elusive because the nanoscale device geometry restricts the contact area and increases optical overlap with the metal, causing strong absorption. At the outset of this PhD, imec realized a major breakthrough by demonstrating CW lasing at room temperature in electrically pumped $In_{0.2}Ga_{0.8}As$/GaAs quantum-well nano-ridge lasers featuring periodic p-type contacts. This was achieved by exploit-

ing a mode-beating mechanism along the cavity, which minimizes the optical field intensity beneath the contacts and enables sustained lasing.

This dissertation builds on that foundation by (i) developing a predictive physical model describing the operation of electrically injected InGaAs/GaAs nano-ridge lasers on Si, (ii) performing comprehensive static and dynamic characterization to extract intrinsic device parameters and identify performance-limiting factors, and (iii) proposing and evaluating new DFB cavity architectures designed for compact, single-mode operation with enhanced performance. Together, these efforts establish a coherent framework that advances monolithic III–V nanolasers toward scalable, high-performance silicon-photonic integration.

Results

The first step of this work focused on developing a semi-analytical model capable of describing the operating principles of electrically injected nano-ridge lasers working with the mode-beating approach and guiding their optimization. The model successfully reproduced the observed mode dynamics and threshold behavior by capturing the interaction between the fundamental and higher-order transverse modes that reduce contact-induced absorption. Its predictions showed excellent agreement with both experimental measurements and FDTD simulations, validating the underlying physical assumptions and demonstrating its effectiveness as a predictive tool for optimizing monolithic nano-ridge and related guided-wave photonic structures.

Optical loss measurements performed using the FPI technique revealed scattering losses of approximately 8.5 cm^{-1} in undoped nano-ridge waveguides with trench widths between 150 nm and 300 nm—accounting for roughly 30% of the total internal loss in the electrically pumped devices. The dependence of the scattering loss on the trench width was systematically analyzed, showing an increase with wider trenches due to reduced defect confinement. In addition, free-carrier absorption in doped regions was quantified, revealing strong dependence on carrier concentration and doping type, thereby providing a comprehensive understanding of the intrinsic optical losses governing device efficiency.

Extensive static and dynamic characterizations established the key performance parameters of the fabricated devices. Measured linewidths ranged from 37 to 216 MHz, while far-field analyses revealed pronounced emission anisotropy resulting from the asymmetric ridge geometry. Small-signal modulation and RIN analyses yielded carrier capture times of 100–125 ps, D-factors of approximately 1 GHz/mA$^{1/2}$, and K-factors of 0.5–0.8 ns. The extracted carrier capture times are notably longer than those typical of conventional quantum-well lasers, primarily due to the sparse metal-plug configuration, which increases the carrier transport time before capture and consequently limits the modulation speed.

Recombination analysis from S_{11} measurements showed that defect-related non-radiative processes contribute less than 5% of the threshold current in 60 nm and 80 nm trenches and below 10% in 100 nm devices, confirming the effectiveness of aspect-ratio trapping and nano-ridge engineering in producing high-quality III–V material on silicon. The dependence of recombination coefficients on trench width was also established, revealing trends consistent with dislocation confinement and passivation quality variations across different geometries.

Building upon these insights, several DFB laser architectures were proposed and evaluated, including DFBs with partly loss-coupled, side-Si, and top p-GaAs gratings. These designs achieved single-mode lasing in significantly shorter cavities (300–800 µm) while maintaining acceptable optical efficiency and narrow linewidths. Among them, the first-order side-Si and top p-GaAs structures provided the best performance trade-offs, whereas the second-order p-GaAs design demonstrated full compatibility with 193 nm DUV, enabling scalable fabrication. Complementary TCAD simulations confirmed that continuous-contact architectures incorporating moderately doped InGaP layers improve carrier injection uniformity with minimal voltage overhead, offering a promising pathway toward more efficient and manufacturable monolithic nano-ridge laser systems.

Conclusion and perspectives

This work has established a comprehensive analytical and experimental framework for monolithic InGaAs/GaAs nano-ridge lasers on silicon, demonstrating their viability as compact, efficient, and scalable on-chip light sources for CMOS-compatible silicon photonics. By combining detailed optical loss characterization, semi-analytical modeling, and extensive static and dynamic measurements, the research clarified the mechanisms governing optical losses, modulation speed and carrier dynamics in nano-ridge structures. The proposed DFB laser architectures further addressed the limitations of mode-beating devices, offering compact single-mode operation with competitive efficiency, linewidth, and manufacturability.

Future research should focus on reducing scattering losses—measured at roughly 8.5 cm^{-1} in undoped nano-ridge waveguides—by refining fabrication uniformity and optimizing structural design. The fabrication and testing of the proposed DFB architectures will be crucial for benchmarking performance, supported by systematic static and dynamic characterization to identify the most efficient configurations and assess their scalability through DUV lithography. Further improvement may also come from alternative device geometries, such as continuous-contact schemes incorporating a faceted, hat-shaped p-GaAs layer that minimizes optical absorption while maintaining efficient carrier injection. Looking forward, extending the emission wavelength of electrically injected nano-ridge lasers to the O- and C-bands remains a major research frontier. This can be pursued using $In_{0.45}Ga_{0.55}As$ quantum wells on $In_{0.25}Ga_{0.75}As$ nano-ridge bases, GaInNAs/GaAs material systems,

or InAs quantum dots combined with $In_xGa_{1-x}As$ metamorphic buffers to achieve 1.3–1.5 μm emission. In parallel, continued advances in thermal management and efficient optical coupling to silicon photonic circuits will be key to realizing fully integrated, high-performance III–V/Si laser systems.

1

Introduction

Contents

Silicon photonics is a key enabler of scalable, high-speed, and energy-efficient optical interconnects, offering dense integration of photonic components within CMOS infrastructure. Yet, the lack of efficient light emission due to silicon's indirect bandgap presents a major limitation. To overcome this, research has focused on integrating direct-bandgap III–V materials onto silicon. Among these efforts, monolithically integrated InGaAs/GaAs nano-ridge lasers have shown strong potential for compact, electrically pumped light sources. This chapter builds toward their realization by outlining the fundamentals of silicon photonics, surveying III–V integration strategies, and addressing the challenges of electrical injection in monolithically grown lasers on silicon.

The chapter is organized as follows. Section 1.1 introduces the scientific background, covering silicon photonics, III–V on silicon integration strategies, and the design principles of electrically injected nanolasers. Section 1.2 outlines the key objectives that guide this research. Section 1.3 provides a roadmap of the thesis structure, highlighting the content of each subsequent chapter.

1.1 Research background

1.1.1 Silicon Photonics

Silicon photonics is a rapidly evolving field dedicated to integrating photonic components and systems onto silicon-based platforms by leveraging the well-established CMOS manufacturing infrastructure. The foundation of this field dates back to the 1980s, when researchers began exploring silicon's optical properties for telecommunications. However, it was in the early 2000s that the field gained momentum, propelled by advances in nanofabrication and a growing need for higher data bandwidths in the telecommunications industry. Key early developments included the demonstration of high-speed modulators and low-loss silicon waveguides [1]. By the mid-2000s, the prospect of large-scale integration of photonics with electronics attracted significant academic and industrial investment. As shown in Figure 1.1, successive generations of photonic integration—ranging from small-scale integration (SSI) to very-large-scale integration (VLSI)—reflect a dramatic increase in the complexity and functionality of silicon photonic integrated circuits (PICs) [2, 3].

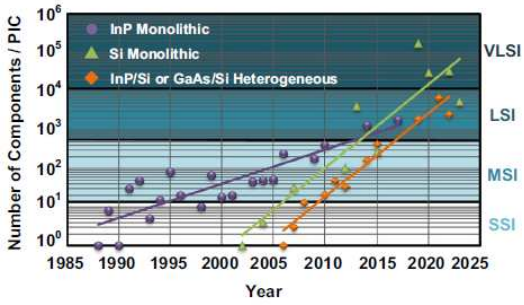

Figure 1.1: Timeline showing the number of components integrated on a silicon photonic integrated circuit (PIC) across successive generations of integration—SSI, medium-scale integration (MSI), large-scale integration (LSI), and VLSI. Each component represents a unit cell, such as a waveguide, directional coupler, heater, or grating coupler, that can be combined to form complex circuits. Reproduced from [3].

The appeal of silicon photonics lies in its unique combination of optical and fabri-

cation advantages. Silicon is transparent in the infrared range (1.1–7 μm), making it compatible with telecommunication wavelengths (1.3–1.55 μm). Its compatibility with standard CMOS processes allows for scalable and cost-effective manufacturing, facilitating co-integration with electronics. Additionally, the high refractive index contrast between silicon and silicon dioxide enables tight optical confinement, allowing for ultra-compact photonic circuits. These characteristics have led to its widespread application in high-speed communications [2–8], light detection and ranging (LiDAR) [9–13], biomedical sensing [14–16], programmable photonics [17], optical switching [18], imaging [19], and emerging computing paradigms such as photonic artificial intelligence (AI) [20, 21].

A cornerstone of any silicon photonics platform is its passive waveguide technology. The two main waveguide platforms in silicon photonics are silicon (Si) on insulator and silicon nitride (Si_3N_4) on insulator, each offering distinct trade-offs [22]. Silicon waveguides support tight bending radii and compact layouts due to their high index contrast with the buried oxide, albeit at the cost of comparatively higher propagation losses—primarily due to sidewall roughness. Advances in fabrication techniques have reduced these losses significantly, with propagation loss values as low as 0.1 dB/cm in the C-band for silicon rib waveguides [23]. Silicon nitride waveguides, on the other hand, offer lower loss—reported down to 1.77 dB/m [24]—and a wider transparency window, making them ideal for various applications. The choice of material is thus driven by application-specific trade-offs between loss, integration density, and spectral performance.

Passive silicon photonic components for filtering and routing include microring resonators (MRRs), Mach–Zehnder interferometers (MZIs), and arrayed waveguide gratings (AWGs). MRRs are valued for their compact footprint and high extinction ratios, achieving up to 60 dB [25], with large free spectral ranges exceeding 180 nm [26]. MZI-based filters offer greater design flexibility and thermal tunability; recent developments have demonstrated a single-stage multi-mode interferometer-Mach-Zehnder interferometer (MMI-MZI) filter with a 3-dB bandwidth of 60 nm and extinction ratio of 61.2 dB [27]. Meanwhile, AWGs are indispensable for dense wavelength division multiplexing (DWDM), with modern implementations achieving 32 channels at 100 GHz spacing and insertion loss of just 4.5 dB [28]. Recent design methodologies—such as inverse design [29] and subwavelength gratings (SWGs) [30]—are further enhancing performance by improving bandwidth, insertion loss, and fabrication tolerance. Nonetheless, challenges such as polarization control, wafer-scale uniformity, and ultra-low loss remain active areas of research.

On the active front, silicon photonic modulators and photodetectors have made impressive progress. Modulators—implemented in waveguides, MRRs, or MZIs—now

support extremely high data rates. For example, a recent microring modulator array demonstrated 200 Gbps per channel and 1 Tbps aggregate throughput at sub-10 fJ/bit energy efficiency [31]. MZI modulators based on hybrid material platforms such as silicon-lithium niobate have achieved modulation bandwidths up to 110 GHz while handling optical powers of 110 mW [32]. On the detection side, germanium-on-silicon photodetectors now deliver both high responsivity—up to 1.15 A/W at 1.55 μm [33]—and high bandwidths of 60 GHz [34], underscoring their readiness for next-generation optical transceivers.

The discussion now turns to the realization of light sources—arguably the most challenging component in silicon photonics. The following section addresses key barriers to on-chip laser integration and surveys the various approaches currently under development to overcome these hurdles.

1.1.2 III/V on Si Integration Approaches

One of the principal limitations of silicon photonics lies in the material's intrinsic nature: silicon is an indirect bandgap semiconductor and, therefore, an inefficient light emitter. To circumvent this challenge, several strategies have been explored. One of the earliest efforts was the development of silicon Raman lasers that leverage stimulated Raman scattering (SRS). Intel researchers demonstrated the first CW silicon Raman laser in 2005 using a reverse-biased p-i-n diode to suppress free-carrier absorption (FCA) caused by two-photon absorption (TPA), achieving single-mode lasing with a linewidth below 80 MHz and side-mode suppression greater than 55 dB [35]. Further advances, particularly using photonic crystal (PhC) nanocavities with high quality factors and small mode volumes, have brought lasing thresholds down to the microwatt range [36]. Despite this progress, silicon Raman lasers still face challenges such as reliance on external optical pumping and persistent FCA losses.

A more promising route for achieving efficient on-chip light emission is through the integration of direct-bandgap III–V semiconductors with silicon. III–V materials exhibit superior optical properties, including high radiative efficiency and carrier mobility, enabling electrically pumped lasers across a wide spectral range. This method offers clear advantages in efficiency and operational simplicity over silicon Raman lasers, making it a preferred strategy for achieving on-chip lasing in silicon photonics.

One prominent method for integrating III–V lasers onto silicon is hybrid flip-chip bonding [37, 38], which offers considerable flexibility by supporting a wide range of materials and device architectures. This technique allows for the independent optimization of both the III–V laser structures and the silicon photonic circuits prior

to integration. However, despite its adaptability, flip-chip bonding is inherently slow and cost-intensive, making it less suitable for high-volume manufacturing.

An alternative is heterogeneous die-to-wafer bonding [39–42], a widely adopted approach over the past decade. This technique enables parallel processing and the integration of pre-fabricated devices using optimized materials and structures. Nonetheless, it faces challenges such as limited thermal dissipation, the need for precise control over bonding layer thickness to ensure efficient optical coupling, significant III–V material wastage post-bonding, and elevated fabrication costs.

A third integration strategy is transfer printing [43–46], which offers higher throughput by enabling the simultaneous placement of a large number of devices onto a target substrate. Unlike die-to-wafer bonding, it avoids the need to remove unused III–V material, making it potentially more material-efficient. However, it demands high alignment accuracy for effective coupling and can suffer from bonding quality issues due to the high aspect ratios commonly associated with laser device geometries.

To address the limitations of the aforementioned methods, the monolithic integration of III–V materials on silicon emerges as the ultimate solution, offering scalability and cost-effectiveness that make it highly attractive for large-scale production. However, direct integration of III–V materials onto silicon presents several critical challenges. Chief among them is the significant lattice mismatch between silicon and common III–V materials (such as GaAs and InP), which leads to the formation of line defects like threading dislocations (TDs) and misfit dislocations (MDs) [47]. These defects act as nonradiative recombination centers, severely degrading the performance and reliability of active devices. Additionally, the mismatch in crystallographic polarity between III–V (polar) and silicon (nonpolar) materials can result in planar defects such as antiphase boundaries (APBs) and stacking faults. Thermal expansion coefficient disparities between the two materials further introduce mechanical strain during fabrication and thermal cycling, increasing the risk of cracking and delamination in the epitaxial layers.

To overcome these issues, two main monolithic approaches have been developed: blanket epitaxy and selective epitaxy. Blanket epitaxy focuses on uniformly growing III–V layers over large silicon areas. Techniques to suppress APBs include Si(111) faceting and surface treatments, while TDs are mitigated using thick buffer layers and dislocation filter structures. Using this approach, high-performance lasers comparable to those on native III–V substrates have been demonstrated [48–53]. While blanket epitaxy enables the integration of III/V devices with larger volume, it necessitates thick buffer layers, which complicates co-integration with other silicon-based components. Additionally, to prevent covering the entire silicon wafer with III–V material, localized growth may be required.

In the second approach of selective epitaxy, III–V materials are grown on predefined areas of the substrate, guided by dielectric masks or templates [47, 54]. Variants of the selective epitaxy technique are discussed below.

Aspect Ratio Trapping (ART)
ART involves growing III–V materials within narrow, high-aspect-ratio trenches formed in silicon and lined with SiO_2 spacers. Growth often starts with V-shaped silicon grooves which play a critical role in suppressing anti-phase domains (APDs) [55], while the more detrimental TDs are effectively trapped and terminated at the oxide sidewalls [47]. Using the selective growth technique, InP-based DFB laser arrays have been monolithically grown on (001) silicon, demonstrating single-mode lasing under pulsed optical pumping at 920 nm [56]. The lasing wavelength was later extended to the O-band by growing InGaAs layers on InP templates [57]. Room-temperature C-band operation has also been achieved with in-plane InP/InGaAs nanolaser arrays on (001) SOI substrates under pulsed optical pumping [58].

Nano-ridge Engineering (NRE)
In this approach, the ART technique is initially employed to selectively grow III–V materials within narrow oxide trenches. This is followed by nano-ridge engineering, wherein the III–V material is extended beyond the trench to achieve high modal gain [59]. By changing the growth rate on different crystal planes, the dimensions, composition, and geometry of the resulting nano-ridge structures can be precisely tailored to meet specific application requirements [60–62].

Using the NRE concept, extensive research at imec has demonstrated the successful epitaxial growth of GaAs and GaSb nano-ridges on silicon [60–62]. Figures 1.2 (a)–(c) present cross-sectional SEM images of GaAs nano-ridges formed in oxide trenches with widths of 60 nm, 100 nm, and 500 nm (denoted as 'W') [63]. These nano-ridges act as fully relaxed buffers for the pseudomorphic growth of the active region, consisting of three compressively strained $In_{0.2}Ga_{0.8}As$ quantum wells, each 9–10 nm thick. A lattice-matched InGaP passivation layer is finally deposited around the nano-ridges to mitigate non-radiative surface recombination at the defective GaAs interfaces. Figure 1.2 (d) presents a high-angle annular dark-field scanning transmission electron microscopy (HAADF-STEM) image of a nano-ridge grown with a 100 nm wide trench, featuring three InGaAs quantum wells and an InGaP passivation layer. In this technique, V-shaped silicon grooves effectively suppress the formation of APDs, while ART confines TDs and inclined planar defects (PDs) using the vertical oxide sidewalls.

Devices based on these structures have demonstrated lasing under pulsed optical

pumping near 1020 nm [64], and with higher In content, emission has been extended to the O-band [65]. Electrically injected $In_{0.2}Ga_{0.8}As$/GaAs nano-ridge laser arrays, fully fabricated in a 300 mm CMOS pilot line, have also been demonstrated [66], achieving continuous-wave lasing at room temperature with emission wavelengths around 1020 nm. The present work focuses on a detailed investigation of these lasers, with further discussion provided in the subsequent chapters.

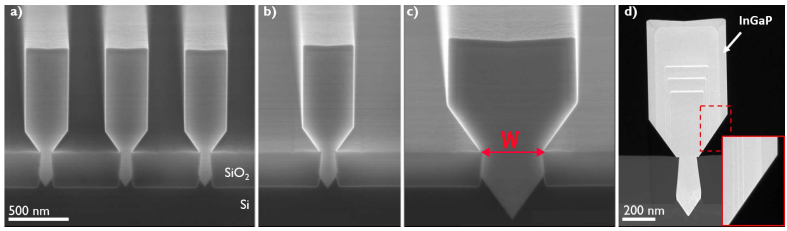

Figure 1.2: (a)–(c) display scanning electron microscopy (SEM) cross-sectional images of GaAs nano-ridges formed in oxide trenches with widths of 60 nm, 100 nm, and 500 nm (denoted by 'W'), respectively, all shown at the same scale. (d) presents a HAADF-STEM image of a nano-ridge grown with a 100 nm-wide trench, featuring three InGaAs quantum wells and an InGaP passivation layer. Reproduced from [63].

Other Methods

Template-Assisted Selective Epitaxy (TASE) is another variant of selective epitaxy that effectively suppresses TDs by minimizing the III–V/Si nucleation area. In this technique, growth initiates from a small silicon seed and is guided laterally through a predefined oxide template. Due to the confined nucleation and controlled lateral expansion, the laterally grown regions remain virtually dislocation-free. In [67], this approach enabled the demonstration of optically pumped AlGaAs/GaAs microdisk lasers operating at room temperature.

To achieve larger III–V volumes—on the order of tens of micrometers—beyond the trench region, Corrugated Epitaxial Lateral Overgrowth (CELOG) can be employed. In this method, III–V material is first grown vertically within a microchannel, and lateral overgrowth commences once the growth front reaches the end of a designed spacer. The resulting laterally overgrown region is free from threading dislocations, offering a high-quality material platform for advanced photonic integration [68].

Another implementation of selective area growth (SAG) involves the vertical growth of III–V nanowires through nanometer-scale openings in dielectric masks, enabling defect-filtered epitaxy on Si(111) [69]. By confining the nucleation area, both misfit and threading dislocations are minimized, facilitating high-quality nanowire formation without buffer layers.

1.1.3 Electrically pumped nanolasers

Electrically pumped nanolasers are compact semiconductor lasers capable of generating coherent light at subwavelength scales through direct electrical pumping. These nanoscale light sources have garnered significant attention due to their potential to meet the growing demands for high-speed, energy-efficient optical communication and integration into densely packed photonic circuits [70, 71]. Their defining characteristics include ultra-small physical footprints, low power consumption, and the ability to achieve high modulation speeds [71, 72]. Such traits are made possible by engineering cavities with minimal volumes, which not only enhance the confinement of electromagnetic fields in space, time, and frequency but also increase the spontaneous emission coupling factor (β) [72]. A higher β enables stimulated emission to occur at lower pump levels, leading to reduced lasing thresholds and, in some cases, thresholdless operation. The miniaturization of laser cavities—achieved through advanced designs such as dielectric and plasmonic structures—has also opened new pathways for integrating optical feedback, thermal management, and electrical contacts within nanoscale dimensions [73]. These innovations have expanded the applicability of nanolasers across a wide spectrum of fields, including on-chip optical interconnects, biosensing, super-resolution imaging, ultra-dense data storage, nanolithography, and near-field spectroscopy [70–78]. As a result, electrically injected nanolasers are positioned as key enablers of next-generation optoelectronic systems, where their compact size and superior performance characteristics are critical for realizing scalable, high-density photonic integration.

Electrically pumped nanolasers can be categorized based on the type of optical cavity used to achieve lasing, as well as their specific structural configurations tailored to different application requirements. The following sections will explore these classifications in detail.

1.1.3.1 Lasing cavities for nanolasers-different strategies

One of the key factors influencing the performance of electrically injected nanolasers is the design of the optical cavity used to sustain lasing. The cavity enables strong optical confinement, leading to the formation of resonant modes at discrete frequencies determined by the cavity geometry and material properties. Lasing occurs when the optical gain provided by the active region compensates for the losses within the cavity for one of the resonant modes. In the following sections, we discuss the primary cavity architectures employed to realize lasing in electrically pumped nanolasers.

Fabry–Perot cavity

In a Fabry–Perot (FP) nanolaser, the optical cavity is typically formed by a semiconductor nanowire or nano-ridge structure with reflective end facets that act as mirrors. The light propagates back and forth between these facets, forming a standing wave. The allowed lasing wavelengths are determined by the resonance condition [79]:

$$\lambda_m = \frac{2n_{eff}L}{m} \tag{1.1}$$

where m is an integer (mode number), λ is the wavelength of the lasing mode in vacuum, n_{eff} is the effective index of the guided mode, and L is the physical length of the cavity.

The spectral separation (mode spacing) between adjacent longitudinal modes (also called the free spectral range (FSR)) is:

$$\Delta\lambda = \frac{\lambda^2}{2L\left(n_{eff} - \lambda\frac{\mathrm{d}n_{eff}}{\mathrm{d}\lambda}\right)} = \frac{\lambda^2}{2n_gL} \tag{1.2}$$

where n_g is the group index of the mode.

Whispering Gallery Mode (WGM)

WGM nanolasers operate based on the principle of light confinement via continuous total internal reflection within curved dielectric boundaries, typically found in microdisks, microspheres, or microrings. Analogous to the acoustic whispering gallery effect, light in WGM cavities circulates along the periphery of the resonator, creating high-quality (high-Q) optical modes due to minimal scattering and radiation losses. The tight optical confinement results in enhanced light–matter interaction, making these cavities particularly attractive for low-threshold lasing at the nanoscale. A key feature of WGM nanolasers is their ability to support high-Q resonances in very compact geometries, allowing them to operate efficiently with low energy consumption and high spectral purity [80].

For a WGM resonator, the mode spacing is given by [81]:

$$\Delta\lambda_m = \frac{\lambda^2}{L\left(n_{eff} - \lambda\frac{\mathrm{d}n_{eff}}{\mathrm{d}\lambda}\right)} = \frac{\lambda^2}{n_gL} \tag{1.3}$$

where L is the optical path length traversed by light in the specific WGM cavity.

Photonic Crystal Cavity (PCC)

PCCs play a critical role in nanolaser design due to their ability to confine light in

ultrasmall volumes with exceptionally high quality (Q) factors. These cavities are formed by introducing a defect into a periodic dielectric structure, which creates a localized optical mode within the photonic bandgap, effectively trapping photons in a very small volume (V) of approximately $(\lambda/2n)^3$ [82]. This strong optical confinement enhances light–matter interaction, substantially increasing the spontaneous emission coupling factor (β), which is crucial for enabling low-threshold or even thresholdless lasing, as well as supporting high-speed modulation [83].

Metallic Cavity (MC)
MCs have become a critical enabler in the scaling of nanolasers to truly subwavelength dimensions, thanks to their ability to support plasmonic or hybrid plasmonic modes that confine light beyond the diffraction limit. Unlike dielectric cavities, which are limited in spatial confinement by the optical wavelength, metallic structures exploit surface plasmon polaritons (SPPs)—electromagnetic waves coupled to collective electron oscillations at metal-dielectric interfaces—to achieve extreme field localization at the nanoscale [84]. These cavities provide strong feedback and mode confinement even in deeply subwavelength volumes, which enhances light–matter interaction and significantly increases the spontaneous emission rate through the Purcell effect [85].

1.1.3.2 Nanolaser configurations

The various cavity architectures described above for electrically injected nanolasers can be realized through several device configurations, the most prominent of which are discussed below.

Nanowire Lasers
These devices use semiconductor nanowires whose end facets serve as reflective mirrors to form a Fabry–Pérot cavity. Early demonstrations by Duan et al. [86] realized electrically driven lasing in single-crystal CdS nanowires under electrical injection, with clear mode spacing inversely proportional to the nanowire length. Figure 1.3 illustrates the device structure and emission characteristics of this work, where the cross-sectional schematic shows carrier injection along the CdS nanowire from the top metal and bottom p-Si contacts, and the optical and electroluminescence images confirm nanowire placement and light emission at the exposed end under $\sim 80\ \mu A$ current at room temperature.

Nanowires can also be utilized in the form of organized arrays, where multiple nanowires are aligned in a controlled orientation to function collectively as an active medium. This configuration offers enhanced modal confinement and improved

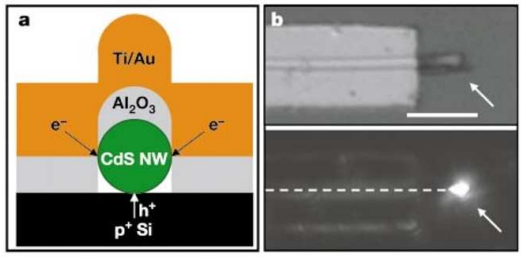

Figure 1.3: (a) A cross-sectional schematic of the nanowire by Duan et al. showing the material stack (b) Optical image of the nanowire, with an arrow indicating the exposed end of the CdS nanowire (top panel) and a room-temperature electroluminescence image at ~ 80 *μA injection, highlighting emission from the nanowire end and its position with a dashed line (bottom panel). Reproduced from [86].*

thermal and electrical performance. For instance, InGaN/GaN nanowire arrays grown on silicon substrates (as illustrated in the schematic and material stack in Figure 1.4) have exhibited continuous-wave lasing with modulation bandwidths reaching up to $5.8\ GHz$ [87].

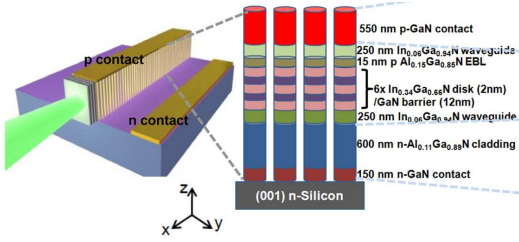

Figure 1.4: Schematic illustration of the nanowire array configuration with edge emission (left) and the corresponding material stack structure (right). Reproduced from [87].

Nanobeam Lasers

Nanobeam lasers utilize PCCs for achieving optical confinement. These cavities rely on periodic dielectric structures that exhibit a photonic bandgap, as discussed in the preceding section. By introducing a localized defect within the periodic lattice, a confined optical mode is created inside the bandgap. This configuration leads to strong spatial confinement of photons, resulting in ultrasmall mode volumes and high quality (Q) factors, both of which are critical for achieving low-threshold lasing and enhanced light–matter interactions.

Several key demonstrations have highlighted the potential of electrically injected nanobeam lasers for integrated photonics. Crosnier et al. [88] developed an electrically pumped hybrid InP-on-silicon nanolaser that integrates a one-dimensional

PhC nanocavity into a silicon-on-insulator (SOI) platform. The design incorporates a precisely engineered nanorib structure to effectively confine carriers, enabling continuous-wave, single-mode operation at room temperature. The laser emits at $1.56\ \mu m$ with a threshold current of $100\ \mu A$, and its output is coupled into silicon waveguides. Figure 1.5 presents a 3D schematic of the hybrid nanolaser comprising an InP-based 1D PhC cavity, along with a cross-sectional view of the nanorib structure bonded onto a silicon waveguide.

In a more recent work, Dimopoulos et al. [89] reported a record-low threshold for an electrically driven PhC nanolaser using an InP-on-silicon platform. Their device achieved continuous-wave lasing at $1.54\ \mu m$ and operated at room temperature, with a threshold current of just $10.2\ \mu A$.

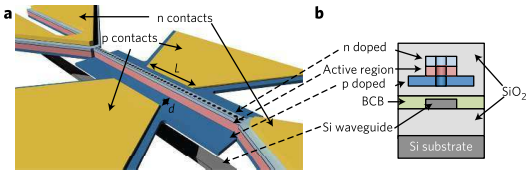

Figure 1.5: (a) 3D schematic of the hybrid nanolaser incorporating an InP-based 1D PhC cavity. (b) Cross-sectional view of the nanorib structure bonded atop a silicon waveguide. Reproduced from [88].

Plasmonic Nanolasers

A plasmonic nanolaser, also known as surface plasmon amplification by stimulated emission of radiation (spaser), employs a MC to couple light with SPPs, enabling optical confinement at subwavelength scales—in volumes well below the diffraction limit ($< (\lambda/n)^3$) [70]. A typical spaser consists of three essential components: a core containing the gain medium, a metal cavity for plasmon confinement, and an external pumping source [90]. When electrically excited, the gain medium transfers energy to the plasmonic mode, while feedback provided by metal nanostructure boundaries or dielectric reflectors facilitates stimulated emission of plasmons. This strong optical confinement, as discussed in the previous section, significantly enhances the Purcell effect, thereby increasing the spontaneous emission coupling factor β and reducing the lasing threshold—even under room-temperature operation.

Initially, the realization of plasmonic nanolasers was limited to cryogenic conditions due to substantial metal and radiation losses. However, recent advancements in device engineering and fabrication techniques have enabled the development of electrically injected plasmonic nanolasers operating at room temperature [90]. A notable example is the work by Zhang *et al.*, who demonstrated an electrically driven ultraviolet (UV) plasmonic nanolaser operating at room temperature by

integrating a GaN nanowire gain medium with a dielectric-insulator-metal (DIM) waveguide structure capped by a silver film [91]. As illustrated in Figure 1.6, the device incorporates a material stack of p-GaN/MgO/ZnO/MgO/Ag, engineered to facilitate strong plasmonic coupling and enable a hybrid optical cavity with deep subwavelength mode confinement. Under continuous-wave electrical injection, the nanolaser exhibits single-mode lasing at $\sim$365 nm in the near-UV with a low threshold current density of 70.2 A cm^{-2}.

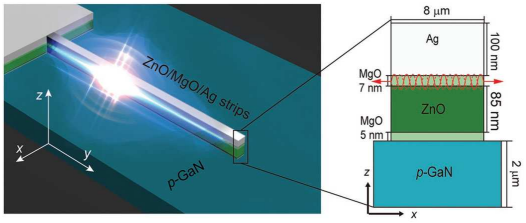

Figure 1.6: Illustration of the device structure for the electrically injected ZnO-based plasmonic nanolaser. Reproduced from [91].

1.1.3.3 Challenges in Electrically Pumped Nanolasers

The development of electrically pumped nanolasers presents a host of challenges that stem from the stringent physical and technological demands of scaling light sources to the nanoscale. A primary difficulty lies in achieving efficient carrier injection into ultra-compact active regions. As device dimensions shrink, resistive losses and current crowding effects become increasingly pronounced, resulting in localized heating and elevated threshold currents. Uniform current injection becomes particularly difficult in subwavelength geometries featuring vertical or lateral p–i–n junctions. To address these limitations, evolving device architectures now incorporate optimized contact schemes, sidewall passivation, and precisely engineered doping profiles to enhance injection efficiency while minimizing nonradiative recombination [92, 93].

Closely linked to carrier injection is the need to support high-speed modulation. Electrically pumped nanolasers often suffer from parasitic resistive-capacitive (RC) delays introduced by metal contacts, nanoscale cavity structures, and dielectric layers. These parasitics limit the modulation bandwidth and energy efficiency, particularly in devices targeting high-speed optical interconnects or on-chip communication. Efforts to mitigate this include using low-permittivity dielectrics, reducing metal interconnect lengths and minimizing junction and pad capacitances [94].

Another critical challenge involves the trade-off between optical confinement and

material losses. Nanolasers achieve tight mode confinement, often necessary for threshold reduction and Purcell enhancement, by using high-index contrast materials or metal-based cavities. However, such configurations frequently suffer from increased absorption losses, particularly in plasmonic or metal-clad designs. To balance this trade-off, hybrid photonic-plasmonic architectures have been proposed, combining dielectric materials for low-loss guidance with metallic layers strategically placed to enable electrical injection. These structures can maintain high confinement while suppressing unwanted absorption, leading to improved efficiency and lower thresholds [95].

Thermal management adds further complexity. Electrically injected nanolasers generate significant heat in very small volumes, and without efficient heat dissipation, the resulting temperature rise can degrade gain media, shift emission wavelengths, and impair device reliability [96]. Mitigating strategies include employing materials with high conductivity as substrates and using pulsed operation to avoid thermal damage [73].

Challenges in electrically pumped nanolasers fabricated by SAG

Beyond these general challenges, nanolasers fabricated through SAG face additional integration-specific hurdles. First, coupling light from these nanostructures into silicon photonics must reconcile the requirements of electrical contact placement and optical mode integrity. Butt or evanescent-coupling interfaces must be engineered with minimal loss, especially when metal contacts approach the optical mode [97]. To facilitate coupling between the III/V structures and silicon photonics platform, recent designs using adiabatic couplers have also been proposed [98].

Maintaining growth uniformity and precise control over nanostructure morphology are critical in SAG. Variations in trench geometry and mask orientation can result in non-planar growth fronts with multiple crystal facets, leading to spatially inconsistent material composition—particularly problematic in ternary alloys such as InGaAs quantum wells [99]. It is therefore essential to ensure that the chosen SAG approach promotes single-facet growth, enabling smoother interfaces and more uniform quantum well formation.

Finally, the inherent geometry of SAG imposes limitations on the volume of selectively grown III–V material, thereby constraining the available design space for electrical contact placement. As a result, metal contacts are often positioned in close proximity to the optical mode, which increases the risk of pronounced absorption losses[54, 97]. In addition to optical concerns, electrical performance can also be compromised by carrier injection across the defect-rich III–V/Si interface, which

tends to exhibit high electrical resistance and contributes to degraded injection efficiency [97]. Effective electrical injection under these constraints also demands precise doping profile optimization along the nanolaser, while preserving favorable optical characteristics. To address these challenges, one promising strategy involves the use of the lateral growth technique. This approach spatially displaces the active gain region away from the defective III–V/Si interface and positions the metal contacts outside the high-intensity regions of the optical mode. A notable example of this concept is the architecture proposed by Yu Han et al., in which a lateral ART technique is used to form well-oriented InGaAs quantum wells on InP-on-SOI substrates. This design enables efficient electrical injection and reduced threshold current, thereby advancing the feasibility of electrically pumped nanolasers on silicon. The corresponding device structure is shown in Figure 1.7 [97].

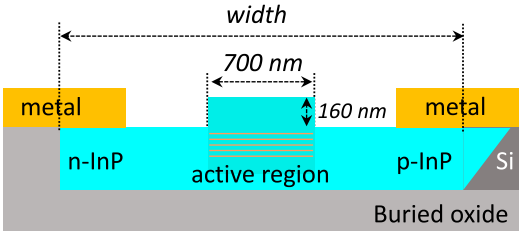

Figure 1.7: Schematic illustration of the device architecture proposed by Yu Han et al., utilizing a lateral ART approach to enable electrically injected nanolasers. The design features flat-oriented InGaAs quantum wells regrown on InP-on-SOI templates. Reproduced from [97].

Until recently, all III–V lasers grown on silicon using SAG operated only under pulsed optical excitation due to challenges arising from a combination of the different factors discussed above. However, the integration of ART and NRE techniques has led to new device concepts. A key milestone was the demonstration of monolithically grown $In_{0.2}Ga_{0.8}As$/GaAs multi-quantum well photodetectors on V-grooved Si substrates incorporating periodic tungsten p-type plugs for vertical injection [100]. These devices featured n-type contacts formed through tungsten plugs linked to heavily doped silicon. Figure 1.8 shows the corresponding cross-sectional SEM and schematic of a GaAs nano-ridge with three InGaAs quantum wells. Despite these advances, electrically pumped operation remained elusive for some time, primarily due to significant overlap between the optical mode and the p-type metal contact—leading to high absorption losses. However, at the onset of this PhD research, imec achieved a significant breakthrough by demonstrating CW lasing at room temperature from these electrically pumped $In_{0.2}Ga_{0.8}As$/GaAs quantum well nano-ridge lasers by exploiting a mode-beating effect along the device length [66]. These lasers operate around 1020 nm and were fabricated directly on standard 300 mm Si (001) wafers using a CMOS-compatible pilot manufacturing

line—underscoring the practicality of monolithic III–V/Si integration within existing semiconductor process flows. This dissertation presents an in-depth modeling and experimental characterization of these electrically injected nano-ridge lasers.

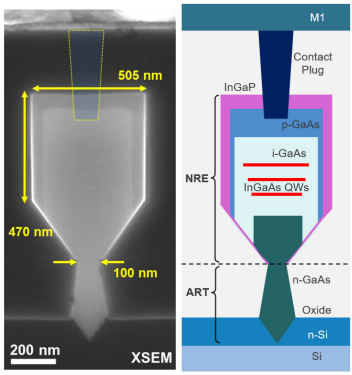

Figure 1.8: SEM image and schematic of a cross-section of a GaAs nano-ridge having three InGaAs QWs. Reproduced from [100].

1.2 Research Objectives

Building on the foundational achievement of the first electrically pumped lasing demonstration in $In_{0.2}Ga_{0.8}As$/GaAs quantum well nano-ridge lasers—monolithically grown on silicon using ART and NRE at imec—this PhD research is guided by the following primary objectives.

- To develop a comprehensive physical model capable of accurately describing the operating principles of electrically injected InGaAs/GaAs nano-ridge lasers grown on silicon.
- To employ this model for optimizing the device geometry and contact layout, with the aim of achieving precise control over emission wavelength, reducing threshold gain, and improving slope efficiency.
- To conduct comprehensive static and dynamic characterization, including parameter extraction, of the fabricated devices, with the goal of identifying the dominant physical mechanisms limiting their performance.
- To propose and evaluate novel DFB laser design strategies for enhancing both the optical laser performance and electrical injection efficiency of the nanolasers.

The first phase of the research focused on constructing a validated device model that could reliably explain the lasing behavior observed in the imec-fabricated structures. This model served as the foundation for investigating key performance metrics such as threshold gain, wavelength tuning, and slope efficiency. In parallel, experimental characterization of the provided devices was conducted, offering critical insight into practical performance limitations. These insights were then used to guide the development of new design strategies aimed at overcoming current bottlenecks in device performance.

The research was conducted within the Photonics Research Group at Ghent University, in close partnership with imec, which provided all fabricated devices used in this study.

1.3 Thesis Outline

This dissertation is structured into seven chapters, each addressing a distinct component of the research conducted on electrically injected InGaAs/GaAs nano-ridge lasers monolithically integrated on silicon. The organization follows a logical sequence from foundational concepts and modeling to experimental characterization and novel device design strategies.

Chapter 1 introduces the scientific background and motivation for this work. It begins with an overview of silicon photonics, followed by a discussion of various III–V on silicon integration approaches, and the specific challenges associated with realizing electrically pumped nanolasers. The research objectives of the dissertation are then presented, along with a brief outline of the thesis structure. The chapter concludes with a list of publications in international journals and conferences that have resulted from this work.

Chapter 2 focuses on analyzing optical loss mechanisms in nano-ridge waveguides, which are critical for understanding the performances of the integrated laser structures. It specifically investigates scattering losses in undoped waveguides and free-carrier absorption in doped waveguides. The chapter describes the experimental setups used, presents the results, and concludes with a discussion of their implications for device design.

Chapter 3 develops a semi-analytical model to describe the lasing behavior of electrically injected InGaAs/GaAs nano-ridge lasers. It details the coupling between guided modes in nano-ridge waveguides and introduces a round-trip gain model used to evaluate key parameters such as threshold gain, emission linewidth, and differential quantum efficiency. The model's predictions are validated against

experimental results, demonstrating its accuracy and applicability.

Chapter 4 presents the static characterization of the fabricated devices. It covers light–current–voltage (LIV) and spectral measurements, linewidth characterization, and far-field measurements. For each characterization technique, the measurement setup is described and results are discussed in terms of their relevance to understanding device operation and limitations.

Chapter 5 extends the characterization to dynamic behavior, providing insight into the modulation performance and noise characteristics of the devices. Small-signal modulation and RIN measurements are presented, along with the extraction of recombination coefficients. These measurements are used to quantify device performance limitations and provide a deeper understanding of the carrier dynamics under electrical excitation.

Chapter 6 builds upon the insights developed in the preceding chapters to propose and evaluate several novel design strategies for electrically injected nano-ridge lasers. Specifically, it introduces three innovative DFB laser architectures: the metal contact grating, the top fin grating, and the side silicon grating structures. These configurations are compared in terms of optical performance and device behavior. Furthermore, Sentaurus TCAD electrical simulations are employed to assess each design's current–voltage characteristics and carrier injection efficiency, providing a detailed analysis of their respective advantages and trade-offs.

Chapter 7 concludes the dissertation by summarizing the main research contributions and findings. It also presents perspectives for future work, discussing opportunities for improving device performance.

1.4 List of publications

1.4.1 Publications in international journals

1. **Yimam, Andualem Ali**, Colucci, Davide, Caer, Charles, Yudistira, Didit, De Koninck, Yannick, Sar, Huseyin, Baryshnikova, Marina, Verheyen, Peter, Van Campenhout, Joris, Kunert, Bernardette, Van Thourhout, Dries, and Morthier, Geert, "Advanced characterization and parameter extraction of electrically injected InGaAs/GaAs nano-ridge lasers monolithically integrated on silicon," *Optics Express*, vol. 33, no. 13, pp. 27929, 2025.

2. **Yimam, Andualem Ali**, Colucci, Davide, Caer, Charles, Yudistira, Didit, De Koninck, Yannick, Sar, Huseyin, Baryshnikova, Marina, Verheyen, Peter, Van Campenhout, Joris, Kunert, Bernardette, Morthier, Geert, and Van Thourhout,

Dries, "Semi-analytical model for electrically injected GaAs nano-ridge laser diodes monolithically integrated on silicon," *Optics Express*, vol. 33, no. 2, pp. 2101, 2025.

3. De Koninck, Yannick, Caer, Charles, Yudistira, Didit, Baryshnikova, Marina, Sar, Huseyin, Hsieh, Ping-Yi, Özdemir, Cenk Ibrahim, Patra, Saroj Kanta, Kuznetsova, Nadezda, Colucci, Davide, Milenin, Alexey, **Yimam, Andualem Ali**, Morthier, Geert, Van Thourhout, Dries, Verheyen, Peter, Pantouvaki, Marianna, Kunert, Bernardette, and Van Campenhout, Joris, "GaAs nano-ridge laser diodes fully fabricated in a 300-mm CMOS pilot line," *Nature*, vol. 637, no. 8044, pp. 63–69, 2025.

4. Ouyang, Z., Fahmy, E. M. B., Colucci, D., **Yimam, Andualem Ali**, Van Campenhout, J., Kunert, B., and Van Thourhout, D., "Ultra-compact InGaAs/-GaAs nano-ridge laser monolithically grown on 300 mm silicon substrate," *Optics Letters*, vol. 50, no. 7, pp. 2358, 2025.

5. Ouyang, Z., Colucci, D., Fahmy, E. M. B., **Yimam, Andualem Ali**, Van Campenhout, J., Kunert, B., and Van Thourhout, D., "InGaAs/GaAs nano-ridge laser with an amorphous silicon grating monolithically grown on a 300 mm Si wafer," *Optics Letters*, vol. 49, no. 16, pp. 4741, 2024.

1.4.2 Publications in international conferences

1. **Yimam, Andualem Ali**, Colucci, Davide, Caer, Charles, Yudistira, Didit, De Koninck, Yannick, Sar, Huseyin, Baryshnikova, Marina, Verheyen, Peter, Van Campenhout, Joris, Kunert, Bernardette, Morthier, Geert, and Van Thourhout, Dries, "Extraction of Recombination Coefficients for Electrically Injected InGaAs/GaAs Monolithic Nano-ridge Laser Diodes Integrated on Silicon," *2025 IEEE Silicon Photonics Conference (SiPhotonics)*, pp. 1–2, Apr. 2025.

2. Ouyang, Zhongtao, Colucci, Davide, Fahmy, Eslam Mostafa Bakry, **Yimam, Andualem Ali**, Van Campenhout, Joris, Kunert, Bernadette, and Van Thourhout, Dries, "Compact 1.31 μm-emission $In_{0.45}Ga_{0.55}As/In_{0.25}Ga_{0.75}As$ photonic crystal nano-ridge laser monolithically grown on 300 mm silicon substrate," *Integrated Photonics Platforms III (SPIE)*, pp. 22, Jun. 2024.

3. **Yimam, Andualem Ali**, Morthier, Geert, and Van Thourhout, Dries, "Accurate Laser Model for Electrically Injected Monolithic GaAs on Silicon Nano-ridge Laser Diodes," *CLEO 2024*, paper JTu2A.35, Optica Publishing Group, 2024.

4. **Yimam, Andualem Ali**, Morthier, Geert, and Van Thourhout, Dries, "Semi-analytical model for electrically injected monolithic GaAs on silicon nano-ridge laser diodes," *IEEE Benelux Photonics Chapter: Annual Symposium*, 2023.

5. Ouyang, Zhongtao, Fahmy, Eslam, Colucci, Davide, **Yimam, Andualem Ali**, Kunert, Bernadette, and Van Thourhout, Dries, "Side-amorphous-silicon-grating InGaAs/GaAs nano-ridge distributed feedback laser monolithically grown on 300 mm silicon substrate," *Asia Communications and Photonics Conference (ACP)/International Photonics and Optoelectronics Meetings (POEM)*, pp. 1–3, Nov. 2023.

6. Ouyang, Z., Fahmy, E. M. B., Colucci, D., **Yimam, Andualem Ali**, Kunert, B., and Van Thourhout, D., "Low-optical-pumping-threshold InGaAs/GaAs Nano-ridge Laser Monolithically Grown on 300 mm Silicon Substrate," *CLEO 2023*, paper STh3H.3, Optica Publishing Group, 2023.

7. Ouyang, Z., Fahmy, E. M. B., Colucci, D., **Yimam, Andualem Ali**, Kunert, B., and Van Thourhout, D., "Top-amorphous-silicon-grating InGaAs/GaAs nano-ridge distributed feedback laser monolithically grown on 300 mm silicon substrate," *IEEE Benelux Photonics Chapter: Annual Symposium*, 2022.

References

[1] R. Soref, The past, present, and future of silicon photonics, *IEEE Journal of selected topics in quantum electronics*, vol. 12, no. 6, pp. 1678–1687, 2007.

[2] N. Margalit, C. Xiang, S. M. Bowers, A. Bjorlin, R. Blum, and J. E. Bowers, Perspective on the future of silicon photonics and electronics, *Applied Physics Letters*, vol. 118, no. 22, 2021.

[3] S. Shekhar et al., Roadmapping the next generation of silicon photonics, *Nature Communications*, vol. 15, no. 1, p. 751, 2024.

[4] R. Jones et al., Heterogeneously integrated InP/silicon photonics: Fabricating fully functional transceivers, *IEEE Nanotechnology Magazine*, vol. 13, no. 2, pp. 17–26, 2019.

[5] C. Doerr and L. Chen, Silicon photonics in optical coherent systems, *Proceedings of the IEEE*, vol. 106, no. 12, pp. 2291–2301, 2018.

[6] K. Fotiadis et al., Silicon photonic 16× 16 cyclic AWGR for DWDM O-band interconnects, *IEEE Photonics Technology Letters*, vol. 32, no. 19, pp. 1233–1236, 2020.

[7] M. Pantouvaki et al., Active components for 50 Gb/s NRZ-OOK optical interconnects in a silicon photonics platform, *Journal of lightwave technology*, vol. 35, no. 4, pp. 631–638, 2016.

[8] C. Minkenberg, R. Krishnaswamy, A. Zilkie, and D. Nelson, Co-packaged datacenter optics: Opportunities and challenges, *IET optoelectronics*, vol. 15, no. 2, pp. 77–91, 2021.

[9] Z. Wang and M. Menenti, Challenges and opportunities in lidar remote sensing, *Frontiers in Remote Sensing*, vol. 2, p. 641 723, 2021.

[10] X. Sun, L. Zhang, Q. Zhang, and W. Zhang, Si photonics for practical lidar solutions, *Applied Sciences*, vol. 9, no. 20, p. 4225, 2019.

[11] J. Riemensberger et al., Massively parallel coherent laser ranging using a soliton microcomb, *Nature*, vol. 581, no. 7807, pp. 164–170, 2020.

[12] X. Zhang, K. Kwon, J. Henriksson, J. Luo, and M. C. Wu, A large-scale microelectromechanical-systems-based silicon photonics lidar, *Nature*, vol. 603, no. 7900, pp. 253–258, 2022.

[13] C. Rogers et al., A universal 3D imaging sensor on a silicon photonics platform, *Nature*, vol. 590, no. 7845, pp. 256–261, 2021.

[14] E. Luan, H. Shoman, D. M. Ratner, K. C. Cheung, and L. Chrostowski, Silicon photonic biosensors using label-free detection, *Sensors*, vol. 18, no. 10, p. 3519, 2018.

[15] M. Iqbal et al., Label-free biosensor arrays based on silicon ring resonators and high-speed optical scanning instrumentation, *IEEE Journal of selected topics in quantum electronics*, vol. 16, no. 3, pp. 654–661, 2010.

[16] B. D. Reed et al., Real-time dynamic single-molecule protein sequencing on an integrated semiconductor device, *Science*, vol. 378, no. 6616, pp. 186–192, 2022.

[17] W. Bogaerts et al., Programmable photonic circuits, *Nature*, vol. 586, no. 7828, pp. 207–216, 2020.

[18] T. J. Seok, K. Kwon, J. Henriksson, J. Luo, and M. C. Wu, Wafer-scale silicon photonic switches beyond die size limit, *Optica*, vol. 6, no. 4, pp. 490–494, 2019.

[19] M. Raval, A. Yaacobi, and M. R. Watts, Integrated visible light phased array system for autostereoscopic image projection, *Optics Letters*, vol. 43, no. 15, pp. 3678–3681, 2018.

[20] B. J. Shastri et al., Photonics for artificial intelligence and neuromorphic computing, *Nature Photonics*, vol. 15, no. 2, pp. 102–114, 2021.

[21] F. Ashtiani, A. J. Geers, and F. Aflatouni, An on-chip photonic deep neural network for image classification, *Nature*, vol. 606, no. 7914, pp. 501–506, 2022.

[22] Y. Su, Y. Zhang, C. Qiu, X. Guo, and L. Sun, Silicon photonic platform for passive waveguide devices: Materials, fabrication, and applications, *Advanced Materials Technologies*, vol. 5, no. 8, Jun. 2020.

[23] Q. Wilmart et al., A complete Si photonics platform embedding ultra-low loss waveguides for O- and C-band, *J. Lightwave Technol.*, vol. 39, no. 2, pp. 532–538, Jan. 2021.

[24] D. Bose et al., Anneal-free ultra-low loss silicon nitride integrated photonics, *Light: Science & Applications*, vol. 13, no. 1, p. 156, 2024.

[25] D. Liu, J. He, Y. Xiang, Y. Xu, and D. Dai, High-performance silicon photonic filters based on all-passive tenth-order adiabatic elliptical-microrings, *APL Photonics*, vol. 7, no. 5, p. 051 303, May 2022.

[26] W. Hu et al., A silicon micro-ring resonator with unprecedented large free spectral range via double injection, *Optics Communications*, vol. 546, p. 129 767, 2023.

[27] S. Xie, S. Veilleux, and M. Dagenais, On-chip high extinction ratio single-stage mach-zehnder interferometer based on multimode interferometer, *IEEE Photonics Journal*, vol. 14, no. 4, pp. 1–6, 2022.

[28] C. Xie, X. Zou, F. Zou, Y. Zhang, L. Yan, and W. Pan, Design and fabrication optimization of low-crosstalk silicon arrayed waveguide gratings with 32 channels and 100-GHz spacing, *Optics & Laser Technology*, vol. 163, p. 109 330, 2023.

[29] B. Shen, P. Wang, R. Polson, and R. Menon, An integrated-nanophotonics polarization beamsplitter with $2.4\times$ 2.4 μm^2 footprint, *Nature Photonics*, vol. 9, no. 6, pp. 378–382, 2015.

[30] P. Cheben, R. Halir, J. H. Schmid, H. A. Atwater, and D. R. Smith, Sub-wavelength integrated photonics, *Nature*, vol. 560, no. 7720, pp. 565–572, 2018.

[31] Y. Yuan et al., A 5× 200 Gbps microring modulator silicon chip empowered by two-segment Z-shape junctions, *Nature Communications*, vol. 15, no. 1, p. 918, 2024.

[32] F. Valdez et al., 110 GHz, 110 mW hybrid silicon-lithium niobate mach-zehnder modulator, *Scientific reports*, vol. 12, no. 1, p. 18 611, 2022.

[33] H. Liu et al., Near-infrared germanium PIN photodiodes with >1 A/W responsivity, *Light: Science & Applications*, vol. 14, no. 1, p. 9, 2025.

[34] X. Hu et al., High-speed and high-power germanium photodetector with a lateral silicon nitride waveguide, *Photon. Res.*, vol. 9, no. 5, pp. 749–756, May 2021.

[35] H. Rong et al., A continuous-wave raman silicon laser, *Nature*, vol. 433, no. 7027, pp. 725–728, 2005.

[36] Y. Takahashi, Y. Inui, M. Chihara, T. Asano, R. Terawaki, and S. Noda, A micrometre-scale raman silicon laser with a microwatt threshold, *Nature*, vol. 498, no. 7455, pp. 470–474, 2013.

[37] A. Marinins et al., Wafer-scale hybrid integration of InP DFB lasers on Si photonics by flip-chip bonding with sub-300 nm alignment precision, *IEEE Journal of Selected Topics in Quantum Electronics*, vol. 29, no. 3: Photon. Elec. Co-Inte. and Adv. Trans. Print. Pp. 1–11, 2023.

[38] S. Lin et al., Efficient, tunable flip-chip-integrated III-V/Si hybrid external-cavity laser array, *Opt. Express*, vol. 24, no. 19, pp. 21 454–21 462, Sep. 2016.

[39] G. Roelkens et al., III-V-on-silicon photonic devices for optical communication and sensing, *Photonics*, vol. 2, no. 3, pp. 969–1004, 2015.

[40] S. Bao et al., A review of silicon-based wafer bonding processes, an approach to realize the monolithic integration of Si-CMOS and III–V-on-Si wafers, *Journal of Semiconductors*, vol. 42, no. 2, p. 023 106, Feb. 2021.

[41] C. Xiang et al., High-performance silicon photonics using heterogeneous integration, *IEEE Journal of Selected Topics in Quantum Electronics*, vol. 28, no. 3: Hybrid Integration for Silicon Photonics, pp. 1–15, 2022.

[42] Y. Hu, D. Liang, and R. G. Beausoleil, An advanced III-V-on-silicon photonic integration platform, *Opto-Electronic Advances*, vol. 4, no. 9, pp. 200 094–1, 2021.

[43] H. Yang et al., Transfer-printed stacked nanomembrane lasers on silicon, *Nature Photonics*, vol. 6, no. 9, pp. 615–620, 2012.

[44] J. Justice, C. Bower, M. Meitl, M. B. Mooney, M. A. Gubbins, and B. Corbett, Wafer-scale integration of group III–V lasers on silicon using transfer printing of epitaxial layers, *Nature Photonics*, vol. 6, no. 9, pp. 610–614, 2012.

[45] J. Zhang et al., III-V-on-Si photonic integrated circuits realized using micro-transfer-printing, *APL Photonics*, vol. 4, no. 11, p. 110 803, Nov. 2019.

[46] G. Roelkens et al., Micro-transfer printing for heterogeneous Si photonic integrated circuits, *IEEE Journal of Selected Topics in Quantum Electronics*, vol. 29, no. 3: Photon. Elec. Co-Inte. and Adv. Trans. Print. Pp. 1–14, 2023.

[47] B. Kunert, Y. Mols, M. Baryshniskova, N. Waldron, A. Schulze, and R. Langer, How to control defect formation in monolithic III-V hetero-epitaxy on (100) Si? a critical review on current approaches, *Semiconductor Science and Technology*, vol. 33, no. 9, p. 093 002, Aug. 2018.

[48] S. Chen et al., Electrically pumped continuous-wave III–V quantum dot lasers on silicon, *Nature photonics*, vol. 10, no. 5, pp. 307–311, 2016.

[49] D. Jung et al., Highly reliable low-threshold inas quantum dot lasers on on-axis (001) Si with 87% injection efficiency, *ACS Photonics*, vol. 5, no. 3, pp. 1094–1100, 2018.

[50] C. Shang et al., A pathway to thin GaAs virtual substrate on on-axis Si (001) with ultralow threading dislocation density, *physica status solidi (a)*, vol. 218, no. 3, p. 2 000 402, 2021.

[51] C. Shang et al., Electrically pumped quantum-dot lasers grown on 300 mm patterned Si photonic wafers, *Light: Science & Applications*, vol. 11, no. 1, p. 299, 2022.

[52] W.-Q. Wei et al., Monolithic integration of embedded III-V lasers on SOI, *Light: Science & Applications*, vol. 12, no. 1, p. 84, 2023.

[53] K. Cheng et al., Epitaxial growth of high-quality GaAs on Si(001) using ultrathin buffer layers, *AIP Advances*, vol. 14, no. 3, p. 035 239, Mar. 2024.

[54] Y. Han and K. M. Lau, III–V lasers selectively grown on (001) silicon, *Journal of Applied Physics*, vol. 128, no. 20, p. 200 901, Nov. 2020.

[55] M. Paladugu et al., Site selective integration of III–V materials on Si for nanoscale logic and photonic devices, *Crystal Growth & Design*, vol. 12, no. 10, pp. 4696–4702, 2012.

[56] Z. Wang et al., Room-temperature InP distributed feedback laser array directly grown on silicon, *Nature Photonics*, vol. 9, no. 12, pp. 837–842, 2015.

[57] B. Tian et al., Room temperature O-band DFB laser array directly grown on (001) silicon, *Nano Letters*, vol. 17, no. 1, pp. 559–564, 2017.

[58] Y. Han, W. K. Ng, Y. Xue, Q. Li, K. S. Wong, and K. M. Lau, Telecom InP/InGaAs nanolaser array directly grown on (001) silicon-on-insulator, *Opt. Lett.*, vol. 44, no. 4, pp. 767–770, Feb. 2019.

[59] B. Kunert, W. Guo, Y. Mols, R. Langer, and K. Barla, Integration of III-V hetero-structures by selective area growth on Si for nano-and optoelectronics, *Ecs Transactions*, vol. 75, no. 8, p. 409, 2016.

[60] B. Kunert, R. Langer, M. Pantouvaki, J. Van Campenhout, and D. Van Thourhout, Gaining an edge with nano-ridges, *Compound Semiconductor*, vol. 24, no. 5, pp. 36–41, 2018.

[61] M. Baryshnikova et al., Nano-ridge engineering of GaSb for the integration of InAs/GaSb heterostructures on 300 mm (001) Si, *Crystals*, vol. 10, no. 4, 2020.

[62] B. Kunert et al., Application of an sb surfactant in InGaAs nano-ridge engineering on 300 mm silicon substrates, *Crystal Growth & Design*, vol. 21, no. 3, pp. 1657–1665, 2021.

[63] Y. Shi et al., Time-resolved photoluminescence characterization of InGaAs/-GaAs nano-ridges monolithically grown on 300 mm Si substrates, *Journal of Applied Physics*, vol. 127, no. 10, p. 103 104, Mar. 2020.

[64] Y. Shi et al., Optical pumped InGaAs/GaAs nano-ridge laser epitaxially grown on a standard 300-mm Si wafer, *Optica*, vol. 4, no. 12, pp. 1468–1473, Dec. 2017.

[65] D. Colucci et al., Unique design approach to realize an O-band laser monolithically integrated on 300 mm Si substrate by nano-ridge engineering, *Opt. Express*, vol. 30, no. 8, pp. 13 510–13 521, Apr. 2022.

[66] Y. De Koninck et al., GaAs nano-ridge laser diodes fully fabricated in a 300-mm CMOS pilot line, *Nature*, vol. 637, no. 8044, pp. 63–69, 2025.

[67] S. Wirths et al., Room-temperature lasing from monolithically integrated GaAs microdisks on silicon, *ACS Nano*, vol. 12, no. 3, pp. 2169–2175, 2018.

[68] Y.-T. Sun, H. Kataria, W. Metaferia, and S. Lourdudoss, Realization of an atomically abrupt InP/Si heterojunction via corrugated epitaxial lateral overgrowth, *CrystEngComm*, vol. 16, no. 34, pp. 7889–7893, 2014.

[69] K. Tomioka et al., Selective-area growth of III-V nanowires and their applications, *Journal of Materials Research*, vol. 26, no. 17, pp. 2127–2141, 2011.

[70] K. Ren, C. Li, Z. Fang, and F. Feng, Recent developments of electrically pumped nanolasers, *Laser & Photonics Reviews*, vol. 17, no. 5, Jan. 2023.

[71] M. T. Hill, Electrically pumped metallic and plasmonic nanolasers, *Chinese Physics B*, vol. 27, no. 11, p. 114 210, Nov. 2018.

[72] R.-M. Ma and R. F. Oulton, Applications of nanolasers, *Nature Nanotechnology*, vol. 14, no. 1, pp. 12–22, Dec. 2018.

[73] S. I. Azzam et al., Ten years of spasers and plasmonic nanolasers, *Light: Science & Applications*, vol. 9, no. 1, May 2020.

[74] C.-Z. Ning, Semiconductor nanolasers and the size-energy-efficiency challenge: A review, *Advanced Photonics*, vol. 1, no. 01, p. 1, Jan. 2019.

[75] S. S. Deka, S. Jiang, S. H. Pan, and Y. Fainman, Nanolaser arrays: Toward application-driven dense integration, *Nanophotonics*, vol. 10, no. 1, pp. 149–169, 2021.

[76] Y. Liang, C. Li, Y.-Z. Huang, and Q. Zhang, Plasmonic nanolasers in on-chip light sources: Prospects and challenges, *ACS Nano*, vol. 14, no. 11, pp. 14 375–14 390, 2020.

[77] M.-S. Hwang et al., Recent advances in nanocavities and their applications, *Chemical Communications*, vol. 57, no. 40, pp. 4875–4885, 2021.

[78] Z. Gu, Q. Song, and S. Xiao, Nanowire waveguides and lasers: Advances and opportunities in photonic circuits, *Frontiers in Chemistry*, vol. Volume 8 - 2020, 2021.

[79] L. A. Coldren, S. W. Corzine, and M. L. Mashanovitch, *Diode lasers and photonic integrated circuits*. John Wiley & Sons, 2012.

[80] K. J. Vahala, Optical microcavities, *Nature*, vol. 424, no. 6950, pp. 839–846, Aug. 2003.

[81] S. B. Bashar, C. Wu, M. Suja, H. Tian, W. Shi, and J. Liu, Electrically pumped whispering gallery mode lasing from Au/ZnO microwire schottky junction, *Advanced Optical Materials*, vol. 4, no. 12, pp. 2063–2067, Sep. 2016.

[82] K.-Y. Jeong, M.-S. Hwang, J. Kim, J.-S. Park, J. M. Lee, and H.-G. Park, Recent progress in nanolaser technology, *Advanced Materials*, vol. 32, no. 51, Sep. 2020.

[83] H. Altug, D. Englund, and J. Vučković, Ultrafast photonic crystal nanocavity laser, *Nature Physics*, vol. 2, no. 7, pp. 484–488, Jul. 2006.

[84] R. F. Oulton et al., Plasmon lasers at deep subwavelength scale, *Nature*, vol. 461, no. 7264, pp. 629–632, Aug. 2009.

[85] M. Khajavikhan et al., Thresholdless nanoscale coaxial lasers, *Nature*, vol. 482, no. 7384, pp. 204–207, Feb. 2012.

[86] X. Duan, Y. Huang, R. Agarwal, and C. M. Lieber, Single-nanowire electrically driven lasers, *Nature*, vol. 421, no. 6920, pp. 241–245, Jan. 2003.

[87] T. Frost et al., Monolithic electrically injected nanowire array edge-emitting laser on (001) silicon, *Nano Letters*, vol. 14, no. 8, pp. 4535–4541, Jul. 2014.

[88] G. Crosnier et al., Hybrid indium phosphide-on-silicon nanolaser diode, *Nature Photonics*, vol. 11, no. 5, pp. 297–300, Apr. 2017.

[89] E. Dimopoulos et al., Electrically-driven photonic crystal lasers with ultra-low threshold, *Laser & Photonics Reviews*, vol. 16, no. 11, Aug. 2022.

[90] R. Wang et al., Recent progress in low threshold plasmonic nanolasers, *Advanced Optical Materials*, vol. 11, no. 15, May 2023.

[91] X. Yang et al., Room temperature electrically driven ultraviolet plasmonic lasers, *Advanced Optical Materials*, vol. 7, no. 10, Mar. 2019.

[92] G. Shambat et al., Electrically driven photonic crystal nanocavity devices, *IEEE Journal of Selected Topics in Quantum Electronics*, vol. 18, no. 6, pp. 1700–1710, Nov. 2012.

[93] A. Higuera-Rodriguez et al., Ultralow surface recombination velocity in passivated InGaAs/InP nanopillars, *Nano Letters*, vol. 17, no. 4, pp. 2627–2633, Mar. 2017.

[94] A. N. AL-Omari, I. K. AL-Kofahi, and K. L. Lear, Fabrication, performance and parasitic parameter extraction of 850 nm high-speed vertical-cavity lasers, *Semiconductor Science and Technology*, vol. 24, no. 9, p. 095 024, Aug. 2009.

[95] D. K. Gramotnev and S. I. Bozhevolnyi, Plasmonics beyond the diffraction limit, *Nature Photonics*, vol. 4, no. 2, pp. 83–91, Jan. 2010.

[96] W. You, S. Balabadrapatruni, B. J. Thompson, R. Gibson, S. Arafin, and S. C. Badescu, Thermal modeling of electrically-pumped continuous-wave microring resonator-based topological insulator lasers, *Optics Express*, vol. 32, no. 3, p. 3342, Jan. 2024.

[97] Y. Han, Y. Xue, Z. Yan, and K. M. Lau, Selectively grown III-V lasers for integrated Si-photonics, *J. Lightwave Technol.*, vol. 39, no. 4, pp. 940–948, Feb. 2021.

[98] Y. Shi, B. Kunert, Y. D. Koninck, M. Pantouvaki, J. V. Campenhout, and D. V. Thourhout, Novel adiabatic coupler for III-V nano-ridge laser grown on a Si photonics platform, *Opt. Express*, vol. 27, no. 26, pp. 37 781–37 794, Dec. 2019.

[99] B. Wang et al., Principles of selective area epitaxy and applications in III–V semiconductor lasers using mocvd: A review, *Crystals*, vol. 12, no. 7, p. 1011, Jul. 2022.

[100] C. I. Ozdemir et al., Low dark current and high responsivity 1020nm InGaAs/GaAs nano-ridge waveguide photodetector monolithically integrated on a 300-mm Si wafer, *J. Lightwave Technol.*, vol. 39, no. 16, pp. 5263–5269, Aug. 2021.

2

Scattering and carrier-induced absorption losses in nano-ridge waveguides

Contents

Chapter 1 provided an overview of silicon photonics, with a particular focus on the various integration strategies for incorporating optical sources onto silicon. The advantages and limitations of these approaches were critically examined. Additionally, the chapter introduced electrically injected nanolasers and outlined the key challenges associated with realizing electrical pumping at the nanoscale. Special attention was given to devices fabricated using selective area epitaxy, leading to a discussion of the central objectives of this PhD research.

Building upon that foundation, Chapter 2 explores two key optical loss mechanisms in GaAs nano-ridge waveguides (NRWs)—propagation and carrier-induced absorption—which are critical to the performance of the devices investigated throughout this work. The chapter begins with a review of waveguide loss measurement techniques reported in the literature, outlining their respective advantages and limitations. Propagation losses in undoped GaAs NRWs are experimentally assessed using the FPI method, with particular focus on how these losses vary with the trench width. The analysis further distinguishes the contributions of scattering and substrate leakage to the total propagation loss. Coupling efficiency between lensed fibers and NRWs is also examined, given its influence on overall transmission performance. Furthermore, the chapter examines carrier-induced absorption in doped NRWs, supported by relevant data from the literature. Finally, the feasibility of applying the Fabry–Perot method to measure losses in doped nano-ridge structures is assessed. The scattering loss measurements for undoped NRWs, along with the absorption coefficients for various doped materials presented in this chapter, provide essential input parameters for the modeling, simulation, and characterization efforts discussed in the subsequent chapters.

2.1 Waveguide loss measurement techniques

Accurate characterization of optical waveguide losses is essential for evaluating the performance of integrated photonic devices. Over the years, a variety of techniques have been developed to quantify propagation loss, each with specific advantages and limitations depending on factors such as waveguide material, geometry, and integration platform. This section provides a comprehensive review of the most widely adopted loss measurement methods, detailing their underlying principles, experimental setups, and comparative strengths. Particular emphasis is placed on evaluating the suitability of these methods for GaAs NRWs. Based on this analysis, the FPI method is identified and justified as the most appropriate approach for the extraction of propagation losses in undoped GaAs NRWs.

2.1.1 Cut-back method

The cut-back method is one of the earliest and most straightforward techniques for waveguide loss measurement. In this approach, the output power of a waveguide is measured for varying lengths and compared to the input power to evaluate insertion loss [1]. When insertion loss is plotted against waveguide length—assuming consistent coupling conditions—a linear trend typically emerges on a semi-logarithmic scale, with the slope indicating the propagation loss of the waveguide. This technique assumes identical coupling conditions before and after the cuts, which can be challenging to achieve in practice.

The cut-back method is valued for its conceptual simplicity and minimal analytical requirements. However, its major limitations include the destructive nature of the technique and the difficulty in ensuring reproducible coupling efficiency after cleaving. Small deviations in alignment or facet quality can significantly affect measurement accuracy, making it less suitable for nanoscale or integrated waveguides where cleaving introduces additional uncertainties.

2.1.2 Prism coupling method

The prism coupling method is a well-established approach for characterizing thin-film optical waveguides [2–4]. This method relies on evanescent wave coupling, whereby light from a high-refractive-index prism is phase-matched into discrete guided modes of the waveguide. By adjusting the angle of incidence of a collimated laser beam directed at the base of the prism, specific propagation modes are excited when the phase-matching condition is satisfied. In a typical experimental arrangement, a laser beam is directed at the base of a coupling prism that is placed in close physical contact with the waveguide film. When the phase-matching angle is reached, light couples efficiently into one of the waveguide's guided modes. The coupled light propagates along the waveguide, and its output is captured using a photodetector or observed on a screen to analyze the angular distribution. In some variants, the propagation length under the prism is systematically varied by translating the prism along the waveguide, allowing the output power to be measured as a function of distance. This spatially resolved power decay can then be used to extract the propagation loss through exponential fitting.

One of the key advantages of the prism coupling method is its ability to provide mode-resolved measurements of effective refractive index with high precision. The technique is entirely non-destructive and well-suited to characterizing slab and thin-film waveguides, particularly in early-stage fabrication and material verification. It also facilitates detailed insights into waveguide thickness and refractive index

profiles, as each mode can be individually addressed and analyzed.

Despite these strengths, the method has notable limitations that restrict its application to certain classes of waveguides. First, maintaining a stable and repeatable coupling condition can be challenging, as the efficiency of evanescent coupling is highly sensitive to the exact gap between the prism and the waveguide surface. Even minor variations in pressure or alignment during measurement can result in inconsistent coupling and lead to data scatter, particularly when assessing loss as a function of waveguide length. Second, the choice of materials for the prism is constrained by the need for a refractive index higher than that of the waveguide core. While this is readily achievable for low-index materials, it becomes problematic for high-index waveguides like silicon or III–V semiconductors, where available high-index prisms may introduce absorption losses in the near-infrared. Finally, the method is inherently limited to planar geometries; it does not accommodate nanostructured or deeply etched waveguides with subwavelength confinement and non-uniform topography, such as those commonly encountered in modern silicon photonics platforms.

As a result, while the prism coupling method remains a powerful diagnostic tool for planar optical films and early-stage photonic devices, its applicability diminishes in contexts requiring precise control over nanoscale waveguide architectures or in integration scenarios where accessibility and material constraints become prohibitive.

2.1.3 Scattering imaging method

The scattering imaging method, often referred to as the scattered light collection technique, is a powerful tool for evaluating propagation losses in optical waveguides. This method leverages the Rayleigh scattering mechanism, where a portion of the guided light is scattered out of the waveguide due to imperfections and inhomogeneities within the material [5–7]. By illuminating the waveguide with a continuous-wave laser source and imaging the scattered light using an infrared-sensitive camera and microscope objective, one can visualize the light intensity along the waveguide's length. The captured image typically reveals an exponential decay in intensity along the propagation direction, from which the propagation loss coefficient is extracted using fitting techniques. A fundamental assumption in this method is the existence of a uniform distribution of scattering centers within the waveguide, where the amount of scattered light at any point is proportional to the local guided light intensity.

This method has several distinct advantages. It is non-destructive and spatially resolved, making it highly effective for identifying localized scattering centers and

diagnosing fabrication defects. Additionally, it provides a direct visual representation of loss variations along the waveguide, which is especially useful for planar slab structures. However, the method uses costly imaging systems and its reliability decreases for very low-loss waveguides, where the scattered light may be too weak to detect accurately. The accuracy could also be compromised by background noise, particularly from substrates with high autofluorescence or surface roughness. Moreover, measurements on three-dimensional waveguides are more complex due to anisotropic scattering at boundaries and reduced signal-to-noise ratios. Overall, while the scattering imaging method is an insightful diagnostic technique, it is best suited for planar waveguides with moderate to high propagation losses.

2.1.4 Fabry–Perot Interferometric Method

The FPI method, also called the Hakki-Paoli method, is a widely used technique for measuring optical propagation losses in waveguides, leveraging the interference fringes produced by reflections at the cleaved waveguide end facets, which act as low-finesse mirrors. Loss evaluation in this method is carried out by maintaining a constant laser power while modulating either the cavity length—typically through thermal tuning [8, 9]—or the laser wavelength, using a stabilized, narrow-linewidth tunable laser [10, 11]. The resulting Fabry–Perot interference fringes are recorded in the transmission spectrum of the waveguide, from which loss is extracted by analyzing the contrast between adjacent peaks and valleys.

The optical loss coefficient, α, is calculated using the following expression [10, 11]:

$$\alpha = -\frac{1}{L} ln \left(\frac{1}{R} \frac{\sqrt{K} - 1}{\sqrt{K} + 1} \right) \tag{2.1}$$

Here, L is the waveguide length, and K is the ratio of the power transmission at a fringe peak to that at the neighboring valley. The term $R = \sqrt{R_1 R_2}$ represents the geometric mean of the power reflectivities of the two waveguide end facets. Accurate knowledge of facet reflectivity is crucial for reliable loss estimation and may be obtained through mode solver simulations or effective index approximations. It is also important to note that this method relies on high-visibility, coherent interference fringes, necessitating a stable light source and minimal spurious intracavity reflections. Furthermore, single-mode operation is essential to prevent fringe distortion due to modal dispersion.

For the loss characterization of GaAs NRWs, the FPI method is particularly well suited, and it has been selected in our measurements for several compelling reasons. GaAs waveguides exhibit a high refractive index contrast at the GaAs–air

interfaces, which enhances facet reflectivity and improves fringe visibility—key attribute for reliable FPI-based loss extraction. In contrast to the cut-back method, which necessitates the cleaving and alignment of multiple waveguides while assuming consistent coupling conditions, the FPI technique enables accurate loss estimation from a single, unmodified device and is, in principle, independent of the coupling efficiency. This simplifies the experimental workflow and avoids errors associated with cleaving and facet preparation of multiple waveguides. In our case, where there is significant mismatch between the NRW mode profile and the lensed fiber spot size—an issue elaborated later in this chapter—coupling efficiency may vary significantly between measurements. The FPI method mitigates this issue by analyzing relative fringe intensities rather than absolute transmitted power, rendering it more robust against such variations. Compared to other techniques, such as scattering imaging—which offers spatially resolved defect characterization but requires costly imaging equipment and is better suited to planar waveguides—the Fabry–Perot interferometric (FPI) method is more practical for GaAs NRWs.

2.2 Propagation losses in undoped nano-ridge waveguides

2.2.1 Inspection of samples

This section presents an overview of the waveguide samples used in the optical loss measurements and describes the inspection techniques employed to evaluate their structural characteristics.

The waveguides under investigation were fabricated at imec using metal-organic vapour-phase epitaxy (MOVPE), following a monolithic integration process on silicon that combines ART and NRE, as described in Chapter 1. Comprehensive inspection was carried out using both optical and SEM images to evaluate key attributes such as geometry, surface quality, and inter-waveguide spacing.

Initial optical inspection was performed using a Keyence microscope. Device lengths were measured at $80\times$ magnification. For a more detailed surface assessment—particularly to identify structural imperfections such as cuts and waviness—stitched images were acquired at a higher magnification of $500\times$. These images provided a continuous and detailed view of the entire waveguide length, revealing that certain waveguides exhibited noticeable waviness and surface cuts. These features are of concern, as they can contribute to increased optical propagation losses. Figure 2.1 displays a zoomed-in stitched image of NRWs with varying trench widths, highlighting the presence of cuts and waviness along their lengths in

some waveguides.

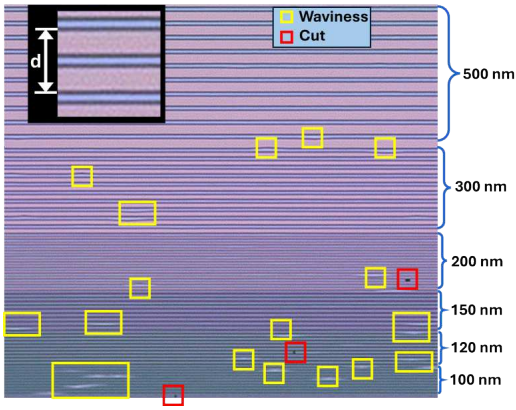

Figure 2.1: Keyence microscope image at 500× magnification, showing NRWs with varying trench widths (10 waveguides for each group). Waviness and cuts could be observed in some waveguides.

To gain further structural insight, cross-sectional SEM imaging was conducted by the imec-epi team. Figure 2.2 presents SEM cross-sections of NRWs fabricated with trench widths of $80\ \mathrm{nm}$, $100\ \mathrm{nm}$, $120\ \mathrm{nm}$, $150\ \mathrm{nm}$, $200\ \mathrm{nm}$, $300\ \mathrm{nm}$ and $500\ \mathrm{nm}$ on the same scale. These images were used to extract key geometrical parameters, which served as inputs for optical simulations used to estimate facet reflectivity and group index.

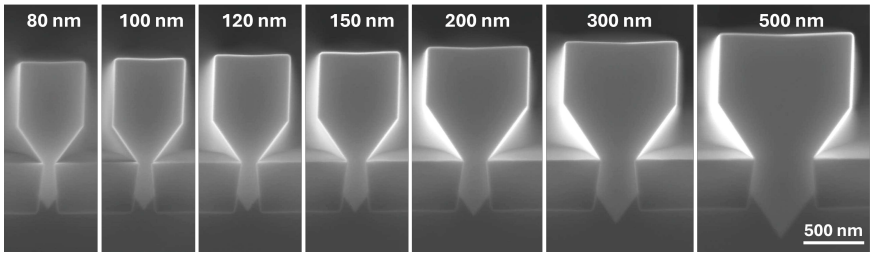

Figure 2.2: Cross-sectional SEM images of NRWs with trench widths of 80 nm, 100 nm, 120 nm, 150 nm, 200 nm, 300 nm, and 500 nm on the same scale.

An additional and critical aspect of the inspection involved evaluating the lateral separation between adjacent waveguides. This was necessary to determine the feasibility of coupling light into a single waveguide using a lensed fiber, a method highly sensitive to spatial alignment. The lensed fiber employed in the measurements has a spot size diameter of $\sim 2.5\ \mu\mathrm{m}$, which imposes a constraint on the minimum waveguide separation needed to avoid cross-talk. The separation distance, denoted

Table 2.1: Extracted values of width parameter d (referenced in the inset of Figure 2.1) from SEM cross-sectional images for NRWs with varying trench widths.

$Trench\ width$ (nm)	d (μm)
80	1.2
100	1.6
120	2
150	2.6
200	3.5
300	5.6
500	9.8

as 'd' in the inset of Figure 2.1, was extracted from the SEM cross-sections for each trench width configuration. These results are summarized in Table 2.1. It is evident from the data that coupling to an individual waveguide becomes increasingly difficult for trench widths below $120\ \mathrm{nm}$, as the reduced spacing between adjacent ridges results in a coupling area smaller than the lensed fiber's spot size diameter.

2.2.2 Measurement setup

As detailed in Section 2.1.4, the FPI method is employed to measure propagation losses in the NRWs. Figure 2.3 presents the schematic of the experimental setup. Light from a Santec TSL510-1310 tunable laser source, operating in the 1260-1360 nm wavelength range, is directed through a polarization controller (PC) to maximize the transmitted signal. The output of the polarization controller is connected to a lensed fiber, which couples light into the nano-ridge waveguide. At the output facet of the waveguide, light is collected by another lensed fiber and directed to a Newport power meter for optical power measurement.

During the measurement, the output power of the laser source is maintained at a constant level of $10\ \mathrm{dBm}$. The wavelength is swept over a $1\ \mathrm{nm}$ span around $1350\ \mathrm{nm}$, a wavelength at which material absorption in both the GaAs NRWs and the silicon substrate is negligible. Under these conditions, the measured losses are primarily attributed to scattering and leakage to the silicon substrate. The wavelength sweep of the laser source and the acquisition of the transmitted power spectra are automated via a Python script running on a control computer.

Figure 2.4 shows a $10\times$ magnification CMOS camera image of the lensed fiber coupling to the nano-ridge waveguide. Since the camera allows observation of the nano-ridge only from above, a red laser was employed to assist with coarse alignment along the vertical (z) axis, as shown in Figure 2.4. This initial alignment

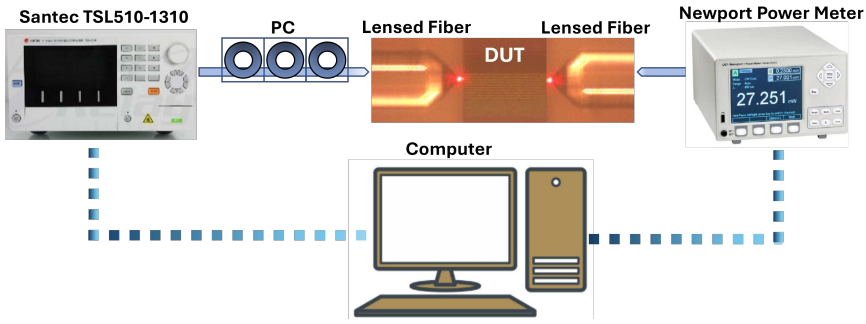

Figure 2.3: Schematic for the experimental setup. Santec TSL510-1310, laser source wavelength: 1260-1360 nm; PC, polarization controller; device under test(DUT), (undoped nano-ridge waveguide); Newport power meter; Single mode lensed fiber with red laser used for edge coupling alignment.

was achieved by carefully lowering the lensed fiber from above the surface until a reflection from the edge of the nano-ridge became visible, as illustrated in Figure 2.4.

Following the initial coarse alignment at both cleaved facets, fine alignment was performed by monitoring the transmitted optical power in real time. The lensed fiber, characterized by a working distance of $\sim 14\ \mu\mathrm{m}$ and mounted on a piezo-electrically driven translation stage, was precisely adjusted in all three spatial directions (x, y, and z) to maximize the transmitted signal. This procedure ensured optimal coupling efficiency between the lensed fiber and the nano-ridge waveguide.

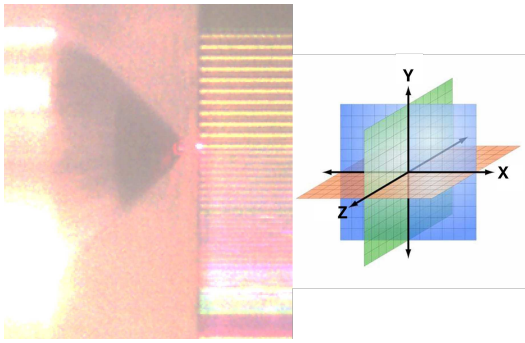

Figure 2.4: CMOS camera image (under 10× objective) showing coarse alignment of a lensed fiber to a nano-ridge waveguide, assisted by a red alignment laser.

2.2.3 Results

To quantify facet reflections in the NRWs, 3D FDTD simulations were performed using Lumerical software [12]. The simulations modeled the fundamental quasi-transverse electric (quasi-TE) mode, incorporating structural dimensions directly extracted from SEM cross-sectional images to ensure accurate physical representation. The resulting power reflection coefficients, presented in Figure 2.5, are subsequently incorporated into the loss calculations as described in Equation 2.1.

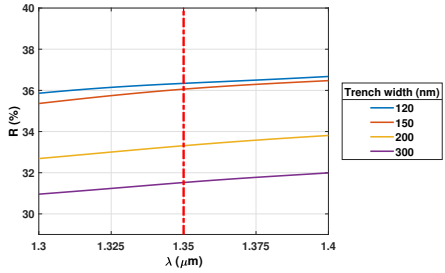

Figure 2.5: Power reflection coefficients at the waveguide facets evaluated via Lumerical FDTD simulations for NRWs with varying trench widths.

Figure 2.6 (a) presents the measured transmission from two waveguides on the same die, with trench widths of $200\ \mathrm{nm}$ and $300\ \mathrm{nm}$. Using the facet reflection coefficients obtained from the simulations (Figure 2.5) and the waveguide length of $3.734\ \mathrm{mm}$—measured using a Keyence optical microscope—the propagation losses were calculated according to Equation 2.1. The extracted loss values are shown in Figure 2.6 (b).

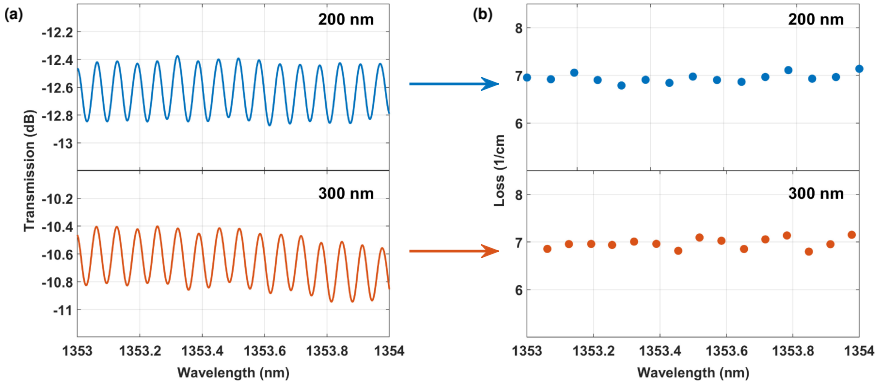

Figure 2.6: (a) Measured transmission through NRWs with trench widths of 200 nm and 300 nm. (b) Calculated waveguide propagation losses using the simulated facet reflection coefficients and measured waveguide length.

Figure 2.7 shows the extracted average propagation losses for waveguides fabricated on the same die that exhibited measurable transmission, specifically those with trench widths of 150 nm, 200 nm, and 300 nm. While a general trend in the propagation loss as a function of trench width is evident—and will be analyzed in more depth using a broader dataset below— there is a noticeable spread within each trench width group. This scatter likely arises from a combination of factors, including fluctuations in waveguide waviness along the propagation axis, variations in the density of structural defects, and dimensional non-uniformities (in both height and width) among waveguides nominally defined by the same trench width. Such dimensional deviations for nano-ridges with the same trench width are attributed to process variability in the MOVPE growth [13].

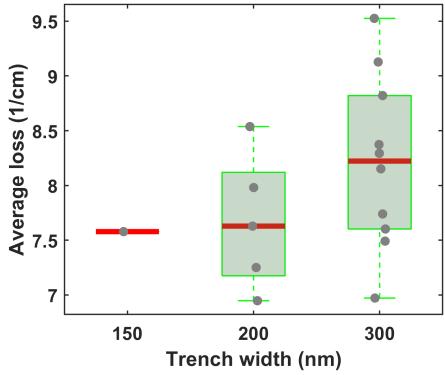

Figure 2.7: Box plot of extracted average propagation losses for NRWs on the same die with trench widths of 150 nm, 200 nm, and 300 nm. Each box shows the distribution of losses from multiple waveguides of the same trench width, with the red bar indicating the median, the green box spanning the interquartile range (IQR), and individual measurements plotted as gray markers.

To further investigate the impact of the trench width on the propagation losses, we extended our measurements to nine additional dies, evaluating a total of 117 waveguides. Table 2.2 provides the list of dies, the number of measured waveguides per trench width, and their corresponding waveguide lengths. The extracted average propagation losses for waveguides with trench widths of 120, 150, 200, and 300 nm are summarized in Figure 2.8 (a). These values fall within the range of approximately 8.5 cm^{-1}, a substantial figure that accounts for roughly 30% of the total optical losses in the electrically pumped nano-ridge lasers, as will be discussed in later chapters.

Several mechanisms may contribute to these propagation losses. One key factor is waveguide waviness, which can modulate the effective index along the propagation direction, thereby inducing scattering. This structural irregularity is visible in

Table 2.2: Number of measured devices per die for each trench width. A dash (–) indicates no measurable device for the specified trench width.

Die No.	120 nm	150 nm	200 nm	300 nm	L (mm)
1	–	2	4	7	3.64
2	–	1	5	10	3.83
3	1	2	4	10	3.55
4	2	–	3	4	2.83
5	1	–	3	3	3.28
6	–	–	2	1	3.66
7	–	1	5	10	3.73
8	–	3	7	10	2.91
9	1	2	1	7	3.98
10	–	–	1	4	2.89
Total	**5**	**11**	**35**	**66**	

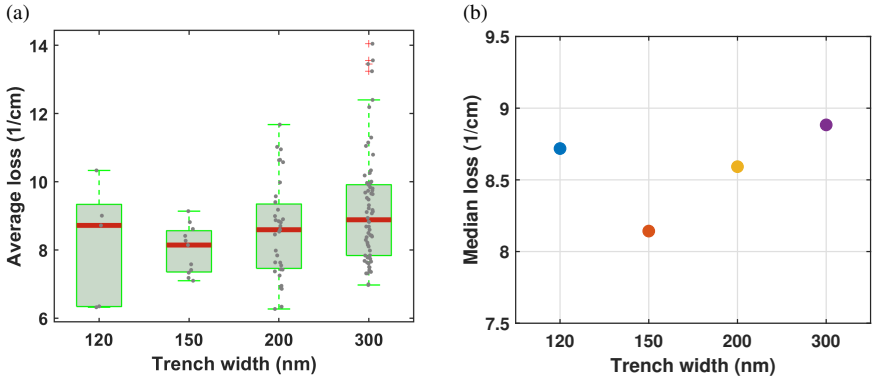

Figure 2.8: (a) Box plot of average propagation loss in NRWs with trench widths of 120 nm, 150 nm, 200 nm, and 300 nm. Each group shows the distribution of measurements, with red bars indicating medians and gray dots denoting individual data points. (b) Median propagation loss as a function of trench width.

Figure 2.1. Additional scattering loss contributions may come from unconfined defects—particularly prominent in wider trenches—as well as surface roughness on the waveguide sidewalls. Moreover, leakage into the high-index silicon substrate may also be another potential source of the propagation loss.

The spread observed in the loss data within each trench width group can likely be attributed to variability in these structural imperfections. Moreover, waveguides with the same nominal trench width but located on different dies may exhibit variation in facet reflectivity, influenced by cleaving quality and facet alignment,

which further contributes to measurement variability.

When analyzing the dependence of the propagation loss on the trench width, the limited number of devices with $120\ \mathrm{nm}$ trenches precludes a definitive conclusion. However, a consistent trend emerges when moving from $150\ \mathrm{nm}$ to $200\ \mathrm{nm}$ and $300\ \mathrm{nm}$ trenches: both Figure 2.8 (a) and the median loss plot in Figure 2.8 (b) indicate an increase in the propagation loss, culminating in a complete absence of measurable transmission for waveguides with $500\ \mathrm{nm}$ trench widths.

To quantify the contribution of substrate leakage to the overall propagation loss, 3D FDTD simulations were conducted for NRWs with trench widths of 120, 150, 200, 300, and 500 nm. A sufficiently long propagation length of $250\ \mu\mathrm{m}$ was used to ensure accurate estimation of the leakage loss around the wavelength of 1350 nm for the quasi-TE_{00} mode. The simulated leakage loss values are summarized in Figure 2.9.

As illustrated, leakage loss increases progressively with trench width due to reduced optical confinement in the GaAs ridge box as the trenches widen. A particularly sharp increase is observed between 300 nm and 500 nm, where the leakage loss escalates from approximately $0.5\ \mathrm{cm}^{-1}$ to $19\ \mathrm{cm}^{-1}$ at 1350 nm. This substantial increase may explain the absence of detectable transmission in devices with 500 nm wide trenches. For trench widths up to and including 300 nm, leakage losses remain below or around $0.5\ \mathrm{cm}^{-1}$, indicating that their impact on the total propagation loss is minimal. Accordingly, in this regime, the dominant contribution to the propagation loss can be ascribed to the scattering mechanisms discussed above.

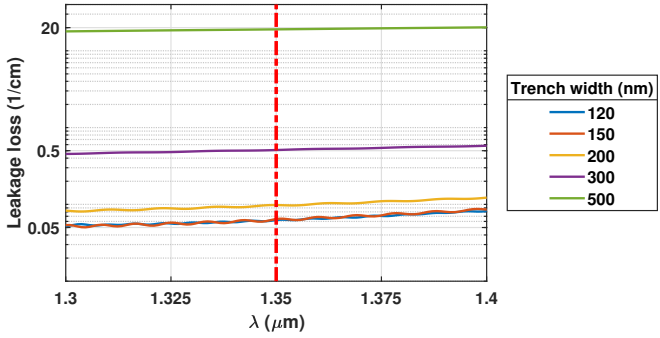

Figure 2.9: Simulated substrate leakage losses for quasi-TE_{00} modes in NRWs with trench widths of 120, 150, 200, 300 and 500 nm, calculated using 3D FDTD over the 1300–1400 nm wavelength range. Wider trenches exhibit increased leakage due to reduced mode confinement in the GaAs box.

To interpret the trend in the propagation loss as a function of the trench width observed in Figure 2.8(a) and (b), particularly in relation to the scattering losses,

a deeper insight into the monolithic growth process is essential. As introduced in Chapter 1, the GaAs nano-ridges are grown on silicon substrates using ART in combination with NRE. V-shaped silicon grooves help suppress the formation of APDs, while ART confines TDs and inclined PDs using vertical oxide sidewalls. A critical parameter in defect confinement is the aspect ratio (AR), defined as the oxide mask height divided by the trench width. It has been shown that effective defect trapping requires an AR greater than 1.43 [14].

Figures 2.10 (a)–(c) show cross-sectional transmission electron microscopy (TEM) images of GaAs nano-ridges taken along the trench direction, corresponding to trench widths of $40\ \mathrm{nm}$, $100\ \mathrm{nm}$, and $300\ \mathrm{nm}$, respectively [14]. The oxide shallow trench isolation (STI) boundaries are marked by white brackets. In the narrower trenches ($40\ \mathrm{nm}$ and $100\ \mathrm{nm}$), structural defects remain largely confined within the trench region, effectively trapped by the oxide sidewalls. However, in the wider $300\ \mathrm{nm}$ trench—where the AR approaches 1—defects propagate beyond the trench and into the overgrown ridge volume. This observation is consistent with findings of another work from imec [15], where the threading dislocation density (TDD) was shown to increase with trench width, reaching values exceeding $10^8\ \mathrm{cm}^{-2}$ for trenches with trench widths $\geq 300\ \mathrm{nm}$, as illustrated in Figure 2.11.

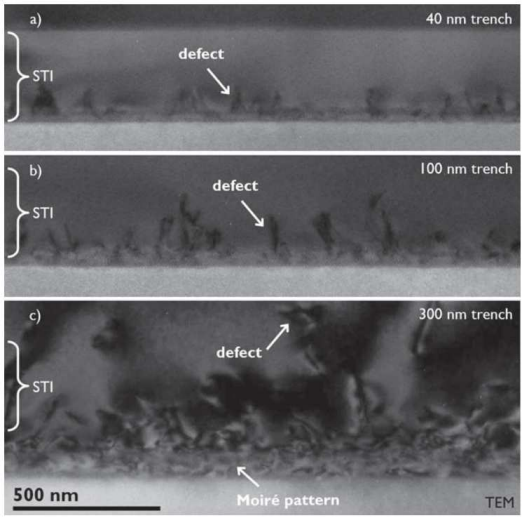

Figure 2.10: Longitudinal TEM cross-section images of GaAs nano-ridges with trench widths of (a) 40 nm, (b) 100 nm, and (c) 300 nm along the trench direction. The STI regions are indicated by the white brackets. Reproduced from [14].

To corroborate this further, ARs were extracted from SEM cross-sections (refer to Figure 2.2) for trench widths ranging from $120\ \mathrm{nm}$ to $500\ \mathrm{nm}$. These ARs are plotted in Figure 2.12. The AR decreases from approximately 3 for $120\ \mathrm{nm}$

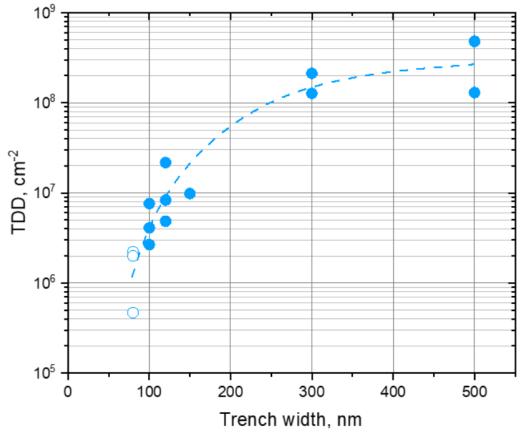

Figure 2.11: Threading dislocation density (TDD) as a function of trench width. TDD increases significantly with trench width, exceeding 10^8 cm^{-2} beyond 300 nm. Reproduced from [15].

trenches to 1.44 for 300 nm and drops further to 0.82 for 500 nm trenches—well below the 1.43 threshold required for effective defect confinement. These results suggest that wider trenches result in increased defect densities within the nano-ridge volume, likely exacerbating scattering losses. These observations provide a compelling explanation for the increasing propagation losses observed with trench widths up to 300 nm, primarily driven by enhanced scattering. In devices with a 500 nm trench width, these scattering losses compound the already substantial leakage losses, resulting in significantly degraded optical transmission.

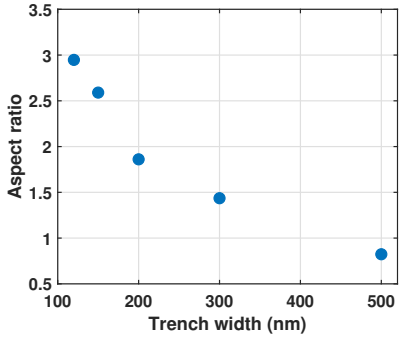

Figure 2.12: Aspect ratio (oxide mask height divided by trench width) as a function of trench width. The aspect ratio decreases below the critical value of 1.43 for trench widths >300 nm, indicating diminished defect confinement.

Group index extraction

To determine the group index of the fundamental quasi-TE mode, the FSR was extracted from the transmission spectra of NRWs with varying trench widths. The group index n_g was calculated using:

$$\Delta\lambda = \frac{\lambda^2}{2L\left(n_{\text{eff}} - \lambda\frac{\partial n_{\text{eff}}}{\partial\lambda}\right)} = \frac{\lambda^2}{2n_g L} \tag{2.2}$$

where $\Delta\lambda$ is the FSR, L is the cavity length, and n_{eff} and its wavelength derivative represent the effective index and its dispersion, respectively. An example of an FSR extraction from the transmission spectrum of the waveguide with 300 nm trench width from Figure 2.6 (a) is shown in Figure 2.13 (a). The experimentally determined group indices employing Equation 2.2 for the different trench width nano-ridges listed in Table 2.2 were then compared to those obtained from Lumerical MODE simulations, using cross-sectional dimensions extracted from SEM images (see Figure 2.2). This comparison is presented in Figure 2.13 (b).

Overall, good agreement is observed between the group indices extracted from measurements and those obtained from simulations. Minor discrepancies can be attributed to fabrication-induced variations in waveguide dimensions which affect both the mode confinement and the dispersion.

The observed reduction in group index with increasing trench width can be attributed to the interplay between the effective index and its wavelength dispersion. As the trench width increases, n_{eff} of the waveguide mode also increases due to stronger optical confinement. However, the dispersion of the effective index could diminish in larger waveguides. This decrease in dispersion leads to an overall reduction in n_g despite the higher n_{eff}. This behavior is illustrated in Figures 2.14 (a) and 2.14 (b), which present Lumerical MODE simulation results showing how the effective index, group index, and effective index dispersion vary as a function of the trench width.

2.3 Coupling loss between lensed fiber and GaAs nano-ridge waveguides

Efficient light coupling between external optical components and integrated waveguides is critical for characterizing device performance. In this section, coupling losses between lensed fibers and GaAs NRWs are analyzed through both experimental measurements and numerical simulations.

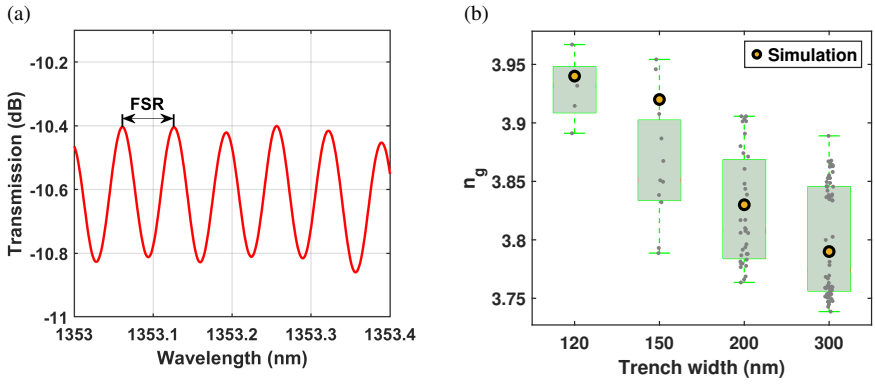

Figure 2.13: (a) Transmission spectrum of a nano-ridge waveguide with a 300 nm trench width, showing the FSR between adjacent peaks. (b) Comparison of group index n_g values extracted from measurements and Lumerical MODE simulations for NRWs with different trench widths.

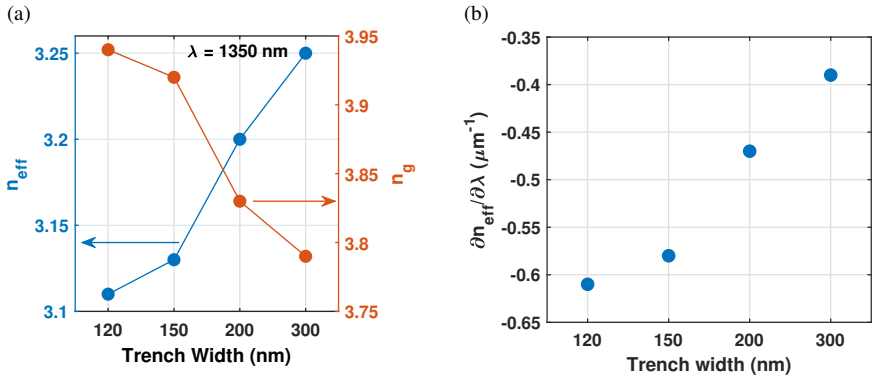

Figure 2.14: (a) Simulated effective index n_{eff} and group index n_g versus trench width at λ = 1350 nm, illustrating the inverse correlation due to dispersion. (b) Wavelength derivative of the effective index $\partial n_{eff}/\partial\lambda$ as a function of trench width, showing decreased dispersion in wider waveguides.

To isolate the intrinsic coupling loss mechanisms, two primary contributions are considered:

1. **Lensed fiber misalignment and insertion loss ($Loss_1$):** This loss component captures the coupling inefficiencies arising from imperfect alignment between the lensed fiber tips and the waveguide facets, in addition to intrinsic insertion losses of the fibers themselves. To quantify $Loss_1$, a back-to-back

configuration was used in which two lensed fibers were aligned without any waveguide in between. The measured insertion loss in this configuration was approximately 1 dB, which is attributed to alignment imperfections at both facets and inherent fiber insertion losses.

2. **Mode mismatch loss ($Loss_2$):** Additional losses arise from the mismatch between the Gaussian beam profile of the lensed fiber (with a mode field diameter of $\sim$2.5 μm) and the tightly confined mode of the nano-ridge waveguide. This loss was evaluated using Lumerical Finite Difference Eigenmode (FDE) simulations. The simulations utilized cross-sectional geometries extracted from SEM images to ensure realistic overlap integrals between the fiber and the waveguide modes. Figure 2.15 (a) presents the simulated mode mismatch losses at both facets of NRWs with varying trench widths.

The total estimated coupling loss is the sum of these two contributions:

$$Loss_{\text{cpl}} = Loss_1 + Loss_2 \tag{2.3}$$

To experimentally determine the coupling loss for each waveguide, the propagation loss was subtracted from the total insertion loss measured in the transmission setup:

$$Loss_{\text{cpl}}(\text{dB}) = P_{\text{in}} - \alpha \cdot L - P_{\text{measured}} \tag{2.4}$$

where P_{in} is the launched optical power (dBm), α is the propagation loss (dB/cm) evaluated by the FPI method, L is the waveguide length (cm), and P_{measured} is the transmitted power (dBm).

Figure 2.15 (b) compares the simulated and measured coupling losses across waveguides with different trench widths. The overall trend reveals a reduction in coupling loss with increasing trench width due to improved mode overlap. The measured values agree well with simulations, considering inevitable fabrication variations and practical alignment uncertainties.

2.4 Carrier-induced absorption in doped nano-ridge waveguides

Accurate modeling of optical loss is vital for the design of efficient integrated photonic circuits. Among the key sources of optical attenuation in doped semiconductor waveguides is carrier-induced absorption, which arises from the interaction

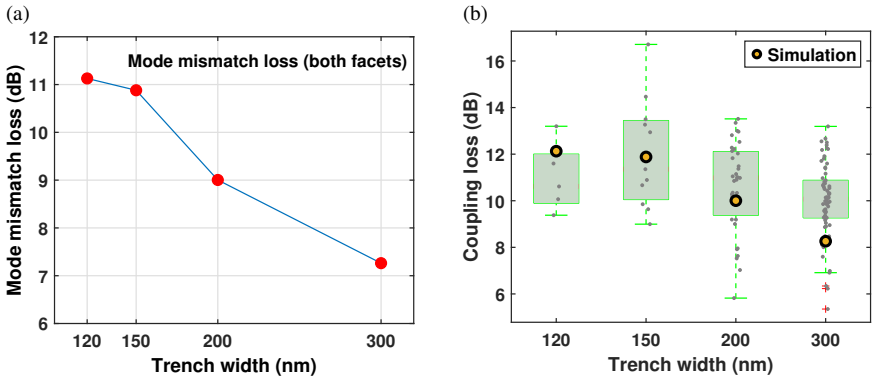

Figure 2.15: (a) Mode mismatch losses (for both facets) of GaAs NRWs with varying trench widths, evaluated via Lumerical FDE simulations. (b) Comparison between simulated and measured coupling losses showing good agreement across trench widths.

of free carriers—electrons in n-type or holes in p-type material—with the optical field. This interaction leads to non-resonant intra-band or inter-band transitions that absorb photons within the sub-bandgap region, i.e., below the bandgap energy [16].

As the nano-ridge laser structures considered in later chapters incorporate silicon-doped n-GaAs, carbon-doped p-GaAs, zinc-doped p-InGaP, and phosphorus-doped n-Si, this section focuses on the carrier-induced absorption characteristics of these materials.

In n-doped GaAs, free electrons contribute to absorption through two primary mechanisms [16]:

- **Free-carrier intra-band transitions**, enabled by phonon or impurity scattering to conserve momentum.
- **Inter-conduction-band valleys transitions**, where electrons absorb photons to transition between energy valleys in the conduction band.

The absorption coefficient due to electrons is directly proportional to the electron concentration N. For example, Weber reported an empirical model for InGaAsP material systems:

$$\alpha_N = 3.1 \times 10^{-18} \cdot N \quad (\text{cm}^{-1})$$

where N is in cm^{-3} [17].

In the case of phosphorus-doped silicon, the absorption coefficient at 10^{19} cm^{-3} between 1000–1500 nm has been reported by Baker-Finch *et al.* [18]. This dataset

is summarized in Figure 2.16 and will be used in optical loss simulations discussed in later chapters.

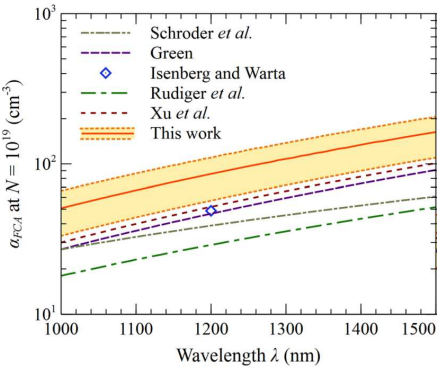

Figure 2.16: Free carrier absorption coefficient of phosphorus-doped n-Si as a function of wavelength at a doping concentration of 10^{19} cm^{-3}, extracted from multiple literature sources [18].

In p-doped semiconductors such as GaAs and InGaP, absorption is dominated by intervalence band absorption (IVBA), where holes transition between valence sub-bands, primarily from the split-off to the heavy-hole band [19]. The absorption scales with the hole concentration P, and increases rapidly at higher doping levels.

For p-GaAs, Kazuaki *et al.* demonstrated that carbon doping induces up to twice the absorption seen in zinc-doped GaAs at $\lambda = 1300$ nm [20], as shown in Figure 2.17 (a). On the other hand, Dubravko *et al.* quantified absorption coefficients for zinc-doped p-GaAs at 980 nm [21]. To approximate the absorption for carbon-doped p-GaAs around this wavelength, we scale these values by a factor of two. The compiled results, shown in Figure 2.17 (b), will be used in the subsequent chapters to estimate carrier-induced absorption in p-GaAs regions for simulations around 1000 nm.

For Zn-doped InGaP, Murphy *et al.* fit the below-bandgap absorption spectra to the following exponential model:

$$\alpha_{\text{IVB}}(\lambda, P) = 4.25 \times 10^{-16} \cdot \exp\left(\frac{-4.533}{\lambda}\right) \cdot P \tag{2.5}$$

where λ is the wavelength in μm and P is the hole density in cm^{-3} [16]. This relationship will be employed in optical simulations involving p-InGaP in subsequent chapters.

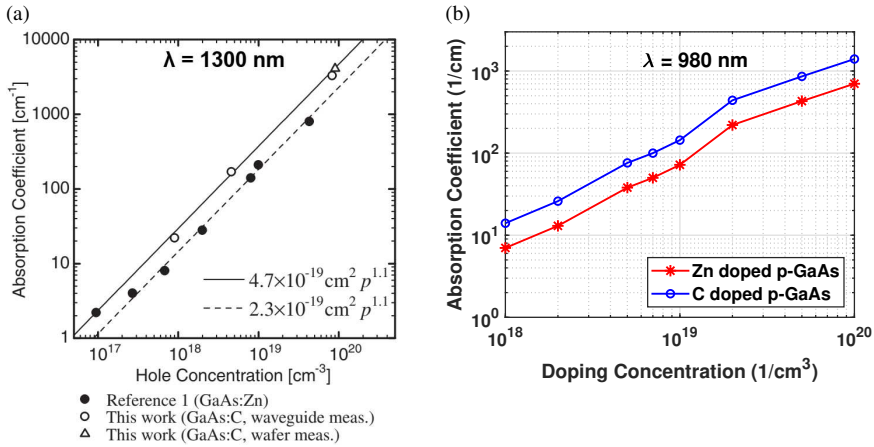

Figure 2.17: (a) Comparison of absorption coefficients for C-doped and Zn-doped p-GaAs at $\lambda = 1300$ nm, showing nearly two-fold increase in absorption for carbon doping [20]. (b) Absorption coefficient vs. doping concentration at $\lambda = 980$ nm, derived from experimental data by Dubravko et al. for Zn-doped GaAs [21] and extended to C-doped GaAs by scaling.

2.5 Feasibility of loss measurement for doped nano-ridge waveguides

This section examines the feasibility of applying the FPI method to extract propagation losses in doped GaAs NRWs with varying doping concentrations and trench widths. Both numerical simulations and practical limitations are considered.

The analysis is guided by two primary criteria:

1. Is the transmitted power sufficient to be detected by a standard power meter?
2. Is the round-trip loss low enough to permit reliable extraction of transmission fringe maxima and minima?

To address these questions, the total transmission and round-trip losses are evaluated using the following relations:

$$\text{Transmission Loss} = (\alpha_{\text{dop}} + \alpha_{\text{scat}}) \cdot L + Loss_{\text{cpl}} \tag{2.6}$$

$$\text{Round-trip Loss} = [2(\alpha_{\text{dop}} + \alpha_{\text{scat}}) + \alpha_{\text{mirror}}] \cdot L \tag{2.7}$$

Here, α_{dop} denotes doping-induced loss taken from the references in the previous section as starting point, $\alpha_{\text{scat}} = 34.7$ dB/cm is the estimated scattering loss for

undoped NRWs from section 2.2.3, $Loss_{\text{cpl}}$ accounts for coupling losses, α_{mirror} represents mirror losses at both waveguide facets (evaluated from extracted reflectivities from FDTD simulations), and $L = 3$ mm is the assumed waveguide length.

The feasibility of transmission detection is based on the assumption of a source power of $10\ \text{dBm}$ and a detector sensitivity threshold of $-65\ \text{dBm}$, corresponding to a maximum allowable transmission loss of approximately $75\ \text{dB}$.

Fringe visibility (K) is also evaluated as a function of the round-trip loss using Equation 2.1 and Equation 2.7. As shown in Figure 2.18, visibility rapidly degrades and becomes lower than $0.1\ \text{dB}$ when the round-trip loss exceeds $40\ \text{dB}$. Therefore, a round-trip loss of $40\ \text{dB}$ is considered the upper limit for reliable FPI-based loss measurement.

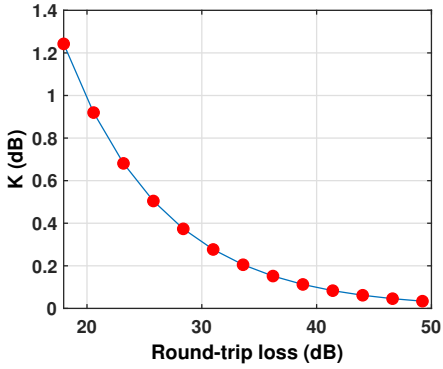

Figure 2.18: Calculated fringe visibility (K) as a function of round-trip loss for a 3 mm waveguide. Below 40 dB round-trip loss, K remains sufficiently high for reliable fringe extraction.

Figure 2.19 shows the contour plots of the transmission and round-trip losses for 3 mm-long fully n-doped GaAs NRWs. As depicted in Figure 2.19(a), the transmission loss exhibits a general decrease with increasing trench width, primarily attributed to reduced coupling losses in wider waveguides. Based on the defined power detection threshold, transmission is expected to be feasible across all trench widths and doping levels considered. However, Figure 2.19(b) indicates that the round-trip loss exceeds the 40 dB threshold for doping concentrations above $N > 2 \times 10^{18}\ \text{cm}^{-3}$, beyond which reliable extraction of interference fringes becomes challenging.

For fully p-doped GaAs NRWs, the contour plots shown in Fig. 2.20 illustrate a similar trend. Although transmission is feasible up to $2 \times 10^{18}\ \text{cm}^{-3}$, the round-trip losses remain above the critical 40 dB threshold even at moderate doping levels,

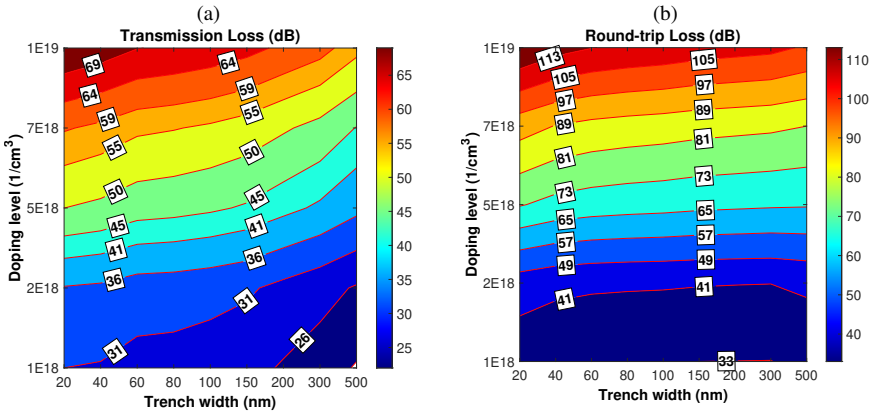

Figure 2.19: (a) Contour plot for transmission losses of 3 mm-long fully n-GaAs doped NRWs. (b) Contour plot for corresponding round-trip losses. Transmission remains detectable across the range, but round-trip loss becomes prohibitive for doping levels beyond 2×10^{18} *cm*$^{-3}$.

limiting the use of FPI methods for loss extraction in these structures.

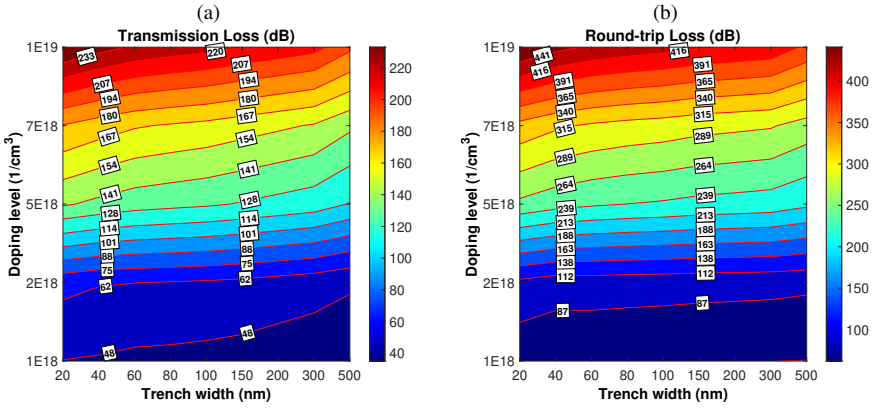

Figure 2.20: (a) Contour plots for transmission losses of 3 mm-long fully p-GaAs doped NRWs. (b) Contour plots for round-trip losses of the same configurations. Round-trip loss exceeds acceptable range across all doping levels.

Another assessment involves a complete p-i-n doping profile for 80 nm trench width NRW, as schematically illustrated in Figure 2.21. Table 2.3 summarizes the estimated transmission and round-trip losses for two representative p-GaAs doping concentrations. While the profile with 2×10^{18} cm^{-3} doping level appears suitable

for FPI measurement, the 1×10^{19} cm^{-3} doping concentration results in excessive round-trip loss, precluding accurate fringe detection.

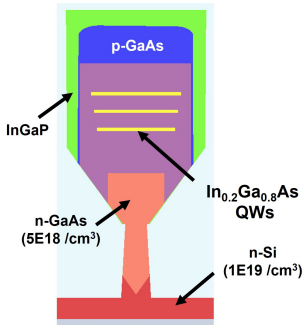

Figure 2.21: Cross-sectional schematic of the p-i-n doped 80 nm trench width NRW used for loss simulations.

Table 2.3: Estimated transmission and round-trip losses for p-i-n doped 80 nm trench width NRW.

p-GaAs Doping Level (cm^{-3})	**Transmission Loss (dB)**	**Round-trip Loss (dB)**
2×10^{18}	31.2	42.0
1×10^{19}	54.6	88.8

In summary, while transmission detection is generally feasible across a broad range of trench widths and doping levels, the high round-trip losses in heavily doped n-GaAs and p-GaAs waveguides significantly limit the applicability of the Fabry–Perot method. These results can serve as an initial design guideline for future experimental efforts aimed at measuring losses in doped NRWs.

2.6 Conclusion

In this chapter, we presented a comprehensive study of optical loss mechanisms in GaAs NRWs, encompassing both propagation and carrier-induced absorption losses. A critical comparison of waveguide loss measurement techniques was conducted, with the FPI method identified as the most suitable for GaAs NRWs due to its compatibility with high-index contrast interfaces and its robustness to coupling variability. The FPI technique enabled accurate extraction of propagation losses

from a single device without the need for cleaving or repeated alignment, making it an efficient and reliable approach for characterizing undoped GaAs NRWs.

An in-depth investigation of the propagation loss in GaAs NRWs revealed a clear dependence on the trench width, with losses increasing steadily from 150 nm to 300 nm and culminating in a complete lack of transmission for 500 nm-wide trenches. 3D FDTD simulations confirmed that leakage into the silicon substrate remains negligible (below $0.5\ \mathrm{cm}^{-1}$) for trench widths up to 300 nm, while surging to $19\ \mathrm{cm}^{-1}$ at 500 nm—explaining the absence of measurable transmission at that width. However, the dominant loss mechanism for narrower trenches was attributed to scattering. Waveguides with wider trenches (smaller AR) exhibited higher scattering losses, which is potentially attributed to reduced defect confinement—permitting dislocations to extend into the overgrown ridge volume. Coupling losses between lensed fibers and NRWs were also analyzed, highlighting significant contributions from mode mismatch between the confined waveguide mode and the larger spot size of the lensed fiber. Notably, simulated coupling losses were found to be in good agreement with measurement results.

Carrier-induced absorption represents a significant loss mechanism in doped GaAs NRWs, with its magnitude strongly dependent on doping type, concentration, and operating wavelength. Empirical data from the literature shows that n-type doping induces absorption through intra-band and inter-conduction band valleys transitions, while p-type doping results in pronounced intervalence band absorption. Absorption coefficients for key materials of importance in the coming chapters—including p-GaAs, n-GaAs, n-Si, and p-InGaP—have been studied. Additionally, a feasibility analysis was conducted to evaluate the applicability of the FPI method for characterizing doped waveguides. While transmission measurements remain viable across a broad doping range, elevated round-trip losses in heavily doped structures—especially in p-type GaAs—pose challenges for fringe extraction, thereby limiting the practicality of the FPI method under such conditions.

The scattering loss data from FPI measurements and the absorption coefficients for the different doping profiles studied in this chapter will serve as essential inputs for the simulation and optimization of electrically pumped nano-ridge lasers presented in the following chapters.

References

[1] R. G. Hunsperger and J. R. Meyer-Arendt, Integrated optics: Theory and technology, *Applied Optics*, vol. 31, no. 3, p. 298, 1992.

[2] A. Boudrioua and J. Loulergue, New approach for loss measurements in optical planar waveguides, *Optics Communications*, vol. 137, no. 1–3, pp. 37–40, Apr. 1997.

[3] Y. H. Won, P. C. Jaussaud, and G. H. Chartier, Three-prism loss measurements of optical waveguides, *Applied Physics Letters*, vol. 37, no. 3, pp. 269–271, Aug. 1980.

[4] J. Naden, G. Reed, and B. Weiss, Analysis of prism-waveguide coupling in anisotropic media, *Journal of Lightwave Technology*, vol. 4, no. 2, pp. 156–159, 1986.

[5] T. A. Strasser and M. C. Gupta, Optical loss measurement of low-loss thin-film waveguides by photographic analysis, *Applied Optics*, vol. 31, no. 12, p. 2041, Apr. 1992.

[6] Y. Okamura, A. Miki, and S. Yamamoto, Observation of wave propagation in integrated optical circuits, *Applied Optics*, vol. 25, no. 19, p. 3405, Oct. 1986.

[7] S. Dutta, H. Jackson, J. Boyd, R. Davis, and F. Hickernell, CO_2 laser annealing of Si_3N_4, Nb_2O_5, and Ta_2O_5 thin-film optical waveguides to achieve scattering loss reduction, *IEEE Journal of Quantum Electronics*, vol. 18, no. 4, pp. 800–806, Apr. 1982.

[8] R. Walker, Simple and accurate loss measurement technique for semiconductor optical waveguides, *Electronics Letters*, vol. 21, no. 13, pp. 581–583, Jun. 1985.

[9] R. Regener and W. Sohler, Loss in low-finesse Ti:$LiNbO_3$ optical waveguide resonators, *Applied Physics B Photophysics and Laser Chemistry*, vol. 36, no. 3, pp. 143–147, Mar. 1985.

[10] I. Henning and P. Rodgers, Improved method of measuring loss and phase shifts in waveguide devices, *Electronics Letters*, vol. 23, no. 23, pp. 1245–1246, Nov. 1987.

[11] S. Taebi, M. Khorasaninejad, and S. S. Saini, Modified fabry-perot interferometric method for waveguide loss measurement, *Applied Optics*, vol. 47, no. 35, p. 6625, Dec. 2008.

[12] *Lumerical photonics simulation and design software official website*, https://www.ansys.com/products/photonics.

[13] Y. De Koninck et al., GaAs nano-ridge laser diodes fully fabricated in a 300-mm CMOS pilot line, *Nature*, vol. 637, no. 8044, pp. 63–69, 2025.

[14] B. Kunert, Y. Mols, M. Baryshniskova, N. Waldron, A. Schulze, and R. Langer, How to control defect formation in monolithic III-V hetero-epitaxy on (100) Si? a critical review on current approaches, *Semiconductor Science and Technology*, vol. 33, no. 9, p. 093 002, Aug. 2018.

[15] M. Baryshnikova et al., Nano-ridge engineering of GaSb for the integration of InAs/GaSb heterostructures on 300 mm (001) Si, *Crystals*, vol. 10, no. 4, 2020.

[16] E. J. Murphy, *Integrated Optical Circuits and Components: Design and Applications* (Optical Science and Engineering), 1st. CRC Press, 1999.

[17] J.-P. Weber, Optimization of the carrier-induced effective index change in InGaAsP waveguides-application to tunable bragg filters, *IEEE Journal of Quantum Electronics*, vol. 30, no. 8, pp. 1801–1816, 1994.

[18] S. C. Baker-Finch, K. R. McIntosh, D. Yan, K. C. Fong, and T. C. Kho, Near-infrared free carrier absorption in heavily doped silicon, *Journal of Applied Physics*, vol. 116, no. 6, Aug. 2014.

[19] M. Asada, A. Adams, K. Stubkjaer, Y. Suematsu, Y. Itaya, and S. Arai, The temperature dependence of the threshold current of GaInAsP/InP DH lasers, *IEEE Journal of Quantum Electronics*, vol. 17, no. 5, pp. 611–619, May 1981.

[20] K. Kiyota, T. Kageyama, H. Shimizu, and Y. Kawakita, Measurement of absorption coefficient of carbon-doped GaAs, *Japanese Journal of Applied Physics*, vol. 48, no. 11, p. 111 103, Nov. 2009.

[21] D. Babic et al., Design and analysis of double-fused 1.55-μm vertical-cavity lasers, *IEEE Journal of Quantum Electronics*, vol. 33, no. 8, pp. 1369–1383, 1997.

3

Semi-analytical model for electrically injected InGaAs/GaAs nano-ridge lasers monolithically integrated on silicon

Contents

In the previous chapter, we investigated scattering losses in undoped nano-ridge waveguides (NRWs), focusing on their dependence on the trench width. We also quantified the coupling losses between the lensed fiber and NRWs in a horizontal coupling configuration. Additionally, we conducted a feasibility study on loss

characterization in doped NRWs, which can serve as a foundation for future measurements in doped waveguides using the Hakki-Paoli method.

As discussed in Chapter 1, one of the key challenges hindering electrical pumping in monolithic lasers fabricated via selective epitaxy is the limited material volume available. This constraint makes it difficult to integrate metal contacts without incurring significant optical losses. Specifically, minimizing the overlap between the optical mode and the metal contact is critical to reduce absorption losses. Addressing this challenge has been a primary focus of research on monolithic III–V nano-ridge lasers, both at imec and within our group, over the past decade. Meanwhile, a significant milestone was reached with the demonstration of monolithic $In_{0.2}Ga_{0.8}As$/GaAs multi-quantum well photodetectors by ART and NRE, which utilized periodic tungsten p-type plugs [1]. Building on this achievement, the next logical step was to realize electrically injected lasing. However, progress was initially hindered by the strong optical mode overlap with the p-type contact, leading to substantial losses. A major breakthrough occurred with the successful demonstration of electrically pumped $In_{0.2}Ga_{0.8}As$/GaAs nano-ridge lasers, fully fabricated on 300-mm silicon wafers using a CMOS pilot manufacturing line. This was made possible by exploiting a mode-beating effect, as reported in [2]. These nano-ridge laser arrays exhibited continuous-wave lasing at room temperature, with emission wavelengths around 1020 nm.

In this chapter, we develop a semi-analytical model for these monolithic nano-ridge lasers to gain insight into their internal operation. The model provides a framework for optimizing the device cross-section and contact scheme to achieve low threshold gain and tailored emission characteristics. It also enables the analysis of the differential quantum efficiency. This work has been published in [3].

The chapter is organized as follows: Section 1 introduces the device structure under investigation. In Section 2, we examine mode coupling within the nano-ridge waveguide. Section 3 is dedicated to the formulation and application of the round-trip laser model. Using this model, we evaluate the threshold gain, determine the full width at half maximum (FWHM) of the round-trip gain, assess the impact of the device height on the lasing behavior, and analyze the differential quantum efficiency. Throughout this section, we incorporate results from Chapter 2 to support the model development. Finally, in Section 3.4, we validate the model by comparing its predictions with experimental data.

3.1 Device structure

The fabrication of the nano-ridge lasers is carried out through a combination of ART and NRE, as introduced in Chapter 1. The NRE process enables the epitaxial growth of fully relaxed, box-shaped structures emerging from the trenches. These outgrown nano-ridges incorporate a p-i-n heterojunction within their geometry. A schematic representation of the resulting device architecture is shown in 3D in Figure 3.1 (a) while (b) depicts a cross-section at a position of a tungsten metal plug. At the core of the laser lies the active region, composed of three compressively strained $In_{0.2}Ga_{0.8}As$ quantum wells (QWs), confined by GaAs barriers. The $In_{0.5}Ga_{0.5}P$ layer serves as a passivation layer to reduce surface non-radiative recombination at the GaAs–air interface [4]. Electrical injection is facilitated through two contacts: the n-type side is established by a tungsten plug connecting to a heavily doped n-type silicon substrate, which is electrically interfaced with the n-type GaAs region that extends from the bottom V-groove to the ridge structure. On the p-side, electrical contact is achieved using a periodic array of tungsten vias that pierce through the $In_{0.5}Ga_{0.5}P$ layer to make contact with the underlying p-type GaAs. Final metallization is carried out using standard copper (Cu) deposition over both contact regions to complete the electrical pathway.

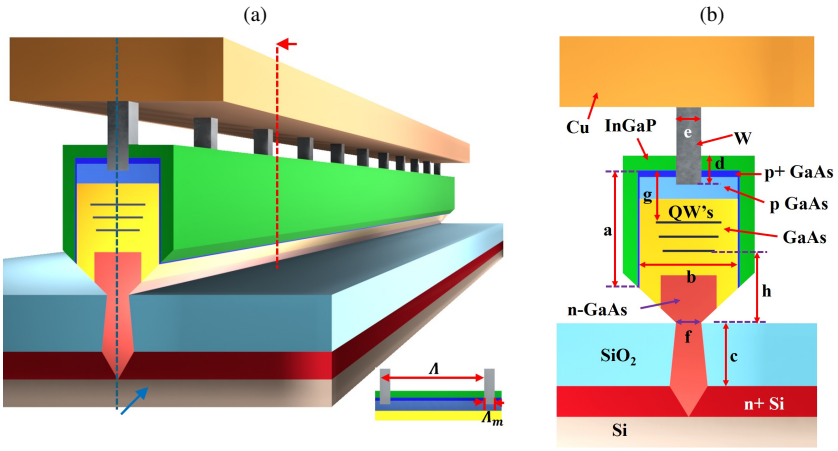

Figure 3.1: (a) Schematic illustration of a nano-ridge waveguide featuring a tungsten metal grating with a period $\Lambda = 4.8\ \mu m$ and metal plug length $\Lambda_m = 100\ nm$ (not to scale). (b) Cross-sectional view of the nano-ridge waveguide at the location of a tungsten plug, as indicated by the red dashed line in (a). The doping levels are specified in Table 3.2.

For the model developed in the following sections, the key dimensional parameters defining the cross-sectional geometry are summarized in Table 3.1. The periodic

tungsten plugs (with permittivity of $-4.31 + i21.89$ around $1035\ \mathrm{nm}$) feature a pitch of 4.8 µm, carefully engineered to induce a loss dip near the target wavelength of 1035 nm. A more detailed discussion of this design choice is provided in the next section. Additionally, the doping concentrations corresponding to the various doped regions depicted in Figure 3.1(b) are listed in Table 3.2.

Table 3.1: Parameters for GaAs nano-ridge cross-section in Fig. 3.1(b).

a **(nm)**	***b*** **(nm)**	***c*** **(nm)**	***d*** **(nm)**	***e*** **(nm)**	***f*** **(nm)**	***g*** **(nm)**	***h*** **(nm)**
490	400	265	125	100	100	222	308

Table 3.2: Doping levels for the different doped regions in Fig. 3.1(b).

No.	**Region**	**Doping Level (cm^{-3})**
1	n Si	1×10^{19}
2	n GaAs	2×10^{18}
3	p GaAs	2×10^{18}
4	p+ GaAs	1×10^{19}

3.2 Coupling between modes in a nano-ridge waveguide

At this stage, we consider the nano-ridge cross-section depicted in Figure 3.1 (b), excluding any specified doping. The eigenmodes of the waveguide are computed at a wavelength of 1035 nm using the Lumerical FDE MODE solver [5], with each mode characterized by a distinct effective refractive index.

In realistic high-index-contrast dielectric waveguides, guided modes are inherently hybrid, possessing non-zero electric field components in all three spatial directions. In the transverse XY plane, both E_x and E_y components are generally present, although one typically dominates. For clarity and consistency with integrated photonics literature, we adopt the notation *quasi-TE*$_{mn}$ (quasi-transverse electric) or *quasi-TM*$_{mn}$ (quasi-transverse magnetic), where the "quasi" qualifier indicates the hybrid nature of the fields, and the TE/TM designation corresponds to the dominant transverse polarization [6]. Specifically, a mode is labeled quasi-TE when the dominant electric field component lies in-plane (E_x for z as the propagation axis and y as the vertical axis), and quasi-TM when the dominant component is out-of-plane (E_y, the vertical component).

Following this convention, the first six confined modes supported by the nano-ridge are illustrated in Figure 3.2. Their corresponding effective indices and TE polarization fractions, calculated as [5]

$$\text{TE polarization fraction (Ex)} = \frac{\int |E_x|^2 \, dx \, dy}{\int \left(|E_x|^2 + |E_y|^2\right) dx \, dy},$$

are summarized in Table 3.3.

The fundamental quasi-TM mode, identified as the first supported mode, exhibits greater vertical extension, which results in increased leakage into the underlying silicon substrate. In contrast, the second mode corresponds to the fundamental quasi-TE mode. Owing to its reduced substrate leakage and superior optical confinement, this mode is the primary focus of further analysis in this work. The remaining modes are higher-order hybrid modes having the specified TE polarization fraction.

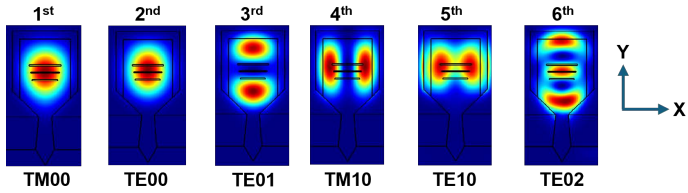

Figure 3.2: Transverse optical mode intensities supported by the nano-ridge structure near 1035 nm*, computed using the Lumerical FDE solver.*

Table 3.3: Effective indices and TE-mode power fractions for the first six confined modes near 1035 nm*, as depicted in Figure 3.2.*

No.	Mode	n_{eff}	TE fraction
1	TM00	3.26	0
2	TE00	3.24	100
3	TE01	2.98	90
4	TM10	2.85	6
5	TE10	2.71	99
6	TE02	2.59	73

To investigate the evolution of optical power in the fundamental TE_{00} mode within a nano-ridge waveguide incorporating a periodic p-type tungsten contact with a 4.8 µm pitch, simulations were performed using the FDTD solver. A modal source was positioned at $Z = 0$, and two power monitors were placed at $Z = 50\,\mu$m and $Z = 100\,\mu$m, as illustrated in the schematic of Figure 3.3. The resulting power

attenuation spectrum, corresponding to the decay in the modal power between the two monitoring points, is presented in Figure 3.4. Notably, distinct dips are observed in the attenuation spectrum, prompting further analysis to understand their origin.

To this end, the longitudinal electric field distribution was examined along the nano-ridge at wavelengths near 1035 nm, where the most prominent attenuation dip occurs. The field profile at this wavelength reveals an interference pattern characterized by low-intensity regions located beneath the metal plugs. Further analysis attributes this phenomenon to modal beating between the TE_{00} and TE_{02} modes, which have a beating length of 1.6 µm. This interaction results in periodic field minima beneath the plugs, thereby reducing the overlap with the lossy metal regions. The intensity of the beating-induced interference pattern is visualized in Figure 3.5, confirming its role in the observed attenuation dip.

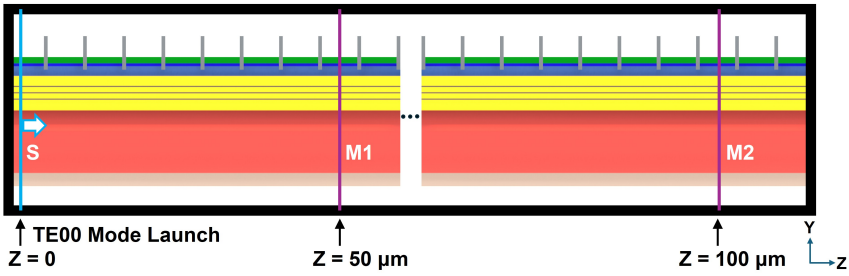

Figure 3.3: Schematic of the longitudinal cross-section of the nano-ridge, including periodic metal plugs, along the dashed blue line indicated in Figure 3.1 (a). This configuration is used to set up the Lumerical FDTD simulations (S: modal source, M1: Monitor 1, M2: Monitor 2).

Building on the insights gained from the numerical simulations, this section presents an analytical framework to explain the underlying physical mechanisms, with particular relevance to the laser round-trip model developed in the next section.

We begin by considering two dominant propagating modes in the nano-ridge waveguide. The total electric field can be expressed as a superposition of these modes:

$$E(x,y,z) = E_1(z)U_1(x,y)e^{-j\beta_1 z} + E_2(z)U_2(x,y)e^{-j\beta_2 z}, \tag{3.1}$$

where $U_1(x,y)$ and $U_2(x,y)$ represent the transverse field distributions of the two modes, β_1 and β_2 denote their respective propagation constants in the unperturbed waveguide, and $E_1(z)$, $E_2(z)$ are the corresponding mode amplitudes along the propagation direction.

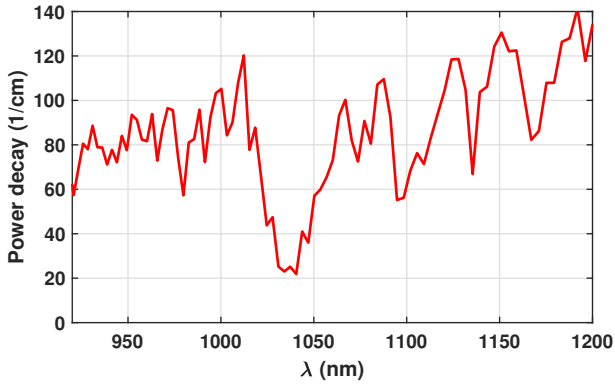

Figure 3.4: Simulated power attenuation spectrum of the TE_{00} mode, calculated from power monitors positioned at $z = 50\,\mu m$ and $z = 100\,\mu m$.

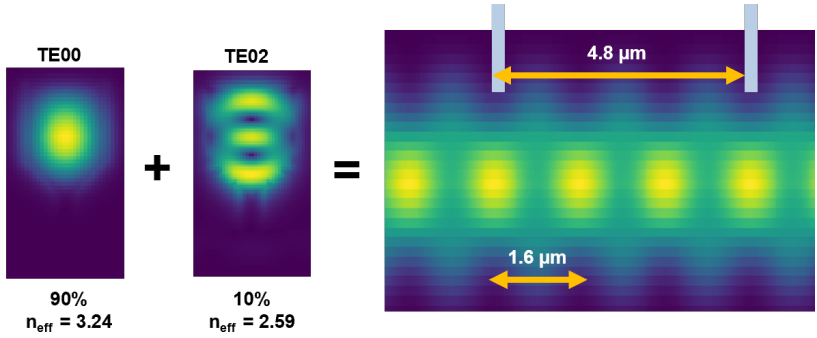

Figure 3.5: Mode beating intensity pattern resulting from the interference between the TE_{00} and TE_{02} modes at a wavelength of 1.035 µm, exhibiting a beating length of 1.6 µm and revealing low-intensity regions directly beneath the metal contacts.

To model the interaction of these modes in the presence of a periodic perturbation in permittivity, $\Delta\epsilon$, we apply the Helmholtz equation to the total field. This leads to a system of coupled-mode equations that describe how the amplitudes E_1 and E_2 evolve along z [7]:

$$\frac{dE_1(z)}{dz} = -j\frac{\kappa_0^2}{2\beta_1}E_1\frac{\int \Delta\epsilon U_1^2\,dA}{\int U_1^2\,dA} - j\frac{\kappa_0^2}{2\beta_1}e^{-j(\beta_2-\beta_1)z}E_2\frac{\int \Delta\epsilon U_1 U_2\,dA}{\int U_1^2\,dA}, \quad (3.2)$$

$$\frac{dE_2(z)}{dz} = -j\frac{\kappa_0^2}{2\beta_2}E_2\frac{\int \Delta\epsilon U_2^2\,dA}{\int U_2^2\,dA} - j\frac{\kappa_0^2}{2\beta_2}e^{-j(\beta_1-\beta_2)z}E_1\frac{\int \Delta\epsilon U_1 U_2\,dA}{\int U_2^2\,dA}, \quad (3.3)$$

where κ_0 is the free-space propagation constant.

The permittivity perturbation $\Delta\epsilon(x, y, z)$ is assumed to be periodic along the propagation direction and is represented by a Fourier series:

$$\Delta\epsilon(x, y, z) = \sum_{l=-\infty}^{\infty} \Delta\epsilon_l(x, y) e^{-jl\left(\frac{2\pi}{\Lambda}\right)z}, \tag{3.4}$$

where Λ is the spatial period of the perturbation, and l indexes the spatial harmonics.

Substituting the Fourier expansion into equations (3.2) and (3.3) and retaining only the slowly varying terms yields the simplified coupled-mode equations:

$$\frac{dE_1(z)}{dz} = -j\kappa_{11}E_1 - j\kappa_{12}E_2 e^{j(\beta_1-\beta_2-l\frac{2\pi}{\Lambda})z}, \tag{3.5}$$

$$\frac{dE_2(z)}{dz} = -j\kappa_{22}E_2 - j\kappa_{21}E_1 e^{j(\beta_2-\beta_1+l\frac{2\pi}{\Lambda})z}, \tag{3.6}$$

with the coupling coefficients defined as follows:

$$\kappa_{ii} = \frac{\kappa_0^2 \int \Delta\epsilon_0 U_i^2 \, dA}{2\beta_i \int U_i^2 \, dA}, \quad \kappa_{12} = \frac{\kappa_0^2 \int \Delta\epsilon_{-l} U_1 U_2 \, dA}{2\beta_1 \int U_1^2 \, dA}, \quad \kappa_{21} = \frac{\kappa_0^2 \int \Delta\epsilon_l U_1 U_2 \, dA}{2\beta_2 \int U_2^2 \, dA},$$

where $i = 1, 2$, and l is the harmonic index that satisfies the phase-matching condition $\beta_1 - \beta_2 \approx l\frac{2\pi}{\Lambda}$.

If the perturbation is symmetric about $z = 0$, then $\Delta\epsilon_l = \Delta\epsilon_{-l}$, implying $\kappa_{12} = \kappa_{21}$, assuming the modes are normalized according to $\beta_i \iint U_i^2 \, dx \, dy = 2\mu_0\omega$, where μ_0 denotes the permeability of free space and ω is the angular frequency.

Here, κ_{11} and κ_{22} account for the self-coupling due to the change in the effective index, while κ_{12} and κ_{21} govern the intermodal coupling. The imaginary parts of κ_{11} and κ_{22} specifically account for absorption losses induced by the metal contacts.

In the case of a rectangular complex perturbation in $\Delta\epsilon$, all coupling terms are complex and can be computed as follows [8]:

$$\kappa_{ii} = \frac{\kappa_0^2}{2\beta_i}\left(\frac{\Lambda_m}{\Lambda}\right)\epsilon_{\text{diff}}\frac{\int_G U_i^2 \, dA}{\int U_i^2 \, dA}, \quad i = 1, 2,$$

$$\kappa_{ij} = \frac{\kappa_0^2}{2\beta_i} \frac{\sin\left(\pi \frac{l\Lambda_m}{\Lambda}\right)}{\pi l} \epsilon_{\text{diff}} \frac{\int_G U_i U_j \, dA}{\int U_i^2 \, dA}, \quad i = 1, 2, \quad j = 1, 2, \quad i \neq j,$$

where Λ and Λ_m are defined in Figure 3.1(a), and the integrals over the region G represent the spatial overlap between the modal fields and the perturbation (e.g., metal plugs). The parameter ϵ_{diff} quantifies the difference in permittivity between the perturbed and unperturbed sections.

To investigate the beating behavior between the TE_{00} and TE_{02} modes, we consider an input excitation where only the TE_{00} mode is launched at $z = 0$. Solving the coupled-mode equations (3.5) and (3.6), the modal power along the waveguide for the TE_{00} and TE_{02} modes can respectively be expressed as:

$$P_1(z) = \left| \cos(sz) - j\frac{\delta}{s} \sin(sz) \right|^2 e^{-2\text{Im}(\tilde{\beta})z}, \tag{3.7}$$

$$P_2(z) = \left| \frac{\kappa_{21}}{s} \sin(sz) \right|^2 e^{-2\text{Im}(\tilde{\beta})z}, \tag{3.8}$$

where the parameters are defined as:

$$\tilde{\beta} = \frac{\beta_1 + \kappa_{11} + \beta_2 + \kappa_{22}}{2}, \quad \delta = \frac{\beta_1 + \kappa_{11} - \beta_2 - \kappa_{22}}{2} - l\frac{\pi}{\Lambda}, \quad s = \sqrt{\delta^2 + \kappa_{12}\kappa_{21}}.$$

Here, $\beta_1 = \frac{2\pi n_1}{\lambda}$ and $\beta_2 = \frac{2\pi n_2}{\lambda}$, where n_1 and n_2 are the effective indices of the unperturbed modes. Note that all quantities including $\tilde{\beta}$, δ, s, and the coupling coefficients are wavelength-dependent.

To validate the analytical model developed for mode coupling in the nano-ridge waveguide, a comprehensive numerical workflow was employed. This process involved extracting the electric field profiles, effective indices, and relative permittivity data using the Lumerical MODE solver. The analysis focused on the two dominant optical modes—TE_{00} and TE_{02}—whose transverse field profiles and effective indices were exported and subsequently used for the numerical computation of the mode coupling coefficients.

The coupling coefficients were computed using a MATLAB written code by performing numerical integration of the relevant overlap integrals. These integrals were evaluated over the perturbed region of the waveguide, which featured a rectangular permittivity variation as illustrated in Figure 3.1. This perturbation corresponds to the periodic metal plugs embedded in the waveguide structure. Once the coupling

coefficients were obtained, they were substituted into Equations 3.7 and 3.8 to evaluate the evolution of modal power along the propagation axis.

Figure 3.6 (a) presents a comparison between the analytical results and those obtained from FDTD simulations. The comparison spans the wavelength range from 920 nm to 1200 nm and shows the power spectra in both the TE_{00} and TE_{02} modes at various distances from the input source. A particularly strong agreement is observed around 1035 nm, the wavelength at which phase matching occurs and efficient coupling between the two modes takes place.

Figure 3.6(b) presents a comparison between the analytical and simulated modal power distributions along the propagation direction at the wavelength corresponding to zero detuning. The results demonstrate strong agreement between the two approaches, confirming the accuracy of the analytical model. Notably, within the initial 60 µm of propagation, the TE_{00} mode undergoes a rapid power decay, accompanied by a steady increase in the power of the TE_{02} mode. Beyond this 60 µm distance, the power exchange slows noticeably. This shift in behavior can be attributed to the formation of a standing interference pattern between the TE_{00} and TE_{02} modes. This pattern results in zones of reduced electric field intensity directly beneath the lossy metal plugs. As a consequence, both metal-induced absorption and intermodal coupling are minimized. The system thus enters a regime resembling a quasi-steady-state, in which both modes continue to propagate with minimal further energy transfer, while maintaining a stable beating pattern and exhibiting only gradual attenuation.

Additionally, the secondary dips observed in the numerically calculated attenuation spectrum of the TE_{00} mode, as shown in Figure 3.4, can be attributed to additional mode coupling phenomena. These features emerge from the coupling between the TE_{00} mode and other higher-order modes supported by the nano-ridge structure, leading to the formation of distinct modal beating patterns that give rise to the observed spectral characteristics.

3.3 Round-trip laser model

3.3.1 Evaluation of the threshold gain

To develop a comprehensive model for the round-trip gain in the laser cavity, we begin our analysis at the left facet of the nano-ridge waveguide. As illustrated in Figure 3.7, we assume the fundamental TE_{00} mode and the higher-order TE_{02} mode are excited with normalized input amplitudes a_1 and a_2, respectively. These optical modes propagate along the cavity length L, reaching the right facet with amplitudes

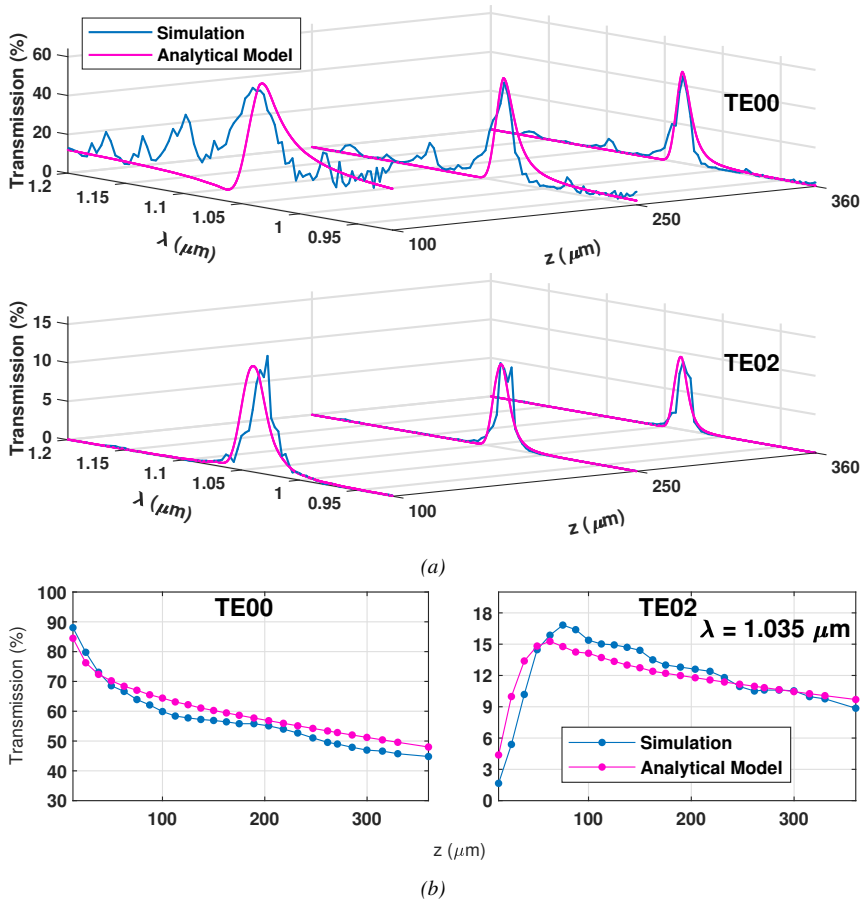

Figure 3.6: Comparison between analytical and FDTD simulation results: (a) Power spectra of the TE_{00} and TE_{02} modes at various positions along the nano-ridge waveguide. (b) Modal power of the TE_{00} and TE_{02} modes at the zero-detuning wavelength as a function of the propagation distance z from the source.

a_1' and a_2'. Upon reflection at the right facet, the amplitudes become b_1' and b_2', and after propagating back over the same distance L, they return to the left facet as b_1'' and b_2''. A final reflection at the left facet yields the amplitudes b_1 and b_2, thereby completing a full round-trip within the cavity.

Using the analytical framework established in the previous section and assuming identical facets on either side, the round-trip behavior can be expressed as:

$$\begin{bmatrix} b_1 \\ b_2 \end{bmatrix} = R \cdot T \cdot R \cdot T \cdot \begin{bmatrix} a_1 \\ a_2 \end{bmatrix} \tag{3.9}$$

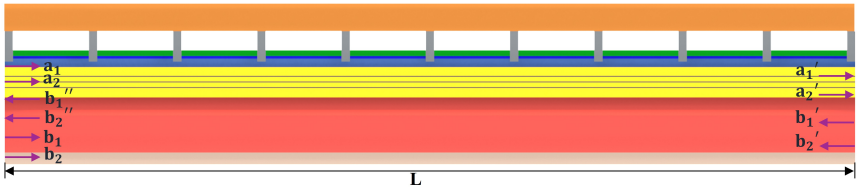

Figure 3.7: Schematic longitudinal cross-section of a nano-ridge waveguide with metal plug grating and end facets, showing the round-trip light propagation model (cross-section along the dashed blue line in Fig. 3.1(a)).

where the propagation and coupling matrix T is given by:

$$T = \begin{bmatrix} (\cos sL - j\frac{\delta}{s}\sin sL)e^{-j(\tilde{\beta}+\frac{l\pi}{\Lambda})L} & -j\frac{\kappa_{12}}{s}\sin(sL)e^{-j(\tilde{\beta}+\frac{l\pi}{\Lambda})L} \\ -j\frac{\kappa_{21}}{s}\sin(sL)e^{-j(\tilde{\beta}-\frac{l\pi}{\Lambda})L} & (\cos sL + j\frac{\delta}{s}\sin sL)e^{-j(\tilde{\beta}-\frac{l\pi}{\Lambda})L} \end{bmatrix}$$

and the reflection matrix R is:

$$R = \begin{bmatrix} r_{11} & r_{12} \\ r_{21} & r_{22} \end{bmatrix}$$

Each reflection coefficient r_{ij} is defined as:

$$r_{ij} = \left.\frac{b_i'}{a_j'}\right|_{a_k'=0,\ k\neq j}, \quad i,j,k = 1,2$$

The reflection coefficients were determined using FDTD simulations and evaluated to be $r_{11} = 0.60$, $r_{22} = 0.82$, and $r_{12} = r_{21} = 0.24$ at the wavelength of 1.035 μm. These values were obtained by launching each mode (TE_{00} and TE_{02}) separately near the facet and decomposing the reflected field into guided modes using a mode expansion monitor. This method provides access not only to the self-reflection of each mode but also to the cross-coupling between the modes at the facet. In the analysis, both facets were assumed to be cleaved and identical. For comparison, Coldren [7] reports a modal amplitude reflection coefficient of $r \approx 0.55$ in an in-plane quantum-well laser with a waveguide width of 2 μm, a height of 250 nm, and an emission wavelength near 980 nm. This comparison shows that the simulated TE_{00} reflectivity of the nano-ridge waveguide is of the same order of magnitude as values previously reported for conventional semiconductor laser geometries.

The complex propagation constants β_i for each mode include both gain and loss contributions, and are defined as:

$$\beta_i = \frac{2\pi n_i}{\lambda} + j\frac{1}{2}\Gamma_i g_m - j\frac{1}{2}\alpha_{d,i} - j\frac{1}{2}\alpha_{s,i}, \quad i = 1, 2$$

with the transverse confinement factor Γ_i computed as:

$$\Gamma_i = \frac{\int_{\text{QW}} U_i^2 \, dA}{\int U_i^2 \, dA}$$

where the overlap integrals are taken over the $In_{0.2}Ga_{0.8}As$ QW regions. Here, g_m denotes the material gain, $\alpha_{d,i}$ represents free-carrier absorption (FCA) losses in the doped regions, and $\alpha_{s,i}$ includes scattering and substrate leakage losses for each mode.

Scattering losses were extracted from experimental measurements on undoped nano-ridge waveguides without metal plugs using the Hakki-Paoli method, as discussed in Chapter 2. These yielded an average scattering loss value of $8 \pm 0.5 \ \text{cm}^{-1}$. Losses due to coherent scattering into radiation modes from the periodic tungsten contacts are considered negligible, owing to the large pitch relative to the optical wavelength, which results in weak higher-order diffraction. This assumption is corroborated by the agreement between the simulation and analytical results presented in the previous section, which omit such scattering phenomena.

The FCA losses associated with the doped regions were computed for both the TE_{00} and TE_{02} modes using the Lumerical FDE MODE solver. This analysis involved introducing the imaginary components of the refractive indices corresponding to the relevant doped semiconductor materials. The doping profile implemented in the simulation, shown in Figure 3.1 (b), was constructed based on physical dimensions extracted from TEM images, combined with carrier concentration estimates obtained via Scanning Spreading Resistance Microscopy (SSRM) and informed by the epitaxial growth parameters.

A detailed analysis of the absorption coefficients for the various doped material systems employed in the nano-ridge laser structure was presented in Chapter 2. Based on this analysis, literature values for the FCA coefficients of phosphorus-doped n-type silicon [9], silicon-doped n-type GaAs [10], and carbon-doped p-type GaAs [11, 12] were used to define the imaginary parts of the refractive indices in the FDE MODE solver. Using these inputs, the FCA losses were calculated to be $5.2 \ \text{cm}^{-1}$ for the TE_{00} mode and $11.6 \ \text{cm}^{-1}$ for the TE_{02} mode.

Equation 3.9 can be simplified as:

$$\begin{bmatrix} b_1 \\ b_2 \end{bmatrix} = \begin{bmatrix} x_{11} & x_{12} \\ x_{21} & x_{22} \end{bmatrix} \begin{bmatrix} a_1 \\ a_2 \end{bmatrix} \tag{3.10}$$

where the 2×2 matrix on the right is the product of the four matrices from Equation 3.9. Lasing occurs when the eigenvalue of this round-trip matrix equals unity, ensuring the field replicates after one round-trip. This leads to the threshold condition:

$$x_{11}x_{22} - x_{12}x_{21} - x_{11} - x_{22} + 1 = 0 \tag{3.11}$$

Applying this condition, the material threshold gain for a device with cavity length $L = 1502.4$ μm was computed to be 792 cm^{-1}. This value was obtained iteratively by adjusting the gain to achieve a round-trip eigenvalue magnitude of unity.

Figure 3.8 presents the calculated eigenvalue magnitude and phase versus wavelength at threshold. Red markers indicate wavelengths at which the round-trip phase satisfies the condition of being an integer multiple of 2π. Lasing occurs at $\lambda \approx 1035.65$ nm. The eigenvector corresponding to the unity eigenvalue of the round-trip matrix determines the specific superposition of the modal amplitudes a_1 and a_2 that leads to lasing within the cavity. Our analysis indicates that this lasing mode comprises approximately 89% of the optical power in the TE_{00} mode and 11% in the TE_{02} mode at $z = 0$.

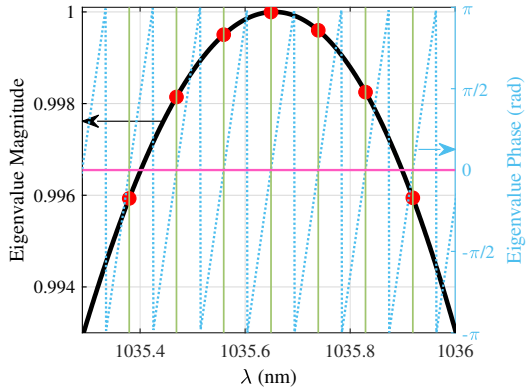

Figure 3.8: Eigenvalue magnitude and phase as a function of wavelength. Red points indicate locations where the eigenvalue phase is zero (corresponding to the intersections of the green and pink curves) and the magnitude is close to unity).

3.3.2 FWHM of the round-trip gain

The FWHM of the round-trip gain plays a crucial role in determining the spectral selectivity of the laser and its susceptibility to multimode operation. A narrower

FWHM typically indicates a sharper resonance, which helps suppress competing modes and increases the gain margin for single-mode lasing.

To examine how modal coupling influences this parameter, we analyzed the sensitivity of the FWHM of the eigenvalue magnitude to variations in the complex coupling coefficient $\kappa_{12} = \kappa_{21}$. The coupling coefficient at threshold was calculated to be $(0.0139 - i\,0.0198)\ \mu\mathrm{m}^{-1}$. By systematically varying both the real and imaginary components of κ_{12} around this value, we observed several trends, as shown in the contour plot of Figure 3.9.

First, a general reduction in the FWHM is observed as the real part of the coupling coefficient decreases. This effect becomes more pronounced when the imaginary part is relatively small in magnitude. Additionally, for imaginary components less than $0.025\ \mu\mathrm{m}^{-1}$, a decrease in FWHM is also evident with increasing imaginary values—an effect that is more significant when accompanied by a higher real part. However, when the imaginary component exceeds $0.025\ \mu\mathrm{m}^{-1}$, its influence on the FWHM diminishes, as indicated by the contour gradients in the figure.

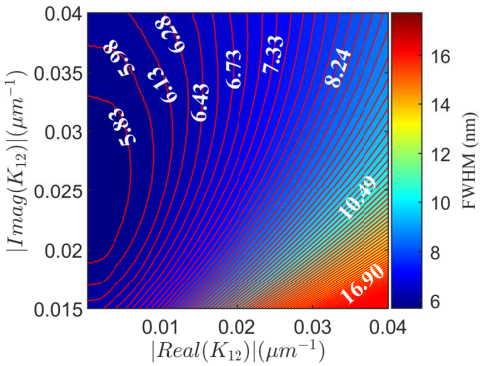

Figure 3.9: Contour plot showing the FWHM of the eigenvalue magnitude as a function of the real and imaginary components of the coupling coefficient $\kappa_{12} = \kappa_{21}$. Trends indicate decreased FWHM with lower real parts and larger imaginary components, particularly below $0.025\ \mu\mathrm{m}^{-1}$.

Although the calculated FWHM of the round-trip gain is around 5 nm—suggesting that single-mode lasing should be difficult—experimental results indicate robust single-mode operation. This apparent contradiction can be explained by nonlinear gain effects, particularly the spectral hole burning (SHB) mechanism [13].

The normalized gain of the i^{th} mode is defined as

$$G_i = \frac{g_i}{\alpha_{int} + \alpha_m}, \tag{3.12}$$

where g_i is the modal gain, α_{int} is the internal loss, and α_m is the mirror loss. The gain margin is given by $\Delta G = G_0 - G_1$, where G_0 and G_1 correspond to the normalized gains of the dominant lasing mode and the nearest side mode, respectively. In a purely linear-gain model, ΔG is constant above threshold and side modes saturate at a fixed intensity.

However, in the presence of SHB, the nonlinear third-order polarization

$$\Delta P_{\mathrm{NL}} = \chi^{(3)} E^3 \tag{3.13}$$

leads to a mode-dependent gain suppression. For two modes with electric fields E_0 (dominant mode) and E_1 (side mode), the nonlinear susceptibilities satisfy $\chi_1 = \frac{4}{3}\chi_0$ where $\chi_0 = \frac{9}{16}\chi^{(3)} E_0^2$ [13]. This results in a greater gain reduction for the side modes than for the central mode, effectively increasing ΔG with optical power:

$$\Delta G = G_L(\lambda_0) - G_L(\lambda_1) + \frac{1}{3} f(\lambda_0, \lambda_0) P_0, \tag{3.14}$$

where $G_L(\lambda)$ is the linear gain spectrum, $f(\lambda_0, \lambda_0)$ is the SHB profile with respect to λ_0 due to the burn-in at λ_0, and P_0 is the power in the dominant mode.

This increase in gain margin with injection current leads to enhanced side-mode suppression and single-mode stabilization, even when the linear round-trip gain FWHM is wide. Figure 3.10 (adapted from [13]) shows the measured light output in the dominant and adjacent modes for a GaAs/GaAlAs stripe laser, clearly illustrating the suppression of side modes at higher injection levels due to SHB.

3.3.3 Influence of GaAs box height on lasing characteristics

The developed model allows for a detailed analysis of how structural variations in the device affect its lasing properties, particularly the threshold gain and the emission wavelength. One key parameter is the height of the GaAs nano-ridge box, denoted as 'a' in Figure 3.1(b). By varying 'a' from $460\ \mathrm{nm}$ to $520\ \mathrm{nm}$ while maintaining a constant ratio $g/h = 0.72$ (where g is the distance from the top of the upper QW to the top of the box, and h is the distance from the top of the trench to the bottom of the lowest QW), we observe a shift in the modeled lasing wavelength from $947\ \mathrm{nm}$ to $1120\ \mathrm{nm}$ as shown in Figure 3.11. This tunability is particularly significant as it enables alignment of the simulated lasing wavelength with the experimentally observed gain peak near $1020\ \mathrm{nm}$, as reported in [14, 15].

As shown in Figure 3.12 (a), increasing the box height results in a progressive rise in the threshold gain, from $745\ \mathrm{cm}^{-1}$ at $a = 460\ \mathrm{nm}$ to $881\ \mathrm{cm}^{-1}$ at $a = 520\ \mathrm{nm}$. This trend is driven by the collective influence of several interdependent factors: the modal confinement factors within the QWs (Figure 3.12 (b)), reflection scattering

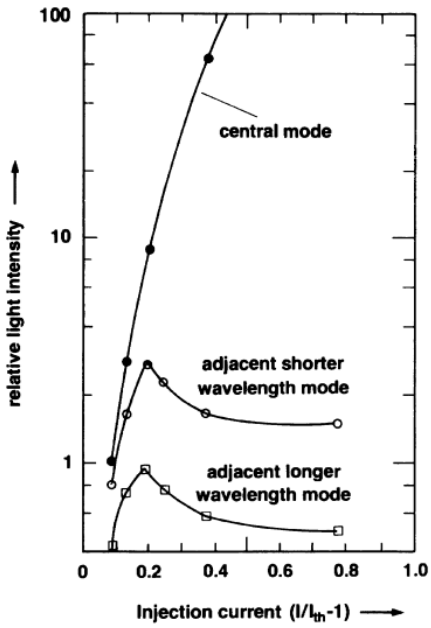

Figure 3.10: Measured output intensity of the primary lasing mode and its neighboring side modes for a GaAs/GaAlAs stripe laser diode. Reproduced from [13].

coefficients (Figure 3.12 (c)), modal power distribution at the left facet (Figure 3.12 (d)), coupling coefficients, and FCA losses (see Table 3.4) of the TE_{00} and the TE_{02} modes.

The coupling coefficients are particularly sensitive to variations in the mode overlap with the metallic contacts and to the wavelength-dependent imaginary component of tungsten's refractive index. As the GaAs box height increases, the confinement factor of the fundamental TE_{00} mode gradually decreases, leading to weaker optical confinement within the QWs. Concurrently, the contribution of the TE_{02} mode to the modal composition at the facet also declines, as shown in Figure 3.12(d). Given that the TE_{02} mode provides stronger facet reflectivity, its reduced presence diminishes the overall optical feedback, thereby contributing to the observed increase in the threshold gain.

Further contributing to the rise in threshold gain is the slight reduction in the imaginary part of the cross-coupling coefficient $\kappa_{12} = \kappa_{21}$, which marginally reduces the magnitude of the eigenvalue. Collectively, these effects lead to an increased threshold gain required to achieve lasing.

Figure 3.12(e) illustrates the variation in the FWHM of the round-trip gain as a

function of the GaAs box height. A gradual increase in the FWHM is observed with increasing box height. This trend can be attributed to changes in the mode coupling coefficient $\kappa_{12} = \kappa_{21}$, as analyzed in the previous sub-section and depicted in the contour plot of Figure 3.9. The observed increase in the FWHM with the GaAs box height can be attributed to an increase in the real component of the coupling coefficient, a decrease in its imaginary component, or a combination of both factors. These trends are quantitatively supported by the coupling coefficient values presented in Table 3.4.

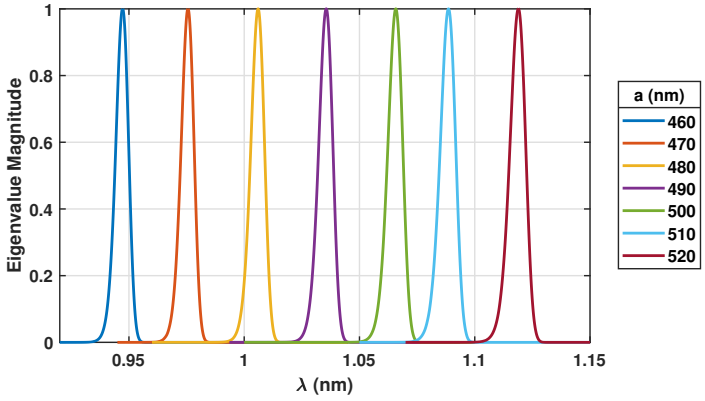

Figure 3.11: Variation of lasing wavelength with GaAs box height 'a' (as labeled in Figure 3.1(b)).

Table 3.4: Coupling coefficients and FCA losses associated with doped regions for varying GaAs box height 'a', as defined in Figure 3.1(b), evaluated at the corresponding lasing wavelengths.

a (nm)	κ_{11} (μm^{-1})	$\kappa_{12} = \kappa_{21}$ (μm^{-1})	κ_{22} (μm^{-1})	$\alpha_{d,1}$ (cm^{-1})	$\alpha_{d,2}$ (cm^{-1})
460	$0.0073 - i0.0106$	$0.0139 - i0.0201$	$0.0295 - i0.0425$	5.00	12.25
470	$0.0072 - i0.0104$	$0.0136 - i0.0197$	$0.0286 - i0.0415$	5.00	12.65
480	$0.0071 - i0.0102$	$0.0137 - i0.0199$	$0.0297 - i0.0429$	5.09	11.76
490	$0.0071 - i0.0102$	$0.0139 - i0.0198$	$0.0302 - i0.0432$	5.17	11.59
500	$0.0071 - i0.0100$	$0.0141 - i0.0198$	$0.0309 - i0.0435$	5.14	11.47
510	$0.0071 - i0.0099$	$0.0142 - i0.0196$	$0.0314 - i0.0435$	5.05	11.83
520	$0.0073 - i0.0098$	$0.0145 - i0.0195$	$0.0322 - i0.0433$	5.17	12.44

3.3.4 Differential quantum efficiency

The differential quantum efficiency (η_d) quantifies the effectiveness with which the optical power generated inside the laser cavity is extracted as usable output from the

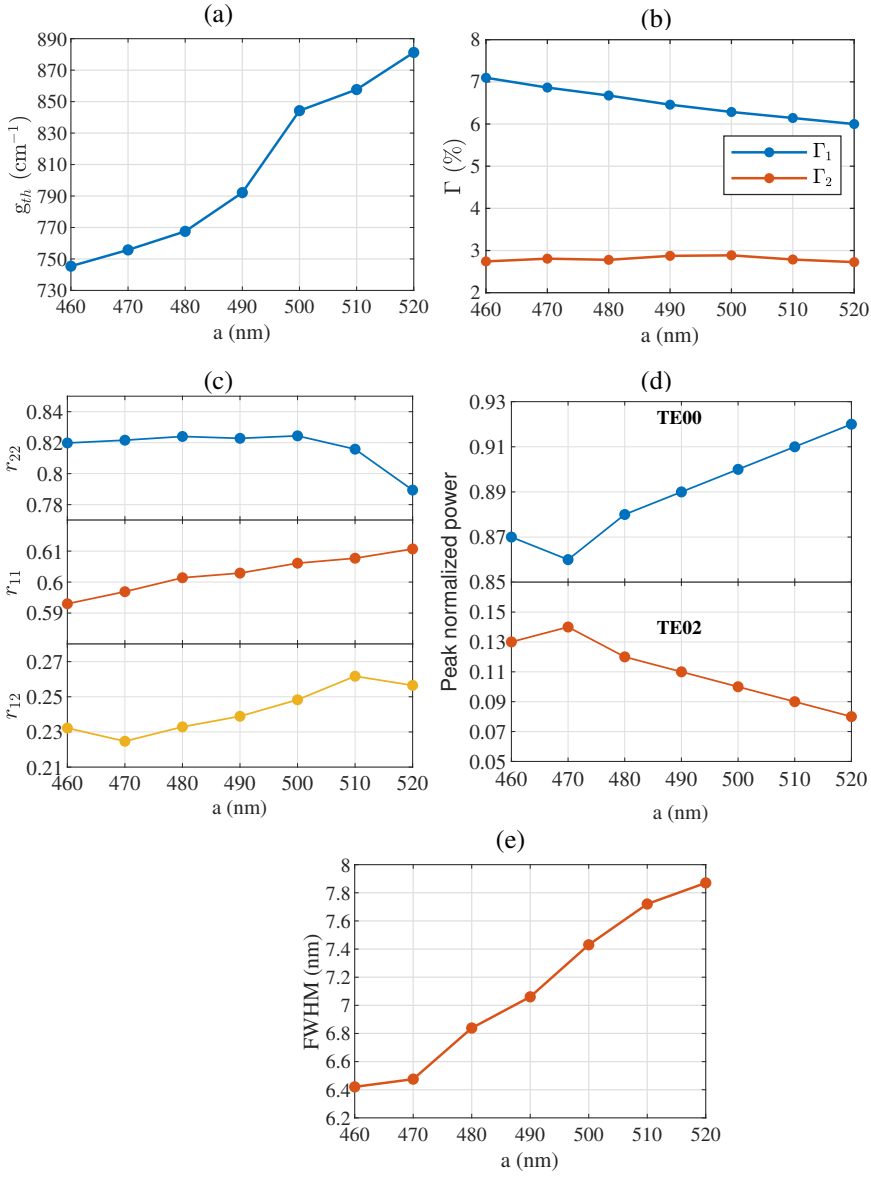

Figure 3.12: Variation of lasing characteristics with GaAs box height 'a' (as labeled in Figure 3.1(b)): (a) Threshold gain, (b) Mode confinement in the QWs for the TE_{00} (Γ_1) and TE_{02} (Γ_2) modes, (c) Reflection scattering coefficients at lasing wavelengths, (d) Power distribution of the TE_{00} and TE_{02} modes at the left facet, (e) FWHM of the round-trip gain.

facets. It is defined as the ratio of the total emitted output power from both facets to

the total power generated through stimulated emission within the cavity. For this analysis, we assume a wide-area detector capable of capturing all the emitted light, and an injection efficiency of 100%.

For a laser cavity symmetric in the placement of the metal plugs, the efficiency is expressed as:

$$\eta_d = \frac{2P_{\text{out}}}{\Gamma_1 g_{\text{th}} \int_0^L (P_{f1} + P_{b1})\, dz + \Gamma_2 g_{\text{th}} \int_0^L (P_{f2} + P_{b2})\, dz} \tag{3.15}$$

Here, P_{out} denotes the total optical power emitted from one facet, while P_{f1} and P_{f2} represent the forward-propagating power of the TE_{00} and TE_{02} modes, respectively. Similarly, P_{b1} and P_{b2} correspond to the power carried by the backward-propagating modes.

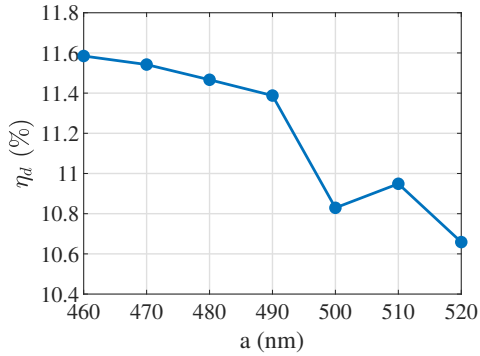

Figure 3.13: Differential quantum efficiency (η_d) as a function of GaAs box height.

Figure 3.13 presents the dependence of the differential quantum efficiency on the GaAs box height. The observed variations in efficiency primarily arise from changes in internal optical losses and the facet reflectivities associated with both the TE_{00} and TE_{02} modes. Across all configurations, the differential quantum efficiency remains relatively low, which is attributed to the extended cavity length of the device (1.5 mm). A longer cavity reduces the fraction of generated power coupled out from the facets.

3.4 Verification of model with experimental results

In this section, we validate the round-trip model described in Section 3.3 by comparing its predictions with experimental measurements from fabricated nano-ridge

laser devices. Specifically, we focus on the dependence of the lasing wavelength and the threshold gain on the metal contact pitch.

To ensure accuracy in the modeling process, detailed device dimensions were extracted from TEM cross-sectional images of the nano-ridge structures. The resulting device cross-sections therefore differ from that described in the preceding sections. These physical dimensions, along with the doping profiles, were used as inputs for full-vectorial FDTD and FDE simulations. From these, we obtained mode effective indices, electric field distributions, facet reflection coefficients, mode confinement factors, and FCA losses. The laser cavity was defined by two dry-etched facets tilted by approximately 12° with respect to the vertical axis, as reported in [2], and this tilt was explicitly accounted for in the reflectivity calculations.

We first examined how the spectral characteristics of an $80\ \mathrm{nm}$ trench-width nano-ridge laser vary with the contact pitch. Figures 3.14 (a) and 3.14 (b) present the cross-sectional TEM image of the fabricated device and its corresponding schematic used in the optical simulations, respectively. The associated doping profile, summarized in Table 3.2, was used in the simulations. These structural and material parameters provided the foundation for the modeling analysis.

The model predicts that the TE_{00} mode loss spectrum exhibits a minimum due to modal beating with the higher-order TE_{01} mode. The resulting lasing wavelengths for contact pitches of $4.7\ \mu\mathrm{m}$, $4.8\ \mu\mathrm{m}$, and $4.9\ \mu\mathrm{m}$ are presented in Figure 3.15(a). These predictions are compared with measured lasing wavelengths from electrically injected nano-ridge devices having the same trench width and contact pitches. The corresponding measurement data, including statistical variation and emission spectra, are shown in Figures 3.15(b) and 3.15(c), respectively.

All spectral measurements were conducted under a constant injection current of $20\ \mathrm{mA}$. The emitted light was collected using a horizontally aligned lensed single-mode fiber and analyzed with an optical spectrum analyzer. A more detailed discussion of the spectral measurement setup and methodology will be presented in the following chapter.

As shown in Figure 3.15(a), the model predicts a blue shift of approximately $40\ \mathrm{nm}$ in the lasing wavelength as the pitch increases from $4.7\ \mu\mathrm{m}$ to $4.9\ \mu\mathrm{m}$. Similarly, the experimental data in Figure 3.15(b) show a corresponding blue shift of around $30\ \mathrm{nm}$. This agreement confirms that the model captures the underlying physical behavior.

The observed blue shift in the lasing wavelength is primarily attributed to the behavior of the detuning parameter δ, which is governed by the difference in the effective indices between the TE_{00} and TE_{01} modes. As established in Section 3.2,

the detuning can be approximated by the expression

$$\delta(\lambda) \approx \frac{\pi \Delta n_{\text{eff}}(\lambda)}{\lambda} - \frac{l\pi}{\Lambda},$$

where Δn_{eff} represents the effective index difference between the coupled modes. Since Δn_{eff} increases significantly with wavelength, $\delta(\lambda)$ exhibits a positive slope as a function of the wavelength. This trend is illustrated in Figure 3.16, which plots the detuning parameter against the wavelength for the various contact pitches. As the contact pitch increases from $4.7\ \mu\text{m}$ to $4.9\ \mu\text{m}$, the phase-matching condition required for lasing is satisfied at progressively shorter wavelengths, resulting in the observed spectral blue shift.

However, as shown in Figure 3.15 (b), some variation in the lasing wavelengths is observed even among devices with identical contact pitch and trench width. For example, a wavelength spread of approximately $10\ \text{nm}$ is observed for devices with a $4.9\ \mu\text{m}$ pitch, and around $5\ \text{nm}$ for those with a $4.7\ \mu\text{m}$ pitch. This variability is likely due to minor deviations in device geometry arising from fabrication-induced non-uniformities [2]. As demonstrated earlier in Section 3.3.3, even a modest change of $10\ \text{nm}$ in the ridge height can lead to a shift in the lasing wavelength of up to $30\ \text{nm}$, underscoring the high sensitivity of the lasing condition to structural parameters. More discussion on this effect is presented in Chapter 4. Furthermore, minor discrepancies between the modeled and measured emission wavelengths may also stem from differences in the actual refractive index profile and the material database values used in the simulation environment.

In addition to the spectral analysis, the influence of the threshold gain on the lasing behavior of the nano-ridge devices was also investigated. This analysis focused on devices from two different dies on the same wafer, each containing nano-ridges with an $80\ \text{nm}$ trench width. For this purpose, we selected three representative devices from each die, with contact pitches of $3.6\ \mu\text{m}$, $4.8\ \mu\text{m}$, and $5.4\ \mu\text{m}$. Using the geometries extracted from the TEM images, we applied the round-trip laser model to calculate the threshold gain as a function of the device length.

Figures 3.17(a) and 3.17(b) present the threshold gain calculations for the devices with different contact pitches on Die 1 and Die 2, respectively. The plots also indicate the specific higher-order transverse mode that couples with the fundamental TE_{00} mode to form a beating pattern, which critically determines the spatial positioning of optical intensity minima and maxima. These patterns, in turn, influence the overlap of the optical modes with the lossy metal contacts and thus the modal losses.

To accommodate potential deviations in the device length resulting from the etching process, the threshold gain was evaluated over a $\pm 2.5\ \mu\text{m}$ range around the nominal cavity length of $1.5\ \text{mm}$. As illustrated in Figure 3.17, the threshold gain exhibits a

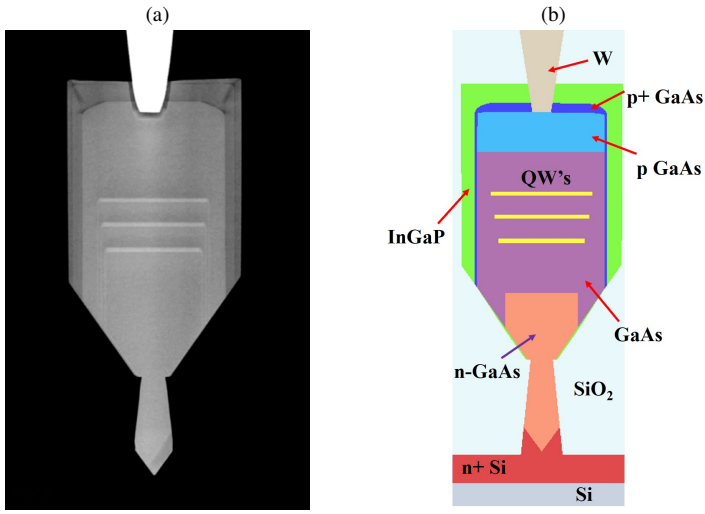

Figure 3.14: (a) Cross-sectional TEM image of a nano-ridge laser structure with an 80 nm trench width. (b) Corresponding schematic extracted from the TEM image and used in the optical simulations, showing material layers and annotated doping profile. The doping concentrations used in the simulations are listed in Table 3.2.

periodic dependence on the device length. The observed local minima correspond to configurations where the cavity length accommodates an integer multiple of the beating length, thereby promoting constructive interference between the forward and backward propagating beating patterns. Under these conditions, the metal contact positions align with the optical intensity minima, minimizing absorption losses. It is therefore important to note that variations in the device length modify the relative position of the right-hand facet with respect to the final metal plug, thereby influencing the threshold gain.

These results highlight the pronounced influence of metal-induced absorption due to modal overlap with the metallic contacts. This effect is captured through the imaginary components of the self-coupling coefficients κ_{11} and κ_{22} in the round-trip matrix formalism (see Eq. 3.9). The calculated coupling coefficients, summarized in Table 3.5, reveal that κ_{22} consistently exhibits larger imaginary parts than κ_{11}, a consequence of the stronger overlap between the higher-order modes and the metal plug. Among these, the TE_{01} mode shows the lowest metal-induced loss, while the TE_{02} mode exhibits the highest, as indicated by the corresponding imaginary parts of κ_{22}. As a result, devices with a $4.8\ \mu\mathrm{m}$ contact pitch—associated with TE_{00}/TE_{01} mode beating—consistently demonstrate the lowest threshold gain across a large portion of the investigated length range. In contrast, devices with $3.6\ \mu\mathrm{m}$ contact

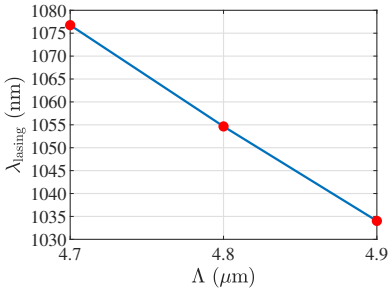

(a) Modeled lasing wavelengths for varying contact pitches.

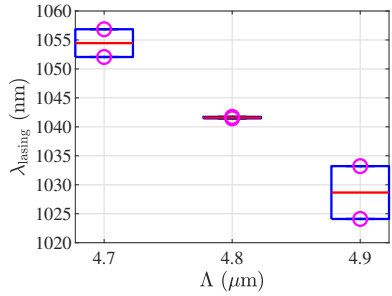

(b) Measured lasing wavelengths and variability for each pitch.

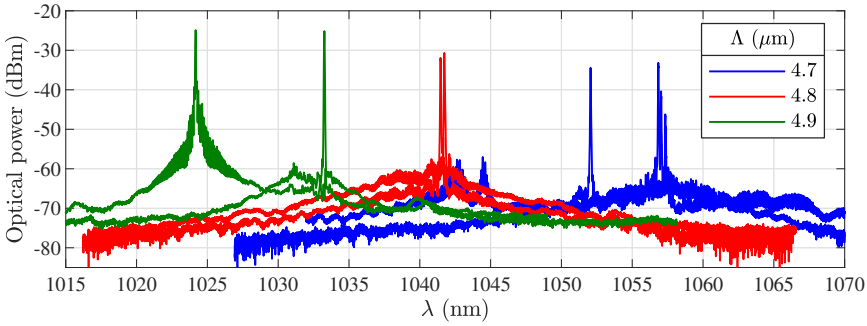

(c) Measured optical spectra at 4.7 μm, 4.8 μm, *and* 4.9 μm *contact pitches.*

Figure 3.15: Comparison between model predictions and experimental measurements for the spectra of 80 nm trench width nano-ridge lasers with different contact pitches.

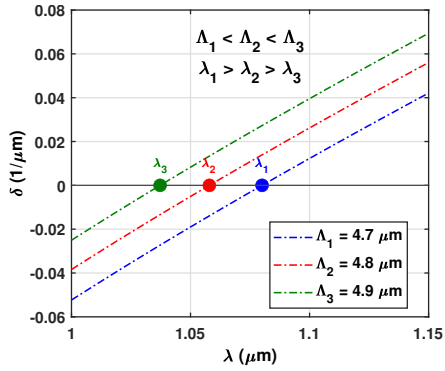

Figure 3.16: Calculated detuning parameter $\delta(\lambda)$ as a function of wavelength for different contact pitches. An increase in contact pitch results in a blue shift of the phase-matching wavelength due to changes in the effective index difference between the coupled modes.

pitch, relying on TE_{00}/TE_{02} mode beating, show the highest threshold gain values. Consistent with these findings, among the six devices studied here, only the $4.8\ \mu m$ pitch devices were observed to lase, whereas the $3.6\ \mu m$ and $5.4\ \mu m$ pitch devices did not exhibit lasing, likely due to their comparatively higher threshold gain requirements.

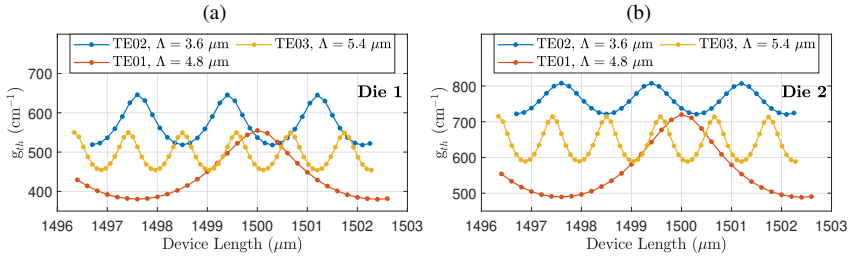

Figure 3.17: Calculated threshold gain as a function of the device length for nano-ridge lasers with an $80\ nm$ *trench width on (a) Die 1 and (b) Die 2. Each plot corresponds to contact pitches of* $3.6\ \mu m$, $4.8\ \mu m$, *and* $5.4\ \mu m$. *The associated higher-order transverse modes that couple with the* TE_{00} *mode to form beating patterns are also indicated.*

Table 3.5: Coupling coefficients at the lasing wavelengths for the devices in Figure 3.17, including self- and cross-coupling terms between the fundamental TE_{00} *mode and higher-order modes.*

Die	Λ (μm)	Coupled mode	κ_{11} (μm^{-1})	$\kappa_{12} = \kappa_{21}$ (μm^{-1})	κ_{22} (μm^{-1})
1	3.6	TE02	$0.0040 - i0.0051$	$0.0103 - i0.0134$	$0.0280 - i0.0364$
1	4.8	TE01	$0.0025 - i0.0036$	$0.0050 - i0.0070$	$0.0098 - i0.0139$
1	5.4	TE03	$0.0022 - i0.0032$	$0.0068 - i0.0097$	$0.0236 - i0.0337$
2	3.6	TE02	$0.0045 - i0.0056$	$0.0118 - i0.0145$	$0.0320 - i0.0394$
2	4.8	TE01	$0.0026 - i0.0037$	$0.0052 - i0.0072$	$0.0103 - i0.0144$
2	5.4	TE03	$0.0023 - i0.0032$	$0.0071 - i0.0101$	$0.0252 - i0.0356$

3.5 Conclusion

In this chapter, a semi-analytical model has been developed for electrically injected InGaAs/GaAs nano-ridge lasers monolithically integrated on silicon. By employing the coupled mode theory, the model captures the essential physical mechanisms governing the interaction of optical modes in the presence of periodic tungsten metal contacts. Analytical expressions describing the codirectional coupling between modes were derived and subsequently validated through rigorous 3D FDTD

simulations, demonstrating the model's accuracy in capturing mode dynamics.

A key result is the identification of low-loss conditions arising from the interference between the TE_{00} mode and higher-order modes. These beating patterns produce low intensity zones beneath the metal contacts, which not only minimize metal-induced absorption but also reduce intermodal coupling—thereby stabilizing the optical power distribution along the cavity. This mechanism leads to an equilibrium condition with minimal propagation loss and plays a pivotal role in achieving lasing.

The round-trip formulation of the model enables the evaluation of key laser performance metrics, including the spectral emission behavior, the threshold gain, and the differential quantum efficiency. By incorporating actual device dimensions obtained from TEM cross-sections, the model was used to study how variations in the contact pitch influence the lasing wavelength and the threshold gain. Comparison with experimental results demonstrated strong qualitative agreement, validating the physical assumptions underlying the model. Minor spectral deviations were observed and attributed to fabrication tolerances and uncertainties in material refractive indices.

Overall, the presented semi-analytical model provides a powerful tool for understanding and predicting the performance of the electrically injected monolithic nano-ridge lasers. Its applicability extends beyond the current structure and can be adapted to other guided-wave systems that utilize loss minimization through mode beating. The model not only offers computational efficiency but also provides clear physical insight into the underlying mechanisms governing laser performance, making it a powerful tool for design optimization in integrated photonic platforms.

References

[1] C. I. Ozdemir et al., Low dark current and high responsivity 1020nm InGaAs/GaAs nano-ridge waveguide photodetector monolithically integrated on a 300-mm Si wafer, *J. Lightwave Technol.*, vol. 39, no. 16, pp. 5263–5269, Aug. 2021.

[2] Y. De Koninck et al., GaAs nano-ridge laser diodes fully fabricated in a 300-mm CMOS pilot line, *Nature*, vol. 637, no. 8044, pp. 63–69, 2025.

[3] A. A. Yimam et al., Semi-analytical model for electrically injected GaAs nano-ridge laser diodes monolithically integrated on silicon, *Optics Express*, vol. 33, no. 2, p. 2101, Jan. 2025.

[4] Y. Shi et al., Time-resolved photoluminescence characterization of InGaAs/-GaAs nano-ridges monolithically grown on 300 mm Si substrates, *Journal of Applied Physics*, vol. 127, no. 10, p. 103 104, Mar. 2020.

[5] *Lumerical photonics simulation and design software official website*, https://www.ansys.com/products/photonics.

[6] A. Kaushalram, M. Minkov, S. Fan, and J. Vuckovic, High-Q photonic crystal cavity on a hybrid silicon platform, *Scientific Reports*, vol. 10, no. 1, p. 19 565, 2020.

[7] L. A. Coldren, S. W. Corzine, and M. L. Mashanovitch, *Diode lasers and photonic integrated circuits*. John Wiley & Sons, 2012.

[8] R. Kazarinov and C. Henry, Second-order distributed feedback lasers with mode selection provided by first-order radiation losses, *IEEE Journal of Quantum Electronics*, vol. 21, no. 2, pp. 144–150, Feb. 1985.

[9] S. C. Baker-Finch, K. R. McIntosh, D. Yan, K. C. Fong, and T. C. Kho, Near-infrared free carrier absorption in heavily doped silicon, *Journal of Applied Physics*, vol. 116, no. 6, Aug. 2014.

[10] J.-P. Weber, Optimization of the carrier-induced effective index change in InGaAsP waveguides-application to tunable bragg filters, *IEEE Journal of Quantum Electronics*, vol. 30, no. 8, pp. 1801–1816, 1994.

[11] K. Kiyota, T. Kageyama, H. Shimizu, and Y. Kawakita, Measurement of absorption coefficient of carbon-doped GaAs, *Japanese Journal of Applied Physics*, vol. 48, no. 11, p. 111 103, Nov. 2009.

[12] D. Babic et al., Design and analysis of double-fused 1.55-μm vertical-cavity lasers, *IEEE Journal of Quantum Electronics*, vol. 33, no. 8, pp. 1369–1383, 1997.

[13] K. Petermann, *Laser Diode Modulation and Noise* (Advances in Opto-Electronics). Springer Dordrecht, 1988, vol. 3, pp. XII+315.

[14] Y. Shi et al., Optical pumped InGaAs/GaAs nano-ridge laser epitaxially grown on a standard 300-mm Si wafer, *Optica*, vol. 4, no. 12, pp. 1468–1473, Dec. 2017.

[15] B. Kunert, W. Guo, Y. Mols, R. Langer, and K. Barla, Integration of III-V hetero-structures by selective area growth on Si for nano-and optoelectronics, *Ecs Transactions*, vol. 75, no. 8, p. 409, 2016.

4

Static characterization of electrically injected InGaAs/GaAs nano-ridge lasers

Contents

In Chapter 3, we presented a semi-analytical model for electrically injected InGaAs/GaAs nano-ridge lasers monolithically integrated on silicon. Based on the coupled mode theory and validation through 3D FDTD simulations, the model accurately captures the coupling between modes in the presence of periodic tungsten metal contacts. By identifying low-loss conditions arising from interference between the fundamental TE_{00} mode and higher-order modes, the model explains how

modal beating minimizes metal-induced absorption. Using a round-trip gain model, key laser parameters such as the threshold gain, the emission wavelength, and the differential quantum efficiency were evaluated for devices with varying geometry. The model showed strong agreement with experimental measurements, confirming its effectiveness in describing lasing behavior and its potential applicability to other integrated photonic systems.

Building on these theoretical insights, Chapter 4 presents the static characterization of electrically injected nano-ridge lasers. Section 4.1 reports measurements of LIV and spectra, including an analysis of the emission wavelength sensitivity to fabrication-induced variations. Section 4.2 examines the linewidth characteristics using both homodyne and heterodyne interferometric techniques. Section 4.3 evaluates the far-field emission profiles to assess the beam divergence of the fabricated devices.

Some parts of the results on the LIV, spectra and linewidth characterization of these devices were reported in [1] and [2].

4.1 Measurements of LIV and spectra

4.1.1 Experimental setup

The LIV mesurements and spectral characterization of the nano-ridge lasers were carried out under CW conditions at room temperature. The setup employed for the LIV measurements is depicted in Figure 4.1. A lensed single mode fiber (SMF) was aligned to the cleaved output facet of the device in a horizontal coupling scheme to efficiently couple the emitted laser light into the fiber. The collected light was directed to an optical power meter (PM 8153A Lightwave Multimeter), while a direct current (DC) source (Keithley 2450 SourceMeter) supplied the injection current to the laser via DC probe needles. The voltage sweep and synchronized acquisition of the output optical power were automated using a Python-based script running on a control computer.

For the spectral measurements, the same setup was used, with the output from the lensed fiber directed to an Anritsu MS9740A optical spectrum analyzer (OSA) with a resolution of 0.03 nm.

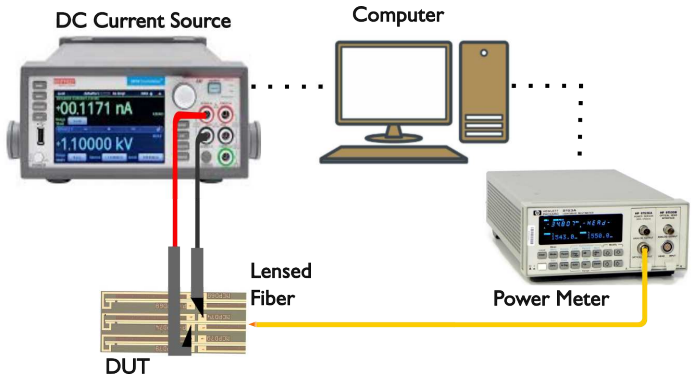

Figure 4.1: Schematic of the experimental setup used for the LIV characterization. The laser (device under test (DUT)) is driven by a DC current source, and its output is collected by a lensed SMF and routed to a power meter.

4.1.2 Results

Figure 4.2 (a) shows the measured LIV characteristics of a representative nano-ridge laser with a cavity length of 1.25 mm and a trench width of 80 nm. The laser cavity is defined by one cleaved facet and a second facet formed by dry etching, which is tilted by 12° relative to the vertical axis [1]. The current–voltage (IV) curve exhibits a turn-on voltage of approximately 1.4 V, while the light–current (LI) trace indicates a lasing threshold of about 7 mA. The coupling loss per facet is around 8 dB.

Figure 4.2 (b) shows representative spectra over a 100 nm wavelength span obtained at various bias currents. A two-dimensional (2D) spectral map with a 10 nm span and centered around the lasing wavelength is displayed in Figure 4.2 (c), clearly demonstrating stable single-mode operation without mode hopping. Additionally, the side-mode suppression ratio (SMSR), shown in Figure 4.2 (d), approaches 40 dB at a drive current roughly three times the lasing threshold.

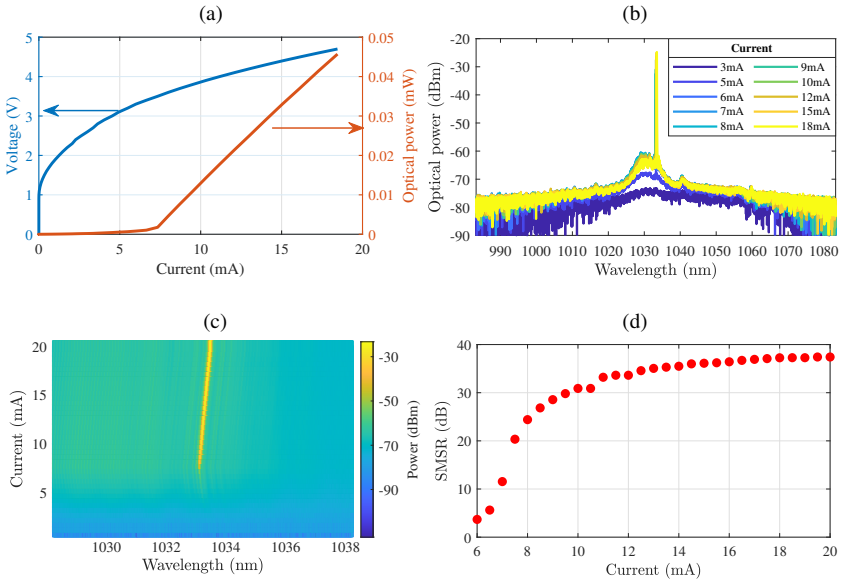

Figure 4.2: (a) LIV curve of a device with 1.25 *mm cavity and* 80 *nm trench width. (b) Measured 100 nm wavelength span spectra at different bias currents. (c) 10 nm span 2D spectral map illustrating single-mode emission without mode hopping. (d) SMSR as a function of injection current.*

Analysis of emission wavelength

As discussed in Section 3.4 of Chapter 3, the lasing wavelength in the nano-ridge lasers is primarily governed by the condition for co-directional mode coupling between the fundamental TE_{00} mode and higher-order transverse modes. For easier reference and clarity, we re-write the phase-matching (detuning) condition.

$$\delta(\lambda) \approx \frac{\pi \Delta n_{\text{eff}}(\lambda)}{\lambda} - \frac{l\pi}{\Lambda} = 0 \tag{4.1}$$

where Δn_{eff} is the effective index difference between the coupled modes, and Λ is the contact pitch. Consequently, the emission wavelength is sensitive to both the waveguide's cross-sectional geometry and the periodicity of the contact plugs. Achieving efficient lasing requires adjusting both the cross-sectional dimensions and the contact pitch so that the loss dip, arising from mode beating, coincides with the material gain peak.

Two distinct effects are observed when varying the contact pitch. First, for devices

with a fixed trench width, increasing the pitch causes a blue shift of the loss dip, as demonstrated in Section 3.4 of Chapter 3. This trend has been confirmed for 80 nm trench width devices with contact pitches of 4.7 μm, 4.8 μm, and 4.9 μm. However, once a specific mode pair is selected for lasing, pitch adjustments must be small; large variations can shift the loss dip far from the material gain peak, preventing lasing. We have seen in the previous chapter that sweeping the pitch from 3.6 μm to 4.8 μm and then to 5.4 μm changes the coupled mode pair entirely, leading to different emission wavelengths.

The emission wavelength also exhibits high sensitivity to variations in the waveguide cross-section caused by fabrication tolerances. As discussed in Section 3.3 of Chapter 3, even a 10 nm change in the ridge height could shift the lasing wavelength by as much as 30 nm. Figure 4.3 shows the measured lasing wavelengths from a set of eight devices with identical design parameters (100 nm trench width and 4.8 µm contact pitch). Despite the nominally identical geometry, the emission wavelength variation approaches 30 nm. This variation is attributed to fabrication-induced fluctuations in the nano-ridge waveguide dimensions, which alter the modal effective indices.

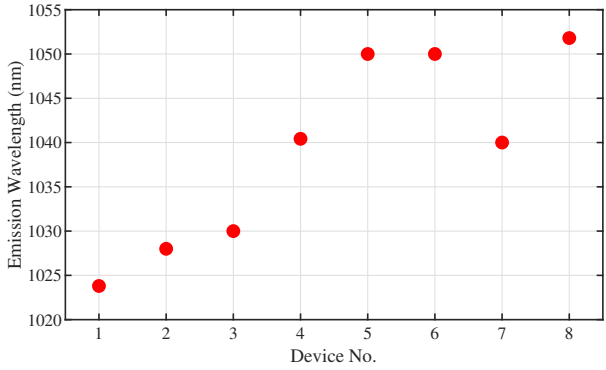

Figure 4.3: Measured emission wavelengths from eight nano-ridge devices with 100 *nm trench width and* 4.8 *µm contact pitch. The spread of* ~ 30 *nm is attributed to variations in the fabricated waveguide cross-sections.*

To further explore the impact of geometry on the modal effective indices, simulations were conducted using Lumerical FDE MODE. The schematic for the simulated waveguide cross-section is shown in Figure 4.4. Starting from reference dimensions of width $W = 399$ nm and height $H = 539$ nm—obtained from a cross-sectional TEM image of an 80 nm trench device—the dimensions were perturbed by ± 10 nm. The angle θ was fixed at the extracted value of $54.9°$, while W and H were varied. Figure 4.5 (a) shows the effective indices (n_{eff}) of the TE_{00}, TE_{01}, TE_{02}, and TE_{03} modes at $\lambda = 1.03$ µm under these dimensional variations.

The magnitudes of the relative changes in the effective index of each mode with respect to the effective index of the reference structure ($n_{\text{eff\_ref}}$) are presented in Figure 4.5 (b). As anticipated, higher-order modes display stronger sensitivity to dimensional perturbations, reflecting their more complex spatial field distributions.

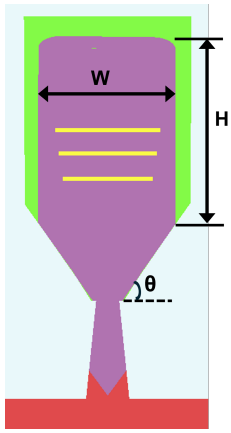

Figure 4.4: Cross-sectional schematic of the nano-ridge waveguide structure used in Lumerical MODE simulations (dimensions taken from TEM image of an 80 nm nano-ridge cross-section). The GaAs box has a nominal width (W) of 399 nm and height (H) of 539 nm.

Consequently process-induced fluctuations in Δn_{eff} in Eq. 4.1 are dominated by variations in the effective indices of the higher-order modes. The magnitude of these variations increases with the order of the mode participating in the beating with the fundamental TE_{00} mode. To quantify this effect, we evaluated the standard deviations for Δn_{eff1}, Δn_{eff2}, and Δn_{eff3}, corresponding to the effective index differences between the TE_{00} mode and the TE_{01}, TE_{02}, and TE_{03} modes, respectively. The extracted results are shown in Figure 4.6. The standard deviation increases from 0.0032 for the TE_{00}/TE_{01} pair to 0.0072 for the TE_{00}/TE_{02}, and further to 0.0143 for the TE_{00}/TE_{03}. Moreover, Figure 4.6 indicates that variations in the box height H exert a stronger influence than those in the width W. This can be attributed to the fact that higher-order modes feature multiple vertical lobes, making them particularly sensitive to perturbations in H.

It should also be emphasized that the variations in the emission wavelength arising from process-induced changes in Δn_{eff} discussed above were examined at a fixed nominal wavelength of 1030 nm. To account for this, we computed the effective indices and the corresponding dispersions ($\partial n_{\text{eff}}/\partial\lambda$) for each mode using the reference geometry ($W = 399$nm, $H = 539$nm) over the wavelength range 1.00–1.10 µm. The results are summarized in Figure 4.7. Figure 4.7 (a) illustrates the absolute variation of n_{eff} with wavelength, while Figure 4.7 (b) shows the corre-

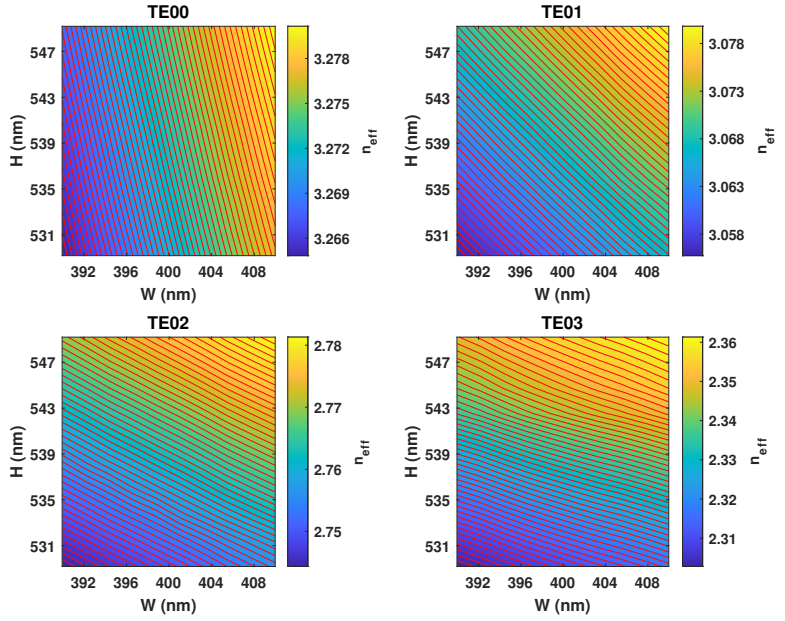

(a) Effective indices of different transverse modes under dimensional variation.

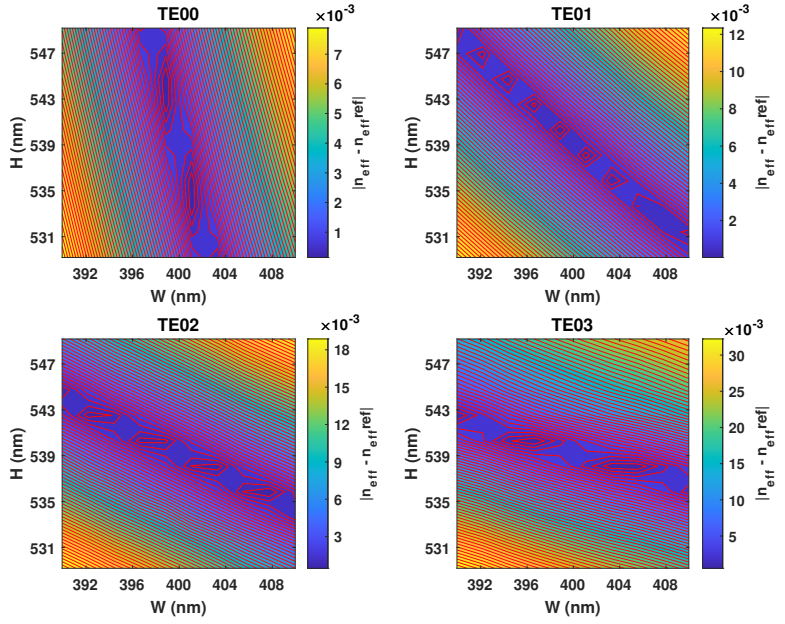

(b) Deviation of n_{eff} from reference values: $|n_{eff} - n_{eff\_ref}|$.

Figure 4.5: Sensitivity of effective indices to variations in GaAs box width and height. Higher-order modes exhibit significantly stronger sensitivity.

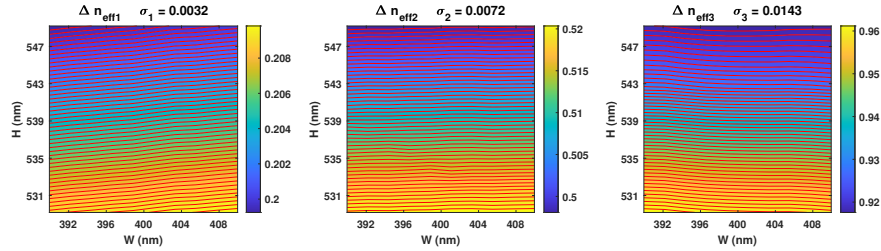

Figure 4.6: Variations in Δn_{eff} as a function of changes in the GaAs box width (W) and height (H). Here, Δn_{eff1}, Δn_{eff2}, and Δn_{eff3} denote the differences in effective indices between the TE$_{00}$ mode and the TE$_{01}$, TE$_{02}$, and TE$_{03}$ modes, respectively. σ_1, σ_2, and σ_3 are the standard deviations for Δn_{eff1}, Δn_{eff2}, and Δn_{eff3} respectively.

sponding dispersion. A clear trend emerges: dispersion systematically increases with mode order, reflecting the stronger wavelength dependence of higher-order modes.

These findings highlight that higher-order modes not only exhibit greater susceptibility to dimensional perturbations but also display more pronounced dispersion characteristics. Therefore, to enhance robustness against fabrication tolerances and reduce emission wavelength variability, it is advantageous to utilize lower-order modes in the coupled-mode design.

The pronounced sensitivity of the effective indices of higher-order modes to variations in waveguide dimensions and dispersion renders these nano-ridge lasers particularly vulnerable to fabrication-induced fluctuations. This heightened susceptibility contrasts with distributed feedback (DFB) lasers, which rely on contra-directional coupling of the fundamental mode and therefore exhibit comparatively greater robustness against such dimensional variations.

4.2 Linewidth characterization

The linewidth of a laser is typically defined as the full width at half maximum (FWHM) of the power spectral density of the emitted radiation and is fundamentally governed by phase fluctuations in the optical field arising from spontaneous emission and carrier density fluctuations [3]. Beyond the intrinsic properties of the gain medium and resonator design, linewidth is also affected by factors such as phase noise, mechanical vibrations, and temperature-induced instabilities [4]. Achieving a narrow linewidth is critical for numerous applications, including coherent optical communication [5], high-resolution spectroscopy [6], and optical sensing [7], where spectral purity and phase stability directly impact performance.

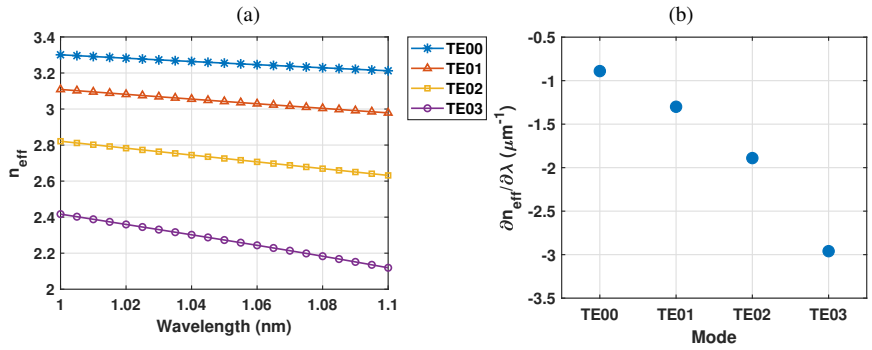

Figure 4.7: (a) Effective index versus wavelength for four guided modes in the nano-ridge waveguide. (b) Corresponding dispersion curves showing $\partial n_{eff}/\partial\lambda$ for each mode.

In contrast, excessive linewidth broadening reduces coherence length, limits interferometric sensitivity, and degrades data transmission fidelity, thereby constraining the practical applicability of the laser.

A variety of techniques have been developed to characterize semiconductor laser linewidths [8]. Among these, homodyne and heterodyne interferometric methods are particularly well established due to their relative simplicity of implementation [4, 8]. In this work, we investigate the linewidth characteristics of the nano-ridge lasers using both homodyne and heterodyne interferometric approaches, providing insights into their coherence properties and noise behavior.

4.2.1 Experimental setup

The initial phase of the linewidth characterization for the nano-ridge lasers was carried out using the self-homodyne interferometric technique [9–11] due to the lack of an acousto-optic modulator (AOM) operating near the lasing wavelength of 1030 nm at the time. The corresponding experimental setup is shown in Figure 4.8.

In this configuration, the DUT—a nano-ridge laser with a cleaved output facet—was mounted on a temperature-controlled stage set to 20°C. Electrical injection was provided via DC probe needles connected to a Keithley 2450 current source. The emitted light from the cleaved facet, which also serves as one of the cavity mirrors, was coupled into a lensed fiber for efficient collection.

The collected light was routed into a single mode fiber-based Mach–Zehnder interferometer. One arm of the interferometer incorporated a PC to maximize the signal-to-noise ratio in the measurement. The other arm contained a 1 km-

long fiber delay line, which ensured that the optical path difference exceeded the laser coherence length, thereby suppressing coherence artifacts and reducing the influence of low-frequency ($1/f$) noise [10].

The outputs from both arms were recombined using a 50:50 fiber coupler, and the resulting interference signal was directed to a balanced photodetector (Thorlabs PDB471C-AC, 400 MHz bandwidth) featuring a transimpedance gain of 10×10^3 V/A. The photodetector's electrical output was subsequently fed into a Rohde & Schwarz Electrical Spectrum Analyzer (9 kHz–13.6 GHz) with a resolution bandwidth of 200 kHz, enabling extraction of the phase noise spectrum and estimation of the laser linewidth.

It is worth noting that no optical isolator was placed between the DUT and the measurement setup. As a result, the device was exposed to parasitic back-reflections, which can artificially broaden or narrow the measured linewidth.

While the homodyne technique avoids the insertion loss introduced by an AOM, the heterodyne approach has become the standard in integrated photonics linewidth measurements, as it suppresses the detector's DC signal, reduces susceptibility to low frequency noise and allows the use of conventional spectrum analyzers [8, 12]. To leverage these benefits, the setup was upgraded by introducing an AOM (AeroDIODE 1064-AOM-1-0-2) in the polarization-controlled arm of Figure 4.8. The modulator, operating in the 1000–1090 nm range, was driven at a radio-frequency (RF) of 200 MHz. Additionally, the balanced photodetector from the homodyne configuration was replaced with a 1.6 GHz model (Thorlabs PDB480C) offering a transimpedance gain of 16×10^3 V/A.

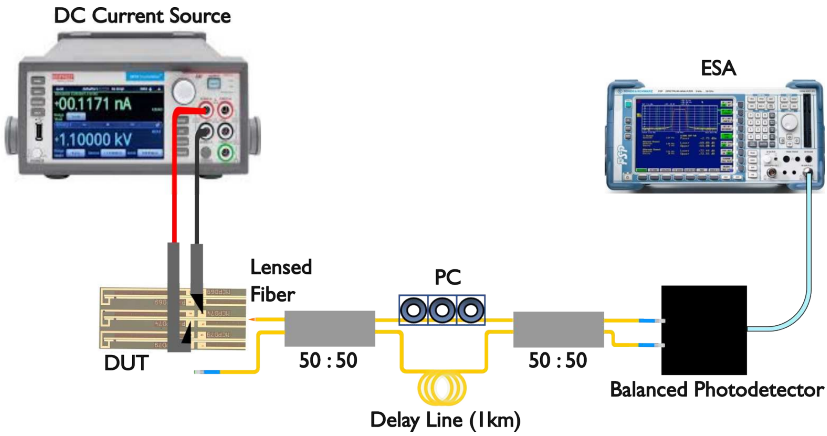

Figure 4.8: Schematic of the self-homodyne interferometric setup used for linewidth measurements of the nano-ridge lasers.

4.2.2 Results

The homodyne interferometric setup was first employed to evaluate the linewidth of a 1.25 mm-long, 80 nm trench width nano-ridge laser, whose LIV and spectral characteristics are shown in Figure 4.2. At a drive current of 18 mA, the measured RF beat note and its corresponding Voigt profile fit are presented in Figure 4.9 (a), yielding a linewidth of 86.5 MHz. Using this approach, multiple devices were characterized, and these results have been reported in [1].

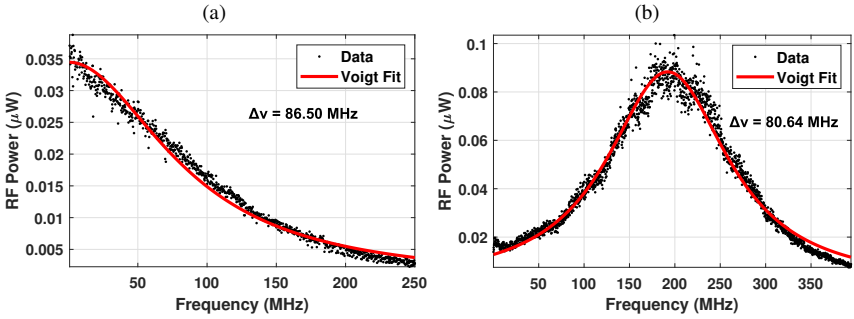

Figure 4.9: Measured RF beat notes (black scatter data) with corresponding Voigt fits (red solid curves) for the nano-ridge laser operated at 18 mA: (a) homodyne interferometric setup; (b) heterodyne interferometric setup with a 200 MHz AOM in one interferometer arm.

With the heterodyne setup, the same device was re-measured at 18 mA. The RF beat note and its Voigt fit are shown in Figure 4.9 (b), indicating a linewidth of 80.6 MHz. The linewidths obtained from the homodyne and heterodyne measurements are in close agreement. Minor discrepancies are expected, given the absence of an optical isolator in both setups, which leaves the devices susceptible to parasitic back reflections. Additionally, the homodyne configuration is inherently more sensitive to low-frequency background noise, contributing to slight differences in the extracted values.

The heterodyne setup was then used to assess linewidth dependence on bias current above threshold for the same device. Figure 4.10 (a) presents the RF beat notes with overlaid Voigt fits for bias currents ranging from 12 to 20 mA, while Figure 4.10 (b) depicts the extracted linewidths vs. $(I - I_{\mathrm{th}})$. A monotonic decrease from 122 MHz to 74 MHz is observed as the bias current increases from 12 mA to 20 mA, consistent with the inverse relationship between linewidth and the output power.

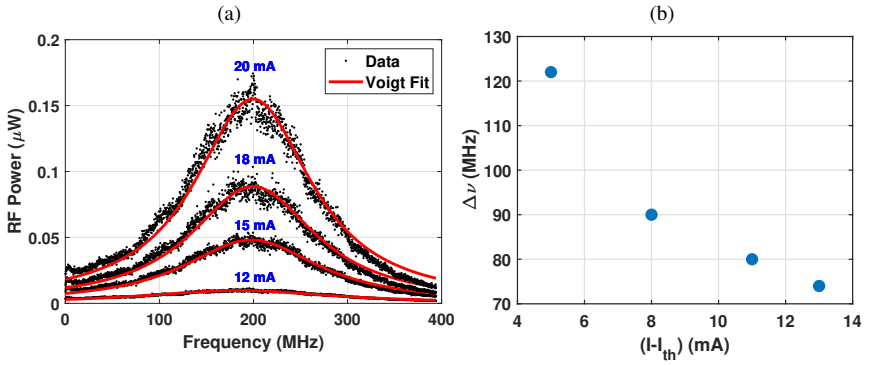

Figure 4.10: Heterodyne linewidth measurements for the 1.25 *mm-long,* 80 *nm trench width device: (a) RF beat notes (black scatter data) with corresponding Voigt fits (solid red curves) for various bias currents above threshold; (b) extracted linewidth as a function of* $I - I_{\mathrm{th}}$.

To examine device-to-device variability, linewidth measurements were performed on 16 lasers with a cavity length of ~ 1.25 mm and 12 lasers with a cavity length of ~ 1.8 mm, all biased at 20 mA. Figure 4.11 shows the linewidth as a function of $I - I_{\mathrm{th}}$. The longer cavity devices exhibit data clustering at lower $I - I_{\mathrm{th}}$ values due to their higher threshold currents, a consequence of their larger active volume. For a given length, linewidth decreases with increasing bias current above threshold, and for comparable threshold currents, the 1.8 mm devices generally show narrower linewidths, attributed to reduced mirror losses.

Overall, the measured linewidths range from 37 MHz to 216 MHz. This spread is influenced by several factors, including the absence of an optical isolator (increasing susceptibility to back reflections), fabrication-induced nano-ridge geometry variations (affecting threshold current, SMSR, and slope efficiency), and the lack of active stabilization beyond temperature control. Despite these variations, the measured linewidths fall between those of commercial DFB lasers ($\leq$1 MHz) [10] and vertical-cavity surface-emitting lasers (VCSELs) ($>$1 GHz) [13]. Further reductions in linewidth could be achieved by minimizing mirror losses, which play a crucial role in the optical feedback. Potential strategies for reducing mirror losses include employing two cleaved facets or integrating a distributed Bragg grating structure. Additional improvements could be realized by operating at higher injection currents and by reducing the linewidth enhancement factor (α).

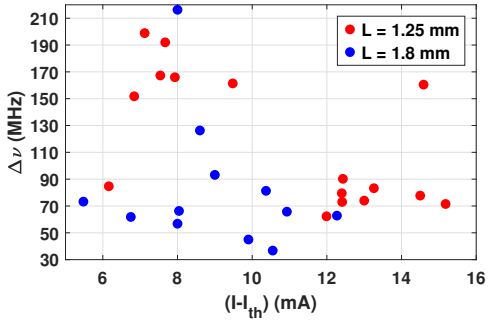

Figure 4.11: Measured linewidths as a function of current above threshold for nano-ridge lasers with cavity lengths of ~ 1.25 *mm (blue) and* ~ 1.8 *mm (red), obtained from Voigt fits to RF beat notes at 20 mA bias.*

4.3 Far-field characterization

The spatial emission properties of semiconductor lasers play a decisive role in determining their applicability for both integrated photonics and free-space optical systems. Among these properties, the far-field divergence angle is a critical figure of merit, as it governs the efficiency of fiber coupling, beam shaping, and overall system performance in both on-chip and off-chip applications [14]. For nano-ridge lasers, precise knowledge of the divergence angles is particularly important. Their non-standard cavity geometries and highly confined waveguide structures give rise to nontrivial beam propagation characteristics, which strongly influence device coupling and integration efficiency.

For many semiconductor lasers, the far-field beam profile can be well approximated by a Gaussian distribution [14, 15]. The transverse intensity variation of such a beam at an axial distance z is expressed as

$$I(x,y,z) = I_0 \frac{w_{0x}}{w_x(z)} \frac{w_{0y}}{w_y(z)} \exp\left[-2\left(\left(\frac{x-x_0}{w_x(z)}\right)^2 + \left(\frac{y-y_0}{w_y(z)}\right)^2\right)\right], \quad (4.2)$$

where I_0 is the peak intensity, x and y are the radial distances from the beam center, x_0 and y_0 denote the position of the beam center, and $w_x(z)$ and $w_y(z)$, called the beam radii, are the radial distances at the $1/e^2$ intensity point in the horizontal and vertical directions respectively. w_{0x} and w_{0y} correspond to the beam waist radii at $z = 0$.

In practice, the FWHM is often extracted experimentally, and the beam radius is

then calculated via [16]

$$w = \frac{\mathrm{FWHM}}{\sqrt{2\ln 2}} \tag{4.3}$$

This procedure is particularly advantageous when the beam divergence is large, and capturing the complete beam profile on the detector plane is difficult.

The far-field divergence angle is determined by evaluating the beam radius at different axial positions from the emitting facet. In the far-field regime, the half-divergence angle θ can be approximated as [14]:

$$\theta \approx \tan^{-1}\left(\frac{w(z)}{z}\right) \tag{4.4}$$

To validate our measurement approach, we first determined the half-divergence angle of light emitted from a cleaved standard SMF (9/125 μm core/cladding diameters) and compared the results with the reported values in the manufacturer's datasheet. Following this benchmark experiment, the far-field characterization of the nano-ridge lasers was carried out.

4.3.1 Experimental setup

The experimental configuration for the far-field measurements is shown in Fig. 4.12. For the validation experiment, the device under test (DUT) was a standard SMF (9/125 μm core/cladding diameters) with a cleaved facet, pigtailed to a DFB laser source operating at 1.55 µm (D2500-Type). For the nano-ridge laser measurements, emission was collected from the cleaved facet of a device lasing around 1030 nm and driven in CW operation above threshold at 20 mA.

The output beam was allowed to propagate freely in air along the z-axis. At selected axial distances, the far-field intensity distribution was recorded using a Xenics Xeva-511 infrared (IR) camera (pixel pitch: 30 µm). Post-processing consisted of extracting line profiles along the x- and y-directions of the beam through its center, followed by Gaussian fitting to determine the FWHM and calculation of the corresponding beam radius at each camera plane.

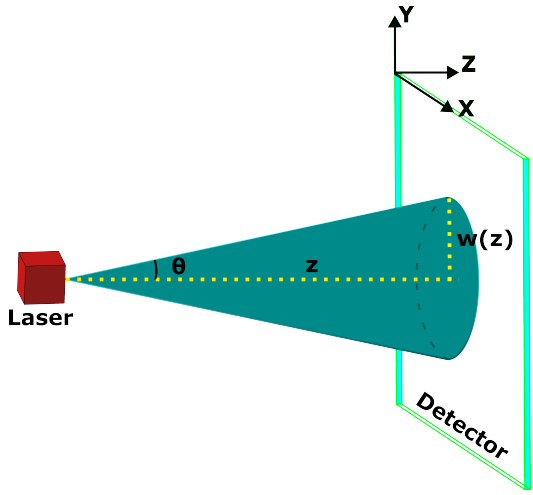

Figure 4.12: Schematic of the far-field measurement setup. The DUT (standard SMF or nano-ridge laser) emits a divergent beam that propagates along the z-axis. The IR camera is translated along z to capture two-dimensional far-field intensity maps. Cross-sectional line profiles in the x- and y-directions are fitted with Gaussian functions to extract the beam radii and divergence angles.

4.3.2 Results

Validation with a single-mode fiber (SMF)

For the SMF validation experiment, the IR camera was positioned at $z = 7$ mm, 13 mm, and 24 mm from the cleaved fiber facet. Figures 4.13 (a)–(c), (d)–(f), and (g)–(i) show the measured two-dimensional far-field intensity distributions together with the corresponding cross-sectional line profiles through the beam center along the x- and y-directions at the respective distances. Gaussian fitting was applied to the intensity profiles to extract the FWHM. From these fits, the beam radii and half-divergence angles at each measurement plane were determined. The calculated values are summarized in Table 4.1.

The extracted half-divergence angles, approximately $6.5°$, are consistent with the reported half-divergence angle range of $5°$–$6°$ for standard single-mode fibers operating at 1550 nm with 9/125 µm core/cladding diameters [17, 18]. This agreement confirms the reliability of our measurement setup and analysis procedure for characterizing the far-field divergence angle.

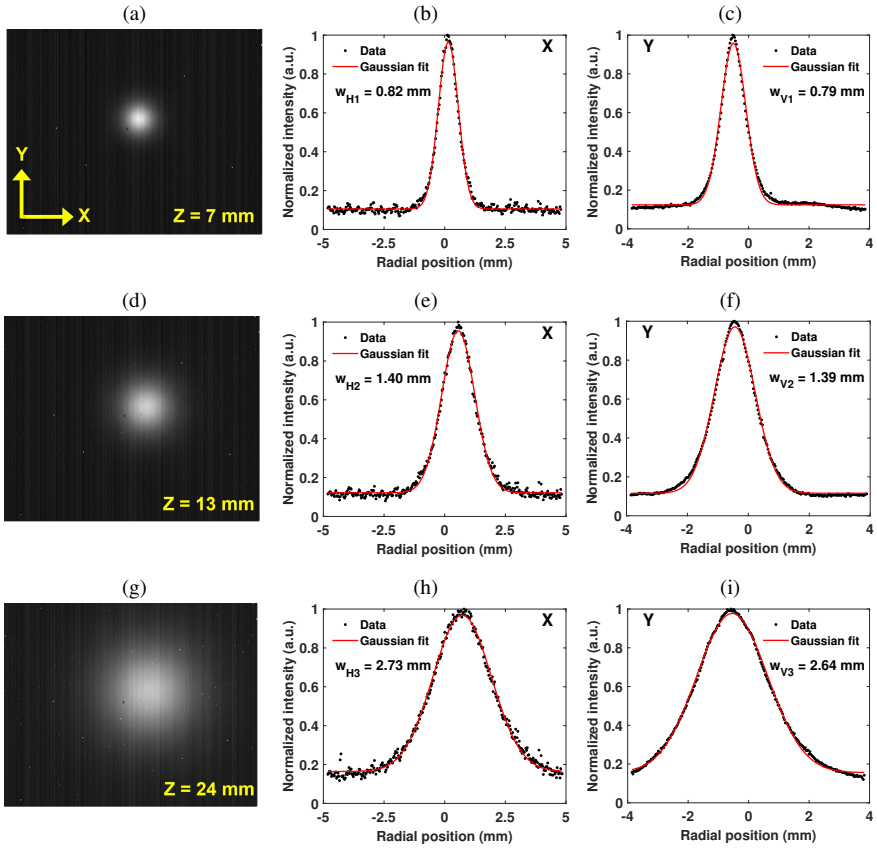

Figure 4.13: Validation experiment with a standard single-mode fiber (SMF). (a,d,g) Far-field intensity maps recorded at 7 mm, 13 mm, and 24 mm from the fiber facet. (b,e,h) Central cross-sectional line profiles along the horizontal (x) direction with Gaussian fits. W_{H1}, W_{H2} and W_{H3} are beam radii in the x-direction at each measurement plane. (c,f,i) Central cross-sectional line profiles along the vertical (y) direction with Gaussian fits. W_{V1}, W_{V2} and W_{V3} are beam radii in the vertical (y) direction at each measurement plane.

Table 4.1: Extracted beam radii and half-divergence angles of the SMF at different camera positions. Values agree well with datasheet specifications (5°–6°).

Camera position (mm)	Horizontal (x)		Vertical (y)	
	w_H (mm)	θ (deg)	w_V (mm)	θ (deg)
7	0.82	6.71	0.79	6.47
13	1.40	6.17	1.39	6.12
24	2.73	6.50	2.64	6.27

Nano-ridge lasers

The same characterization procedure was applied to the nano-ridge laser. In this case, however, the beam exhibited a much stronger divergence, particularly along the horizontal direction. To account for this, the beam center was shifted toward one edge of the recording plane, and the half-width at half maximum (HWHM) was extracted to evaluate the corresponding beam radius. Figures 4.14 (a)–(f) show the recorded intensity distributions together with the central cross-sectional line profiles along the x- and y-directions, measured at $z = 8$ mm and $z = 10$ mm. The extracted beam radii and the calculated half-divergence angles are summarized in Table 4.2.

The results reveal a pronounced asymmetry in the far-field emission, with a horizontal half-divergence angle of $\theta_x \approx 49°$ and a vertical divergence of $\theta_y \approx 30°$. This anisotropic behavior is attributed to the strongly asymmetric waveguide geometry of the nano-ridge structures, where the ridge height significantly exceeds its width.

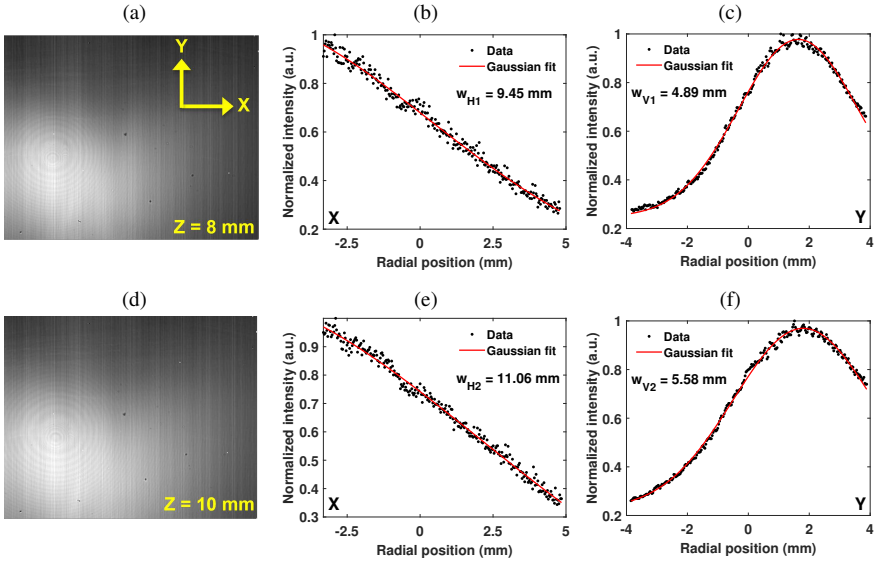

Figure 4.14: Far-field characterization of the nano-ridge laser. (a,d) Two-dimensional far-field intensity maps at 8 mm and 10 mm from the facet. (b,e) Central cross-sectional line profiles along the horizontal (x) direction with Gaussian fits. W_{H1} and W_{H2} are beam radii in the x-direction at each measurement plane. (c,f) Central cross-sectional line profiles along the vertical (y) direction with Gaussian fits. W_{V1} and W_{V2} are beam radii in the vertical (y) direction at each measurement plane.

To further validate the experimental findings, the measured divergence angles were

Table 4.2: Extracted beam radii and half-divergence angles of the nano-ridge laser at different camera positions.

Camera position (mm)	Horizontal (x)		Vertical (y)	
	w_H (mm)	θ (deg)	w_V (mm)	θ (deg)
8	9.45	49.75	4.89	31.46
10	11.06	47.88	5.58	29.15

compared to results obtained from far-field projections of the fundamental TE_{00} mode using Lumerical FDTD simulations. The simulated structure was constructed using cross-sectional dimensions obtained from TEM images of an 80 nm trench-width nano-ridge. The simulated far-field intensity distribution and the cross-sectional profiles along the x- and y-directions are shown in Figures 4.15(a)–(c). From the simulations, the horizontal and vertical half-divergence angles were estimated to be 52° and 43°, respectively.

While the horizontal divergence angles obtained from the measurements and the simulation show close agreement, a larger discrepancy is observed in the vertical direction. This deviation may partly originate from limitations in the curve fitting of the experimental data, as the large divergence caused the far-field pattern to extend beyond the camera field of view, restricting the accuracy of the extracted HWHM. Additional measurements with improved far-field capture would be necessary to refine this comparison and achieve better consistency between experiments and the simulation in the future.

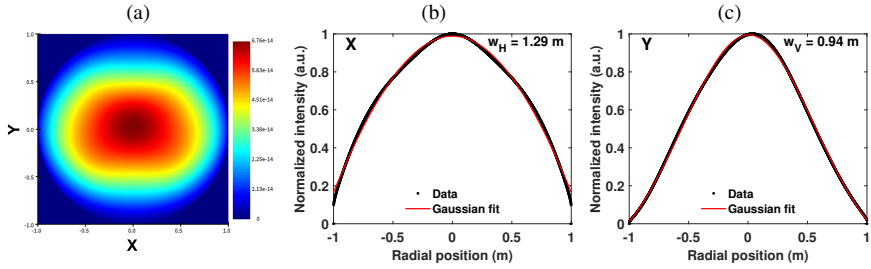

Figure 4.15: (a) Far-field projection from Lumerical FDTD simulations based on TEM-extracted dimensions of an 80 nm trench nano-ridge. (b, c) Central cross-sectional intensity profiles in the horizontal (x) and vertical (y) directions, together with Gaussian fits.

4.4 Conclusion

In this chapter, the static characterization of electrically injected InGaAs/GaAs nano-ridge lasers monolithically integrated on silicon was presented. The study combined LIV, spectral, linewidth, and far-field analyses to establish a detailed understanding of the performance and optical properties of these devices.

The impact of fabrication-induced variations in waveguide geometry on the emission wavelength was investigated by perturbing the GaAs box height and width around reference values. Simulations using Lumerical FDE MODE revealed that the modal effective indices of nano-ridge waveguides are highly sensitive to dimensional fluctuations, with higher-order modes exhibiting the greatest susceptibility. These higher order modes play a dominant role in driving process-induced variability in the detuning condition, thereby strongly influencing the emission wavelength. In addition, the dispersion was observed to increase systematically with mode order, reflecting the stronger wavelength dependence of higher-order modes. The analysis also revealed that variations in ridge height exert a more significant impact than changes in width, attributable to the multiple vertical lobes present in the field profiles of the higher-order modes.

Collectively, these findings emphasize the necessity of stringent dimensional control during fabrication to minimize wavelength variability and improve device reproducibility. Furthermore, employing lower-order modes in the beating mode pair offers greater robustness against fabrication-induced variations.

The linewidth of nano-ridge lasers was characterized using both homodyne and heterodyne interferometric techniques, with the results showing good consistency between the two approaches. The measured linewidths, spanning from 37 MHz to 216 MHz, place the performance of these devices between that of commercial DFB lasers and VCSELs. The observed variation is mainly attributed to parasitic back reflections due to the absence of an isolator in the setup, fabrication-induced geometry fluctuations, and the lack of active stabilization beyond temperature control. Prospects for further linewidth reduction include minimizing mirror losses through improved facet design or incorporating distributed Bragg grating structures, operating the devices at higher injection currents, and reducing the linewidth enhancement factor.

Additionally, the far-field emission characteristics of nano-ridge lasers were systematically investigated following a setup validation experiment using a cleaved standard SMF. The validation experiments confirmed the accuracy of the setup, with the extracted half-divergence angles aligning well with the reported range of $5°$–$6°$. This agreement established confidence in the methodology, which was subsequently applied to a nano-ridge laser. The far-field patterns of the nano-ridge

laser revealed a pronounced anisotropy in the beam divergence: the vertical emission exhibited a moderate half-divergence angle of approximately $30°$, whereas the horizontal direction displayed a significantly larger divergence of nearly $49°$. This asymmetry is attributed to the strongly non-uniform waveguide geometry, where the ridge height substantially exceeds its width.

References

[1] Y. De Koninck et al., GaAs nano-ridge laser diodes fully fabricated in a 300-mm CMOS pilot line, *Nature*, vol. 637, no. 8044, pp. 63–69, 2025.

[2] A. A. Yimam et al., Advanced characterization and parameter extraction of electrically injected InGaAs/GaAs nano-ridge lasers monolithically integrated on silicon, *Optics Express*, vol. 33, no. 13, p. 27 929, Jun. 2025.

[3] L. A. Coldren, S. W. Corzine, and M. L. Mashanovitch, *Diode lasers and photonic integrated circuits*. John Wiley & Sons, 2012.

[4] Z. Zhao et al., Narrow laser-linewidth measurement using short delay self-heterodyne interferometry, *Optics Express*, vol. 30, no. 17, p. 30 600, Aug. 2022.

[5] S. Savory and A. Hadjifotiou, Laser linewidth requirements for optical dqpsk systems, *IEEE Photonics Technology Letters*, vol. 16, no. 3, pp. 930–932, Mar. 2004.

[6] K. Yoshii, H. Sakagami, H. Yamamoto, S. Okubo, H. Inaba, and F.-L. Hong, High-resolution spectroscopy and laser frequency stabilization using a narrow-linewidth planar-waveguide external cavity diode laser at 1063 nm, *Optics Letters*, vol. 45, no. 1, p. 129, Dec. 2019.

[7] L. Shi, T. Zhu, Q. He, and S. Huang, "Effect of laser linewidth on phase-otdr based distributed vibration sensing regime", *23rd International Conference on Optical Fibre Sensors*, J. M. López-Higuera, J. D. C. Jones, M. López-Amo, and J. L. Santos, Eds., vol. 9157, SPIE, Jun. 2014, 91576H.

[8] Z. Bai et al., Narrow-linewidth laser linewidth measurement technology, *Frontiers in Physics*, vol. 9, Nov. 2021.

[9] Z. Zhao et al., The influence of noise floor on the measurement of laser linewidth using short-delay-length self-heterodyne/homodyne techniques, *Micromachines*, vol. 13, no. 8, p. 1311, Aug. 2022.

[10] H. Ludvigsen, M. Tossavainen, and M. Kaivola, Laser linewidth measurements using self-homodyne detection with short delay, *Optics Communications*, vol. 155, no. 1–3, pp. 180–186, Oct. 1998.

[11] A. H. Ali, Simultaneous measurements for tunable laser source linewidth with homodyne detection, *Computer and Information Science*, vol. 4, no. 4, p. 138, 2011.

[12] H. Ludvigsen and E. Bødtker, New method for self-homodyne laser linewidth measurements with a short delay fiber, *Optics Communications*, vol. 110, no. 5–6, pp. 595–598, Sep. 1994.

[13] E. Haglund, Å. Haglund, P. Westbergh, J. S. Gustavsson, B. Kögel, and A. Larsson, 25 Gbit/s transmission over 500 m multimode fibre using 850 nm VCSEL with integrated mode filter, *Electronics letters*, vol. 48, no. 9, pp. 517–519, 2012.

[14] A. E. Siegman, *Lasers*. University Science Books, 1986, ch. 2.

[15] B. E. A. Saleh and M. C. Teich, *Fundamentals of Photonics*, 3rd. Wiley, 2019, ch. 3.

[16] J. Kowalevicz, B. Andrew M., and Frank, "Beam divergence from an smf-28 optical fiber", Defense Technical Information Center, Tech. Rep., Oct. 2006.

[17] Corning Incorporated, *Corning SMF-28 ultra optical fiber product information*, https://www.corning.com/media/worldwide/coc/documents/Fiber/product-information-sheets/PI-1424-AEN.pdf, 2025.

[18] Thorlabs, Inc., *Fiber divergence angle calculation for SMF-28 fiber*, https://www.thorlabs.com/newgrouppage9.cfm?objectgroup_id=14204, 2020.

5

Dynamic characterization and parameter extraction of InGaAs/GaAs nano-ridge lasers

Contents

Chapter 4 established a comprehensive static characterization of electrically injected InGaAs/GaAs nano-ridge lasers through LIV, spectral, linewidth, and far-field measurements. The impact of fabrication-induced waveguide variations on the emission wavelength was systematically studied, revealing the pronounced sensitivity of higher-order modes to dimensional fluctuations and their dominant role in the lasing wavelength variability. Linewidth measurements positioned the performance of the nano-ridge lasers between commercial DFB lasers and VCSELs, while far-field analysis uncovered strong anisotropy in the beam divergence, consistent with the asymmetric waveguide geometry. Together, these results provide critical insights into the static optical behavior of the devices and establish a solid basis for exploring their dynamic response.

Building on this foundation, Chapter 5 focuses on the dynamic characterization and parameter extraction of the nano-ridge lasers. Section 5.1 presents small-signal modulation response measurements, describing both the measurement setup and the extracted results. Section 5.2 discusses characterization of the RIN, outlining both the measurement procedure and the observed trends. In Section 5.3, the recombination coefficients are extracted from S_{11} measurements, with a step-by-step explanation of the methodology. Finally, Section 5.4 consolidates the main findings of the dynamic studies and discusses their implications for optimizing the performance of the nano-ridge lasers.

The results discussed in this chapter were published in [1].

5.1 Small-signal modulation response measurements

5.1.1 Carrier transport effects on the small-signal modulation response

In earlier discussions of laser dynamics, carrier transport effects were often neglected under the assumption that injected carriers instantly populate the active region [2]. While this is a reasonable approximation for simple bulk double-heterostructure (DH) lasers, it becomes inadequate for separate-confinement heterostructure (SCH) designs with quantum-well active regions, where carrier transport across the barrier layers plays a significant role. Experimental observations during the early development of quantum-well lasers revealed that the expected increase in the modulation bandwidth, predicted from their higher differential gain, was not realized. This discrepancy was later attributed to delayed carrier injection caused by transport processes, which effectively reduce the modulation bandwidth

until accounted for in the rate-equation framework [3].

Figure 5.1 illustrates the carrier transport model for a single quantum-well SCH laser adapted from [3]. Carriers are injected into the barrier SCH region and then transferred into the quantum well, where they recombine radiatively or non-radiatively. A fraction of carriers may also leak back into the barriers, introducing an additional loss channel.

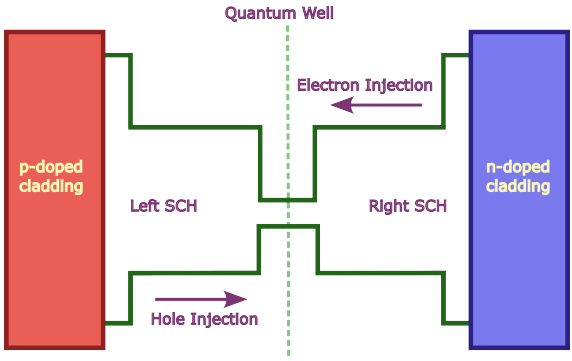

Figure 5.1: Schematic of a single quantum-well laser with SCH, adapted from [3]. Carriers are first injected into the barrier region (N_B) before being captured into the quantum well (N), where they recombine to generate photons (N_p).

To describe this system, the single carrier rate equation is replaced by two coupled equations: one for the carrier density in the barrier region (N_B) and another for the carrier density in the active quantum well (N). Along with the photon density equation (N_p), the resulting rate-equation system, following [3], is:

$$\frac{dN_B}{dt} = \frac{\Gamma_q \eta_i I}{qV} - \frac{N_B}{\tau_s} + \frac{\Gamma_q N}{\tau_e}, \tag{5.1}$$

$$\frac{dN}{dt} = \frac{N_B}{\Gamma_q \tau_s} - N\left(\frac{1}{\tau} + \frac{1}{\tau_e}\right) - v_g g N_p, \tag{5.2}$$

$$\frac{dN_p}{dt} = \left(\Gamma v_g g - \tfrac{1}{\tau_p}\right) N_p + \Gamma R'_{sp}, \tag{5.3}$$

The parameters in these equations are summarized in Table 5.1.

Table 5.1: Summary of parameters in the carrier transport rate equations

Parameter	Description
I	Injection current
η_i	Current injection efficiency
q	Electron charge
V	Active region volume
N_B	Carrier density in the SCH barrier region
N	Carrier density in the quantum well
N_p	Photon density in the cavity
τ_s	Carrier capture time from the barrier to the well
τ_e	Carrier escape time from the well to the barrier
τ	Carrier lifetime in the well
τ_p	Photon lifetime in the cavity
v_g	Group velocity
g	Differential gain
Γ	Optical confinement factor
Γ_q	Fraction of the SCH volume occupied by the QWs (V/V_{SCH})
R'_{sp}	Spontaneous emission rate coupled to the lasing mode

By linearizing Eqs. 5.1–5.3 for small perturbations in the carrier and photon densities and transforming the system into the frequency domain, the small-signal modulation response can be expressed as [3]

$$H(\omega) = \eta_i \eta_0 \frac{h\nu}{q} \cdot \frac{1}{1 + j\omega\tau_s} \cdot \frac{\omega_r^2}{\omega_r^2 - \omega^2 + j\omega\gamma}, \tag{5.4}$$

where η_0 is the optical efficiency, ω_r is the angular resonance frequency, and γ is the damping rate, all defined in the presence of carrier transport effects. The factor $(1 + j\omega\tau_s)^{-1}$ acts as a low-pass filter, introducing a cutoff associated with the finite carrier capture time τ_s. This term provides a direct explanation for the experimentally observed reduction in modulation bandwidth of SCH quantum-well lasers compared to predictions that neglect transport effects.

It should be emphasized that, in the nano-ridge lasers examined in this work, the n-type tungsten contacts on Si exhibit linear Ohmic behaviour, whereas the p-type tungsten contacts on the p-GaAs top layer form Schottky junctions [4]. These Schottky contacts introduce parasitic RC time constants, which can impose a roll-off effect on the modulation response similar to that arising from carrier transport. However, in our case the RC time constants associated with these parasitics are

sufficiently small that their influence can be neglected, given that the modulation response measurements extend only up to 1.6 GHz. A more detailed discussion of this point is provided in the results subsection.

Building on the two-level carrier transport model, the dependence of both the resonance frequency and the damping rate on the injection current above threshold can be expressed in terms of the so-called D- and K-factors [5, 6]. The resonance frequency f_r increases with drive current as

$$f_r = D\sqrt{I - I_{th}}, \qquad D = \frac{1}{2\pi}\sqrt{\frac{\eta_i \Gamma \nu_g g'/\chi}{qV}}, \tag{5.5}$$

while the damping rate γ follows a quadratic dependence on f_r, given by

$$\gamma = K f_r^2 + \gamma_0, \qquad K = 4\pi^2 \left(\tau_p + \frac{\varepsilon}{\nu_g (g'/\chi)}\right). \tag{5.6}$$

In these expressions, g' is the differential gain and ε is the gain compression factor considering average photon density in the cavity. The transport factor $\chi \approx 1 + \tau_s/\tau_e$ accounts for carrier capture and escape dynamics.

In summary, carrier transport effects in SCH-based quantum-well lasers reduce the effective differential gain, introduce a transport-limited cutoff frequency, and increase damping. These effects constrain the achievable modulation bandwidth, making their inclusion essential in accurate modeling of the nano-ridge lasers.

5.1.2 Experimental setup

The experimental setup for the small-signal modulation response measurements is shown in Figure 5.2. The DUT, a nano-ridge laser with a cleaved output facet, was mounted on a temperature-controlled stage stabilized at 20°C. A DC bias from a Keithley 2450 current source was combined with a small-signal modulation from a fully calibrated FieldFox N9926A vector network analyzer (VNA) using a Bias-Tee (SHF BT65R). The combined signal was delivered to the laser via a high-speed microwave probe (Picoprobe). Emission from the cleaved facet was collected with a single-mode lensed fiber and detected by a 1.6 GHz balanced photodetector (Thorlabs PDB480C). The electrical output of the detector was then fed back to the network analyzer to extract the modulation response.

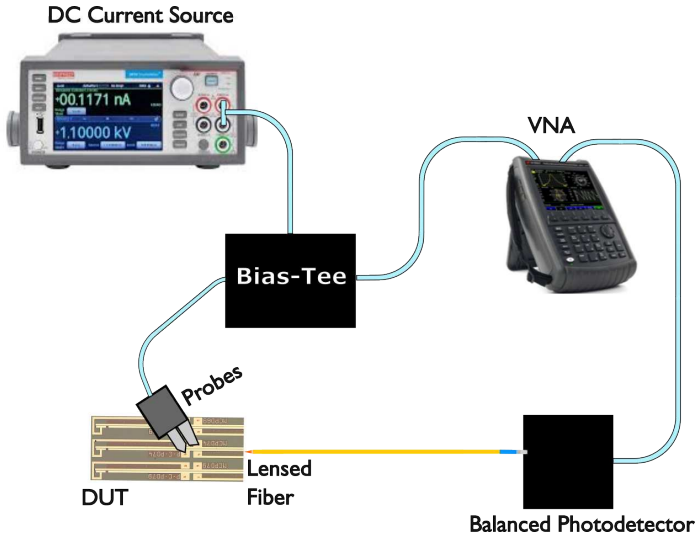

Figure 5.2: Experimental setup for the small-signal modulation response measurements. A Keithley 2450 provides the DC bias, while the VNA supplies the modulation signal. The signals are combined in a Bias-Tee and injected into the laser via a high-speed microwave probe. Light from the cleaved facet is collected by a lensed fiber and detected with a 1.6 GHz balanced photodetector, with the output analyzed by the VNA.

5.1.3 Results

Small-signal modulation response measurements were first carried out on the 1.25 mm-long, 80 nm trench-width nano-ridge laser, whose static characteristics were presented in Chapter 4. To assess device-to-device variability, the same measurements were extended to eight additional nano-ridge lasers. The structural and key operating parameters of all characterized devices are summarized in Table 5.2, where the laser studied in Chapter 4 corresponds to device 3.

Before applying Eq. 5.4 for curve fitting, it is necessary to assess the influence of the RC time constant originating from the reverse-biased Schottky contact formed between the tungsten plug and the p-type GaAs layer [4]. In this case, the corresponding small-signal Schottky capacitance is expressed as [7]

$$C_{Schottky}(V) = A\sqrt{\frac{q\,\varepsilon_s\varepsilon_0\,N_A}{2\,(V_{bi}+V)}}, \tag{5.7}$$

where A is the contact area, $\varepsilon_s = 12.9$ is the dielectric constant for GaAs, ε_0 is the vacuum permittivity, N_A is the doping concentration, V is the applied bias, and V_{bi}

Table 5.2: List of characterized nano-ridge lasers with their structural and key laser parameters

Device No.	Die No.	Length (μm)	I_{th} (mA)	Trench width (nm)	Contact pitch (μm)	α_d (cm^{-1})	α_s (cm^{-1})	α_m (cm^{-1})	$C_{Schottky}$ (fF)	$RC_{Schottky}$ (ps)
1	1	1239	7.6	100	4.6	6.1	8.5	17.2	11.7	1.46
2	1	1288	7.0	100	4.8	6.1	8.5	16.5	11.6	1.45
3	2	1248	7.0	80	4.9	12.8	8.5	17.0	77.0	9.66
4	1	1299	10.0	100	5.4	6.1	8.5	16.4	10.4	1.30
5	3	1804	9.9	80	5.4	6.8	8.5	11.6	14.5	1.81
6	3	1798	11.0	80	5.4	6.8	8.5	11.6	14.4	1.80
7	3	1796	12.0	100	4.6	6.1	8.5	11.8	16.9	2.11
8	3	1798	11.4	100	5.4	6.1	8.5	11.8	14.4	1.80
9	3	1799	9.5	100	4.9	6.1	8.5	11.8	15.9	1.99

is the built-in voltage.

The effective contact area between a plug and the p-GaAs was estimated by summing the five interfacing plug faces (four sidewalls and one bottom face). The sidewalls correspond to a width of 100 nm and a height of the 50 nm p-GaAs recess, while the bottom face is 100 nm $\times$ 100 nm [4]. The total contact area was then scaled by the number of plugs along the device length, determined by the contact pitch.

The built-in potential was evaluated using [7]:

$$V_{bi} = \frac{E_g - (\Phi_W - \chi_{\text{GaAs}})}{q} - \Phi_p, \tag{5.8}$$

with

$$\Phi_p = \frac{kT}{q} \ln\left(\frac{N_v}{N_A}\right),$$

where $\Phi_W = 4.55$ eV is the tungsten work function, $\chi_{\text{GaAs}} = 4.07$ eV is the GaAs electron affinity, $N_v = 7 \times 10^{18}$ cm^{-3} is the effective valence-band density of states for GaAs, $E_g = 1.42$ eV is the GaAs bandgap, and $kT/q = 0.0259$ V is the thermal voltage. All material parameters are taken from [7].

For device 3 in Table 5.2, the p-GaAs doping is 2×10^{19} cm^{-3}, while for the other devices it is 1×10^{18} cm^{-3} and the corresponding calculated built-in voltages are 0.96 V and 0.89 V respectively. Taking an applied bias of approximately 3.5 V near the operating current, the Schottky capacitances were calculated from Eq. 5.7 and are presented in Table 5.2. The uncertainty in the metal work function has a negligible influence on the calculated capacitances, since the applied operating voltage (3.5 V) is much greater than the built-in potentials.

For the Schottky resistance, a conservative estimate was adopted by taking the

total resistance obtained from the zero-frequency real part of the input impedance. This value encompasses contributions from the series resistance, Schottky contact resistance, and diode differential resistance. From S_{11} measurements (Section 5.3), the resistance was found to be approximately 125 Ω around the bias points of interest. The corresponding RC time constants, summarized in Table 5.2, are all below 10 ps, far shorter than the measurement time scales. As such, their influence is negligible within our frequency range of up to 1.6 GHz, and curve fitting therefore only included carrier transport effects.

Using the setup shown in Figure 5.2, S_{21} responses were measured for device 3 in Table 5.2 over bias currents from 8 mA to 9.2 mA in 0.2 mA increments. The measured modulation responses together with their corresponding fits based on Eq. 5.4 are displayed in Figure 5.3 (a). From these data, the resonance frequency the damping factor and the effective carrier capture time were extracted at each bias point. Figure 5.3 (b) shows the resonance frequency as a function of the square root of the bias current above threshold. A linear fit to the data following the relation of Eq. 5.5 yields a D-factor of $1.072\ \mathrm{GHz/mA^{1/2}}$, which quantifies the increase of the resonance frequency with the bias current. In parallel, the extracted damping factor was plotted against the squared resonance frequency, as shown in Figure 5.3 (c). From this analysis, a K-factor of 0.618 ns was determined using Eq. 5.6, corresponding to a damping-limited maximum modulation bandwidth of approximately 14 GHz. Finally, the effective carrier capture times obtained from the fits are presented in Figure 5.3 (d), with a representative value of 115 ps for this device.

To assess device-to-device variability, the procedure was repeated for the eight additional nano-ridge lasers in Table 5.2. Figure 5.3 (e) provides a comparative overview of the effective capture times across all characterized devices. With the exception of a single outlier, most devices exhibited effective capture times within the range of 100–125 ps. These values are indicative of the combined effects of transport delays and carrier capture in the active region [8].The extracted D- and K-factors will be further analyzed in the next section to establish systematic trends and benchmark performance.

Additional validation that Schottky-related RC time constants do not dominate the roll-off behavior comes from comparative analysis. If these parasitics were significant, device 3—with its much higher p-GaAs doping—would exhibit nearly a tenfold increase in the extracted time constant. But this effect is not observed, confirming that RC parasitics are not the limiting factor.

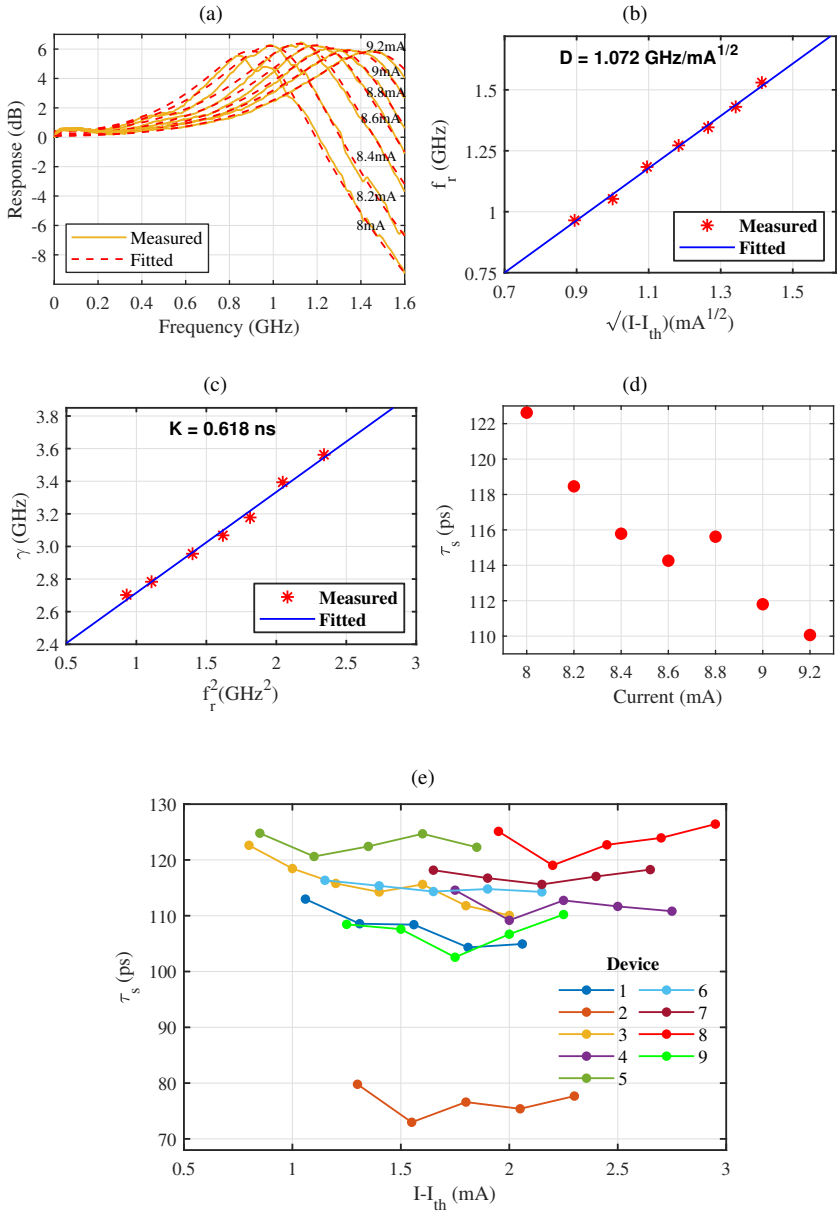

Figure 5.3: Small-signal modulation characterization of nano-ridge lasers. (a) Measured S_{21} responses of device 3 at various bias currents above threshold, together with the corresponding curve fits. (b) Resonance frequency versus $\sqrt{I - I_{\mathrm{th}}}$, yielding the D-factor. (c) Damping factor as a function of f_r^2, used to extract the K-factor. (d) Extracted effective carrier capture time vs. the bias current above threshold. (e) Effective capture times for the nine devices listed in Table 5.2, showing most values in the range of 100–125 ps, except for one outlier.

The measured capture times are slightly longer than the 20–100 ps values typically reported for quantum-well lasers [3]. This deviation can be attributed to carrier transport dynamics specific to the nano-ridge geometry. In particular, the sparse distribution of metal plugs in the device contacting scheme increases the transport path of carriers before they are captured into the quantum wells, thereby extending the overall effective capture time. These prolonged transport times represent an intrinsic limitation that directly influences the dynamic response of the lasers. The results therefore highlight the critical role of device design—particularly the contacting scheme—in shaping the modulation characteristics of the nano-ridge lasers.

5.2 Relative intensity noise (RIN) measurements

5.2.1 RIN – theoretical background

RIN in III–V semiconductor lasers primarily originates from intrinsic carrier–photon dynamics. The dominant contribution arises from spontaneous emission noise, where randomly emitted photons couple into the lasing mode, introducing fluctuations in the optical field. Additionally, carrier density fluctuations caused by stochastic recombination and injection processes modulate the optical gain, translating into amplitude noise in the output. These carrier–photon interactions are particularly enhanced near the relaxation oscillation frequency, where resonant exchange between carriers and photons amplifies the fluctuations, giving rise to the characteristic RIN peak [3, 9]. Together, these processes establish the fundamental RIN floor that can only be mitigated—but not eliminated—through careful device and system design.

Figure 5.4 illustrates a schematic example of a noisy optical signal for analog transmission, highlighting the fluctuations in the output intensity superimposed on the average optical power. Formally, the RIN is defined as the ratio of the mean-square optical power fluctuations to the square of the average output power [3]:

$$\mathrm{RIN} \equiv \frac{\langle \delta P(t)^2 \rangle}{P_0^2}, \tag{5.9}$$

where $\delta P(t)$ denotes the instantaneous power fluctuation, $\langle\rangle$ represents the time average, and P_0 is the average optical output power.

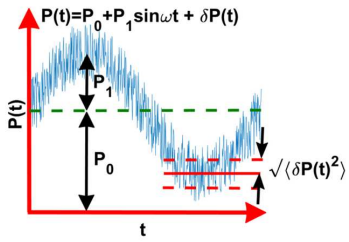

Figure 5.4: Schematic illustration of a noisy modulated laser output in analog applications. The power fluctuations $\delta P(t)$ are superimposed on the average optical output power P_0, leading to relative intensity noise (RIN). Adapted from [3].

A more standard but equivalent formulation expresses RIN in terms of the noise power spectral density (PSD). In this framework, the $\mathrm{RIN}(\omega)$ per unit bandwidth is related to the double-sided spectral density $S_{\delta P}(\omega)$ as [3]

$$\mathrm{RIN}(\omega) = \frac{2S_{\delta P}(\omega)}{P_0^2}, \tag{5.10}$$

This representation is widely used, since normalizing the RIN to a unit bandwidth allows consistent comparison across different devices and measurement conditions.

Specifying RIN in $\mathrm{dB/Hz}$ facilitates direct benchmarking and compliance with international performance requirements. For example, the IEEE 802.3 standard for optical interconnects mandates a maximum RIN of -132 dB/Hz for 50 Gb/s transmission links with a reach of up to 10 km [10]. These stringent limits underscore the importance of minimizing RIN in order to achieve low bit-error rates and ensure robust performance in high-speed and long-haul optical communication systems.

From a theoretical standpoint, the RIN spectrum can be derived from the semiconductor laser rate equations by incorporating Langevin noise sources that describe spontaneous emission and carrier noise [3, 5]. The resulting expression is

$$\mathrm{RIN}(f) = 16\pi(\Delta\nu)_{\mathrm{ST}} \frac{\frac{1}{(2\pi\chi\tau_d)^2} + f^2}{4\pi^2(f_r^2 - f^2)^2 + f^2\gamma^2} + \frac{2h\nu}{P}, \tag{5.11}$$

where τ_d is the differential carrier lifetime, $(\Delta\nu)_{\mathrm{ST}}$ is the modified Schawlow–Townes linewidth, h is Planck's constant, ν is the optical frequency, and P is the laser output power. The other parameters are defined in the previous section. The last term represents the quantum noise limit. This model provides a comprehensive description of the frequency dependence of RIN and its connection to fundamental laser parameters including also carrier transport effects.

5.2.2 Techniques for measuring RIN

Accurate characterization of RIN in semiconductor lasers is crucial for assessing their performance in optical communication, sensing, and precision metrology. Several experimental methods have been developed, each offering distinct advantages and limitations in terms of accuracy, calibration effort, and complexity. In this section, three commonly employed methods are discussed: the subtraction method, the shot-noise calibration method, and the low-RIN laser calibration method. Finally, we explain why the subtraction method was chosen for the characterization of the nano-ridge lasers in this work.

Subtraction method

The subtraction method is among the most straightforward techniques for RIN measurement. The principle is to measure the total single-sided noise power spectral density (PSD) at the output of a receiver when the laser is operating, and then subtract the system noise floor obtained with the optical input blocked. When the laser is on, the measured signal (N_{ON}) includes contributions from the intrinsic laser noise, shot noise of the photodetector, and thermal noise of the detection system. With the laser off, only the thermal noise (N_{OFF}) is recorded. The RIN can then be calculated as [11]

$$RIN(f) = \frac{\frac{N_{ON}(f) - N_{OFF}(f)}{G(f)\Delta f} - N_{shot}}{P_{elec}}, \tag{5.12}$$

where $G(f)$ is the amplification power gain, Δf is the resolution bandwidth of the spectrum analyzer, $N_{shot} = 2qI_{dc}R_L$ is the shot-noise contribution with photocurrent I_{dc} and load resistance $R_L = 50\ \Omega$, and $P_{elec} = I_{dc}^2 R_L$ is the average electrical power at the detector output.

This approach is appealing because it requires no external calibration and can be implemented with standard laboratory equipment. However, its accuracy degrades when the laser's RIN approaches the noise floor of the detection system, as small errors in estimating $N_{OFF}(f)$ may lead to large uncertainties. Consequently, while effective for moderate to high-RIN lasers, the method is less reliable for characterizing very low-noise sources.

Shot-noise calibration method

The shot-noise calibration method offers a more precise approach to RIN characterization, particularly in cases where high measurement accuracy is required. In this technique, the total detected noise is expressed as a function of the average optical power, with contributions arising from both fundamental noise sources (thermal noise and shot noise) and additional fluctuations attributed to the laser itself. In this case, the detected noise power spectral density (PSD) can be written as [12]

$$N_{ON} = Z_{TIG}\left(\mathrm{RIN}_{\mathrm{laser}} I_{dc}^2 + 2qI_{dc}\right) + N_{OFF}, \tag{5.13}$$

where $\mathrm{RIN}_{\mathrm{laser}}$ is the laser RIN per unit bandwidth, N_{OFF} is the dark noise measured with no optical input, and Z_{TIG} represents the transimpedance gain of the detection system.

At a fixed laser bias and frequency, the method employs a curve-fitting procedure in which the total detected noise spectral density, N_{ON}, is extracted as a function of the applied optical attenuation. This is accomplished by recording the RF noise power on a spectrum analyzer for multiple measurements while systematically varying the attenuation level.

By performing noise measurements at several optical power levels, the quadratic dependence of the net detected noise, $N_{ON} - N_{OFF}$, on the average optical power $\langle P \rangle$ can be fitted as

$$N_{ON} - N_{OFF} = a_1\langle P\rangle + a_2\langle P\rangle^2, \tag{5.14}$$

where the coefficients of the quadratic form are given by $a_1 = 2qRZ_{TIG}$ and $a_2 = \mathrm{RIN}_{\mathrm{laser}} R^2 Z_{TIG}$, with R denoting the detector responsivity. Solving for $\mathrm{RIN}_{\mathrm{laser}}$ yields

$$\mathrm{RIN}_{\mathrm{laser}} = \frac{2qa_2}{Ra_1}. \tag{5.15}$$

The key advantage of this method is its self-calibrating nature, eliminating the need for explicit knowledge of the transimpedance gain. It offers higher accuracy compared to the subtraction method. However, its implementation requires curve-fitting at each frequency point, making it time-consuming. Moreover, it is only valid in shot-noise-limited systems, which necessitates either high-power lasers or very low-noise electronic receivers.

Low-RIN laser calibration method

The low-RIN laser calibration method relies on using a reference laser with a well-characterized, near shot-noise-limited RIN to calibrate the measurement setup [13]. The procedure consists of three main steps. First, the dark noise (N_{OFF}) is measured with the optical input blocked. Second, the total noise is recorded when the device under test (DUT) is biased above threshold ($N_{\mathrm{ON-DUT}}$). Finally, the DUT is replaced with the reference laser, which is adjusted to generate the same photocurrent as the DUT, and the corresponding total noise ($N_{\mathrm{ON-ref}}$) is measured.

From these measurements, a system calibration factor is obtained as

$$\mathrm{syscal} = \frac{R_{\mathrm{DUT}}^2}{R_{\mathrm{ref}}^2} \cdot \frac{N_{\mathrm{ON-ref}} - N_{\mathrm{OFF}}}{2qI_{DC}R_L}, \tag{5.16}$$

where R_{DUT} and R_{ref} are the detector responsivities determined from the measured photocurrents and optical powers of the DUT and reference laser, respectively.

The laser (DUT) noise contribution is then calculated by

$$N_L = \frac{N_{\mathrm{ON-DUT}} - N_{\mathrm{ON-ref}}}{\mathrm{syscal}}, \tag{5.17}$$

and the RIN of the DUT is expressed as

$$\mathrm{RIN}_{\mathrm{laser}} = 10\log_{10}\left(\frac{N_L}{I_{DC}^2 R_L}\right) \ \mathrm{dB/Hz}. \tag{5.18}$$

This technique offers high accuracy and is particularly advantageous when the DUT noise approaches the detection system's noise floor. Unlike the shot-noise calibration method, it avoids the need for multiple power-dependent measurements, thereby simplifying the procedure. However, its implementation requires access to a stable, low-RIN reference laser at the operating wavelength of interest, which may not always be readily available or cost-effective. In addition, as with the shot-noise calibration approach, it assumes that the detection system operates under shot-noise-limited conditions.

Choice of method for nano-ridge lasers

Direct RIN measurements around the emission wavelength of 1030 nm were not feasible due to the absence of appropriate instrumentation, necessitating the use of one of the alternative techniques described above. In this work, the subtraction method was adopted for the characterization of the nano-ridge lasers.

This choice was guided by several considerations. Both the shot-noise calibration and the low-RIN laser calibration methods are optimized for shot-noise-limited systems, which generally require either high-power laser sources or ultra-low-noise electronics—conditions not fulfilled by the nano-ridge devices studied here. In addition, the shot-noise calibration method is experimentally demanding, as it relies on a frequency-dependent curve-fitting procedure at each measurement point, while the low-RIN laser calibration approach could not be implemented because no suitable reference source was available near the operating wavelength of the nano-ridge lasers.

Although the subtraction method is known to have reduced accuracy for lasers with exceptionally low RIN, it represents the most practical and robust approach under the present constraints. Its simplicity and compatibility with the experimental setup make it well suited for the characterization of the nano-ridge devices investigated in this dissertation.

5.2.3 RIN measurement setup

The RIN of the nano-ridge lasers was characterized using the subtraction method, as motivated in the preceding section. The corresponding experimental setup is illustrated in Figure 5.5. The laser output was collected by a single-mode lensed fiber and directed to a receiver (balanced photodetector with a transimpedance amplifier) (Thorlabs PDB480C) with a 1.6 GHz bandwidth and a transimpedance gain of 16×10^3 V/A. The DC photocurrent was simultaneously monitored through the built-in monitor port of the detector. To ensure that only the fluctuating components of the detected signal were analyzed, the receiver output was passed through a DC blocker (SHF DCB-65B), which removed the DC photocurrent. The AC-coupled signal was subsequently analyzed with a 44 GHz ESA (Keysight N9010A).

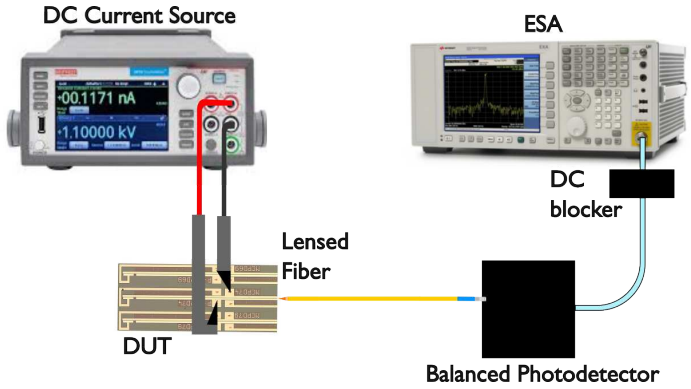

Figure 5.5: Setup for RIN measurements of the nano-ridge lasers using the subtraction method.

5.2.4 Results

The RIN of the same device previously characterized (device 3 in Table 5.2) was further investigated for bias currents between 7.5 mA and 9 mA, in steps of 0.25 mA. Measurements were carried out using the setup shown in Figure 5.5, applying the subtraction method in which two spectra were recorded: one with the laser on and another with the laser off. The RIN at each bias point was subsequently calculated using Eq. 5.12. Figure 5.6 (a) presents the measured RIN spectra along with curve fits based on Eq. 5.11. From these fits, key dynamic parameters—including the resonance frequency, damping factor, modified Schawlow–Townes linewidth, and the effective differential carrier lifetime $\chi\tau_d$—were extracted as functions of the injection current.

The dependence of the resonance frequency on the square root of the current above threshold is shown in Figure 5.6 (b). A linear fit to the data yields a D-factor of 1.056 GHz/mA$^{1/2}$. The damping factor as a function of f_r^2 is plotted in Figure 5.6 (c), from which a K-factor of 0.648 ns is obtained. In addition, the extracted Schawlow–Townes linewidths are presented in Figure 5.6 (d), while Figure 5.6 (e) shows the effective differential carrier lifetimes across the measured bias range. The lifetimes were calculated by assuming a transport factor $\chi \approx 2$, which was determined from S_{11} reflection measurements (to be discussed in Section 5.3).

Finally, Figure 5.6 (f) provides a direct comparison between the D- and K-factors extracted from both S_{21} modulation response measurements and RIN analysis for the set of devices listed in Table 5.2. Overall, the two techniques show excellent agreement, with only minor discrepancies observed in the K-factor values. These deviations are likely due to curve-fitting uncertainties. Quantitatively, the agreement

is supported by a root-mean-square error (RMSE) of 0.036 for the D-factor and 0.132 for the K-factor, underscoring the consistency between the two approaches.

5.2.5 Extraction of differential gain and gain compression factor

The extraction of differential gain and gain compression factors for the nano-ridge lasers listed in Table 5.2 was carried out using Eqs. 5.5 and 5.6. This analysis requires accurate knowledge of several device parameters, including the injection efficiency, the confinement factor, the group velocity, the active region volume, and the photon lifetime. The injection efficiency for devices with different contact pitches was evaluated using Synopsys Sentaurus TCAD Poisson solver [14]. The results are presented in Figure 5.7 (a). The QW active region volumes were extracted from transverse TEM cross-sections of devices with trench widths of 80 nm and 100 nm. These geometrical values were then used in Lumerical MODE simulations [15] to calculate the optical confinement factors and the group velocities of the fundamental quasi-TE mode. The extracted confinement factors are plotted in Figure 5.7 (b). Using these parameters, differential gain values were obtained via Eq. 5.5, resulting in values between 4.3 and 7×10^{-16} cm^2, as shown in Figure 5.7 (c). In this calculation, a transport factor of $\chi \approx 2$, estimated from S_{11} reflection measurements (see Section 5.3), was applied.

The determination of the gain compression factors relies on knowledge of the photon lifetime, which is governed by the total cavity losses. These include metal absorption, mirror losses, scattering and substrate leakage, as well as free-carrier absorption in the doped layers. Metal absorption depends on the specific mode-beating pair involved, as discussed in Chapters 3 and 4, and exhibits fabrication variability. To account for this, a margin of 10–20 cm^{-1} was considered for the metal absorption loss [16, 17]. Mirror losses were estimated from facet reflectivities calculated by FDTD simulations using TEM-derived geometries, where one facet was cleaved and the other dry-etched at 12° from the vertical axis. Scattering and substrate leakage losses were taken from Chapter 2, while free-carrier absorption losses were estimated by introducing the complex refractive indices of the doped materials in the MODE solver, also described in Chapter 2. The evaluated contributions, including doped-region absorption (α_d), scattering and leakage losses (α_s), and mirror losses (α_m), are summarized in Table 5.2.

Photon lifetimes were derived from these total losses, and the gain compression factors were subsequently obtained via Eq. 5.6. As illustrated in Figure 5.7(c), values fall in the range of 1.8–4.4×10^{-17} cm^3. Notably, longer devices (devices 5–9 in Table 5.2) show systematically larger gain compression values. This trend is attributed to enhanced spatial hole burning, arising from the increased number of

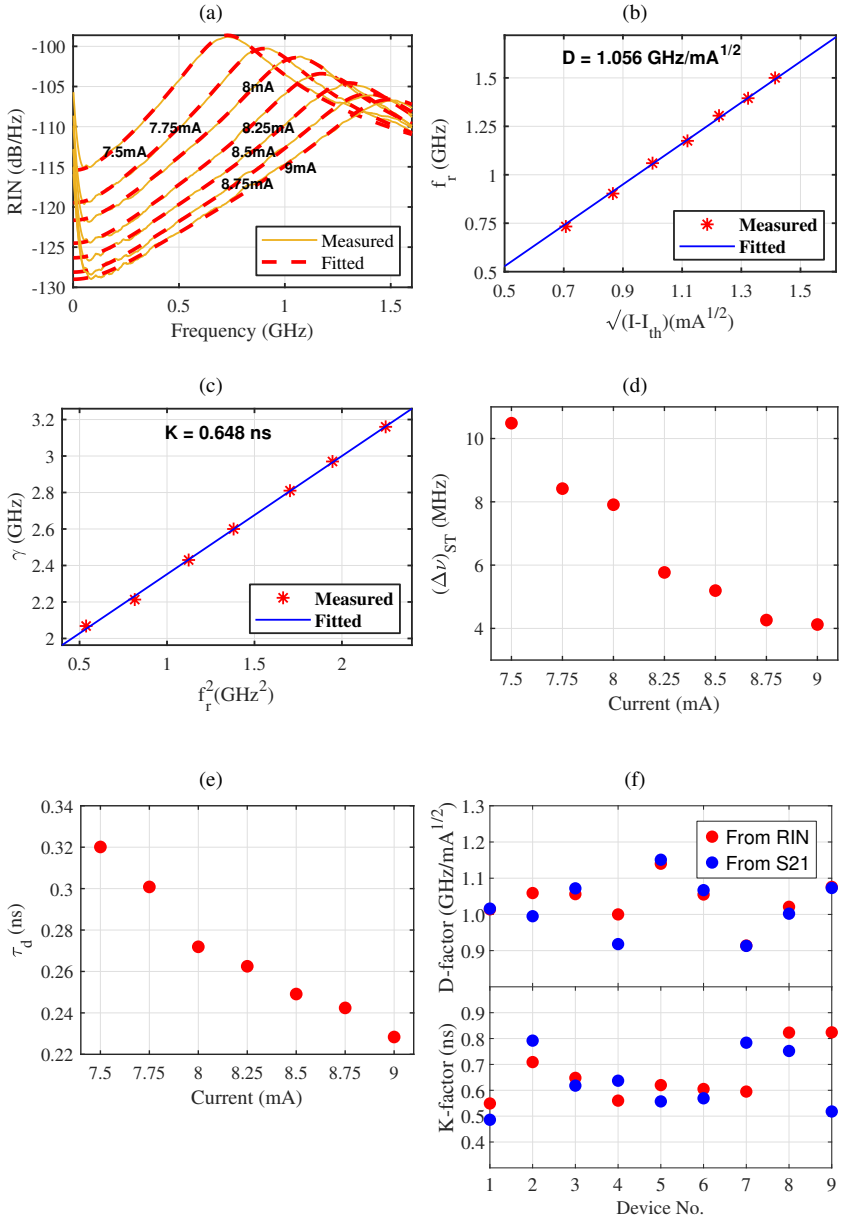

Figure 5.6: RIN-based characterization of nano-ridge lasers. (a) Measured and fitted RIN spectra at different bias currents above threshold. (b) Resonance frequency versus $\sqrt{I - I_{th}}$, yielding the D-factor. (c) Damping factor versus f_r^2, used to extract the K-factor. (d) Modified Schawlow–Townes linewidth versus bias current. (e) Differential carrier lifetime versus bias current. (f) Comparison of D and K factors obtained from RIN and S_{21} measurements.

standing-wave nodes in longer cavities, which intensifies refractive index gratings and amplifies saturation effects [18]. Similar cavity-length-dependent increases in the gain compression have been reported for $In_{0.2}Ga_{0.8}As/GaAs$ quantum-well lasers in earlier studies [19].

It is worth noting that the extracted differential gain values of 4.3–7×10^{-16} cm^2 and gain compression factors of 1.8–4.4×10^{-17} cm^3 are comparable with those reported for $In_{0.2}Ga_{0.8}As/GaAs$ quantum-well lasers, which typically show g' in the range of 5–10×10^{-16} cm^2 and ε between 1–3×10^{-17} cm^3 [3, 19].

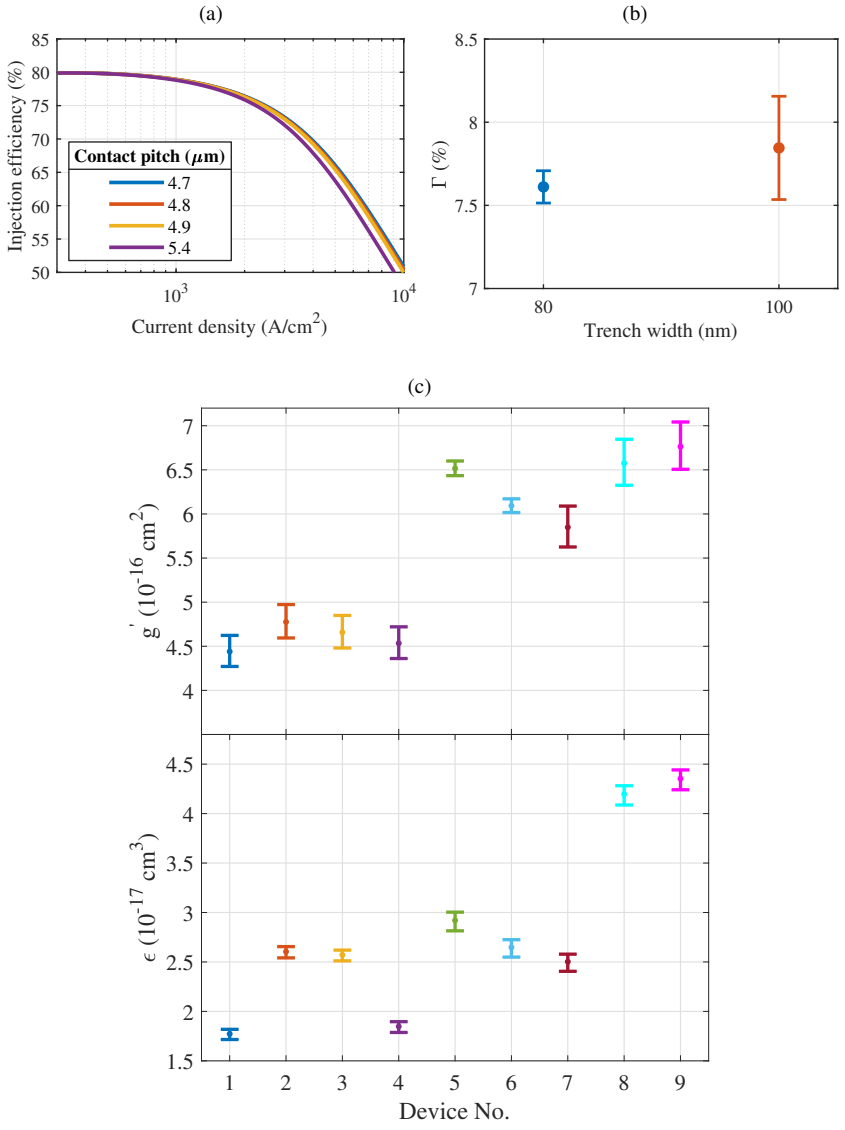

Figure 5.7: Extraction of differential gain and gain compression factor for nano-ridge lasers. (a) Injection efficiency versus current density for devices with varying contact pitches from Sentaurus TCAD simulations. (b) Optical confinement factors of the quasi-TE mode for trench widths of 80 and 100 nm, extracted using Lumerical MODE. (c) Differential gain and gain compression factors for devices in Table 5.2, calculated using Eqs. 5.5 and 5.6.

5.3 Extraction of recombination coefficients

The recombination coefficients of the nano-ridge lasers were extracted by combining small-signal modulation results with calibrated subthreshold impedance measurements. In particular, the reflection coefficient (S_{11}) was recorded using a fully calibrated vector network analyzer, from which the input impedance of the device was derived. By incorporating the effective carrier capture time obtained from the modulation response analysis, the differential carrier lifetime, the carrier escape time, the series resistance and the effective differential diode resistance can be extracted from the real part of the input impedance, following the formalism in [8]:

$$Z(\omega) = R_s + \frac{R_d \left(1 + j\omega \frac{\tau_d \tau_e}{\tau_d + \tau_e}\right)}{(1 + j\omega\tau_d)(1 + j\omega\tau_s) + j\omega \frac{\tau_s \tau_d}{\tau_e}}, \tag{5.19}$$

where Z is the input impedance, R_s is the frequency- and bias-independent series resistance, and R_d represents the frequency and bias dependent resistance associated with the combined contributions of the differential diode resistance and the Schottky p-type contact. Following the discussion in Section 5.1.3, parasitic RC roll-off effects from the Schottky contacts are again neglected. The parameters τ_d, τ_s, and τ_e denote the differential carrier lifetime, the effective carrier capture time, and the carrier escape time, respectively, as defined in earlier sections.

Once the differential carrier lifetimes are established for different bias points, the carrier density N can be determined from the injected current I by integrating over the current-dependent lifetime [20]:

$$N(I) = \frac{\eta_i}{qV} \int_0^I \tau_d(I)\, dI, \tag{5.20}$$

where N is the carrier density, I is the bias current, η_i is the injection efficiency, q is the elementary charge, and V is the active region volume.

Finally, the recombination coefficients are obtained by analyzing the dependence of the differential carrier lifetime on the carrier density. This is achieved using the standard recombination formula [20]:

$$\tau_d(N) = \frac{1}{A + 2BN + 3CN^2}, \tag{5.21}$$

where A, B, and C correspond to the contributions from defect-related (nonradiative), radiative, and Auger recombination processes, respectively. Through

this procedure, the fundamental recombination mechanisms governing the carrier dynamics in the nano-ridge lasers could be quantitatively assessed.

5.3.1 S_{11} measurement setup

The experimental setup for the S_{11} measurements of the nano-ridge lasers is shown in Figure 5.8. The devices under test (DUTs) were mounted on a temperature-controlled stage maintained at 20°C. A Keithley 2450 current source supplied the DC bias, which was combined with the RF signal from a fully calibrated FieldFox N9926A vector network analyzer (VNA) using a Bias-Tee (SHF BT65R). The combined signal was delivered to the DUT via a high-speed microwave probe (Picoprobe). The reflected signal from the device was routed back to the VNA, where the input reflection coefficient (S_{11}) was recorded for subsequent extraction of the device impedance characteristics.

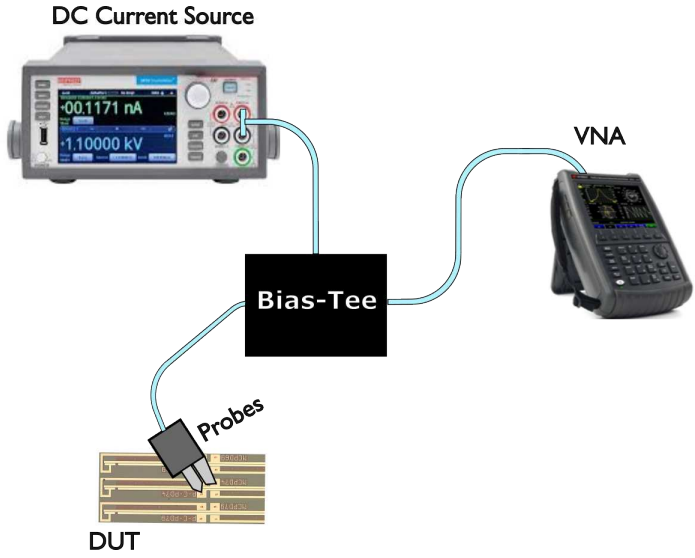

Figure 5.8: Experimental setup for the S_{11} measurement. A Keithley 2450 current source provides the DC bias, which is combined with the RF signal from a FieldFox N9926A VNA using a Bias-Tee (SHF BT65R). The signal is applied to the nano-ridge laser (DUT) via a high-speed prove (Picoprobe), with the reflected signal routed back to the VNA for analysis.

5.3.2 Results

The recombination parameters of the nano-ridge lasers were extracted following the methodology outlined earlier, based on the impedance model defined in Eq. 5.19.

From the S_{11} measurement of device 3 in Table 5.2, conducted up to 10 GHz, the series resistance was determined to be $R_s = 5.1\ \Omega$ (Figure 5.9(a)). Using this result as a baseline, the analysis was extended by incorporating the effective carrier capture time of 115 ps, previously extracted from the small-signal modulation response (Section 5.1.3). Subsequent S_{11} measurements conducted at subthreshold bias levels up to 3.5 mA facilitated the extraction of the effective differential resistance R_d, the differential carrier lifetime τ_d, and the carrier escape time τ_e. An example of these parameter extractions at $I = 2$ mA is presented in Figure 5.9 (b).

To evaluate the carrier density as a function of the injection current, a subthreshold injection efficiency of 80%—derived from TCAD electrical simulations (Figure 5.7 (a))—and the active region volume measured from TEM cross-sections were employed in Eq. 5.20. The resulting carrier density evolution is shown in Figure 5.9 (c). Subsequently, the recombination coefficients A, B, and C were obtained by fitting the measured $\tau_d(N)$ dependence using Eq. 5.21, as presented in Figure 5.9 (d). A complete set of the extracted parameters for this device is summarized in Table 5.3.

Table 5.3: Extracted parameters for device 3 in Table 5.2

τ_s (ps)	τ_e (ps)	g' (10^{-16} cm^2)	ε (10^{-17} cm^3)	A (10^8 s^{-1})	B (10^{-10} cm^3/s)	C (10^{-28} cm^6/s)
115	125	4.66	2.63	2.08	9.95	6.18

To investigate the influence of the trench width on the recombination coefficients, three groups of devices with trench widths of 60 nm, 80 nm, and 100 nm were characterized, with three devices included in each group. To minimize fabrication-induced variability, electrical characterizations were conducted on adjacent devices from the same die that also contained device 3 in Table 5.2. Within these groups, one device with an 80 nm trench and all devices with 100 nm trenches exhibited lasing, whereas the remaining devices functioned as light emitting diodes (LEDs).

The extracted recombination coefficients A, B, and C for the three trench widths are presented in Figure 5.9 (e). The results reveal a general increase in the defect-related coefficient A with increasing trench width. This trend may arise from confined threading dislocation defects being trapped closer to the trench opening (or the nano-ridge volume) as the trenches widen, or alternatively from degraded InGaP surface passivation at the lower $\{111\}$ facets. Moreover, devices with 100 nm trenches exhibit enhanced radiative recombination coefficients (B) and reduced Auger recombination coefficients (C), effects that can be attributed to diminished localized heating near the sparse metal plugs as the device volume increases.

For the $In_{0.2}Ga_{0.8}As$/GaAs material system, the defect-related recombination coeffi-

cient A is typically considered negligible, while reported values for the radiative (B) and Auger (C) coefficients span a broad range in the literature [3, 21]. A comparison between our extracted parameters and those reported in [21] reveals good agreement in B for devices with 60 nm and 80 nm trench widths, with the exception of one outlier exhibiting a value nearly twice as high. In contrast, devices with 100 nm trenches show larger B values, in some cases reaching up to four times the reported literature values. On the other hand, the extracted C coefficients are found to be one to two orders of magnitude higher than those previously reported.

This discrepancy can be partly explained by the different modeling approaches employed. Most reported values are derived using the standard single-carrier-level rate equation model, originally developed for bulk active region lasers. However, as highlighted in [22], such bulk-based analysis may not fully capture the physics of quantum well lasers, where carrier populations in the barrier and SCH regions play an important role. Incorporating carrier transport effects into the analysis, [22] demonstrated that recombination coefficients can increase substantially, with B values nearly doubled and C values enhanced by up to two orders of magnitude compared to bulk-based estimates. This provides a consistent explanation for the elevated B and C values obtained in our nano-ridge lasers. It should also be emphasized that in our analysis the thickness of the three quantum wells was taken as the effective active region thickness.

At a threshold carrier density of about 2×10^{18} cm^{-3}, the contribution of defect-related recombination to the overall threshold current was found to be minimal. Specifically, it accounted for less than 5% in devices with trench widths of 60 nm and 80 nm, and remained below 10% even for the wider 100 nm trenches. These findings highlight the effectiveness of aspect ratio trapping in conjunction with nano-ridge engineering in suppressing defect-related losses. As a result, the approach provides a robust means of realizing high-quality III–V nano-ridge structures directly on silicon substrates, thereby reinforcing its potential as a pathway toward the monolithic integration of III–V lasers within silicon photonic platforms.

The extracted carrier escape times are presented in Figure 5.9 (f). Apart from a single outlier, the values lie between 110 and 130 ps, resulting in a τ_s/τ_e ratio close to unity. This behavior is consistent with observations reported for $In_{0.25}Ga_{0.75}As$/GaAs quantum well lasers in [23] and has a direct impact on the differential gain discussed in the previous section. A τ_s/τ_e ratio near unity effectively reduces the differential gain by a factor of two compared to bulk lasers, offering a plausible explanation for the reduced D-factor and elevated K-factor values observed in Figure 5.6 (f). As reported in [5], the K-factor in $In_{0.2}Ga_{0.8}As$/GaAs quantum-well lasers increased from 0.24 ns to 0.6 ns as a direct consequence of longer carrier transport times introduced by a wider SCH layer.

To achieve higher resonance frequencies and simultaneously suppress the K-factor—thereby extending the modulation bandwidth and improving the damping-limited maximum bandwidth—shorter effective carrier capture times are required. A promising route toward this objective would be the implementation of a continuous contact scheme, which could reduce τ_s and thus enable faster laser dynamics.

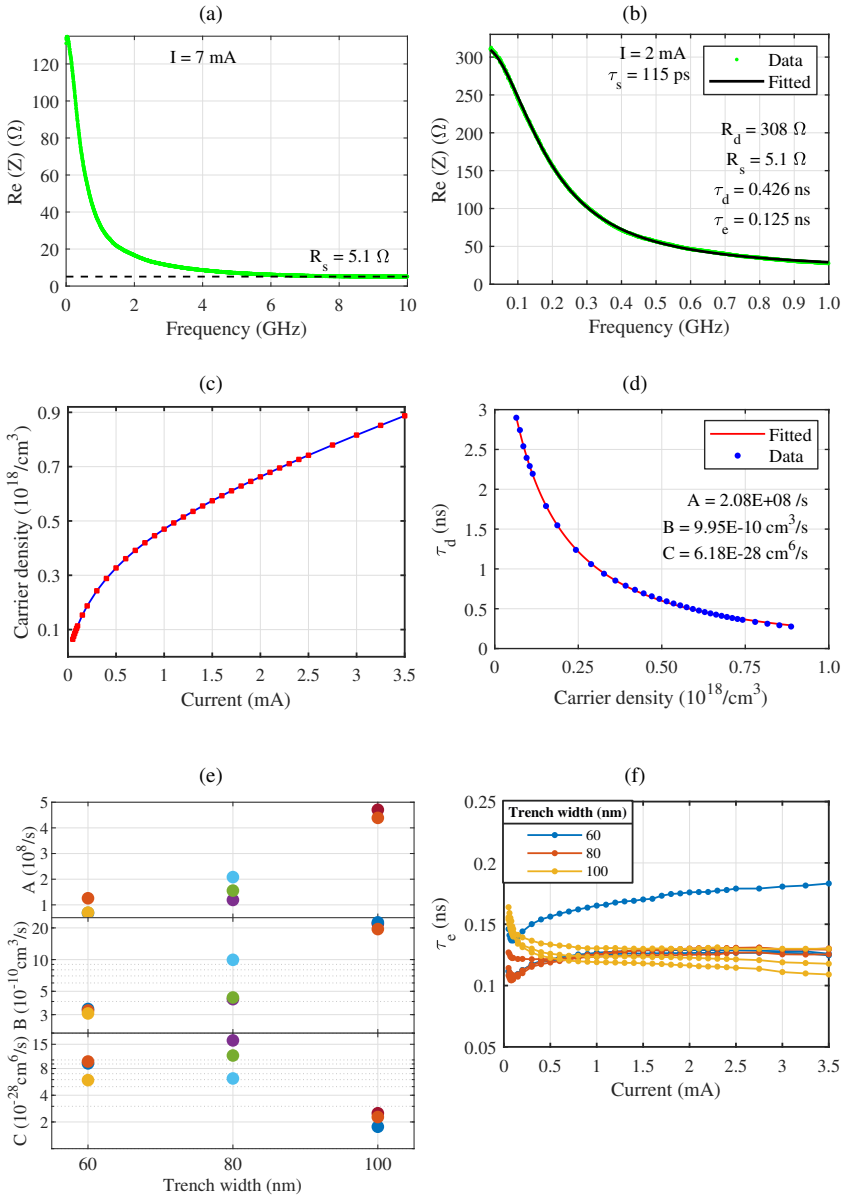

Figure 5.9: Extraction of recombination parameters from S_{11} measurements. (a) Extraction of R_s from an S_{11} measurement up to 10 GHz. (b) Example of R_d, τ_d, and τ_e extraction at $I = 2$ mA. (c) Carrier density versus bias current. (d) Differential carrier lifetime versus carrier density with extracted A, B, and C recombination coefficients. (e) Dependence of A, B, and C on the trench width. (f) Carrier escape times τ_e for devices with trench widths of 60, 80, and 100 nm.

5.4 Conclusion

This chapter has presented a comprehensive investigation of the dynamic behavior of monolithically integrated nano-ridge lasers, providing several important insights into their performance.

From the S_{21} measurements, effective carrier capture times were found to lie predominantly in the range of 100–125 ps, which is somewhat longer than the values typically reported for conventional quantum-well lasers. This extension is attributed to the sparse distribution of metal plugs in the contacting scheme, which increases the transport time of carriers prior to capture. These results highlight the strong influence of the contact design on carrier dynamics and underline the importance of optimized injection schemes to enhance device speed.

RIN analysis further confirmed the extracted dynamic parameters, yielding D-factors of approximately 1 GHz/mA$^{1/2}$ and K-factors between 0.5 and 0.8 ns, in good agreement with the S_{21} results. Using these values, the differential gain was determined to be in the range of 4.3–7×10^{-16} cm^2, while the gain compression factor was estimated between 1.8 and 4.4×10^{-17} cm^3.

Recombination coefficients were also extracted for devices with trench widths of 60 nm, 80 nm, and 100 nm, allowing the role of device geometry to be assessed. Devices with wider trenches (100 nm) exhibited higher A coefficients, which may arise from threading dislocations trapped closer to the trench opening (or the nano-ridge volume) or from reduced passivation quality at the $\{111\}$ facets. At the same time, these wider-trench (100 nm) devices displayed higher radiative recombination (B) and lower Auger recombination (C), a behavior likely linked to the reduced localized heating effects as the device volume increases. Importantly, defect-related recombination was shown to contribute less than 5% of the threshold current in 60 nm and 80 nm devices, and less than 10% in 100 nm devices. These findings confirm the effectiveness of aspect-ratio trapping and nano-ridge engineering in suppressing defect-related recombination, thereby enabling the realization of high-quality III-V material on silicon for monolithic integration.

Comparison with earlier reports [21] shows that the extracted B coefficients for the 60 nm and 80 nm devices are broadly consistent, while those for 100 nm trenches are up to four times larger. The extracted C coefficients, on the other hand, are typically one to two orders of magnitude higher than previously reported. This discrepancy can be explained by the limitations of bulk rate-equation models commonly used in prior works, which, as shown in [22], neglect carrier populations in the barrier and SCH regions. When transport effects are properly accounted for, recombination coefficients can be significantly larger, consistent with the values obtained here.

Finally, the extracted carrier escape times were found to be within 110–130 ps, leading to a τ_s/τ_e ratio close to unity. This ratio effectively reduces the differential gain by approximately a factor of two compared to bulk devices, resulting in higher K-factors and reduced modulation bandwidth. These findings indicate that adopting a continuous contact scheme to achieve shorter τ_s values could significantly improve the modulation performance of the nano-ridge lasers, paving the way for enhanced high-speed operation.

References

[1] A. A. Yimam et al., Advanced characterization and parameter extraction of electrically injected InGaAs/GaAs nano-ridge lasers monolithically integrated on silicon, *Optics Express*, vol. 33, no. 13, p. 27 929, Jun. 2025.

[2] S. Hausser, G. Fuchs, A. Hangleiter, K. Streubel, and W. T. Tsang, Auger recombination in bulk and quantum well InGaAs, *Applied Physics Letters*, vol. 56, no. 10, pp. 913–915, Mar. 1990.

[3] L. A. Coldren, S. W. Corzine, and M. L. Mashanovitch, *Diode lasers and photonic integrated circuits*. John Wiley & Sons, 2012.

[4] P.-Y. Hsieh et al., Advanced current–voltage model of electrical contacts to GaAs- and Ge-based active silicon photonic devices, *IEEE Transactions on Electron Devices*, vol. 70, no. 8, pp. 4274–4279, Aug. 2023.

[5] R. Nagarajan, M. Ishikawa, T. Fukushima, R. Geels, and J. Bowers, High speed quantum-well lasers and carrier transport effects, *IEEE Journal of Quantum Electronics*, vol. 28, no. 10, pp. 1990–2008, 1992.

[6] A. Larsson, P. Westbergh, J. Gustavsson, Å. Haglund, and B. Kögel, High-speed VCSELs for short reach communication, *Semiconductor Science and Technology*, vol. 26, no. 1, p. 014 017, Nov. 2010.

[7] D. A. Neamen, *Semiconductor Physics and Devices: Basic Principles*, 4th. New York, NY 10020: McGraw-Hill Higher Education, 2012, pp. 331–363.

[8] I. Esquivias, S. Weisser, B. Romero, J. Ralston, and J. Rosenzweig, Carrier dynamics and microwave characteristics of GaAs-based quantum-well lasers, *IEEE Journal of Quantum Electronics*, vol. 35, no. 4, pp. 635–646, Apr. 1999.

[9] G. P. Agrawal, *Fiber-optic communication systems*. John Wiley & Sons, 2002, ch. 3, pp. 114–116.

[10] IEEE Working Group, *IEEE 802.3 standard: Relative intensity noise specification for 50 Gb/s, 10 km optical links*, https://ieeexplore.ieee.org/stamp/stamp.jsp?tp=&arnumber=8649797, 2022.

[11] F.-L. Wang, X.-W. Ma, Y.-Z. Huang, Y.-D. Yang, J.-Y. Han, and J.-L. Xiao, Relative intensity noise in high-speed hybrid square-rectangular lasers, *Photonics Research*, vol. 6, no. 3, p. 193, Feb. 2018.

[12] M. Nazarathy, J. Berger, A. J. Ley, I. M. Levi, and Y. Kagan, Progress in externally modulated am catv transmission systems, *Journal of Lightwave Technology*, vol. 11, no. 1, pp. 82–105, Jan. 1993.

[13] M. Cox, N. Copner, and B. Williams, High sensitivity precision relative intensity noise calibration standard using low noise reference laser source, *IEE Proceedings - Science, Measurement and Technology*, vol. 145, no. 4, p. 163, 1998.

[14] *Synopsys TCAD*, https://www.synopsys.com/manufacturing/tcad.html.

[15] *Lumerical photonics simulation and design software official website*, https://www.ansys.com/products/photonics.

[16] Y. De Koninck et al., GaAs nano-ridge laser diodes fully fabricated in a 300-mm CMOS pilot line, *Nature*, vol. 637, no. 8044, pp. 63–69, 2025.

[17] A. A. Yimam et al., Semi-analytical model for electrically injected GaAs nano-ridge laser diodes monolithically integrated on silicon, *Optics Express*, vol. 33, no. 2, p. 2101, Jan. 2025.

[18] H. Sun, Gain saturation enhancement of longitudinal hole burning via standing wave induced wave coupling in a semiconductor laser, *IEEE journal of quantum electronics*, vol. 32, no. 4, pp. 617–619, 1996.

[19] E. Kapon, Ed., *Semiconductor Lasers I: Fundamentals* (Optics and Photonics). San Diego: Academic Press, 1999, ch. 3, pp. 177–290.

[20] G. Shtengel, D. Ackerman, P. Morton, E. Flynn, and M. Hybertsen, Impedance-corrected carrier lifetime measurements in semiconductor lasers, *Applied physics letters*, vol. 67, no. 11, pp. 1506–1508, 1995.

[21] D. Ding, S. R. Johnson, J.-B. Wang, S.-Q. Yu, and Y.-H. Zhang, "Determination of spontaneous emission quantum efficiency in InGaAs/GaAs quantum well structures", *Solid State Lighting and Solar Energy Technologies*, Y. Zhao et al., Eds., vol. 6841, SPIE, Nov. 2007, p. 68410D.

[22] J. Pikal, C. Menoni, H. Temkin, P. Thiagarajan, and G. Robinson, Carrier lifetime and recombination in long-wavelength quantum-well lasers, *IEEE Journal of Selected Topics in Quantum Electronics*, vol. 5, no. 3, pp. 613–619, 1999.

[23] B. Romero, I. Esquivias, S. Weisser, E. Larkins, and J. Rosenzweig, Carrier capture and escape processes in $In_{0.25}$ $Ga_{0.75}$As-GaAs quantum-well lasers, *IEEE Photonics Technology Letters*, vol. 11, no. 7, pp. 779–781, Jul. 1999.

6

New electrically injected nano-ridge laser design approaches

Contents

The previous chapter provided a detailed dynamic characterization of monolithically integrated InGaAs/GaAs nano-ridge lasers, highlighting the key physical mechanisms that govern their high-speed performance. Through small-signal modulation measurements, effective carrier capture times were extracted, revealing prolonged transport delays attributed to the sparse contacting configuration. Complementary RIN measurements further enabled the extraction of key dynamic parameters, including the D-factor, the K-factor, the differential gain, and the gain compression

factor. In parallel, the influence of the trench width on the recombination coefficients was analyzed reflecting the interplay between geometry, material quality, and carrier dynamics. Collectively, these results indicate that both injection scheme and device geometry critically impact performance, motivating the exploration of new design approaches. Building on these findings, the present chapter shifts focus from characterization to design, introducing novel electrically injected nano-ridge laser configurations aimed at overcoming the identified performance bottlenecks.

This chapter is organized as follows. Section 6.1 discusses the fundamental performance constraints of nano-ridge lasers operating under the mode-beating approach, providing the motivation for exploring alternative architectures. Section 6.2 introduces three novel electrically injected laser designs: loss coupled DFB lasers, silicon side-grating DFB lasers and top p-GaAs grating DFB lasers. Section 6.3 presents a comparative analysis of these approaches using Sentaurus TCAD electrical simulations, focusing on their current-voltage characteristics and injection efficiencies. Finally, Section 6.4 summarizes the key findings and outlines design strategies that hold promise for enhancing the performance of monolithically integrated nano-ridge lasers.

6.1 Limitations of electrically injected nano-ridge lasers based on the mode-beating approach

Despite the promising results obtained in Chapters 4 and 5, several limitations of the current generation of electrically injected InGaAs/GaAs nano-ridge lasers remain evident, both in their static and dynamic characteristics. These limitations highlight the need for alternative device geometries and injection strategies, which will be explored in the subsequent sections of this chapter.

On the static side, the emission wavelength was found to be highly sensitive to fabrication-induced dimensional fluctuations, particularly in the ridge height. Since higher-order modes are especially susceptible to such variations, process-induced detuning can significantly compromise wavelength reproducibility. This sensitivity is inherent to the mode-beating approach, which relies on coupling between the fundamental and higher-order modes, and highlights the need for cavity designs that are less vulnerable to geometrical perturbations. For example, adopting a DFB grating configuration—where the lasing condition is defined by contra-directional coupling of the fundamental mode—offers improved robustness against dimensional variations.

Linewidth characterization yielded values in the range of 37–216 MHz, placing the present nano-ridge lasers between commercial DFB lasers and VCSELs. The large

variation in the measured linewidths are attributed to parasitic back reflections due to the absence of an optical isolator in the measurement setup, fabrication-induced geometry fluctuations, and the lack of active stabilization beyond temperature control. Narrowing the linewidth requires minimizing internal losses, reducing mirror losses through optimized facet designs or the incorporation of distributed Bragg gratings, operating at higher injection currents, and lowering the linewidth enhancement factor.

Spectral measurements on a wider set of devices further revealed that many lasing devices exhibit a side mode suppression ratio (SMSR) below 30 dB, consistent with the broad round-trip gain spectrum discussed in Chapter 3. Increasing the SMSR will require gratings with higher spectral selectivity to better suppress competing side modes, as will be discussed in the following sections.

Another limitation lies in the relatively large cavity lengths (1–2 mm) required for lasing in most working devices. Shorter cavities suffer from high distributed mirror losses, preventing stable lasing operation. Achieving reliable lasing in devices with lengths of 200–300 μm will require reducing the threshold gain, which in turn demands careful optimization of the cavity geometry, doping profiles, and grating coupling efficiency.

From a reliability standpoint, localized high current densities beneath the sparse plug contacts have been identified as a primary failure mechanism [1]. Current crowding in these regions generates hot spots that accelerate device degradation and ultimately limit lifetime. Achieving uniform current injection along the entire cavity length is therefore critical. Potential solutions include employing a continuous contact scheme or adopting a periodic contact scheme with a significantly smaller grating pitch. However, both approaches introduce additional optical losses, making their implementation nontrivial. Careful device engineering is thus required to strike an optimal balance between homogeneous current injection and tolerable optical loss.

On the dynamic side, modulation performance is constrained by extended carrier transport times. Effective capture times of 100–125 ps—longer than in conventional quantum-well lasers—were linked to the sparse contacting scheme, which increases the distance carriers must traverse before being captured into the quantum wells. The extracted τ_s/τ_e ratio close to unity suppresses the differential gain by nearly a factor of two relative to bulk devices, leading to lower D-factors and higher K-factors that ultimately limit the achievable modulation bandwidth. Introducing a continuous contact scheme or a periodic contact configuration with a small pitch could alleviate this limitation by reducing the carrier transport path; however, such approaches must again be carefully designed to prevent excessive optical losses.

Geometry-dependent recombination effects add another layer of complexity. Devices with wider trenches exhibited relatively higher A coefficients, while simultaneously showing higher radiative B coefficients and lower Auger C coefficients. Although defect-related recombination accounted for only a small percentage of the threshold current across all devices, these findings confirm that geometry continues to play a critical role in recombination dynamics and must be carefully optimized.

In summary, the performance of the present nano-ridge lasers is limited by (i) strong sensitivity to fabrication variations, (ii) broad linewidths and low SMSR, (iii) reliance on long cavities for lasing operation, (iv) non-uniform current injection leading to reliability issues, and (v) extended carrier capture times that restrict modulation bandwidth. Addressing these bottlenecks requires rethinking both the cavity design and the injection scheme. The remainder of this chapter introduces and evaluates new electrically injected nano-ridge laser architectures designed to mitigate these limitations and enable higher performance for silicon-integrated photonic systems.

6.2 New laser design approaches

Building on the limitations of the current nano-ridge lasers discussed above, two potential pathways towards improved reliability and modulation bandwidth have been identified: (i) employing a periodic contact configuration with substantially smaller pitch and (ii) adopting a continuous contact scheme. While both approaches promise more uniform carrier injection, they inevitably introduce significant optical losses—an issue that is particularly critical for devices fabricated by selective epitaxy with small active volumes.

In collaboration with the imec epitaxy team, a mitigation strategy was pursued in which a p-doped GaAs layer was deposited on top of the InGaP passivation. This configuration allows an electrical contact to be formed on the top p-GaAs surface while simultaneously shifting the optical mode further away from the metal, thereby reducing absorption losses. A schematic of this concept is shown in Figure 6.1. However, this architecture introduces a new challenge: the presence of an undoped, higher bandgap InGaP layer sandwiched between two p-GaAs layers, which may inhibit efficient current injection into the quantum wells. A potential solution is to p-dope the InGaP layer itself, thereby enhancing vertical carrier transport. Evaluating the impact of such a modification on current injection efficiency will be a key part of the design analysis presented later in this chapter.

The central question that arises is whether grating structures can be designed for this device architecture to enable shorter-cavity lasers (200–300 μm) with

reduced threshold current, narrower linewidth, and acceptable optical efficiency. To address this, three alternative grating-based design approaches are investigated and compared in terms of performance:

1. Partly loss-coupled metal contact gratings,
2. Silicon side-gratings and
3. Gratings formed in the top p-GaAs layer.

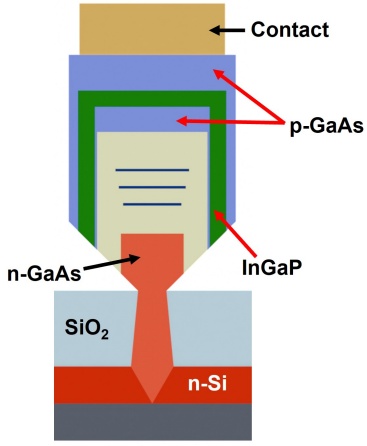

Figure 6.1: Schematic illustration of a proposed device architecture with a p-doped GaAs layer deposited on top of the InGaP passivation. The contact is formed on the p-GaAs surface, thereby shifting the optical mode away from the metal and reducing optical loss. The structure, however, introduces an undoped InGaP layer between two p-GaAs layers, which may hinder efficient carrier injection.

6.2.1 Partly loss-coupled DFB lasers

DFB lasers most commonly employ periodic index perturbations along the cavity to provide the feedback required for lasing. These devices, generally referred to as index-coupled DFB lasers, form the foundation of many commercial implementations. When the periodic modulation is instead introduced through spatial variations of the gain or loss, the resulting structures are called gain-coupled or loss-coupled DFB lasers [2].

The use of gain/loss coupling provides several benefits compared to purely index-coupled designs. A key feature is that mode selectivity depends strongly on the overlap between the standing-wave intensity distribution and the periodic modulation

of gain or loss [3]. This enhanced overlap leads to improved mode discrimination, resulting in a much higher probability of stable single-mode operation.

An additional advantage is the reduced sensitivity to reflections. Both theoretical analyses and experimental demonstrations have shown that gain/loss-coupled DFB lasers perform more robustly in the presence of imperfect antireflection (AR) coatings or cleaved facets [2, 3]. Moreover, careful engineering of the gain coupling enables mitigation of spatial hole burning within the cavity.

For loss-coupled gratings, however, an additional penalty arises from internal absorption introduced by the grating itself. Achieving high coupling strength requires significant overlap of the optical field with the lossy grating material, which simultaneously increases the internal loss. Thus, device design must carefully balance coupling strength with tolerable absorption losses.

Considering an AR–coated cavity incorporating a top first-order metal grating of length L, as illustrated in Fig. 6.2, the forward and backward-propagating fields, $A(z)$ and $B(z)$, are governed by the standard coupled-wave equations [2, 4]:

$$\frac{dA(z)}{dz} = j\,b\,A(z) + j\,\kappa_{AB}\,B(z), \qquad -\frac{dB(z)}{dz} = j\,b\,B(z) + j\,\kappa_{BA}\,A(z), \tag{6.1}$$

where the complex propagation parameter b incorporates detuning and loss/gain,

$$b = \delta - j\,\frac{\Gamma g_{\text{th}} - \alpha_i}{2}, \qquad \delta = \frac{2\pi n_{\text{eff}}}{\lambda} - \beta_{\text{Bragg}}, \qquad \beta_{\text{Bragg}} = \frac{\pi}{\Lambda}. \tag{6.2}$$

Here, κ_{AB} (κ_{BA}) denotes the first-order coupling coefficient from B to A (from A to B). A summary of symbols is provided in Table 6.1.

Table 6.1: Definitions of parameters used in the coupled-wave formalism.

Parameter	Description
κ_{AB}, κ_{BA}	First-order diffraction coupling coefficients
g_{th}	Threshold material gain
Γ	Optical confinement factor
δ	Detuning from the Bragg condition
β_{Bragg}	First-order Bragg propagation constant
n_{eff}	Average effective index of the guided mode
α_i	Internal optical loss

For AR-coated facets, symmetry arguments yield the general solutions [2]

$$A(z) = \sinh\big[\gamma\,(z + L/2)\big], \qquad -B(z) = \pm\sinh\big[\gamma\,(z - L/2)\big], \tag{6.3}$$

where $\gamma = \gamma' + j\gamma''$ satisfies the dispersion relation

$$\gamma^2 = \kappa^2 - b^2, \qquad \kappa^2 = \kappa_{AB}\kappa_{BA}. \tag{6.4}$$

In mixed index–loss coupling, the coupling coefficient is complex and equal for forward/backward coupling [2]: $\kappa_{AB} = \kappa_{BA} = \kappa = \kappa_{\text{real}} + j\kappa_{\text{imag}}$.

Under the assumption of zero facet reflections, the threshold condition gives rise to the eigenvalue equation [2, 3]

$$\kappa = \frac{\pm j\,\gamma}{\sinh(\gamma L)}. \tag{6.5}$$

By solving for γ satisfying the eigenvalue equation, the threshold gain and the Bragg detuning of the two main modes can be found by [2, 3]:

$$\Gamma g_{\text{th},i} = \alpha_i + \alpha_m \pm 2\,\kappa_{\text{imag}}\, f_{\text{st}}, \quad i = 1, 2, \tag{6.6}$$

$$\delta = \pm\,\mathrm{Im}\big[j\kappa\cosh(\gamma L)\big], \tag{6.7}$$

where $\Gamma g_{\text{th},i}$ correspond to the two dominant modes on opposite sides of the stop-band. From the set of the infinite longitudinal modes satisfying the eigenvalue equation, the one with the lowest threshold gain will be lasing. $\alpha_m = 2\alpha_{\text{end}}$ is the mirror loss. The facet loss α_{end} in the presence of complex γ is calculated by taking the mode amplitudes in Eqs. 6.3 and is given by [2]

$$\alpha_{\text{end}} L = \frac{\sinh^2(\gamma' L) + \sin^2(\gamma'' L)}{\dfrac{\sinh(2\gamma' L)}{2\gamma' L} - \dfrac{\sin(2\gamma'' L)}{2\gamma'' L}}. \tag{6.8}$$

The parameter f_{st}, which quantifies the depth of the standing-wave pattern, is defined as [3]

$$f_{\text{st}} = \frac{\mathrm{Re}\Big\{2\int_{-L/2}^{L/2} AB^*\,dz\Big\}}{\int_{-L/2}^{L/2}(|A|^2 + |B|^2)\,dz} = \frac{\kappa_{\text{real}}}{\delta}, \tag{6.9}$$

The standing-wave effect, i.e., the interaction between the field distribution and the periodic gain/loss modulation, is central to mode discrimination. In loss-coupled, AR-coated DFB lasers, one mode overlaps more strongly with regions of high absorption while the other overlaps with low-loss regions. This asymmetry produces distinct threshold gains, with the threshold gain difference (gain margin) given by [3]

$$\Gamma|g_{\text{th},1} - g_{\text{th},2}| = |4\,\kappa_{\text{imag}}\, f_{\text{st}}|. \tag{6.10}$$

The optical efficiency, defined as the ratio of the facet loss rate to the stimulated-emission rate, is [3]

$$\eta = \frac{2\alpha_{\text{end}}}{\Gamma g_{\text{th}}} = \frac{2\alpha_{\text{end}}}{\alpha_i + 2\alpha_{\text{end}} - 2|\kappa_{\text{imag}} f_{\text{st}}|}, \tag{6.11}$$

where g_{th} is the smaller of the two modal thresholds in Eq. (6.6).

Finally, neglecting nonlinearities such as spatial hole burning, the linewidth–power product of the lasing mode is given by [3, 4]

$$\Delta\nu P_1 = C\,(\Gamma g_{\text{th}})^2\,\eta, \tag{6.12}$$

where

$$C = \frac{v_g^2\, h\nu\, n_{\text{sp}}(1+\alpha^2)}{8\pi}, \tag{6.13}$$

and P_1 is the output power per facet, $h\nu$ is the photon energy, n_{sp} is the spontaneous emission factor, α is the linewidth enhancement factor, and v_g is the group velocity.

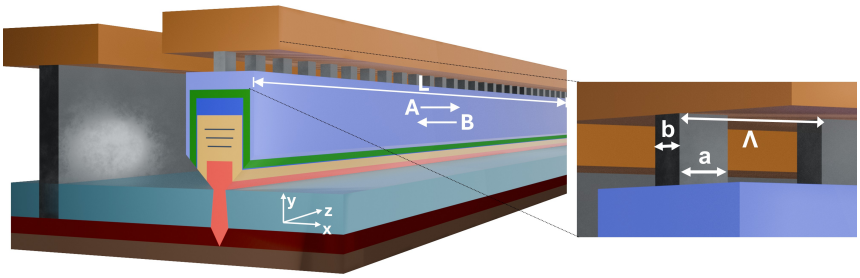

Figure 6.2: Partly loss-coupled DFB cavity of length L with AR-coated facets. Periodic loss modulation couples the forward (A) and backward (B) waves. The standing-wave pattern interacts with the loss profile, producing intrinsic mode discrimination and a modal threshold split in Eq. (6.6).

To quantify these relationships for the nano-ridge geometries, two first-order metal-grating implementations were analyzed, each with a period of 154 nm designed to produce a reflection band centered at 1020 nm. The configurations considered include tungsten (W) plugs and gold (Au) plugs, with the latter incorporating a 5 nm titanium (Ti) adhesion layer at the metal–semiconductor interface to ensure reliable contact formation. The cross-section follows an 80 nm trench-width nano-ridge (dimensions from SEM images) with a top p-GaAs layer on InGaP passivation, and doping profiles as illustrated schematically in Fig. 6.3.

Using Lumerical FDE MODE, we evaluated the transverse losses at the two local cross-sections sampled by a rectangular grating: one section containing air, the other

containing metal. The average internal loss α_i is then obtained by weighting these two values by the duty cycle $\sigma = a/\Lambda$, and adding a scattering loss contribution of $8.5\ \mathrm{cm}^{-1}$ (Chapter 2).

Figure 6.4(a) illustrates the variation of the internal loss as a function of the duty cycle for both W and Au contacts. The results reveal that devices employing W contacts exhibit consistently higher internal losses compared to those with Au contacts incorporating a 5 nm Ti adhesion layer. Moreover, the internal loss increases with the width of the W plug (b in Fig. 6.2), whereas it decreases as the width of the Au plug is enlarged. This asymmetric behavior stems from the materials' complex refractive indices. The optical constants used (from the Lumerical database) are summarized in Table 6.2 [5]. At a wavelength of 1020 nm, the real refractive index of tungsten is relatively close to that of GaAs and InGaP, while gold possesses a markedly lower real refractive index. Consequently, widening the W plug increases the modal field overlap with the lossy medium, raising the internal loss; by contrast, widening the Au plug pushes the mode further away from the metal because of Au's low real index, reducing field overlap and hence the loss. This Au-driven reduction would be even more pronounced without the 5 nm Ti layer: Ti's relatively large real index pulls the mode upward slightly, partially counteracting the Au-induced displacement.

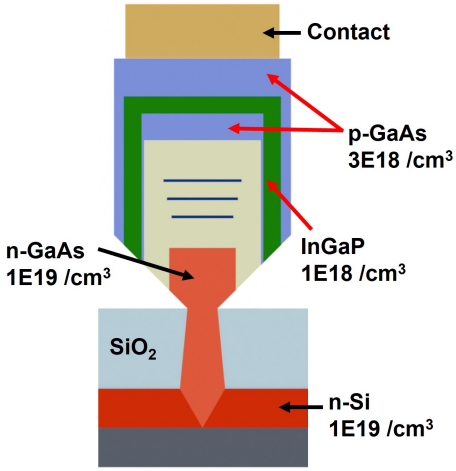

Figure 6.3: Cross-sectional schematic of the simulated nano-ridge laser structure (trench width: 80 nm), illustrating the top p-GaAs layer grown on the InGaP passivation layer and the associated doping profiles across the various material regions. The rectangular metal plugs define a longitudinal grating along the cavity.

Table 6.2: Representative complex refractive indices near $\lambda \approx 1020$ nm (Lumerical database; data from Palik [5]). The optical constants explain the opposite trends observed for W and Au in Fig. 6.4(a).

Material	n	k
W	3.00	3.60
Au	0.27	6.99
Ti	3.35	3.30
GaAs	3.49	–
InGaP	3.21	–

For a rectangular grating, the first-order coupling coefficient can be expressed [6] as

$$\kappa = \frac{\Gamma_{xy}\,\Delta\varepsilon\,\sin(\pi\sigma)}{n_{\text{eff}}\lambda}, \tag{6.14}$$

where $\sigma = a/\Lambda$ is the duty cycle (see Fig. 6.2), $\Delta\varepsilon$ is the permittivity contrast between the metal and air, and

$$\Gamma_{xy} = \frac{\displaystyle\int_G |U|^2\,dA}{\displaystyle\int |U|^2\,dA}$$

is the transverse overlap of the quasi-TE_{00} modal field U with the grating region G.

By using the electric field profile of the quasi-TE_{00} mode together with the permittivity and effective index data obtained from Lumerical MODE, we computed κ for W and Au (with Ti) as a function of plug width and duty cycle. The trends in Fig. 6.4(b)–(c) align with the discussion above: for W, increasing the plug width from 200 nm to 300 nm increases the overlap with the field and hence increases the real and imaginary components of κ; beyond 300 nm the overlap saturates and κ changes minimally. For Au, the opposite occurs: widening the plug tends to push the mode downward (away from the metal region due to Au's small n), which reduces the overlap and thus decreases the real and imaginary parts of κ; the change from 300 nm to 400 nm is small. The presence of the thin Ti layer slightly moderates this Au trend by pulling the mode upward.

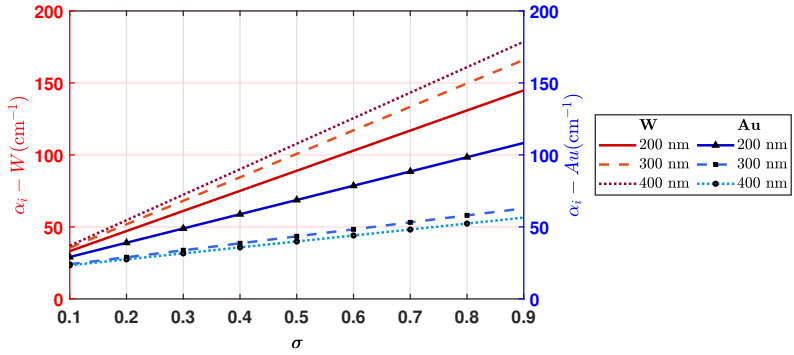

(a) Total internal loss α_i versus duty cycle for Au (with 5 nm Ti) and W contacts; a scattering loss of $8.5\ \mathrm{cm}^{-1}$ is included. W losses rise with plug width (greater field overlap with a lossy medium), while Au losses fall (mode pushed away by Au's small real index).

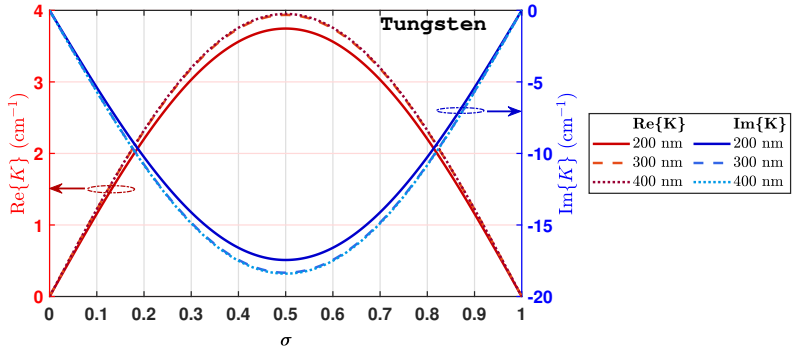

(b) Real and imaginary parts of the calculated coupling coefficient κ for W contacts. κ increases from 200 nm to 300 nm as overlap rises, then saturates for larger plugs.

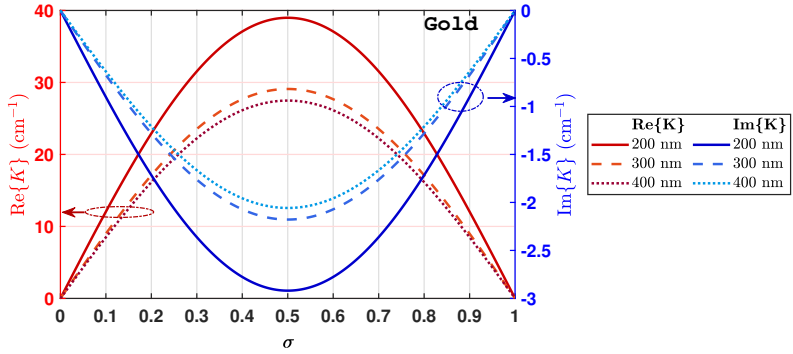

(c) Real and imaginary parts of the calculated coupling coefficient κ for Au + Ti contacts. κ decreases from 200 nm to 300 nm because the mode is displaced away from the metal; changes beyond 300 nm are small.

Figure 6.4: Internal loss and first-order coupling trends for metal-grating implementations in the nano-ridge geometry. The opposite W/Au behaviors arise from their distinct optical constants (Table 6.2) and the resulting field redistribution.

The facet mirror loss was calculated using Eq. 6.8, while the standing-wave factor f_{st}, obtained from Eq. 6.9, is shown in Fig. 6.5(a). Using these results, the threshold gain was evaluated via Eq. 6.6 and is presented in Fig. 6.5(b), while Fig. 6.5(c) shows the product $\Gamma g_{\text{th}} L$.

Overall, the threshold gain values for devices with gold contacts are consistently lower, a consequence of their smaller internal losses combined with larger coupling coefficients (real part). In contrast, the tungsten contact case is dominated by very high internal losses, which strongly influence the threshold characteristics. For tungsten, working at small duty cycles (0.1–0.2) reduces the threshold gain, yielding $\Gamma g_{\text{th}} \approx 120$/cm and $\Gamma g_{\text{th}} L \approx 9.6$ for an 800 μm long cavity. For gold contacts, particularly at plug widths of 300 nm and 400 nm and the same cavity length of 800 μm, the lowest threshold gain is obtained in the duty cycle range of 0.3–0.5, where values of $\Gamma g_{\text{th}} \approx 77$/cm and $\Gamma g_{\text{th}} L \approx 6.2$ are achieved.

The threshold gain difference between the two competing modes was then evaluated using Eq. 6.10 and is shown in Fig. 6.6(a). For stable single-mode operation, a threshold gain margin of $\Gamma |g_{\text{th1}} - g_{\text{th2}}| L \geq 0.05$ is generally required [7]. For both Au and W contacts across all specified plug widths, this criterion is satisfied when the duty cycle ranges between 0.15 and 0.85 for an 800 μm cavity. Hence, single-mode operation can be expected over a broad duty-cycle window for both contact types.

The optical efficiencies were next evaluated using Eq. 6.11, with the results shown in Fig. 6.6(b). The observed trends closely follow the variations in both the coupling coefficients and the total internal losses. Specifically, large coupling coefficients reduce the effective facet loss, thereby lowering the efficiency, while higher internal losses further degrade performance. For an 800 μm cavity and plug widths of 300 nm, the efficiency at a duty cycle of 0.5 was found to be 47 % for gold gratings, compared to 36.5 % for tungsten contacts. These results highlight the interplay between material choice, plug geometry, and grating design in determining the overall device efficiency.

Finally, the product of the linewidth and the optical output power per facet ($\Delta\nu P_1$) was calculated using Eq. 6.12, with $n_{\text{sp}} = 1.5$, $\alpha = 4.5$ [8], and $v_g = 3.96$ (obtained from Lumerical MODE). The corresponding results are presented in Fig. 6.6(c). For a cavity length of 800 μm, devices employing Au contacts exhibited $\Delta\nu P_1 < 50$ MHz·mW over the duty-cycle range of 0.3–0.6, while those with W contacts achieved $\Delta\nu P_1 < 125$ MHz·mW for duty cycles between 0.2 and 0.4.

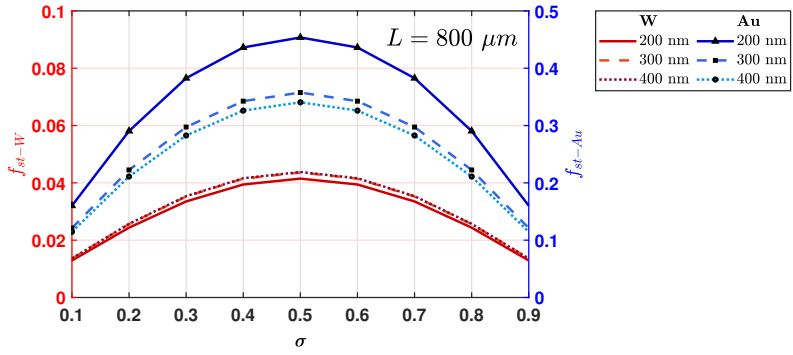

(a) Standing-wave factor f_{st} versus duty cycle and plug width.

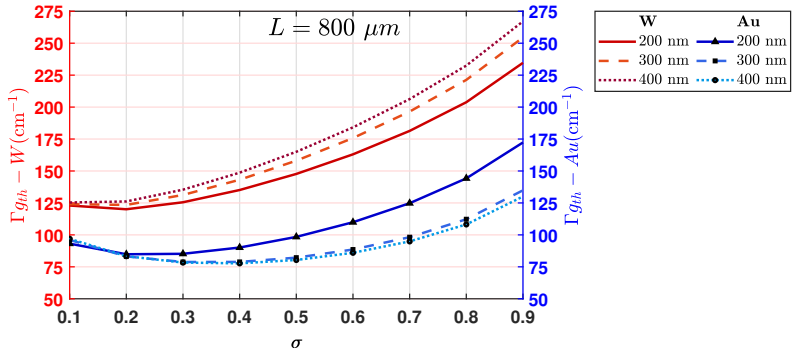

(b) Threshold gain Γg_{th} versus duty cycle and plug width.

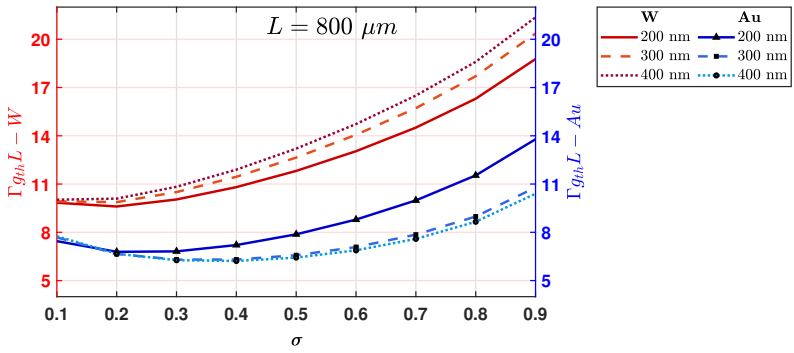

(c) Product $\Gamma g_{th} L$ versus duty cycle and plug width. Minima occur near $\sigma \approx 0.3$–0.5 for Au and at small σ for W.

Figure 6.5: Standing-wave factor, threshold gains, and $\Gamma g_{th} L$ for Au (with Ti) and W partly loss-coupled DFBs at $L = 800\ \mu m$. The trends reflect the interplay of internal loss and coupling strength established in Fig. 6.4.

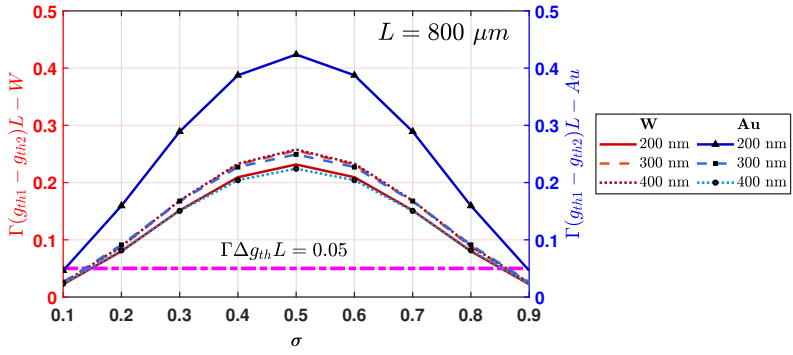

(a) Threshold gain difference (gain margin) versus duty cycle, from Eq. (6.10)*. Single-mode criterion* $\Gamma|g_{th,1} - g_{th,2}| \geq 0.05$ *highlights workable duty-cycle windows.*

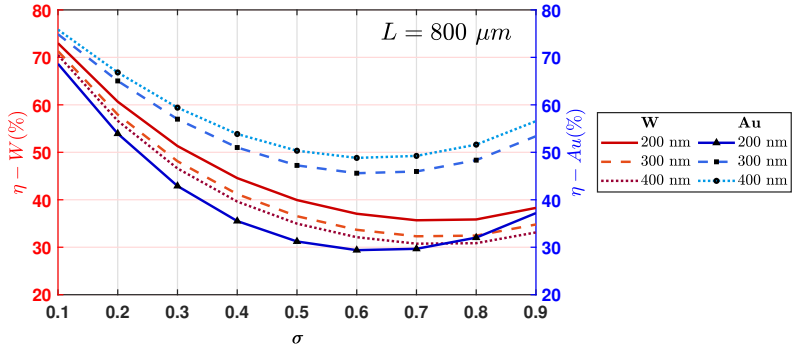

(b) Optical efficiency η *from Eq.* (6.11)*. Larger* κ *reduces mirror loss and thus* η*, while larger* α_i *also degrades* η*.*

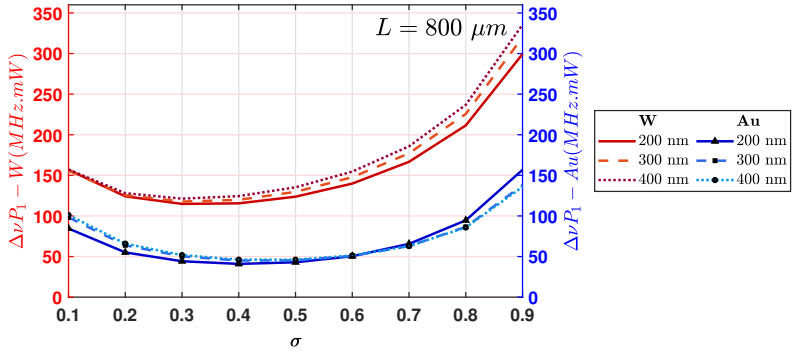

(c) Linewidth–power product $\Delta\nu P_1$ *versus duty cycle and plug width.*

Figure 6.6: Gain margin, efficiency, and linewidth–power product for Au (with Ti) and W partly loss-coupled DFBs at $L = 800\ \mu m$*.*

6.2.2 Silicon side-grating first-order DFB laser

An alternative strategy for implementing a DFB laser on the nano-ridge platform is to use a $\lambda/4$-shifted, index-guided, first-order silicon side-grating with a 154 nm period targeting operation around the wavelength of 1020 nm. The grating structure is positioned symmetrically on both sides of the ridge. The device facets are again assumed to be anti-reflection (AR) coated. Schematics of the device layout, doping profile, and relevant structural parameters are shown in Fig. 6.7(a) and (b).

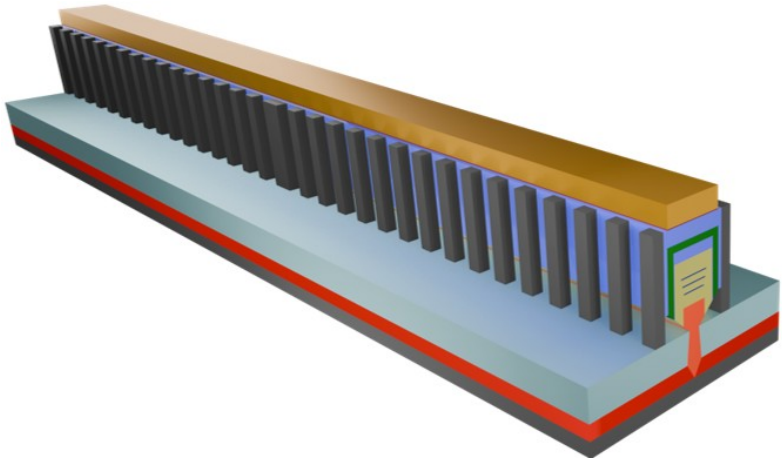

(a) 3D Schematic of the nano-ridge with silicon side-gratings.

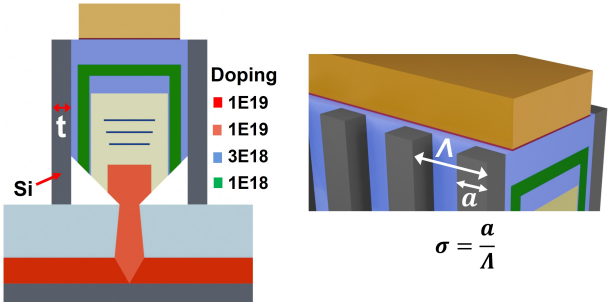

(b) Doping profile and structural parameters for the Si side-grating configuration.

Figure 6.7: Schematics of the $\lambda/4$-shifted index-guided Si side-grating DFB laser integrated with the nano-ridge structure.

To describe the device, we follow the coupled-wave formalism introduced in [4]. Considering the longitudinal cross-section of the waveguide with two symmetric grating sections of length $L/2$ separated by a $\lambda/4$ phase-shifted central region as

shown in Figure 6.8, the forward- and backward-propagating fields $A(z)$ and $B(z)$ are governed by Eq. 6.1, with parameters as defined in Eq. 6.2 and Table 6.1. The field reflection coefficients at the boundaries Z_a and Z_b are denoted r_1 and r_2, respectively.

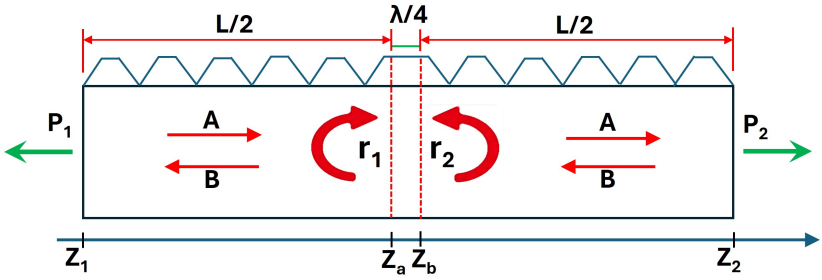

Figure 6.8: Schematic of the longitudinal cross-section of the grating structure with $\lambda/4$-shifted central region.

The lasing threshold condition is then expressed as [4]

$$r_1 r_2 \exp(j2\psi) = 1, \tag{6.15}$$

where ψ is the phase accumulated in the central $\lambda/4$ region. The reflection coefficients are given by:

$$r_i = \chi \frac{1 - \exp(\gamma L_i)}{1 - \chi^2 \exp(\gamma L_i)}, \quad i = 1, 2, \tag{6.16}$$

where γ is the complex propagation constant satisfying Eq. 6.4, and χ is

$$\chi = -\frac{j\kappa}{\gamma + jb} = -\frac{j\kappa}{\gamma \pm \sqrt{\gamma^2 - \kappa^2}}. \tag{6.17}$$

The sign ambiguity in χ is solved by requiring $|\chi| < 1$.

For a $\lambda/4$ phase shift, the lasing mode aligns with the Bragg wavelength, and the threshold gain can be extracted from the eigenvalue equation above.

In this configuration, gold with a 5 nm Ti adhesion layer is selected as the continuous contact, since it exhibits lower internal optical loss than the tungsten contact as discussed in the previous section. The contact width is designed to closely match that of the top p-GaAs layer (~ 562 nm), leaving narrow ~ 20 nm margins on either side. The internal loss is determined by averaging the transverse cross-sections of the waveguide with and without the side silicon, weighted by the duty cycle, and

incorporating an additional scattering loss of $8.5\ \mathrm{cm}^{-1}$ as established in Chapter 2. The resulting internal loss as a function of the side-grating width (t in Fig. 6.7(b)) for a duty cycle of 0.5 is shown in Fig. 6.9(a). As t increases, the high refractive index of silicon ($n \approx 3.56$ at 1020 nm [5]) pulls the mode into the grating, increasing its overlap with the doped p-GaAs regions adjacent to the silicon gratings and thereby raising internal losses.

The first-order coupling coefficient was subsequently calculated for various grating widths, assuming a rectangular grating profile, using Eq. 6.14, and the results are presented in Fig. 6.9(b). The coupling strength generally increases with grating width due to greater mode overlap; however, the variation saturates beyond $t = 100$ nm.

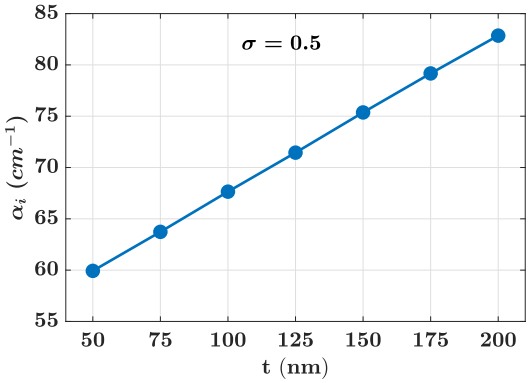

(a) Internal losses versus Si side-grating width (t) for a duty cycle of 0.5.

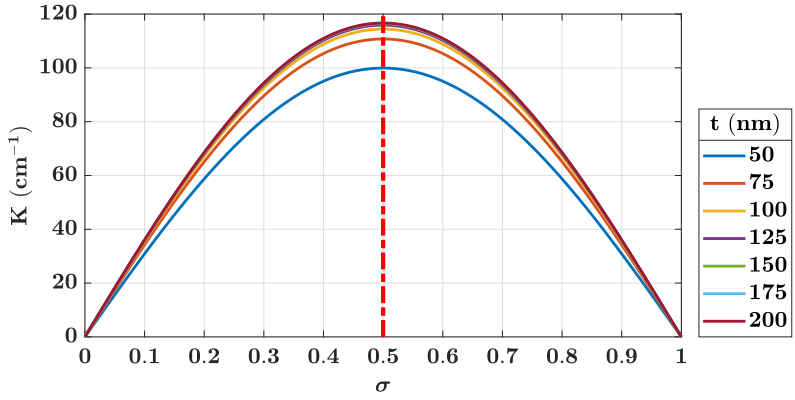

(b) Coupling coefficient versus duty cycle for different Si side-grating widths (t), showing saturation beyond 100 nm.

Figure 6.9: Calculated internal losses and coupling coefficients for the Si side-grating DFB laser.

The threshold gain Γg_{th} was determined by solving the eigenvalue equation (Eq. 6.15) for $\lambda/4$-shifted gratings. Results for cavity lengths of 150–400 μm and a duty cycle of 0.5 are plotted in Fig. 6.10(a). Two competing effects determine the threshold gain: (i) wider side-gratings increase internal losses [Fig. 6.9(a)], while (ii) coupling strength increases with grating width [Fig. 6.9(b)]. The trade-off leads to an optimal region around $t = 75$ nm, where threshold gain is minimized, particularly for cavity lengths below 350 μm. The corresponding $\Gamma g_{\text{th}} L$ curves are plotted in Fig. 6.10(b).

For a 300 μm cavity with $t = 75$ nm, the threshold gain is $\Gamma g_{\text{th}} = 80.8$ cm^{-1}, with $\Gamma g_{\text{th}} L = 2.4$. Compared to the gold partly loss-coupled gratings analyzed in the previous section, the threshold gain is similar, but the cavity length is nearly three times shorter. Consequently, the product $\Gamma g_{\text{th}} L$ is reduced compared to ~ 6.2 for the gold partly loss-coupled DFB laser. This improvement is attributed to the roughly threefold larger coupling coefficient of the Si side-grating design (cf. Figs. 6.4(c) and 6.9(b)).

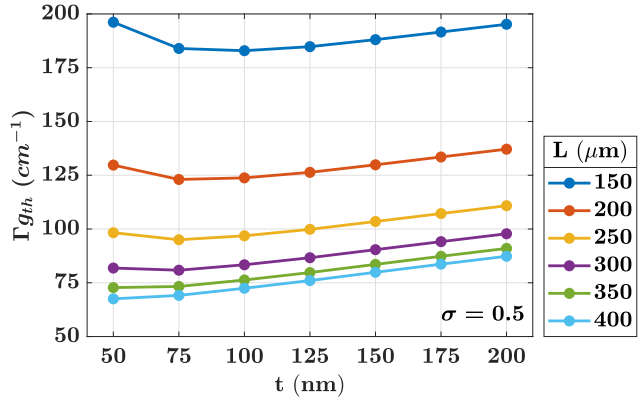

(a) Threshold gain Γg_{th} versus side-grating width for different cavity lengths.

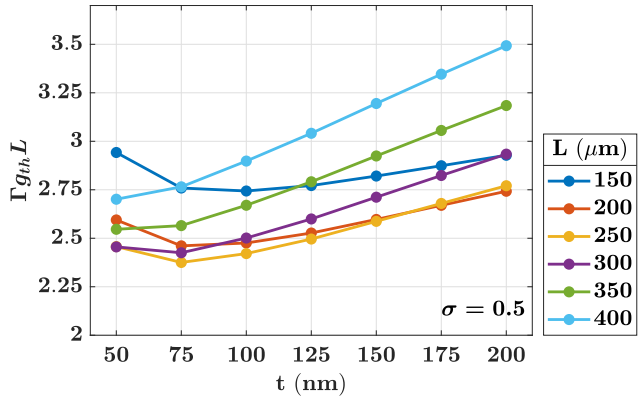

(b) Variation of $\Gamma g_{th} L$ with side-grating width for different cavity lengths.

Figure 6.10: Threshold gain analysis for Si side-grating DFB lasers of different cavity lengths.

Assuming no facet reflections, the optical efficiency is expressed as

$$\eta_{\text{opt}} = \frac{\Gamma g_{\text{th}} - \alpha_i}{\Gamma g_{\text{th}}}. \tag{6.18}$$

The resulting efficiencies for different cavity lengths are plotted in Fig. 6.11(a). For a cavity length of $L = 300$ μm and a side-grating width of $t = 75$ nm, the efficiency reaches approximately 21%. Although this value is lower than that obtained for the partly loss-coupled gold grating design—primarily due to the stronger coupling coefficients in the present structure—it still lies within a practically acceptable range for efficient optical operation.

Finally, the product of linewidth and output power per facet ($\Delta\nu P_1$) was evaluated using Eq. 6.12, with results shown in Fig. 6.11(b). For $L \geq 300$ μm and $t \geq 75$ nm,

$\Delta\nu P_1$ remains below 20 MHz·mW.

In summary, the first-order Si side-grating DFB laser offers significantly improved threshold performance compared to gold partly loss-coupled gratings. It enables shorter cavity devices ($\sim$ 300 μm) while maintaining acceptable optical efficiencies and linewidth characteristics, making it a promising alternative design for nano-ridge based integrated lasers.

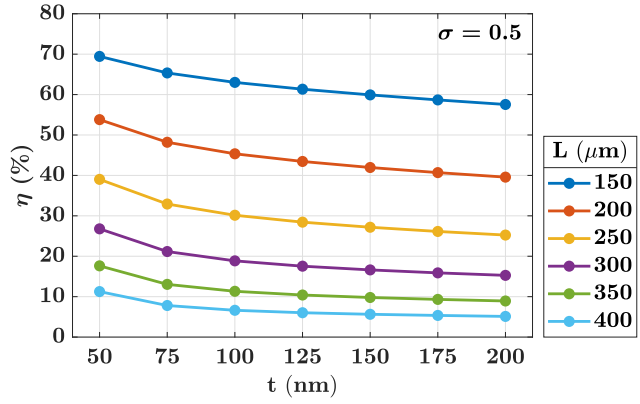

(a) Optical efficiency versus side-grating width for different cavity lengths.

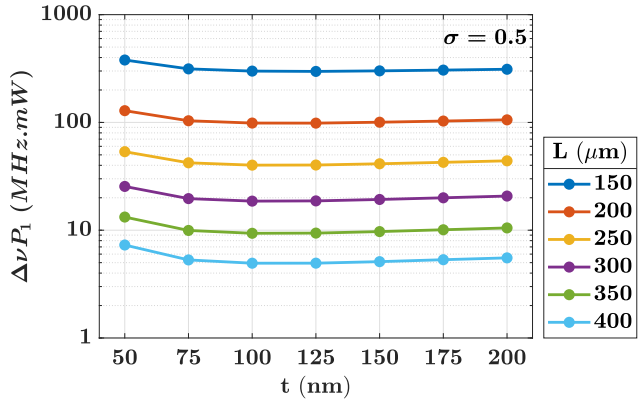

(b) Linewidth–power product ($\Delta\nu P_1$) versus side-grating width for different cavity lengths.

Figure 6.11: Optical efficiency and linewidth–power product of Si side-grating DFB lasers.

6.2.3 Top p-GaAs first-order DFB laser

In this section, we examine a third configuration for realizing a DFB laser on the nano-ridge platform: a first-order, $\lambda/4$-shifted, index-coupled DFB structure

formed by etching a periodic grating with a 154 nm period into the top p-GaAs layer on both sides of a continuous p-type contact. The p-type contact is defined on the central fin structure after completing the grating etch on both sides. A schematic representation of the device geometry, the doping profile and relevant structural parameters are shown in Fig. 6.12(a) and (b).

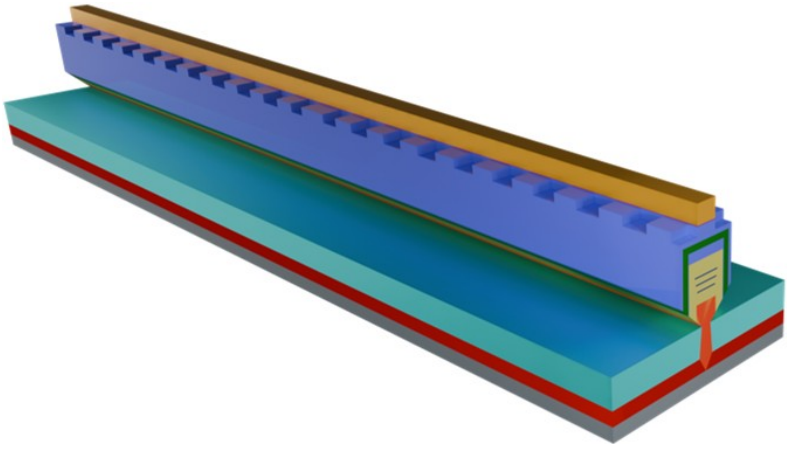

(a) 3D schematic representation of the top p-GaAs first-order DFB laser structure showing the etched grating regions and the continuous top contact.

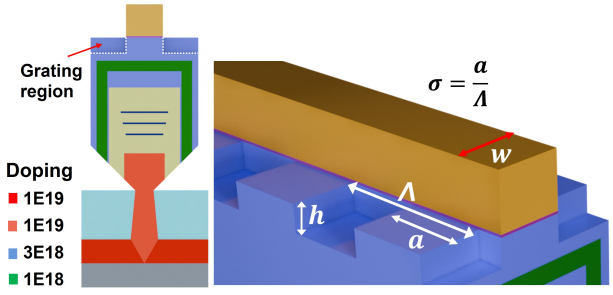

(b) Cross-sectional view illustrating the doping profile and main structural parameters. The grating depth is denoted by h.

Figure 6.12: Design of the top p-GaAs first-order DFB laser with periodic grating etched into the p-GaAs layer on both sides of the continuous Au/Ti contact.

The grating is realized by etching the p-GaAs layer to a controlled depth (h), thereby introducing a periodic modulation of the refractive index. A continuous gold contact with a 5 nm titanium adhesion layer is again employed, owing to its lower optical loss compared to the tungsten contact. The contact width (w in Fig. 6.12(b)) is set to 200 nm, providing sufficiently large grating regions on both sides of the contact

while maintaining efficient current injection into the device.

Following the same procedure used for the silicon side-grating first-order DFB laser, we calculated the internal loss and coupling coefficients for this structure. The dependence of the total internal loss on the grating etch depth (h in Fig. 6.12(b)) for a duty cycle of 0.5 is presented in Fig. 6.13(a). As the etch depth increases, the optical mode is slightly pushed downward, reducing its overlap with the metallic contact. As a result, the total internal loss decreases marginally with larger h.

The calculated first-order coupling coefficients as a function of the duty cycle for different etch depths are shown in Fig. 6.13(b). As expected, a deeper etch enhances the modulation strength of the refractive index and increases the field overlap with the grating region, resulting in a larger coupling coefficient.

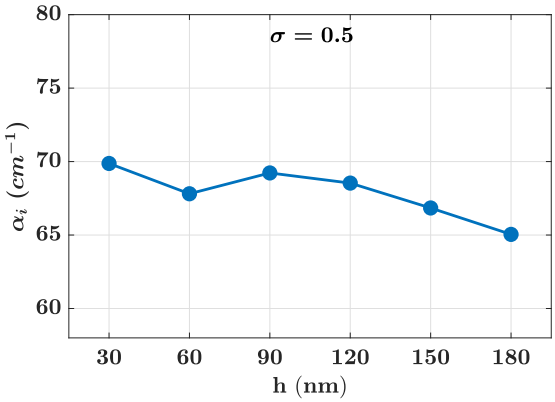

(a) Total internal loss as a function of the grating etch depth (h) for a duty cycle of 0.5.

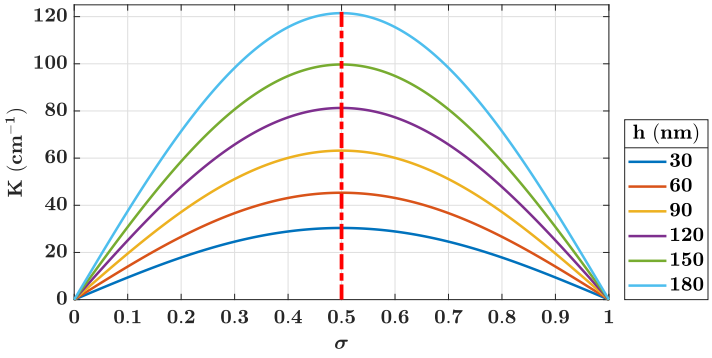

(b) Calculated coupling coefficient as a function of the duty cycle for different etch depths, showing an increase with deeper gratings as the field overlap strengthens.

Figure 6.13: Dependence of the internal optical loss and coupling coefficient on the grating parameters for the top p-GaAs first-order DFB laser.

The threshold gain, Γg_{th}, for cavity lengths between 150 and 400 μm was evaluated using the eigenvalue equation for $\lambda/4$-shifted gratings, as in the previous DFB laser analyses. The results for a duty cycle of 0.5 are plotted in Fig. 6.14(a). The combination of slightly reduced internal losses and enhanced coupling coefficients at greater etch depths results in a progressive decrease in the threshold gain with increasing h. The product $\Gamma g_{\text{th}} L$ is shown in Fig. 6.14(b), illustrating the dependence on both cavity length and grating depth.

For a representative cavity length of 300 μm and an etch depth of $h = 180$ nm, the threshold gain is $\Gamma g_{\text{th}} = 78.4$ cm^{-1}, corresponding to $\Gamma g_{\text{th}} L = 2.4$. These values are comparable to those obtained for the silicon side-grating first-order DFB laser design.

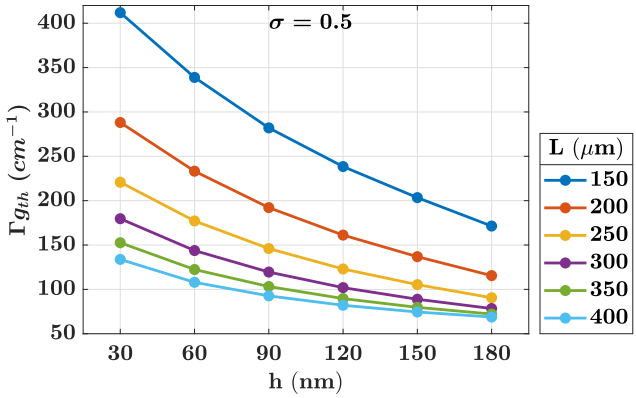

(a) Variation of the modal threshold gain (Γg_{th}) with grating etch depth (h) for different cavity lengths at a duty cycle of 0.5.

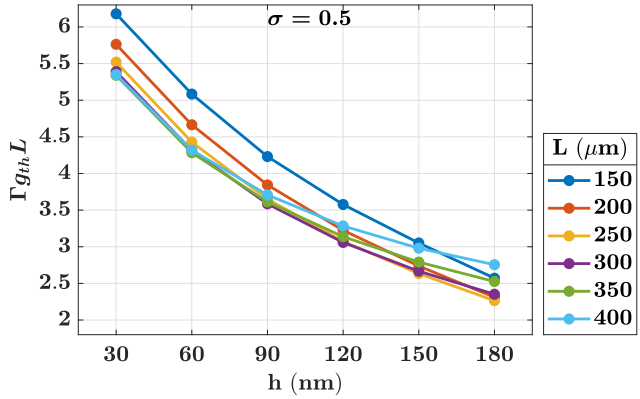

(b) Dependence of the product $\Gamma g_{th} L$ on cavity length and etch depth, showing smaller values for deeper gratings.

Figure 6.14: Calculated threshold gain and $\Gamma g_{th} L$ for the top p-GaAs first-order DFB laser at a duty cycle of 0.5.

The corresponding optical efficiencies for different cavity lengths are displayed in Fig. 6.15(a). For a cavity of $L = 300$ μm and $h = 180$ nm, the optical efficiency reaches approximately 17%. This value is slightly lower than the 21% efficiency achieved with the silicon side-grating DFB laser but remains within a practical range for efficient operation.

The linewidth–power product ($\Delta\nu P_1$) was also calculated and is shown in Fig. 6.15(b). For devices with $L \geq 300$ μm and $h = 180$ nm, $\Delta\nu P_1$ remains below 20 MHz $\cdot$ mW.

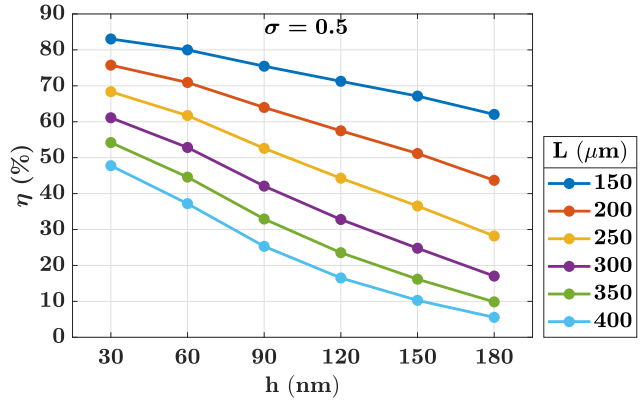

(a) Optical efficiency as a function of cavity length for various grating depths. For $L = 300$ μm and $h = 180$ nm, $\eta \approx 17\%$.

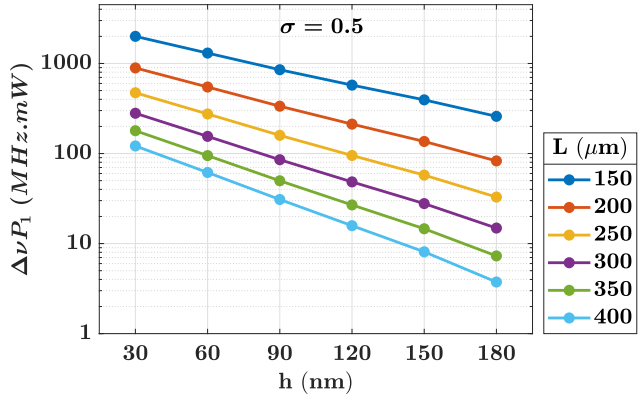

(b) Calculated product of linewidth and output power per facet ($\Delta\nu P_1$) versus cavity length and grating depth.

Figure 6.15: Optical efficiency and linewidth–power product for the top p-GaAs first-order DFB laser.

In summary, for a device length of 300 μm and an etch depth of 180 nm in the top p-GaAs grating, the first-order top p-GaAs DFB laser exhibits performance metrics that are closely comparable to those of the silicon side-grating DFB laser of the same length with a side-grating width of 75 nm. The threshold gain values of the two designs are nearly identical, while the optical efficiency of the top p-GaAs DFB laser is marginally lower.

6.2.4 Top p-GaAs second-order DFB laser

In recent years, optically pumped first-order grating nano-ridge DFB lasers fabricated by electron-beam lithography (EBL) were demonstrated in our group [9–11]. Although EBL can routinely define features below 10 nm owing to its direct-write, high-resolution capability [12], its inherently serial nature leads to extremely low throughput and high cost per wafer, limiting its practicality for large-scale fabrication [13]. In contrast, DUV lithography exposes entire fields in parallel using projection optics, enabling orders-of-magnitude higher throughput [14] and much lower cost per unit area in high-volume manufacturing [15]. The DUV ecosystem also benefits from mature resist chemistries, optimized etch processes, and well-developed optical proximity correction and metrology frameworks [16, 17], ensuring high uniformity and reproducibility.

For the present design, we use 193-nm DUV lithography under targeted specifications requiring a minimum lithographic pitch of 240 nm and a minimum feature size of 120 nm. The operation wavelength is again 1020 nm. For a first-order grating with a duty cycle of 0.5, the required grating pitch is 154 nm with a minimum feature size of 77 nm—both dimensions falling below the specification. In contrast, a second-order grating yields a grating pitch of 308 nm, which exceeds the 240 nm minimum pitch requirement and is therefore compatible with the DUV process. However, achieving maximum coupling strength at a duty cycle of 0.25 would still require a minimum feature size of 77 nm, below the targeted critical dimension limit. Increasing the duty cycle to 0.4 relaxes this constraint, resulting in a feature size of approximately 125 nm—within the specification—though at the expense of reduced coupling strength. Consequently, this section focuses on analyzing the performance characteristics of a second-order DFB laser designed with a 0.4 duty cycle as a compromise between fabrication feasibility and optical coupling efficiency.

As discussed in previous sections, conventional index-coupled first-order DFB lasers require a $\lambda/4$ phase-shift section or asymmetric facet reflectivities to break the degeneracy of the two stopband modes and enable single-mode operation. In contrast, second-order DFB lasers inherently provide both optical feedback and radiation coupling: second-order diffraction ensures longitudinal feedback for lasing, while first-order diffraction couples part of the guided mode to the surface, enabling vertical emission. This built-in radiation pathway introduces an intrinsic mode discrimination mechanism—destructive interference between radiating fields for one of the stopband modes, resulting in stable single-mode operation [4].

From a theoretical standpoint, second-order DFB lasers are governed by the same coupled-wave formalism as first-order structures (Eq. 6.1), but with an additional

term accounting for distributed radiation loss. This modifies the complex propagation parameter b (defined in Eq. 6.2) as

$$b = \delta - j\,\frac{\Gamma g_{\text{th}} - \alpha_i}{2} + j\kappa_1, \tag{6.19}$$

where κ_1 is the coupling coefficient associated with first-order diffraction in the vertical direction. The complex coupling coefficient is therefore

$$\kappa = \kappa_2 + j\kappa_1, \tag{6.20}$$

with κ_2 representing the second-order coupling coefficient responsible for longitudinal feedback. The second-order Bragg propagation constant is given by $\beta_{\text{Bragg}} = 2\pi/\Lambda$.

For a rectangular second-order grating, the coupling coefficients are expressed as [18]:

$$\kappa_2 = \frac{\Gamma_{xy}\,\Delta\varepsilon\,\sin(2\pi\sigma)}{2n_{\text{eff}}\lambda}, \tag{6.21}$$

$$\kappa_1 = \frac{\Gamma_{xy1}\,\Delta\varepsilon\,\kappa_2\,\tan(\pi\sigma)}{n_{\text{eff}}\lambda}, \tag{6.22}$$

where the transverse field overlap factors are defined as

$$\Gamma_{xy} = \frac{\displaystyle\int_G |U|^2\,dA}{\displaystyle\int |U|^2\,dA}, \qquad \Gamma_{xy1} = \frac{\left|\displaystyle\int_G U\,dA\right|^2}{\displaystyle\int_G |U|^2\,dA},$$

and $\sigma = a/\Lambda$ is the duty cycle. All other parameters are as defined in the preceding sections.

The threshold condition for second-order DFB operation is again determined from the eigenvalue equation in Eq. 6.15. According to [4], introducing a $\lambda/4$ phase-shift region at the center of a symmetric second-order grating leads to optimal mode discrimination at low duty cycles (around 0.1), which would correspond to a feature size of approximately 30.8 nm—below the specified lithography limit. Therefore, in this work, a symmetric second-order grating without a central phase-shift section is adopted to achieve adequate mode discrimination near a duty cycle of 0.4, consistent with fabrication constraints.

For calculation of the optical efficiency, we follow the formulation in [4]. For a symmetric cavity (Fig. 6.8) without a central phase shift and with equal output powers of P_1 and P_2 at the two facets, the efficiency at position z_1 is expressed as

$$\eta_1 = \frac{P_1}{P_{\text{stim}}} = \left(1 - \frac{\alpha_i}{\Gamma g_{\text{th}}}\right)\frac{1}{2 + (P_{\text{rad}}/P_1)}, \tag{6.23}$$

where P_{rad} is the radiation loss in the cavity: $P_{\text{rad}} = 2\kappa_1 \int_{z_1}^{z_2} |A+B|^2\, dz$ and $P_{\text{stim}} = \Gamma g_{\text{th}} \int_{z_1}^{z_2} (|A|^2 + |B|^2)\, dz$ is the stimulated emission power. The ratio P_{rad}/P_1 is evaluated as [4]:

$$\frac{P_{\text{rad}}}{P_1} = \frac{2\kappa_1}{|1-\chi^2|^2} \left\{ |\chi|^2 \frac{e^{\gamma' L} - 1}{2\gamma''} + \frac{1 - e^{-\gamma' L}}{2\gamma'} - 2\,\text{Re}\left[\chi \frac{e^{j\gamma'' L} - 1}{2j\gamma''} \right] \right\} \tag{6.24}$$

where $\gamma = \gamma' + j\gamma''$, and χ are defined in the previous sections.

After determining the optical efficiency considering both facets, the linewidth–power product of the lasing mode is subsequently evaluated using Eq. 6.12.

The top p-GaAs grating structure and doping profiles shown in Fig. 6.12(a) and (b) are now adopted, but with a grating pitch of 308 nm corresponding to a second-order grating and no central phase-shift region. The quasi-TE_{00} mode is considered in all calculations. Using the mode profiles, effective indices, and permittivity data from LUMERICAL MODE, the real and imaginary components of the coupling coefficients for different etch depths (h in Fig. 6.12(b)) were calculated using Eqs. (6.21) and (6.22). The results are plotted in Fig. 6.16(a) and (b), showing similar dependencies on h as observed for the first-order case, albeit with smaller overall coupling strengths. For this analysis, a duty cycle of 0.4 is maintained.

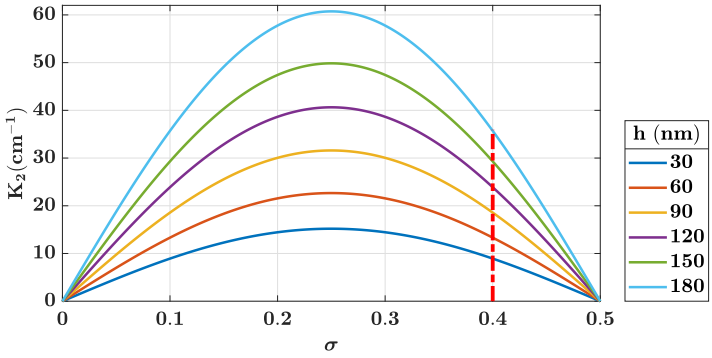

(a) Real part of the coupling coefficient κ_2 versus the duty cycle for different etch depths (h).

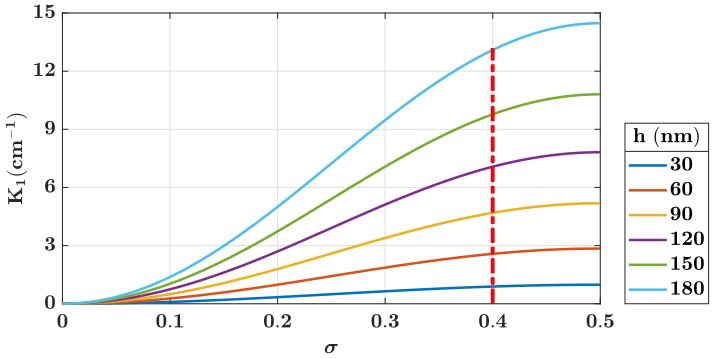

(b) Imaginary part of the coupling coefficient κ_1 versus the duty cycle for different etch depths.

Figure 6.16: Calculated coupling coefficients for the second-order top p-GaAs DFB laser as a function of the duty cycle for different etch depths (h).

To examine the effect of first-order diffraction (κ_1) on the reflectivity spectrum, the power reflectivity was calculated using Eq. 6.16 for cases with $\kappa_1 = 0$ and with κ_1 values obtained for $h = 180$ nm, assuming no internal loss or gain. Figures 6.17(a) and (b) show the resulting power reflectivity spectra for cavity lengths ranging from 80 μm to 800 μm. The inclusion of κ_1 suppresses one branch of the reflectivity spectrum (on the negative detuning side) due to constructive interference between the radiations from the forward- and backward-propagating waves. This effect introduces an inherent mode discrimination mechanism that favors the mode on the opposite side of the stopband, thereby enabling single-mode lasing [18].

Apart from radiation losses, the cavity also experiences absorption from free carriers in the doped regions, absorption in the metal contact, and scattering losses. The first two contributions are normalized to the grating duty cycle, after which a fixed scattering loss of 8.5 cm^{-1} is added to obtain the total internal loss. The resulting dependence of the internal loss on the etch depth is shown in Fig. 6.17(c).

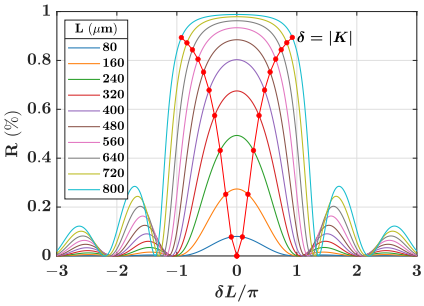

(a) Power reflectivity with $\kappa_1 = 0$.

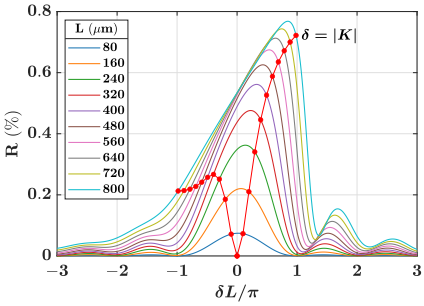

(b) Power reflectivity including κ_1 (vertical radiation).

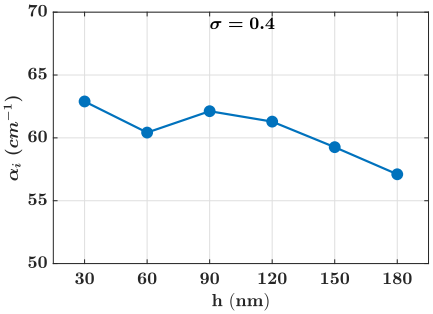

(c) Calculated internal loss versus the etch depth h at a duty cycle of 0.4.

Figure 6.17: Simulated optical characteristics of the top p-GaAs second-order DFB laser: (a) Power reflectivity spectrum without vertical radiation, (b) corresponding spectrum including the effect of vertical radiation, and (c) variation of the total internal loss with etch depth at a duty cycle of 0.4.

The threshold gain was then computed by solving the eigenvalue equation (Eq. 6.15) without a phase-shift region for the two stopband modes. Results for the lasing mode are shown in Fig. 6.18(a) for a duty cycle of 0.4 and cavity lengths between 400 μm and 800 μm. The corresponding $\Gamma g_{\text{th}} L$ values are plotted in Fig. 6.18(b). The general trend mirrors that of the first-order DFB laser—threshold gain decreases with etch depth due to stronger coupling. However, because second-order gratings exhibit weaker coupling overall, longer cavities are required to achieve comparable threshold gains. For a 600 μm device with $h = 180$ nm, $\Gamma g_{\text{th}} = 89$ cm^{-1} and $\Gamma g_{\text{th}} L = 5.3$, more than twice the value obtained for the $\lambda/4$-shifted first-order DFB lasers discussed in the preceding two sections ($\Gamma g_{\text{th}} L \approx 2.4$). The threshold gain difference between the two competing modes located on opposite sides of the stopband is presented in Fig. 6.18(c). Based on the single-mode criterion $\Gamma|g_{\text{th1}} - g_{\text{th2}}| \geq 0.05$ [7], single-mode operation is expected for all device lengths in the range 400–800 μm when $h \geq 60$ nm.

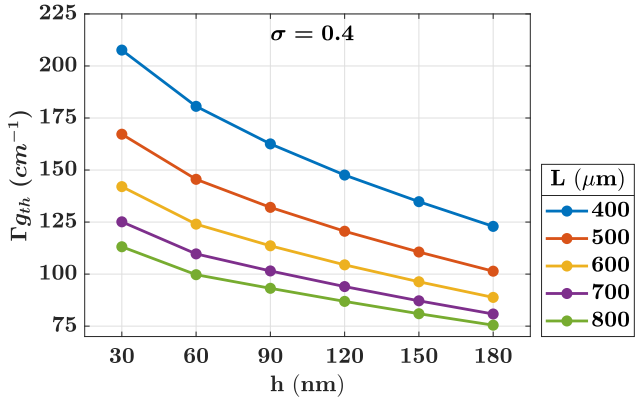

(a) Threshold gain Γg_{th} versus etch depth for different cavity lengths.

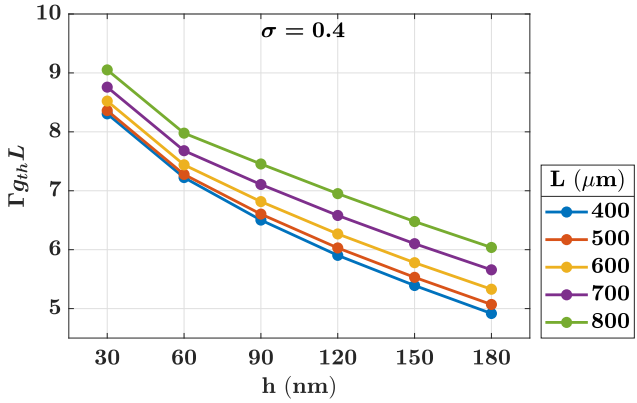

(b) $\Gamma g_{th} L$ versus etch depth for different cavity lengths.

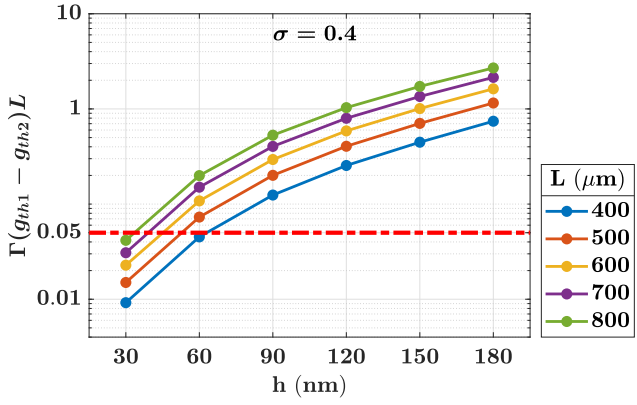

(c) Threshold gain difference $\Gamma|g_{th1} - g_{th2}|$ versus etch depth for various cavity lengths.

Figure 6.18: Calculated threshold characteristics of the top p-GaAs second-order DFB laser as a function of the etch depth h and cavity length L.

Assuming a symmetric cavity with equal facet powers ($P_1 = P_2$), the optical efficiencies were calculated using Eq. (6.23), doubled to include both facets, and are plotted in Fig. 6.19(a). For a device with $L = 600$ μm and $h = 180$ nm, the optical efficiency is approximately 19%. The linewidth–power product ($\Delta\nu P_1$), calculated from Eq. 6.12, is shown in Fig. 6.19(b). For $L \geq 600$ μm and $h = 180$ nm, $\Delta\nu P_1$ remains below 22 MHz·mW.

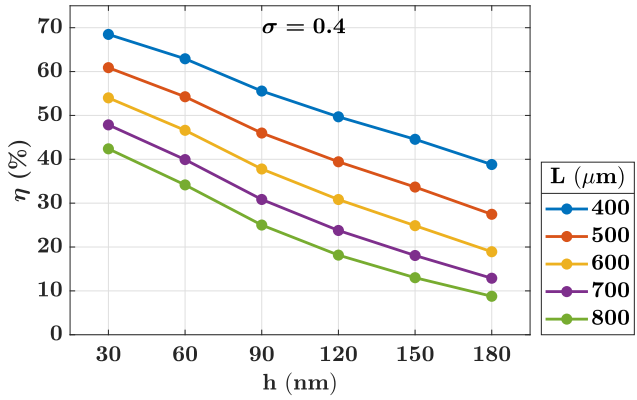

(a) Optical efficiency η versus etch depth for various cavity lengths.

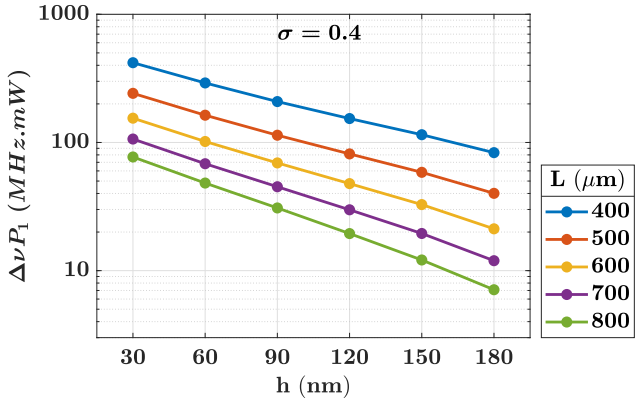

(b) Linewidth–power product $\Delta\nu P_1$ versus etch depth for various cavity lengths.

Figure 6.19: Performance characteristics of the top p-GaAs second-order DFB laser: (a) optical efficiency and (b) linewidth–power product as a function of etch depth h and cavity length L.

6.2.5 Summary of DFB laser design approaches

As discussed at the beginning of this chapter, one of the primary limitations of nano-ridge lasers operating via the mode-beating mechanism is the relatively large cavity

lengths (1–2 mm) typically required for lasing. Shorter devices generally experience excessive mirror losses, preventing efficient operation. To enable a meaningful comparison with the newly proposed device architectures, we revisit the results for the 80 nm trench-width nano-ridge laser operating under the mode-beating regime, as analyzed in Chapter 3, for various mode-pair combinations.

Figure 6.20(a) presents the calculated threshold gain–length product ($\Gamma g_{\text{th}} L$) as a function of the cavity length within a 5 μm range centered around 1.5 mm. The values fall within the range of 5–8.7. The optical efficiency, previously determined in Chapter 3 and shown in Fig. 6.20(b), is approximately 11% for a cavity length of 1.5 mm, evaluated as a function of the GaAs box height.

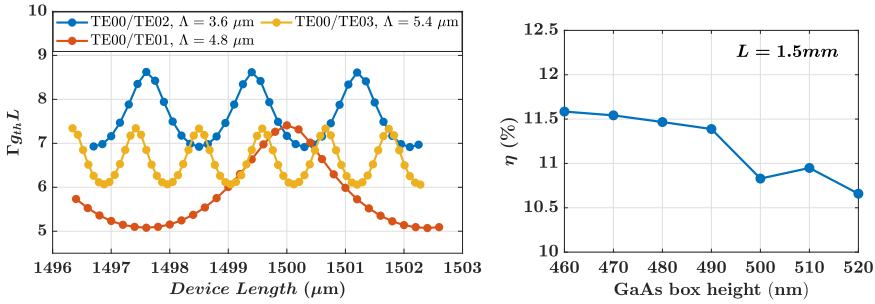

(a) Calculated threshold gain–length product ($\Gamma g_{th} L$) versus cavity length for the mode-beating nano-ridge laser.

(b) Optical efficiency as a function of GaAs box height for a 1.5 mm-long mode-beating laser.

Figure 6.20: Performance of a nano-ridge laser operating with the mode-beating approach.

Figures 6.21(a)–(c) summarize the comparison among the four DFB laser design approaches discussed in the preceding sections in terms of the threshold gain–length product ($\Gamma g_{\text{th}} L$), optical efficiency (η), and linewidth–power product ($\Delta\nu P_1$), respectively. The red-circled dots indicate the chosen operating duty cycles for each design configuration.

Compared to the mode-beating approach, all four DFB-based designs enable lasing in significantly shorter cavities (300–800 μm) while offering improved optical efficiency. Among the four approaches, the partly loss-coupled Au/Ti-contact DFB laser exhibits the highest $\Gamma g_{\text{th}} L$ values and therefore requires the longest cavity (800 μm) to achieve lasing, followed by the second-order top p-GaAs DFB laser with a 600 μm cavity. In contrast, both the Si side-grating and top p-GaAs first-order DFB lasers demonstrate superior optical performance, supporting lasing in much shorter devices (300 μm) with $\Gamma g_{\text{th}} L \approx 2.4$. For context, reported values for standard $\lambda/4$-shifted DFB lasers with 300 μm cavities span $\Gamma g_{\text{th}} L \approx 0.9$–$5.5$ as the coupling strength (κL) is reduced from 4 to 0.5 [19], placing the performance of

the present designs well within the range of conventional DFB lasers.

The optical efficiencies and linewidths across the four DFB laser designs are influenced by the coupling strength within the cavity and the internal optical losses. Cavities with weaker coupling coefficients generally exhibit higher optical efficiencies but this occurs at the cost of a broader linewidth and a higher threshold gain. Conversely, stronger coupling improves mode confinement and feedback, thereby enhancing spectral purity and reducing the threshold gain; however, it concurrently diminishes efficiency by limiting the fraction of optical power coupled out of the cavity. Hence, these parameters must be evaluated jointly to establish an optimal trade-off between efficiency, linewidth, and threshold performance. In practical device design, it is therefore common to define a target efficiency range that delivers adequate output power while maintaining robust single-mode operation and acceptable spectral characteristics.

For the device lengths and duty cycles considered here, the partly loss-coupled DFB laser achieves an optical efficiency of approximately 47%, while the other three DFB architectures exhibit efficiencies around 20%. The linewidth–power product for the partly loss-coupled DFB laser is about 45 MHz·mW, compared to 15–22 MHz·mW for the remaining approaches. For reference, Agrawal reports linewidths in the range of 1–10 MHz for DFB lasers operating at an output power of 10 mW [20]. Representative datasheets for commercial DFB lasers also specify linewidths on the order of a few megahertz—for example, around 2 MHz for a C-band device [21] and about 3 MHz for an O-band device [22]— providing useful benchmarks for evaluating the linewidth performance of the proposed architectures.

In summary, both the side-Si first-order DFB laser and the top p-GaAs first-order DFB laser exhibit favorable optical performance, enabling compact devices (around 300 μm) with balanced efficiencies and linewidth characteristics. The second-order p-GaAs DFB laser, while slightly inferior in optical performance, offers a significant fabrication advantage: its grating dimensions are compatible with 193 nm DUV lithography, enabling high-volume, low-cost manufacturing. This makes it an attractive alternative for scalable integration on silicon photonic platforms.

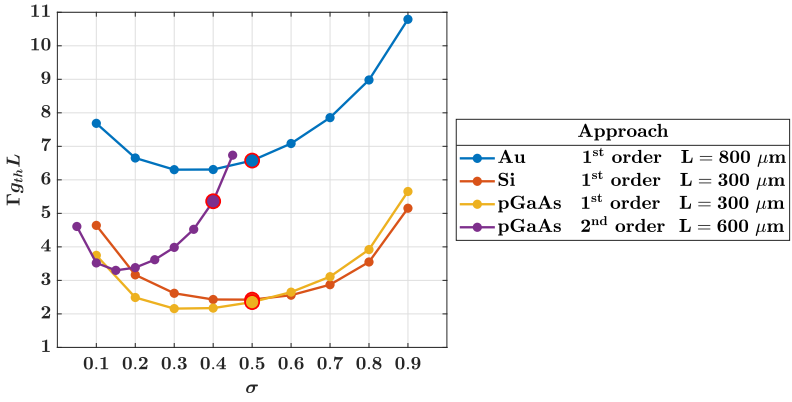

(a) Comparison of threshold gain–length product ($\Gamma g_{th} L$) for the four DFB laser configurations.

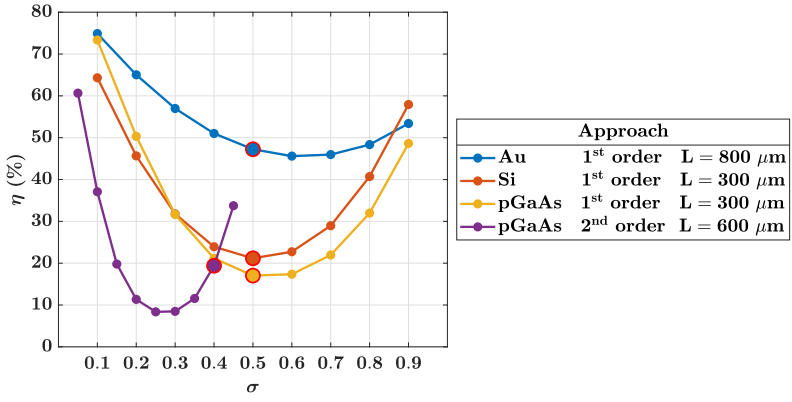

(b) Optical efficiencies (η) of the four DFB laser designs at their optimized duty cycles.

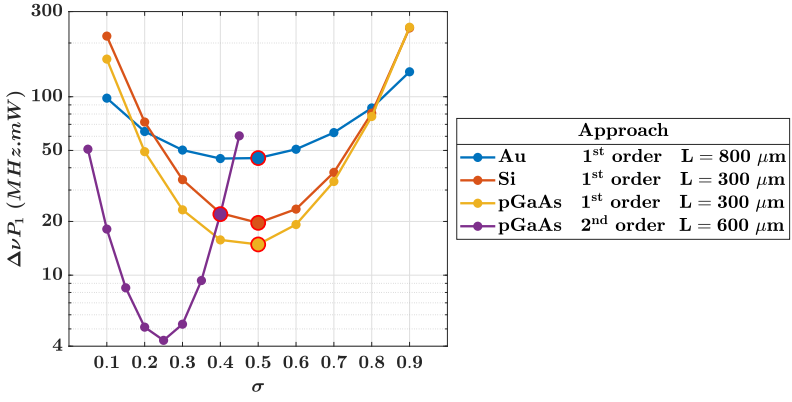

(c) Linewidth–power products ($\Delta\nu P_1$) for the four DFB configurations.

Figure 6.21: Comparison of performance metrics for the four DFB laser approaches: (a) threshold gain–length product, (b) optical efficiency, and (c) linewidth–power product. Red-circled points indicate the chosen operating duty cycles for each design.

6.3 IV and injection efficiency comparisons of design approaches

Having established the optical performance of the different laser design approaches, it is equally important to evaluate their electrical injection characteristics. In particular, this section compares the voltage required to reach the threshold current, the injection efficiency, and the average carrier density in the quantum wells near the threshold current density.

Electrical simulations were performed using the commercial SENTAURUS TCAD simulator from Synopsys [23]. The models employed include the Poisson and drift–diffusion equations with Fermi–Dirac carrier statistics, supplemented by the density-gradient quantum correction model to account for carrier confinement effects. For structures incorporating a continuous p-type contact on the p-GaAs layer grown atop the InGaP passivation, additional tunneling and thermionic emission models were implemented at the p–p isotype heterojunctions [24] to accurately capture carrier transport across these interfaces.

The first comparison focuses on the voltage required to achieve the threshold current, assumed to be approximately 10 mA for a 1 mm-long device. When tungsten or gold contacts are formed on p-GaAs, Schottky barriers naturally arise at the metal–semiconductor interface. Accurate modeling of such Schottky contacts requires detailed knowledge of the metal work function, adhesion-layer properties, and the doping concentration of the contacting semiconductor region. However, as an initial step, Ohmic contacts were assumed in all simulations to enable a consistent comparison of the I–V characteristics across the different design approaches. Future work should incorporate refined simulations that explicitly model Schottky behavior using experimentally determined barrier heights from transfer length method (TLM) measurements [25]. These studies should consider the specific contact stack—including the metal, adhesion layer, and doping level of the p-GaAs region—to more accurately reproduce the experimental device behavior.

For the subsequent comparisons involving injection efficiency and the average carrier density within the quantum wells, the current density in the GaAs box (around 1500 A/cm^2, corresponding to the approximate threshold value) is used as the reference parameter.

Two representative nano-ridge laser configurations were analyzed:

- **NR1:** A periodic p-contact configuration (pitch = 4.8 μm), corresponding to the mode-beating operation scheme.
- **NR2:** A continuous metal contact design featuring a p-GaAs/p-InGaP/p-

GaAs heterostructure stack.

For NR2, two doping scenarios were investigated in the p-InGaP passivation layer: an unintentionally doped (UID) case with $N_A = 1 \times 10^{16}$ cm^{-3} and a moderately doped case with $N_A = 1 \times 10^{18}$ cm^{-3}. The schematics for the simulated structures and the corresponding doping profiles are presented in Fig. 6.22(a) and (b), respectively. The epitaxial stack comprises Si-doped n-GaAs, C-doped p-GaAs, Zn-doped p-InGaP, and P-doped n-Si layers. The recombination parameters adopted in the simulations are summarized in Table 6.3.

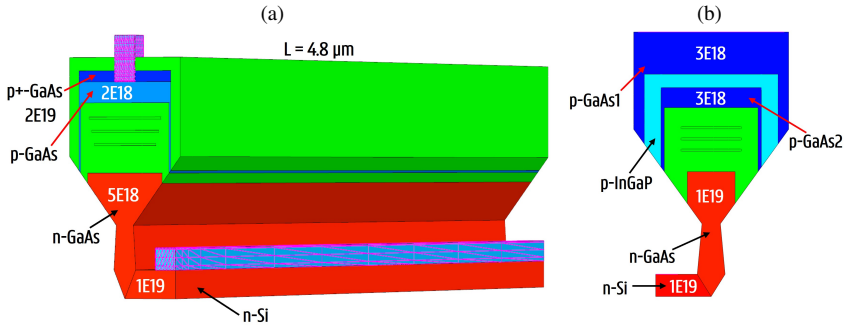

Figure 6.22: Simulated nano-ridge geometries and doping configurations (in cm^{-3}) used in the TCAD analysis. (a) 3D schematic of the NR1 device used for the simulations. (b) Doping profile of the NR2 structure incorporating the p-GaAs/p-InGaP/p-GaAs heterostructure.

Table 6.3: Recombination parameters used for the different material systems.

Material	**SRH lifetime** (ns)	**Radiative** (10^{-10} cm^3/s)	**Auger** (10^{-29} cm^6/s)	**Surface** (10^4 cm/s)
GaAs	1	4	0.4	–
InGaAs	10	3	1	–
GaAs/Oxide	–	–	–	100
InGaP/Oxide	–	–	–	1

IV characteristics

Figure 6.23(a) compares the simulated current–voltage (IV) characteristics for the three configurations (NR1, NR2–UID, and NR2–doped) for a device length of 1 mm. NR1 exhibits the lowest turn-on voltage, attributed to the absence of the p–p–p heterointerfaces present in NR2. In NR2, the middle InGaP layer—with its larger

bandgap ($E_g = 1.8$ eV)—acts as a potential barrier between the lower-bandgap GaAs layers ($E_g = 1.42$ eV), thereby impeding carrier transport. At a drive current of 10 mA (approximately at threshold), the UID InGaP case requires an additional $\sim$1.1 V compared to NR1. When the InGaP layer is doped to 1×10^{18} cm^{-3}, the injection improves significantly, with the voltage penalty reduced to only $\sim$0.1 V near threshold.

Injection efficiency

The injection efficiency η_{inj} quantifies the fraction of the total injected carriers that recombine radiatively or non-radiatively in the quantum wells and is given by:

$$\eta_{\text{inj}} = \frac{R_{\text{QW-total}}}{I/q}, \tag{6.25}$$

where $R_{\text{QW-total}}$ denotes the total recombination rate in the quantum wells and is expressed as

$$R_{\text{QW-total}} = (R_{\text{rad}} + R_{\text{SRH}} + R_{\text{Auger}})V, \tag{6.26}$$

with V being the total QW volume. Here, R_{rad}, R_{SRH}, and R_{Auger} correspond to the radiative, Shockley–Read–Hall (SRH), and Auger recombination rates, respectively, each defined per unit volume and per unit time.

The extracted injection efficiencies as a function of current density are plotted in Fig. 6.23(b). At a current density of approximately 1500 A/cm^2 (near threshold), η_{inj} drops from $\sim$72% in NR1 to $\sim$31% in the NR2–UID case. Doping the InGaP layer to 1×10^{18} cm^{-3} restores the injection efficiency to a value slightly better than that of NR1 ($\sim$76%), confirming the critical role of p-type doping in mitigating the barrier resistance at the heterointerface.

Carrier density in the quantum wells

Figure 6.23(c) compares the average carrier density in the quantum wells around threshold current density for the different configurations. Transitioning from NR1 to NR2–UID reduces the carrier density by approximately 30%. Upon increasing the InGaP doping to 1×10^{18} cm^{-3}, the carrier density profile becomes slightly better than that of NR1. However, this improvement comes at the cost of a voltage penalty, particularly under high-injection conditions.

Summary

These results indicate that the continuous-contact configuration with a moderately doped ($N_A = 1 \times 10^{18}$ cm^{-3}) InGaP layer achieves comparable electrical injection performance to the periodic-contact NR1 design, albeit with a slightly higher

operating voltage. When combined with the superior optical performance demonstrated in the previous sections, this configuration provides a strong foundation for next-generation electrically pumped nano-ridge DFB lasers.

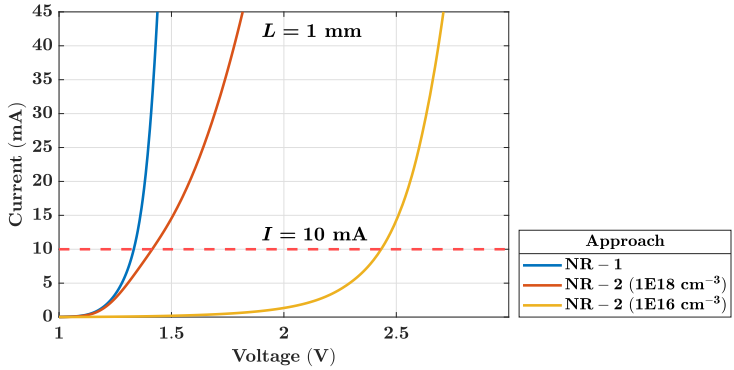

(a) Simulated IV characteristics of NR1, NR2 with unintentionally doped InGaP (1×10^{16} cm^{-3}), and NR2 with doped InGaP (1×10^{18} cm^{-3}) for a 1 mm-long device.

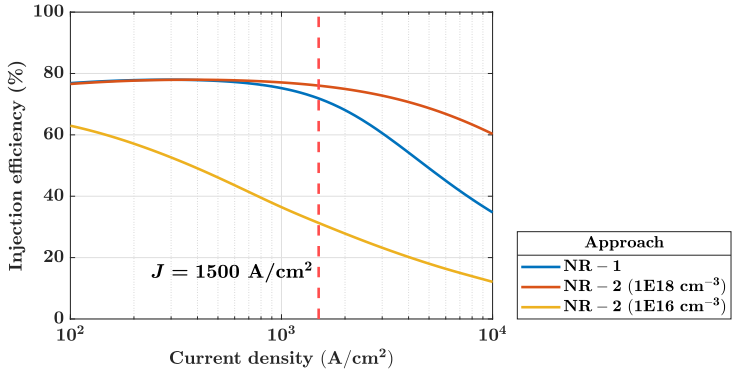

(b) Injection efficiency (η_{inj}) as a function of current density. Increased InGaP doping improves carrier injection, resulting in an efficiency slightly higher than that of NR1.

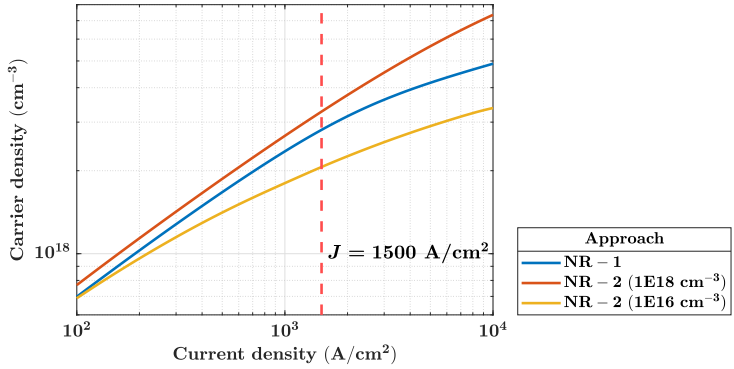

(c) Average carrier density in the quantum wells as a function of current density. The NR2–UID device exhibits ∼30% lower carrier density than NR1 near the threshold current density, which is recovered upon doping the InGaP layer.

Figure 6.23: Electrical injection comparison of NR1 and NR2 configurations showing (a) IV characteristics, (b) injection efficiency, and (c) average QW carrier density as functions of current density.

6.4 Conclusion

The performance of the currently implemented nano-ridge lasers operating via the mode-beating mechanism is constrained by several factors. Chief among these are the strong sensitivity to fabrication variations, broad linewidths and low side-mode suppression ratios, the need for long cavities (1–2 mm) to sustain lasing, and non-uniform current injection leading to reliability concerns. Additionally, extended carrier capture times were shown to limit the achievable modulation bandwidth. These findings collectively highlight the necessity of rethinking both the optical cavity architecture and the electrical injection scheme to enable more efficient, compact, and reliable nano-ridge laser designs for silicon photonic integration.

To overcome these limitations, several DFB laser configurations were proposed and systematically analyzed, including DFBs with partly loss-coupled metal-contact gratings, and index-guided DFBs with silicon side-gratings, and top p-GaAs gratings of both first and second-order. All DFB designs demonstrated the potential for substantially reduced cavity lengths (300–800 µm) compared to the mode-beating devices, while maintaining competitive optical efficiencies and linewidth characteristics. Among these, the first-order side-Si and top p-GaAs DFB lasers offered the most favorable balance between threshold gain, efficiency, and spectral purity, enabling compact, single-mode operation with $\Gamma g_{\text{th}} L \approx 2.4$. Although the second-order p-GaAs DFB laser exhibited slightly inferior optical performance, it provides a key technological advantage—its grating dimensions are fully compatible with a targeted specification for a 193 nm DUV lithography—thereby offering a scalable and cost-effective route for high-volume fabrication. These results collectively demonstrate the feasibility of achieving high-performance nano-ridge DFB lasers with practical manufacturability.

Finally, complementary electrical simulations using SENTAURUS TCAD revealed that the continuous-contact design incorporating a moderately doped ($N_A = 1 \times 10^{18}$ cm^{-3}) p-InGaP passivation layer achieves electrical injection performance comparable to that of the periodic-contact NR1 structure, with only a modest increase in operating voltage near threshold. The injection efficiency and carrier density in the quantum wells were both found to be well preserved, confirming that the continuous-contact architecture does not compromise carrier delivery to the active region.

References

[1] P.-Y. Hsieh et al., Degradation mechanisms of monolithic GaAs-on-Si nano-ridge quantum well lasers, *Journal of Lightwave Technology*, vol. 43, no. 12, pp. 5811–5819, Jun. 2025.

[2] K. David, J. Buus, and R. Baets, Basic analysis of AR-coated, partly gain-coupled DFB lasers: The standing wave effect, *IEEE Journal of Quantum Electronics*, vol. 28, no. 2, pp. 427–434, 1992.

[3] R. Baets, K. David, and G. Morthier, On the distinctive features of gain coupled DFB lasers and DFB lasers with second-order grating, *IEEE Journal of Quantum Electronics*, vol. 29, no. 6, pp. 1792–1798, Jun. 1993.

[4] T. Makino and J. Glinski, Effects of radiation loss on the performance of second-order DFB semiconductor lasers, *IEEE Journal of Quantum Electronics*, vol. 24, no. 1, pp. 73–82, Jan. 1988.

[5] E. Palik, *Handbook of Optical Constants of Solids* (Academic Press handbook series). Academic Press, 1998.

[6] K. David, J. Buus, G. Morthier, and R. Baets, Coupling coefficients in gain-coupled DFB lasers: Inherent compromise between coupling strength and loss, *IEEE Photonics Technology Letters*, vol. 3, no. 5, pp. 439–441, May 1991.

[7] K. David, G. Morthier, P. Vankwikelberge, R. Baets, T. Wolf, and B. Borchert, Gain-coupled DFB lasers versus index-coupled and phase shifted DFB lasers: A comparison based on spatial hole burning corrected yield, *IEEE Journal of Quantum Electronics*, vol. 27, no. 6, pp. 1714–1723, Jun. 1991.

[8] Y. De Koninck et al., GaAs nano-ridge laser diodes fully fabricated in a 300-mm CMOS pilot line, *Nature*, vol. 637, no. 8044, pp. 63–69, 2025.

[9] Y. Shi et al., Optical pumped InGaAs/GaAs nano-ridge laser epitaxially grown on a standard 300-mm Si wafer, *Optica*, vol. 4, no. 12, pp. 1468–1473, Dec. 2017.

[10] D. Colucci et al., Unique design approach to realize an O-band laser monolithically integrated on 300 mm Si substrate by nano-ridge engineering, *Opt. Express*, vol. 30, no. 8, pp. 13 510–13 521, Apr. 2022.

[11] Z. Ouyang et al., Ultra-compact InGaAs/GaAs nano-ridge laser monolithically grown on 300 mm silicon substrate, *Optics Letters*, vol. 50, no. 7, p. 2358, Mar. 2025.

[12] Y. Chen, Nanofabrication by electron beam lithography and its applications: A review, *Microelectronic Engineering*, vol. 135, pp. 57–72, Mar. 2015.

[13] C. Vieu et al., Electron beam lithography: Resolution limits and applications, *Applied Surface Science*, vol. 164, no. 1–4, pp. 111–117, Sep. 2000.

[14] S. Okazaki, High resolution optical lithography or high throughput electron beam lithography: The technical struggle from the micro to the nano-fabrication evolution, *Microelectronic Engineering*, vol. 133, pp. 23–35, Feb. 2015.

[15] K. Stokes, K. Clark, D. Odetade, M. Hardy, and P. Goldberg Oppenheimer, Advances in lithographic techniques for precision nanostructure fabrication in biomedical applications, *Discover Nano*, vol. 18, no. 1, Dec. 2023.

[16] P. Basu, J. Verma, V. Abhinav, R. K. Ratnesh, Y. K. Singla, and V. Kumar, Advancements in lithography techniques and emerging molecular strategies for nanostructure fabrication, *International Journal of Molecular Sciences*, vol. 26, no. 7, p. 3027, Mar. 2025.

[17] Y. Hou and Q. Wu, "Optical proximity correction, methodology and limitations", *2021 China Semiconductor Technology International Conference (CSTIC)*, IEEE, Mar. 2021, pp. 1–5.

[18] R. Kazarinov and C. Henry, Second-order distributed feedback lasers with mode selection provided by first-order radiation losses, *IEEE Journal of Quantum Electronics*, vol. 21, no. 2, pp. 144–150, Feb. 1985.

[19] L. A. Coldren, S. W. Corzine, and M. L. Mashanovitch, *Diode Lasers and Photonic Integrated Circuits*. John Wiley & Sons, 2012, ch. 3, p. 144.

[20] G. P. Agrawal, *Fiber-Optic Communication Systems*, 3rd. New York: John Wiley & Sons, 2002, pp. 116–117.

[21] Optilab, LLC, *DFB-1550D-PM Datasheet (rev. 3)*, https://cdn.shopify.com/s/files/1/0597/2534/9053/files/DFB-1550D-PM_datasheet_REV_3.pdf?v=1718147136, 2023.

[22] LD-PD PTE. LTD., *O-band high power distributed-feedback laser diode chips*, https://www.ld-pd.com/?a=cp3&id=531, 2025.

[23] *Synopsys TCAD*, https://www.synopsys.com/manufacturing/tcad.html.

[24] K. Horio and H. Yanai, Numerical modeling of heterojunctions including the thermionic emission mechanism at the heterojunction interface, *IEEE Transactions on Electron Devices*, vol. 37, no. 4, pp. 1093–1098, Apr. 1990.

[25] A. Firrincieli, K. Martens, E. Simoen, C. Claeys, and J. Kittl, Study of the impact of doping concentration and schottky barrier height on ohmic contacts to n-type germanium, *Microelectronic Engineering*, vol. 106, pp. 129–131, Jun. 2013.

7

Conclusion and outlook

Contents

7.1 Conclusions

This work has provided a comprehensive investigation into the physics, design, characterization, and performance optimization of monolithically integrated InGaAs/GaAs nano-ridge lasers on silicon. The research spanned from fundamental loss characterization and modeling to static and dynamic experimental analyses, culminating in the proposal and evaluation of new device architectures that address the limitations of the current mode-beating designs.

A comprehensive study of optical loss mechanisms in GaAs NRWs was carried out, encompassing both propagation and carrier-induced absorption losses. Measurements on undoped NRWs with trench widths ranging from 150 nm to 300 nm revealed propagation losses in the region of 8.5 cm^{-1}, accounting for a substantial portion of the total internal loss in electrically pumped devices. The losses were found to increase with trench width, becoming prohibitive at 500 nm, for which 3D

FDTD simulations indicated strong optical leakage into the silicon substrate. For the narrower trenches, scattering was identified as the dominant loss mechanism. The gradual rise in the scattering loss between 150 nm and 300 nm trench widths was attributed to reduced defect confinement in lower-aspect-ratio structures, allowing dislocations to propagate deeper into the ridge. Carrier-induced absorption was also quantified for key materials—p-GaAs, n-GaAs, p-InGaP, and n-Si—revealing a strong dependence on doping type and concentration. While the FPI technique remains effective for moderately doped structures, heavily p-doped GaAs exhibited excessive round-trip loss, which limits fringe contrast and hinders reliable extraction of propagation loss.

Following the detailed analysis of optical losses, a semi-analytical model was developed for electrically injected InGaAs/GaAs nano-ridge lasers monolithically integrated on silicon, providing a rigorous framework for understanding and optimizing their optical behavior. Based on the coupled-mode theory, the model quantitatively described the interaction between optical modes in the presence of periodic tungsten contacts and was validated against 3D FDTD simulations, confirming its accuracy in reproducing mode dynamics. A key outcome was the identification of low-loss operating conditions arising from the interference between the TE_{00} and higher-order modes, which generate low-intensity regions beneath the metal contacts—minimizing absorption and allowing lasing operation. The model's round-trip formulation further enabled extraction of key performance parameters such as the threshold gain, lasing wavelength, and differential quantum efficiency, while the inclusion of real device geometries allowed quantitative comparison with experimental data. The close agreement between model predictions and experimental results validates the underlying physical assumptions and confirms the model's reliability in capturing the device physics. Moreover, the model proves to be a versatile and computationally efficient framework that offers both predictive capability and clear physical insight for the design and optimization of monolithic nano-ridge lasers and other guided-wave photonic systems that work with the mode-beating approach.

The static characterization of the fabricated nano-ridge lasers combined LIV, spectral, linewidth, and far-field analyses to establish a detailed understanding of their optical behavior. Simulations revealed that the modal effective indices of the nano-ridge waveguides are highly sensitive to dimensional fluctuations introduced during fabrication, particularly variations in the GaAs box height. Higher-order modes were found to be most susceptible to these perturbations, thereby driving wavelength variability through detuning shifts. These findings highlight the need for precise dimensional control during fabrication and emphasize the advantage of utilizing lower-order mode pairs to improve wavelength stability. Linewidth measurements yielded values between 37 MHz and 216 MHz—intermediate be-

tween those typically observed in commercial DFB lasers and VCSELs. Far-field measurements further revealed pronounced anisotropy in beam divergence, a direct consequence of the asymmetric ridge geometry where the ridge height significantly exceeds its width.

Building on these findings, the dynamic behavior of the InGaAs/GaAs nano-ridge lasers was examined through small-signal modulation, RIN, and S_{11} analyses. From the S_{21} measurements, carrier capture times of 100–125 ps were extracted—longer than in conventional quantum-well lasers—owing to the sparse metal-plug distribution that increases carrier transport time before capture. RIN measurements yielded D-factors of approximately 1 GHz/mA$^{1/2}$ and K-factors of 0.5–0.8 ns, corresponding to differential gains of $(4.3\text{–}7) \times 10^{-16}$ cm^2 and gain compression factors of $(1.8\text{–}4.4) \times 10^{-17}$ cm^3. S_{11} measurements enabled the extraction of recombination coefficients, revealing strong geometry dependence. Wider trenches (100 nm) exhibited higher A-coefficients, likely due to dislocation trapping near the ridge opening or reduced passivation quality. These devices also showed increased radiative (B) and decreased Auger (C) coefficients, indicating mitigated local heating in the larger ridge volumes. Defect-related recombination was found to contribute less than 5% of the threshold current in 60 nm and 80 nm devices, and less than 10% in 100 nm devices, confirming the efficacy of aspect-ratio trapping and nano-ridge engineering in achieving high-quality III-V material on silicon. The extracted B-coefficients showed good agreement with literature, while the higher C-values were consistent with models that account for carrier transport effects typically neglected in bulk rate-equation approaches. Carrier escape times of 110–130 ps and a near-unity τ_s/τ_e ratio were found to limit the modulation bandwidth, suggesting that adopting a continuous-contact design could significantly reduce τ_s and enhance high-speed performance.

To address the intrinsic limitations of the existing mode-beating nano-ridge lasers—including their sensitivity to fabrication variations, broad linewidths, long cavity requirements, non-uniform current injection, and limited modulation speed—several DFB architectures were proposed and systematically evaluated. These included partly loss-coupled DFBs, as well as DFBs with side-silicon and top p-GaAs gratings of both first and second order. All configurations demonstrated the feasibility of single-mode lasing in substantially shorter cavities (300–800 μm) while maintaining acceptable optical efficiency and narrow linewidths. Among them, the first-order side-Si and top p-GaAs DFB structures provided the most favorable trade-off between threshold gain, efficiency, and spectral purity, whereas the second-order p-GaAs DFB design offered a practical manufacturing advantage through full compatibility with 193-nm DUV lithography, enabling scalable and cost-effective integration. Complementary TCAD simulations confirmed that continuous-contact architectures incorporating moderately doped InGaP layers can sustain efficient

carrier injection with only a minor increase in operating voltage, validating the practicality of these advanced designs for future high-performance monolithic laser integration.

Overall, the results presented in this work establish a clear pathway toward high-performance, electrically pumped nano-ridge DFB lasers monolithically integrated on silicon. By combining a deep understanding of optical losses, carrier dynamics, cavity design and carrier injection, the dissertation provides both the theoretical framework and the experimental validation necessary to guide the development of the next generation of compact, efficient, and scalable III–V-on-Si laser sources for silicon photonics.

7.2 Outlook and perspectives

The measured scattering losses of approximately 8.5 cm^{-1} for undoped nano-ridge waveguides represent a significant contribution—about 30%—to the total internal optical loss of the electrically pumped nano-ridge lasers discussed in Chapter 2. These losses primarily originate from waveguide waviness introduced during fabrication, as well as potential surface and sidewall roughness. In wider trench-width nano-ridges, additional scattering may arise from unconfined dislocations that extend into the overgrown ridge volume. Further optimization of the fabrication process, together with structural design adjustments, will therefore be essential to suppress these scattering mechanisms and enhance waveguide performance.

Building on the DFB laser design strategies developed in this work, the next step is to fabricate and experimentally characterize the proposed architectures to validate their simulated optical performance. This should be followed by a comprehensive static and dynamic characterization campaign, enabling extraction of key laser parameters and direct comparison across the different designs to identify the most promising path toward further optimization. Particular attention should be given to assessing the feasibility of implementing these architectures using DUV lithography, which offers a cost-effective and scalable route for high-volume manufacturing.

In collaboration with the imec epitaxy team, an alternative device configuration with continuous-contact has been envisaged, featuring a faceted, hat-shaped top p-GaAs layer as shown in Fig. 7.1. In this structure, the InGaP passivation layer between the p-GaAs layers is thinned to promote enhanced tunneling current toward the quantum wells, while the p-GaAs fin geometry moves the contact further away from the optical mode. This design is expected to reduce optical absorption in the doped p-GaAs region compared to the approach presented in Chapter 6. The electrical performance of this structure should be benchmarked against that of the previous

design in terms of threshold voltage, injection efficiency, and carrier density at a given current density. Future TCAD simulations should incorporate experimentally extracted Schottky barrier heights to more accurately model carrier transport across metal–semiconductor interfaces.

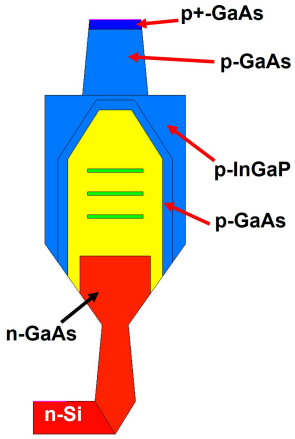

Figure 7.1: Schematic of the proposed continuous-contact configuration featuring a faceted, hat-shaped p-GaAs region. The design incorporates a thinned InGaP passivation layer between the p-GaAs regions to enhance tunneling current toward the quantum wells, while the raised p-GaAs geometry shifts the metal contact away from the optical mode. This configuration is expected to reduce optical absorption in the doped p-GaAs region compared to the structure discussed in Chapter 6.

Extending the emission wavelength of electrically injected nano-ridge lasers to the key telecom bands (O- and C-bands) constitutes an important direction for future research. Optically pumped O-band operation has already been demonstrated using $In_{0.45}Ga_{0.55}As$ quantum wells pseudomorphically strained on an $In_{0.25}Ga_{0.75}As$ nano-ridge base [1]. Achieving electrical injection in such structures will require the development of optimized p-i-n architectures and a systematic assessment of optical losses, injection efficiency, and thermal resistance. The GaInNAs/GaAs material system [2] also offers a promising alternative for realizing O-band quantum well lasers directly on GaAs. Another viable route involves InAs quantum dots (QDs) on GaAs substrates, where single-photon emission around 900 nm has recently been demonstrated in nano-ridge structures within our group [3]. Extending their emission toward longer wavelengths can be accomplished by incorporating $In_xGa_{1-x}As$ metamorphic buffer layers beneath the QDs, as reported in devices achieving 1.3 µm [4] and 1.5 µm [5] emission. Depending on the target application, either quantum well or quantum dot active regions may be favored: while QW lasers typically provide higher modal gain, output power, and modulation speed [6],

QD lasers offer superior temperature stability [7], enhanced defect tolerance [8], and lower linewidth enhancement factors [9].

Effective thermal management remains a critical challenge in selectively grown, small-volume InGaAs/GaAs quantum-well nano-ridge lasers on silicon. Their limited heat-spreading volume and high power density make them prone to localized temperature rise. Sparse contacting schemes exacerbate this by concentrating current flow beneath isolated contacts, leading to Joule heating, contact degradation, and potential thermal runaway [10]. Implementing densely spaced periodic contacts or the continuous-contact scheme proposed in Chapter 6 can significantly improve lateral heat spreading through the metal layer, thereby reducing thermal resistance and enhancing device reliability.

Finally, realizing efficient optical interfacing between monolithic III–V nano-ridge lasers and silicon photonic circuits remains a key milestone. A major advantage of lasers grown via selective epitaxy over those requiring thick buffer layers is their close proximity to the Si substrate, enabling compact and efficient coupling to co-integrated Si waveguides. For the nano-ridge lasers investigated in this PhD work, developing fabrication-tolerant, compact coupling schemes is an important next step. Preliminary designs of directional and adiabatic couplers operating in the O-band have already been demonstrated within our group [11], and further design optimization, fabrication, and experimental validation will be crucial to realize fully integrated III–V/Si photonic platforms.

References

[1] D. Colucci et al., Unique design approach to realize an O-band laser monolithically integrated on 300 mm Si substrate by nano-ridge engineering, *Opt. Express*, vol. 30, no. 8, pp. 13 510–13 521, Apr. 2022.

[2] K. Nakahara, M. Kondow, T. Kitatani, M. Larson, and K. Uomi, 1.3-μm continuous-wave lasing operation in GaInNAs quantum-well lasers, *IEEE Photonics Technology Letters*, vol. 10, no. 4, pp. 487–488, Apr. 1998.

[3] D. Colucci et al., Single-photon source monolithically integrated on a 300 mm silicon wafer using III–V nano-ridge engineering, *ACS Photonics*, vol. 12, no. 7, pp. 3626–3634, Jun. 2025.

[4] S. L. Golovynskyi et al., Photoelectric properties of the metamorphic InAs/InGaAs quantum dot structure at room temperature, *Journal of Applied Physics*, vol. 117, no. 21, Jun. 2015.

[5] M. Paul et al., Single-photon emission at 1.55 μm from MOVPE-grown InAs quantum dots on InGaAs/GaAs metamorphic buffers, *Applied Physics Letters*, vol. 111, no. 3, Jul. 2017.

[6] J. Huang, C. Li, R. Lu, L. Li, and Z. Cao, Beyond the 100 Gbaud directly modulated laser for short reach applications, *Journal of Semiconductors*, vol. 42, no. 4, p. 041 306, Apr. 2021.

[7] Z. Lv et al., Ultra-high thermal stability InAs/GaAs quantum dot lasers grown on on-axis Si (001) with a record-high continuous-wave operating temperature of 150 $^{\circ}C$, *Optics Express*, vol. 31, no. 15, p. 24 173, Jul. 2023.

[8] Z. Liu et al., Origin of defect tolerance in InAs/GaAs quantum dot lasers grown on silicon, *Journal of Lightwave Technology*, vol. 38, no. 2, pp. 240–248, Jan. 2020.

[9] Y.-Q. Qiu, Z.-R. Lv, H. Wang, H.-M. Wang, X.-G. Yang, and T. Yang, Improved linewidth enhancement factor of 1.3-μm InAs/GaAs quantum dot lasers by direct Si doping, *AIP Advances*, vol. 11, no. 5, May 2021.

[10] P.-Y. Hsieh et al., Degradation mechanisms of monolithic GaAs-on-Si nano-ridge quantum well lasers, *Journal of Lightwave Technology*, vol. 43, no. 12, pp. 5811–5819, Jun. 2025.

[11] Y. Shi, B. Kunert, Y. D. Koninck, M. Pantouvaki, J. V. Campenhout, and D. V. Thourhout, Novel adiabatic coupler for III-V nano-ridge laser grown on a Si photonics platform, *Opt. Express*, vol. 27, no. 26, pp. 37 781–37 794, Dec. 2019.